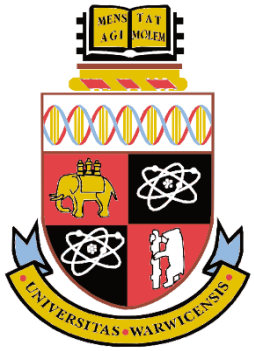

Single Nanoparticle Electrochemistry

By

Minkyung Kang

Thesis

Submitted to the University of Warwick

for the degree of

Doctor of Philosophy

Supervisor: Prof Patrick R. Unwin

Department of Chemistry

September 2017

Contents

List of Figures

List of Tables

Abbreviation

Abbreviation	
ac	Alternating current
AFM	Atomic force microscopy
C_d	Double layer capacitance
CE	Counter electrode
CF	Carbon fibre
C_{stray}	Stray capacitance
CV	Cyclic voltammogram
dc	Direct current
EOF	Electroosmotic flow
ET	Electron transfer
FEM	Finite element method
FE-SEM	Field emission-scanning electron microscopy
FIB	Focused ion beam
FPGA	Field-programmable gate array
GC	Glassy carbon
HER	Hydrogen evolution reaction
HOPG	Highly oriented pyrolytic graphite
LSV	Linear sweep voltammogram
MSE	Mercury sulfate electrode
NP	Nanoparticle
ORR	Oxygen reduction reaction
Pd-H_2	Palladium wire saturated with hydrogen
PZC	Potential of zero charge
QRCE	Quasi-reference counter electrode
RAM	Random assembly microelectrode
RE	Reference electrode
RuO_x	Ruthenium oxide
SAM	Self-assembled monolayer
SCE	Standard calomel electrode
SECCM	Scanning electrochemical cell microscopy

SECM	Scanning electrochemical microscopy
SEPM	Scanning electrochemical probe microscopy
SERS	Surface-enhanced Raman scattering
SICM	Scanning ion conductance microscopy
SNEI	Single nanoparticle electrochemical impact
SWCNT	Single-wall carbon nanotube
TEM	Transmission electron microscopy
UME	Ultramicroelectrode
WE	Working electrode

Acknowledgements

Firstly, I would like to thank my supervisor Prof Patrick R. Unwin for all of his support, encouragement and enthusiasm throughout my PhD. He has given me so many opportunities to develop my scientific skills and knowledge here in Warwick Electrochemistry and Interfaces Group and his advice on research and general life have brought me here to finalise my PhD.

I have truly enjoyed working with the state-of-art electrochemical instrumentation and with the amazing people in the group. I would like to thank all of you who has been in the group (including visitors) throughout my PhD. I sincerely appreciate your expertise and kindness, which has been incredibly helpful for me.

Special thanks to "Team Cell" including Binoy (previous member), David and Ashley for being fantastic to work with and, more importantly, great friends to throw banter at each other. I also would like to acknowledge Faduma, Maria, Emma and Sze who has been through the same years with me in this group and provided "supportive" talks during coffee breaks. Special thanks to Faduma, for introducing me to a great "field" of dank memes. Among the amazing master students who have worked with me in the group, I would like to give special thanks to Erin, who taught me how incredible it is to work with someone so positive and energetic. Also, thanks to all the lads in the group who had a few "Dangerous Wednesday" sessions alongside me and endured drunk MK.

I appreciate support from my parents from South Korea and my lovely sister, Minjung, who visited me in England and spent great time with me here. Finally, a huge thank you to Cameron, who has been the best supporter during my PhD at work and in life and put up with my everyday craziness.

Finally, I acknowledge the University of Warwick Chancellor's International Scholarship.

General Declaration

The work presented in this thesis is entirely original and my own work, except where acknowledged in the list below. I confirm that this thesis has not been submitted for a degree at another University. Material from this thesis has been published, as noted below.

The material in Chapter 3 was published as:

Time-Resolved Detection and Analysis of Single Nanoparticle Electrocatalytic Impacts

Minkyung Kang, David Perry, Yang-Rae. Kim, Alex W. Colburn, Robert A. Lazenby, Patrick R. Unwin

J. Am. Chem. Soc. **2015,** 137 (34), 10902–10905. 3D random walk simulation in the material was performed by Dr. David Perry

The material in Chapter 4 was published as:

Electrochemical Dissolution via Silver Single Silver Nanoparticle Impacts: Morphological Analysis of the Dynamic Response

Jon Ustarroz[†], **Minkyung Kang**[†], Erin Bullions, Patrick R. Unwin

Chem. Sci. **2017,** 8, 1841–1853. ([†]*equally contributed*) The data analysis and presentation in the material were performed with Dr. Jon Ustarroz.

The material in Chapter 5 was published as:

Simultaneous Topography and Reaction Flux Mapping At and Around Electrocatalytic Nanoparticles

Minkyung Kang, David Perry, Cameron L. Bentley, Geoff West, Ashley Page, Patrick R. Unwin

ACS Nano **2017**, 11 (9), 9525-9535. Finite element method (FEM) simulations in the material were performed by Dr. David Perry and characterization of nanoparticles with transmission electron microscopy (TEM) was performed by Dr. Geoff West.

The material in Chapter 6 was submitted as:

Quantitative Visualization of Molecular Delivery and Uptake at Living Cells with Self-Referencing Scanning Ion Conductance Microscopy-Scanning Electrochemical Microscopy

Ashley Page, **Minkyung Kang**, Alexander Armitstead, David Perry, Patrick R. Unwin

Anal. Chem. **2017**, 89, 3021−3028. The material in this paper also provided the basis of a chapter in Ashley Page's thesis (Warwick, expected in 2017) who jointly performed the experiments and fully performed FEM simulations. The substrate samples (*e.g.*, corn roots) were prepared by both Ashley Page and Mr. Alexander Armitstead.

Additionally, during my PhD I have contributed to the following papers whose results are not presented in this thesis:

Electrochemical maps and movies of the hydrogen evolution reaction on natural crystals of molybdenite (MoS_2): basal *vs.* edge plane activity

Cameron L. Bentley, **Minkyung Kang**, Faduma M. Maddar, Fengwang Li, Marc Walker, Jie Zhangb Patrick R. Unwin

Chem. Sci. **2017**, 8, 6583-6593.

Time-Resolved Detection of Surface Oxide Formation at Individual Gold Nanoparticles: Role in Electrocatalysis and New Approach for Sizing by Electrochemical Impacts

Cameron L. Bentley, **Minkyung Kang**, Patrick R. Unwin

J. Am. Chem. Soc. **2016,** 138 (39), 12755–12758.

Characterization of Nanopipettes

David Perry, Dmitry Momotenko, Robert A Lazenby, **Minkyung Kang**, Patrick R. Unwin

Anal. Chem. **2016**, 88 (10), 5523–5530.

Simultaneous Interfacial Reactivity and Topography Mapping with Scanning Ion Conductance Microscopy

Dmitry Momotenko, Kim McKelvey, **Minkyung Kang**, Gabriel N. Meloni, Patrick R .Unwin

Anal. Chem. **2016**, 88 (5), 2838–2846.

High-Speed Electrochemical Imaging

Dmitry Momotenko, Joshua C. Byers, Kim McKelvey, **Minkyung Kang**, Patrick R. Unwin

ACS nano **2015**, 9 (9), 8942–8952

And two review articles, which discusses much of the work published in this thesis and the above-mentioned studies:

Scanning Electrochemical Cell Microscopy: New Perspectives on Electrode Processes in Action

Cameron L Bentley, **Minkyung Kang**, Patrick R Unwin

Curr. Opin. Electrochem. **2017**, 6, 23-30

Frontiers in Nanoscale Electrochemical Imaging: Faster, Multifunctional, and Ultrasensitive

Minkyung Kang,† Dmitry Momotenko,† Ashley Page,† David Perry,† Patrick R. Unwin,

Langmuir, **2016**, 32, 7993–8008. (†*equally contributed*)

Abstract

This thesis presents various pipette-based techniques for resolving the electrochemical activities of single nanoentities (*e.g.*, nanoparticles, NPs) in time and/or space. In particular, the work provides a framework for understanding the (electro)chemistry of single NPs and the development of tools to resolve them temporally and/or spatially. Through the use of the state-of-the-art instrumentation developed by the Warwick Electrochemistry & Interfaces Group (WEIG), electrochemical measurements with a "static" probe (*i.e.*, micro-droplet electrochemical cell) have revealed detailed (temporally-resolved) information on the dynamics of the interaction of colloidal NPs (in solution) with electrode surfaces. Through careful data analysis, and supported by simulations, it has been demonstrated how current-time traces provide information on the physical dynamics of individual NPs on an electrode surface. This regime has been further applied to understand the electrodissolution of individual NPs and has revealed the complexity of the process, through carefully designed experiments and thorough quantitative analysis of large data sets. In addition, through the use of the aforementioned instrumentation, new scanning electrochemical probe microscopy (SEPM) regimes have been developed with a "dynamic" probe, providing spatial resolution. A greatly simplified nanoprobe configuration (*i.e.*, a single channelled probe) has been proposed for simultaneous topography and electrochemical flux mapping at the nanoscale, implemented with a new scanning protocol in scanning ion conductance microscopy (SICM). This was directly applied in tandem with FEM simulations to observe and explain heterogeneities in the ion flux at and around individual catalytic NPs adhered to an inert conductive surface during catalytic turnover conditions with electrochemical activity information on surface heterogeneities at the nanoscale. Finally, to highlight the generalities of the approaches, a new configuration of scanning electrochemical microscopy (SECM) combined with SICM with a double-channelled nanoprobe has been introduced, demonstrating the simultaneous visualisation of topography and uptake rate on a biological entity (cell), which is quantified by finite element method (FEM) simulations. In this configuration the probe is multifunctional, delivering analytes to the cell surface, providing probe positional information and detecting changes in the uptake rate of electroactive molecules across the interface.

Chapter 1. Introduction

1.1 Reactions at Electrodes

Electrochemistry is the branch of chemistry concerning the diverse processes that involve the passage of charge (*e.g.*, electrons and/or ions) across the interface between two phases. Electron transfer between a conducting electrode and a redox active species dissolved in an electrolyte solution is the most commonly encountered electrochemical process and is most relevant to the discussion of the work carried out in this thesis. In this case, applying a potential at the electrode changes the energy level of electrons within the metal (and more importantly, at the electrode surface), resulting in the gain/loss of electrons from/to electrochemically active molecules (oxidised and reduced forms are denoted O and R, respectively) in solution, shown schematically in Figure 1.1. Increasing the energy level of the electrons at the electrode, which can be achieved by externally applying more negative potentials, facilitates electron transfer from the electrode to redox species in solution and this is referred to as a reduction process (Figure 1.1, top). On the other hand, decreasing the energy level of the electrons at the electrode, achieved by applying more positive potentials, enables electron transfer from the redox species in solution to the electrode, referred as an oxidation process (Figure 1.1, bottom).

In both oxidation and reduction processes, the electron flow through an external circuit is measured as current (see below), which can reveal a wealth of information on the nature of the solution and the electrode, as well as the reaction that is occurring at the electrode/electrolyte interface. The net rate of an electrode reaction as a surface flux across the interface, υ (mol m^{-2} s^{-1}), is followed by:

$$\upsilon = \frac{i}{nFA} \qquad \text{eq (1.1)}$$

where i is the current (C s^{-1}), n is the stoichiometric number of electrons involved in the charge transfer, F is Faraday's constant (96485 C mol^{-1}) and A is the area of the electrode (m^2).[1] Therefore, as alluded to above, the current flow during electrochemical reaction at the surface is a measure of the rate of the reaction.

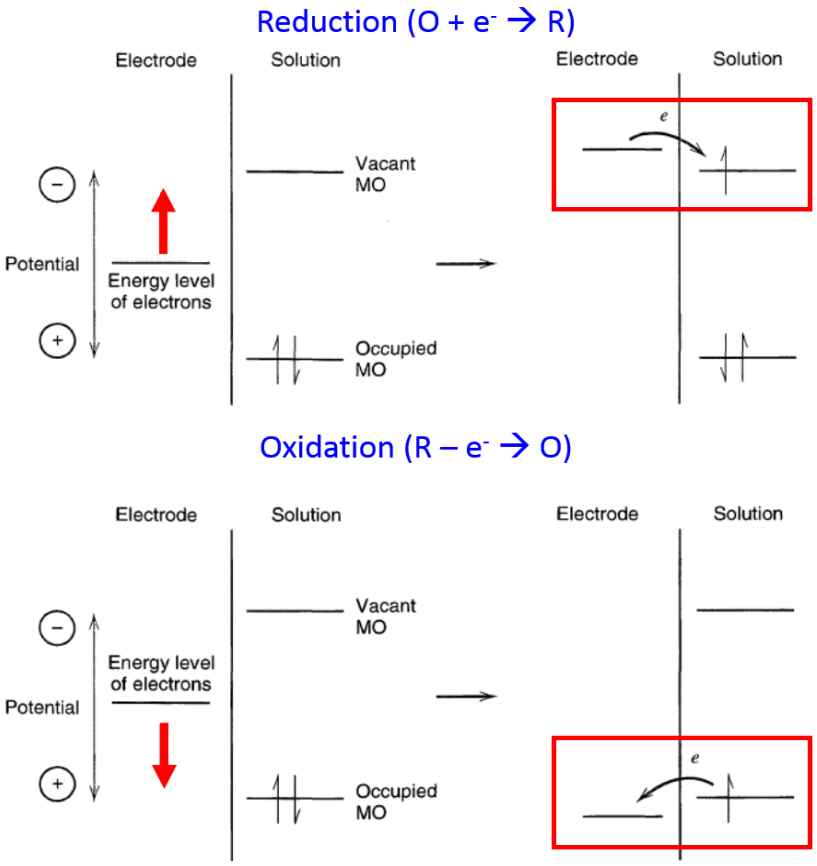

Figure 1.1 Illustration of a reduction (top) and oxidation (bottom) process, occuring between two different redox molecules in solution and an electrode. The oxidised and reduced forms of each molecule are represented as "O" and "R", respectively. The highest occupied molecular orbital (HOMO) of the molecule is denoted "Occupied MO" and lowest unoccupied molecular orbital (LUMO) is denoted "Vacant MO". Figure 1.1 was adapted from Bard and Faulkner (2001).[1]

The pathway of a general electrode reaction is illustrated in Figure 1.2. From this figure, it is clear that the factors that influence the rate of the reaction across the electrode/electrolyte interface are as follows:

- Electron transfer across at the electrode surface;
- Reactions preceding/proceeding the electron transfer;
- Mass-transport to/from the interface;
- Other surface reactions, including adsorption, desorption, or crystallization (*e.g.*, electrodeposition).

As previously outlined, in this thesis, the aim is to elucidate the reaction and mass-transport mechanisms associated with electrochemical reaction at NPs using spatially/temporally sensitive static/dynamic electrochemical probing methods. To this end, the fundamentals of the kinetics of heterogeneous electron transfer and mass-transport are outlined in brief below.

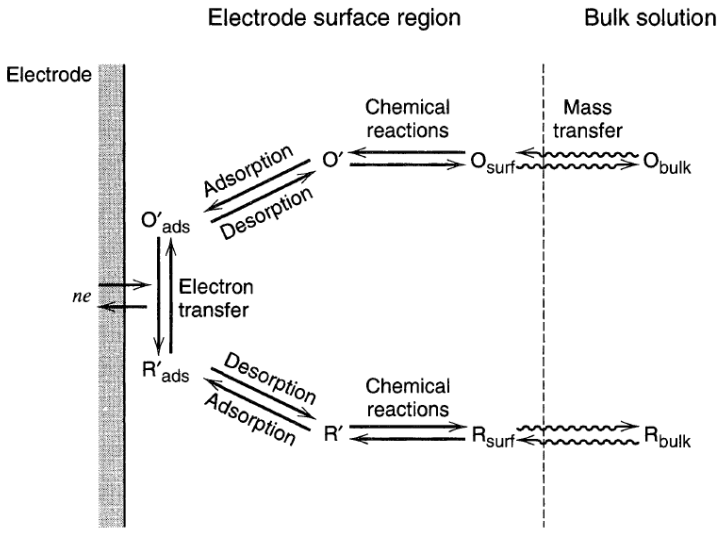

Figure 1.2 Pathway of a general electrode reaction. It needs to be noted that there are redox species limited by mass transfer [e.g., Hexaammineruthenium (III/II)] rather than other processes described in Figure 1.2. Figure 1.2 was adapted from Bard and Faulkner (2001).[1]

1.1.1 Kinetics of Electrode Reactions: Current-Potential Relationship

The classical Butler-Volmer formalism of electrode kinetics is considered herein, which can empirically predict the kinetics of a heterogeneous electron-transfer reaction which is controlled purely by the interfacial potential difference. The general redox reaction can be given by:

$$O + ne^- \underset{k_b}{\overset{k_f}{\rightleftharpoons}} R \qquad \text{eq (1.2)}$$

where O is the oxidised form, R is the reduced form and k_f and k_b are heterogeneous electron-transfer rate constants (cm s^{-1}) for the forward (reduction), *f*, and backward

(oxidation), *b*, reaction pathways, respectively. Reactions of the type shown in eq (1.2) proceed at rates which are proportional to concentrations of O and R at the electrode surface, with the net reaction rate, υ_{net}, given by:

$$\upsilon_{\text{net}} = \upsilon_{\text{f}} - \upsilon_{\text{b}} = k_{\text{f}} C_{\text{O}}(0,t) - k_{\text{b}} C_{\text{R}}(0,t) \qquad \text{eq (1.3)}$$

where $C_j(x,t)$ is the concentration of species *j* at distance *x* from the electrode surface ($x = 0$, at surface; $x = \infty$, in bulk) at time *t*. Combining eq (1.3) with eq (1.1) the overall (net) current, i_{net}, is:

$$i_{net} = i_{\text{f}} - i_{\text{b}} = nFA[k_{\text{f}} C_{\text{O}}(0,t) - k_{\text{b}} C_{\text{R}}(0,t)] \qquad \text{eq (1.4)}$$

If the simplest possible reaction process at the electrode (one step and one electron) is considered:

$$\text{O} + e^- \underset{k_{\text{b}}}{\overset{k_{\text{f}}}{\rightleftharpoons}} \text{R} \qquad \text{eq (1.5)}$$

and it is assumed that k_{f} and k_{b} have an Arrhenius form[1], they can be expressed as:

$$k_{\text{f}} = k^0 e^{-\alpha f(E-E^{0'})} \qquad \text{eq (1.6)}$$

$$k_{\text{b}} = k^0 e^{(1-\alpha) f(E-E^{0'})} \qquad \text{eq (1.7)}$$

where k^0 is the standard heterogeneous rate constant, α is the charge-transfer coefficient, $E^{0'}$ is the formal potential (incorporation of the standard potential and fraction of activity coefficients of the components) and f is defined by F/RT, where *R* is the gas constant and *T* is temperature. Accordingly, the heterogeneous rate constants, k_{f} and k_{b}, are exponentially related to the interfacial potential difference (or more specifically, $E - E^{0'}$) at the electrode. Substituting eq (1.6) and eq (1.7) into eq (1.4) gives the complete current-potential characteristic:

$$i_{net} = FAk^0[C_{\text{O}}(0,t)e^{-\alpha f(E-E^{0'})} - C_{\text{R}}(0,t)e^{(1-\alpha)f(E-E^{0'})}] \qquad \text{eq (1.8)}$$

Although not covered here, analogous *i*-*E* relationships can be derived for more complicated cases which include electrical double-layer effects and multistep reaction mechanisms.[2–4]

For the heterogeneous electron-transfer reactions shown in eq (1.2) and eq (1.5), when there is no net current flowing through the external circuit (*i.e.*, i_{net} is zero and the system is at equilibrium), the electrode potential is characterised by the Nernst equation:

$$E = E^{0'} + \frac{RT}{nF}\ln\left(\frac{C_O(\infty,t)}{C_R(\infty,t)}\right) \qquad \text{eq (1.9)}$$

The Nernst equation is a thermodynamic expression which links the electrode potential to fraction of the bulk concentrations of O and R (more specifically activity, the product of activity coefficients and concentrations of the redox components) regardless of the kinetics at the electrode. On the other hand, k^0 is a kinetic parameter, physically interpreted as a measure of the kinetic facility of a redox process, and is numerically equal to k_f and k_b when $E = E^{0'}$. If k^0 is large, and the system is able to achieve equilibrium on the experimental timescale, the process is termed 'electrochemically reversible'. If the reaction shown in eq (1.5) is assumed to be electrochemically reversible (*i.e.*, k^0 is large), the current-potential relationship eq (1.8) reduces to:

$$E = E^{0'} + \frac{RT}{F}\ln\left(\frac{C_O(0,t)}{C_R(0,t)}\right) \qquad \text{eq (1.10)}$$

In other words, at the electrochemically reversible limit, the surface concentrations of *O* and *R* are directly related to electrode potential simply with an equation of the Nernst form, regardless of the current flow in the system. When k^0 is small, as is the case when the reaction involves significant molecular rearrangement upon electron transfer and/or multistep mechanisms, the system will be sluggish to reach to equilibrium, which is referred to as electrochemically quasireversible or irreversible, depending on magnitude of k^0.

Most electrochemical processes in practice are rather more complicated than that presented in eq (1.5), including several elementary reactions which may or may not be heterogeneous electron transfer steps (*e.g.*, see Figure 1.2). The most sluggish step of the overall reaction mechanism is recognised as the rate-determining step (RDS). In theory, if the RDS is a heterogeneous electron transfer reaction, a Butler-Volmer type current-potential relationship of the type presented above can be applied

to understand the kinetics of the reaction. When the reaction requires a more complex knowledge of the reactions preceding the RDS, in modern electrochemistry, computational simulation can be employed in order to establish the complete theory that applies for a given reaction mechanism.

1.1.2 Mass-transport

In Section 1.1.1, it was assumed that mass-transport is not limiting the overall reaction rate at the electrode. In practice, however, mass-transport often becomes limiting on the experimental timescale (*e.g.*, see Figure 1.2). Mass-transport of a species to an electrode surface is described by the Nernst-Planck equation:

$$J_\mathrm{j} = -D_\mathrm{j}\nabla C_\mathrm{j} - \frac{z_\mathrm{j}F}{RT}D_\mathrm{j}C_\mathrm{j}\nabla\phi + C_\mathrm{j}v_\mathrm{L} \qquad \text{eq (1.11)}$$

where J_j is the flux density (mol cm^{-2} s^{-1}), D_j is the diffusion coefficient, z_j is the charge valence of species j, ϕ is electrostatic potential and v_L is the linear velocity of solution flow. ∇ is a Laplacian operator, the form of which is related to the electrode geometry.[1] When mass-transport to the electrode surface occurs in one dimension (*i.e.*, linear type to a planar electrode), eq (1.11) becomes:

$$J_\mathrm{j}(x,t) = -D_\mathrm{j}\frac{\partial C_\mathrm{j}(x,t)}{\partial x} - \frac{z_\mathrm{j}F}{RT}D_\mathrm{j}C_\mathrm{j}\frac{\partial\phi(x,t)}{\partial x} + C_\mathrm{j}v_\mathrm{L}(x,t) \qquad \text{eq (1.12)}$$

where $\frac{\partial C_i(x,t)}{\partial x}$ and $\frac{\partial\phi(x,t)}{\partial x}$ are concentration and potential gradients species j at distance x from the electrode surface at time t, respectively. The first, second and third terms represent the contributions of diffusion, migration and convection to total flux, respectively.

Diffusion is the movement of a species down a concentration gradient, which, in the current context, is generally induced by an electrode reaction (*e.g.*, the production or depletion of the electroactive species at the electrode surface). Fick's laws, which are differential equations describing the flux of a substance and its concentration as functions of time and position (*e.g.*, see the first term of eq (1.11) and eq (1.12)), can be solved to yield concentration profiles of a redox species. Migration is the movement of charged species (including supporting electrolytes and redox species) within a solution due to the influence of the electric field induced by the

application of a potential at the electrode. As it is described in the second term of eq (1.11), in a fixed electric field, flux due to migration is affected by mobility ($=\frac{z_j F}{RT} D_j$) and concentration of the species. Finally, convection in an electrochemical system can be due to thermal gradients and density variation (natural convection) or the application of an external mechanical force (forced convection).

In electrochemistry, the total flux is measured as a current (*i.e.*,eq (1.1)), and as a result it is difficult to treat an electrochemical system quantitatively in practice when all three modes of mass-transport are in effect. For this reason, electrochemical experiments in practice are often designed to make the contribution of one or more of the processes to the total flux negligible.[1,5] For example, electrochemical experiments are often carried out in the presence of large concentrations of supporting electrolyte, suppressing the migrational component of mass-transport. High concentrations of supporting electrolyte improve conductivity of the solution (*i.e.,* reduce Ohmic effect caused by resistance in the solution) as well as form only thin double layer so that all potential drops between electrode and plane of electron transfer where electron transfer takes places. In addition, natural convection can be simply avoided by maintaining steady temperature and preventing any mechanical perturbation in the electrochemical cell, such as stirring or vibration. Unless otherwise stated, the results discussed herein have been carried out under conditions where mass-transport is governed predominantly by diffusion.

The diffusion coefficient or diffusivity, D_j (m^2 s^{-1}) of a species is the proportionality constant between diffusional flux and the concentration gradient of the species in the vicinity of the electrode surface (*i.e.,* see the first term of eq (1.12)). The diffusivity of a solute in a continuum of solvent (*i.e.,* a solution) is given by the Stokes-Einstein equation:

$$D_j = \frac{k_B T}{6\pi\eta r_j} \qquad \text{eq (1.13)}$$

where k_B is the Boltzmann constant, η is a viscosity of the solution and r_i is the radius (assumed as sphere) of the solute. Treatment of diffusion in this fashion is suitable for most applications in general macro/micro-scale electrochemistry, where the electrode structure and geometry is well-defined and relatively simple.

The use of nanostructured electrode materials has become increasingly prevalent, particularly in materials science, where the mean-free path of species (related to the size of the diffusing molecule) and a unit of the nanostructure in question (*e.g.*, the size of a single nanopore or nanochannel) are comparable, and thus effective diffusion on the length scale of the unit dimension needs to be considered. Nanoporous structures are a representative example for this case, where Knudsen diffusion is suggested.[6,7] For instance, once a molecule enters a nanopore, it is confined within the nanostructure and therefore maintains a close distance to the inner wall of the pore (*i.e.*, the electrode surface, in the context of an electrocatalyst, *vide infra*). Consequently, there is a higher probability for the molecule to interact with the electrode surface inside the nanoporous structure compared to a macroscopic surface. As a result, a diffusing molecule tends to travel between the walls within a nanostructured material, and thus the true concentration gradient is less than the concentration gradient predicted from the first term of eq (1.12).[7]

1.2 Electrochemical Techniques for Single NP Detection: Static Measurements

The electrochemical signals arising from a single NP, for example *i-t* transients, are very small (*e.g.*, << 1 nA), and therefore cannot be probed by conventional macroscopic electrochemical techniques. Recent developments in the electrochemical detection of single NPs, which are broadly classified as static or dynamic measurements depending on whether the electrochemical probe is stationary or mobile during the measurement, respectively, are considered and discussed herein. In the static measurements considered below, the electrochemical probe is stationary throughout the electrochemical measurement and only a small area of electrode (typically nm^2 to μm^2) is exposed, resulting in increased detection sensitivity, as well as low background noise and current. Systems which utilize an ultramicroelectrode or a micro-droplet electrochemical cell for such measurements are described below, which have been used extensively in recent years to study the electrochemical response of single NPs in solution as they make contact or “impact” with the surface of a collector electrode.

1.2.1 Ultramicroelectrodes

Ultramicroelectrodes (UMEs), typically defined as any electrode with a critical dimension in the tens of μm range, have been widely utilised since the 1980s in a range of applications.[8] As shown in Figure 1.3, there are five main UME configurations, however of these, the microdisk is the most popular due to relatively simple fabrication processes compared to other geometries. The beneficial traits of UMEs which result from their characteristic dimensions are highlighted below.

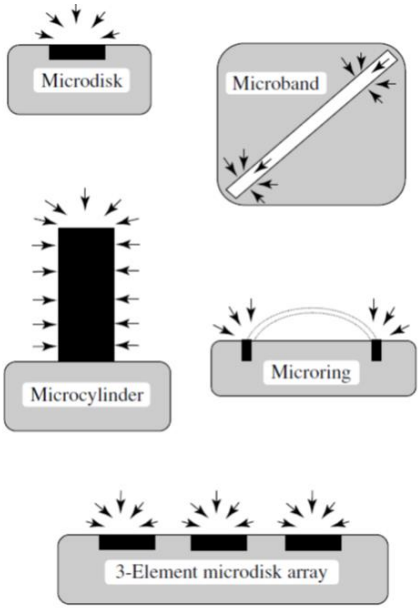

Figure 1.3 Most commonly utilised microelectrode geometries and their associated diffusion field. Figure 1.3 was adapted from Bard *et al*. (2003).[8]

Firstly, the effect of uncompensated resistance or Ohmic drop is often negligible when employing UMEs. In a general electrochemical cell, a potential is applied to the working electrode (WE) with a respect to reference electrode (RE) and the current flowing between the WE and a counter electrode (CE) is concurrently measured. The effective potential at the WE (E_{eff}) can be expressed as:

$$E_{\text{eff}} = E_{\text{app}} - iR_{\text{sol}} \qquad \text{eq (1.14)}$$

where E_{app} is a potential applied at the WE with respect to the RE, and iR_{sol} is the Ohmic term arising from current (i) flow through the finite resistance of the solution.[1] R_{sol} scales inversely with the radius of the electrode,[9] whereas i is typically six orders-

of-magnitude smaller at a UME (μm) compared to a macroelectrode (mm), meaning the influence of the iR_{sol} term is diminished with decreasing electrode size. In other words, when using a UME, $E_{eff} \approx E_{app}$, even in relatively resistive systems. This is beneficial, as it allows the experimental setup to be simplified to a two electrode system [where the RE also serves as a CE, in the form of a quasi-reference counter electrode (QRCE)], as well as expanding the possibility of studying to highly resistive systems, such as organic solutions.[10,11]

Secondly, for a solution-based faradaic process (*i.e.*, the electrochemical reaction of a dissolved redox species), the predominant mass-transport regime (diffusion profile) is time-dependent at an UME, as shown schematically in Figure 1.4. At short timescales, where the diffusion layer is smaller than the radius of the UME, mass-transport is governed by linear diffusion and therefore the faradaic current shows a similar time dependence as a planar macroelectrode (*i.e.*, $i \propto t^{-1/2}$).[1] At long timescales, however, where the diffusion layer is comparable to the radius of the UME, the faradaic current becomes time-independent (*i.e.*, steady state), with a radial diffusion profile near the UME surface. As a result, the current-time relationship for a UME with spherical geometry (r_s, radius of the spherical UME), the simplest case, is given by:[1]

$$i(t) = \frac{nFAD_O^{1/2}C_O}{\pi^{1/2}t^{1/2}} + \frac{nFAD_OC_O}{r_s} \qquad \text{eq (1.15)}$$

where the first and second term arise from planar and radial diffusion, respectively. Evidently from eq (1.15), it is clear that the (faradaic) current densities achievable at UMEs are much higher than planar electrodes, borne out of the much higher mass-transport rates at the former class of electrode. At a disk-UME, the current-time expression is more complicated as the surface is not homogeneously accessible, however, it still possesses planar and radial components, as is the case in eq (1.15). When mass-transport to a disk-UME is governed solely by radial diffusion, the steady-state current (i_{ss}) can simply expressed by:[12]

$$i_{ss} = 4nFD_OC_Or_{disk} \qquad \text{eq (1.16)}$$

when the ratio of a_{disk} to r_{disk} (RG) (Figure 1.4B) is larger than 10.[1] As RG affects the diffusion profile at the UME and i_{ss} can be accordingly modified to:[13]

$$i_{ss}(RG) = i_{ss} + 0.138i_{ss}(RG - 0.6723)^{-0.8686} \qquad \text{eq (1.17)}$$

which highlights the importance of the entire UME architecture.

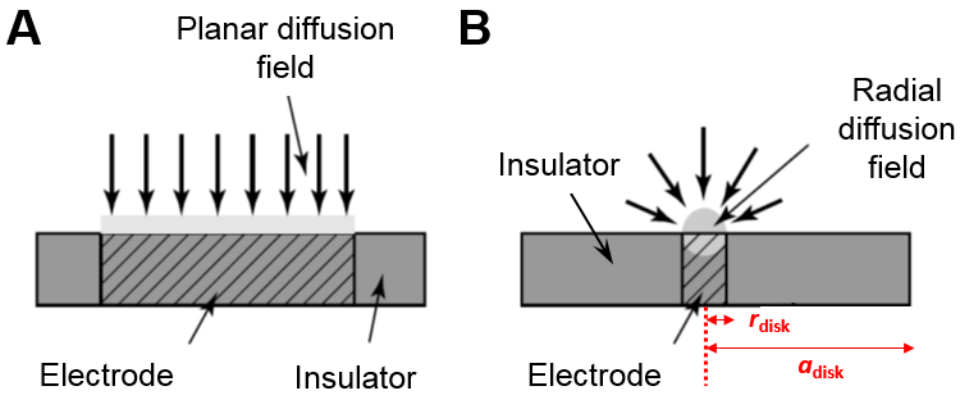

Figure 1.4 Schematic representation of the diffusion profiles on a disk-UME at (A) short (linear diffusion profile) and (B) long (radial diffusion profile) timescales. Figure 1.4 was adapted from Bard *et al*. (2003).[8]

Finally, non-faradaic processes are also affected by the small dimensions of UMEs. Non-faradaic (charging) current is proportional to the double layer capacitance (C_d), which for disk-shaped electrode, is given by:[8]

$$C_d = \pi r_{disk}^2 C_s \qquad \text{eq (1.18)}$$

where r_{disk} is radius of the disk electrode and C_s is specific double-layer capacitance of the electrode. As alluded to above, the faradaic current density achieved at a UME is much higher than at planar electrodes, meaning the faradaic to non-faradaic current ratio is greatly enhanced, and thus UMEs are a great tool for analytical studies requiring high sensitivity, with diminished background (double-layer) charging current.[8]

The RC time constant is another important consideration, which is usually given by product of R_{sol} and C_d, meaning it is proportional to r_{disk} (see below). Electrochemical signals, which are meaningful to be analysed, are only to be extracted at the time scale of five to ten times higher that of the RC time constant.[1] It also needs to be highlighted that a small RC time constant allows higher temporal resolution to be achieved at UMEs compared to conventional macroelectrodes, enabling high-speed transient measurements. Nevertheless, although C_d is minimal, stray capacitance (C_{stray}) arising from electrical components/connections in the instruments and the

UME (*e.g.*, especially small imperfections in the seal between the metal electrode and insulating sheath)[14] can limit the temporal resolution by increasing the RC time constant:[8]

$$RC = \frac{1}{4\kappa r_{disk}}(\pi r^2 C_s + C_{stray}) \qquad \text{eq (1.19)}$$

where κ is the conductivity of the solution. Therefore, it is important to note that non-faradaic currents may argue from the instrumental setup, as well as the way in which the UME is fabricated (*e.g.*, conductor/insulator seal), which can limit the sensitivity and speed of measurements.

Overall, the unique properties of UMEs enable more sensitive electrochemical analysis in unusual environments compared to conventional macroelectrodes and facilitate high-speed transient measurement as well as spatially resolved measurements in SECM.[8,15] Furthermore, applications of UMEs have been advanced to study the electrochemical properties of nanoscale samples/materials and thus, recent key studies employing UME probes for single entity measurement at the nanoscale are presented in the following sections.

1.2.2 Single Nanoparticle Electrochemical Impact Experiments Using UMEs

The current measured from a single nanoparticle electrochemical impact (SNEI) is expected to be less than 1 nA (depending on the size of NPs and analyte concentration, *vide infra*), which would be impossible to distinguish from the background current (noise) with a conventional macroelectrode. As highlighted above, the background current and current noise level is dramatically diminished at UMEs, rendering SNEI detection possible. In addition, the experimental setup is simplified, as shown in Figure 1.5A, with two electrodes (a RE and a WE) connected to a potentiostat capable of measuring small currents.

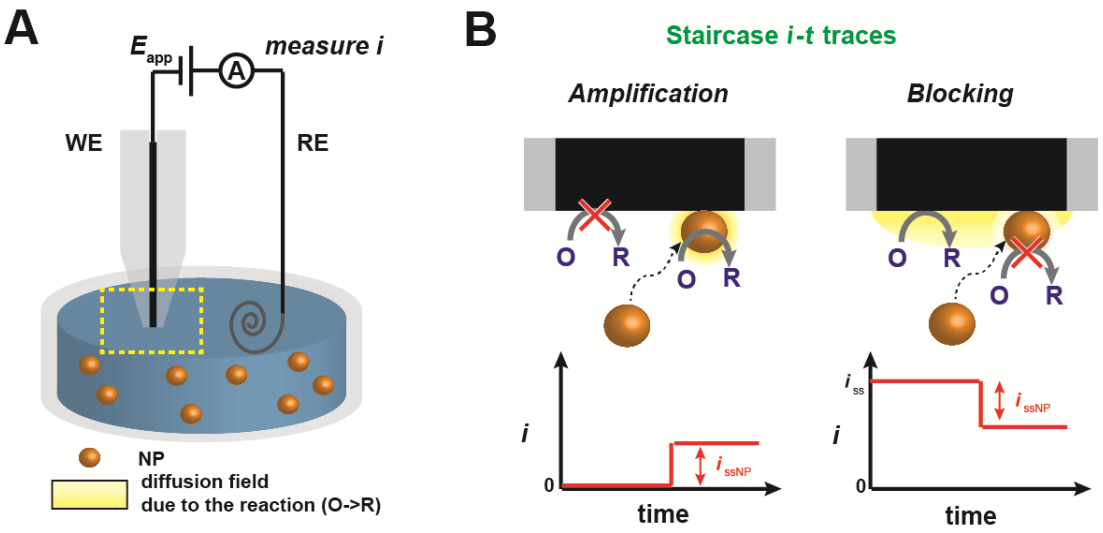

Figure 1.5 (A) Schematic of a SNEI experiment setup using a UME as the WE. (B) Schematics and typical *i-t* transient arising from NPs after a "sticking" impact (*i.e.*, "staircase" response), resulting in either amplification (left) or blocking (right) of the reaction of interest on the collector electrode surface.

The SNEI method term "electrocatalytic amplification" was first demonstrated by Bard *et al.*,[16] who observed the current amplification that occurs during electrocatalytic NP impact on a catalytically inert UME surface (Figure 1.5B, left). In these experiments, a potential is applied at the collector electrode (E_{app}), which is insufficient to drive the reaction of interest (*e.g.*, proton reduction, hydrazine oxidation, borohydride oxidation) at this material, but able to drive it at catalytic NPs (*e.g.*, Pt or Au NPs) present in solution. Hence, when the NPs moving by Brownian motion, "impact" the collector electrode, the electrocatalytic reaction occurs at the NP surface, resulting in "current amplification" and thus a measurable signal (typically an *i-t* transient).[16–21] The collector electrode material (UME) is chosen to be electrochemically inert to target electrocatalytic reactions[16,22] or (electro)chemically modified to block the reaction of interest,[19,23,24] for observation of the NP impact.

Considering a NP of spherical geometry on an infinite (catalytically inert) planar surface, the magnitude of the current for a diffusion controlled reaction at steady state (i_{ssNP}) is given by:[25]

$$i_{ssNP} = 4\pi ln2nD_O C_O r_{NP} \qquad \text{eq (1.20)}$$

where r_{NP} is the radius of a NP (m). Due to the small size of the conventionally used NPs (a few nm to hundreds of nm, typically), the characteristic steady-state diffusion time, $t_{ss} \approx r_{NP}^2/D_O$, is the sub-micro to micro-second timescale, which is too fast to measure with conventional instrumentation. This means that the initial current transient expected during a NP impact, arising from both non-faradaic and non-steady-state faradaic processes, is not measureable with a conventional electrometer and thus, assuming the reaction is diffusion controlled, the initial measured current value is expected to be i_{ssNP} from eq (1.20). Furthermore, the measured current is expected to remain at i_{ssNP} as long as NP resides on to UME without deactivation of electrocatalytic activity. As i_{ssNP} is directly proportional to r_{NP}, the magnitude of i_{ssNP} can be used for NP size analysis[17,26] and there are recent studies analysing the cyclic voltammogram of a residing individual NP after the impact.[27,28]

When the NPs permanently reside (or "stick") on the collector electrode after the initial collision event, the measured current exhibits a "staircase" morphology, as multiple NPs impact on the collector electrode with time (Figure 1B). The frequency of NP impact (f_{NP}) with the collector electrode can be estimated by:[17,29]

$$f_{NP} = 4D_{NP}C_{NP}N_A r_{disk} \qquad \text{eq (1.21)}$$

where D_{NP} is the diffusion coefficient of NPs ($cm^2\ s^{-1}$), C_{NP} is the concentration of NPs (M), N_A is the Avogadro constant ($6.022 \times 10^{23}\ mol^{-1}$) and r_{disk} is the radius of the collector electrode (m), according to a model based on a diffusion-limited flux of NPs at a collector electrode. The D_{NP} also can be reasonably estimated by r_{NP} from the Stokes-Einstein equation [eq (1.13)]:

$$D_{NP} = \frac{k_B T}{6\pi\eta r_{NP}} \qquad \text{eq (1.22)}$$

where η is the dynamic viscosity of the solution (8.90×10^{-4} Pa s for dilute aqueous solution). The proportionality between f_{NP} and NP concentration, size of the NP and size of the collector electrode has been confirmed experimentally, where the results fit the model based on a diffusion-limited flux of NPs.[30] In many reports,[17,26,31,32] however, the empirically obtained f_{NP} did not correspond to the estimated f_{NP} from eq (1.21), which is thought to be attributable to incomplete (non-conductive) contact of NPs during the impact (not measurable) or a non-diffusion-limited (stochastic) interaction between the NP and the collector electrode (*vide infra*). Additionally, it is possible that there are electrostatic interactions between the charged surface and the

NPs, although this is diminished through the addition of a high concentration of supporting electrolyte.

A similar SNEI regime has also been applied to investigate the blockage of electrochemical current by impacting non-conductive NPs (Figure 1.5B, right).[29,33] For example, an Au UME biased at a potential where an electrochemical reaction (*e.g.*, ferrocene methanol oxidation) occurs at a diffusion-limited rate generates a constant current (*i.e.*, see eq (1.16)), which decreases in a "staircase" fashion as (negatively) charged insulating NPs (*e.g.*, carboxylated latex beads) impact and adhere to the collector electrode surface. It was found that the motion of the charged NP in the vicinity of the electrode surface was also affected by electrophoretic migration, with f_{NP} increasing with decreasing ionic strength.[29] Furthermore, f_{NP} and the associated decrease of electrochemical current is enhanced at the interface between the metal electrode and insulating sheath (*i.e.*, electrode edge), due to the high electric field at the interface.[33] This enhancement was visualised and confirmed using optical microscopy combined with the SNEI setup, while simultaneously monitoring the change in current magnitude.[34] The electrochemical current blocking regime has been further expanded to detect the impact of single biological entities, such as enzymes, DNA macromolecules and viruses, as most of these entities are electrochemically inert.[35–37]

The *i-t* transient associated with NP impact is observed as "blips" rather than a "staircase" in SNEI when: (i) the NP sticks to the collector electrode and then deactivates; (ii) the NP undergoes electrodissolution after contact with the collector electrode; or (iii) the NP undergoes a non-sticking interaction with the collector electrode surface (Figure 1.6). In processes (i) and (ii), the collector electrode acts as a "NP sink" and therefore are diffusion controlled, with f_{NP} predicted by eq (1.21) above, whereas in process (iii), the NPs "escape" the collector electrode "sink" and thus is not a diffusion controlled process (*vide infra*). One theory regarding "deactivation" during the impact is progressive surface contamination on the NP surface, which was observed experimentally by considering the hydrogen reduction reaction during Pt NP impacts on carbon fibre (CF) UME.[17] This electrocatalytic reaction involves adsorption of hydrogen on the Pt NP surface and is thus sensitive to surface contamination.[17,38]

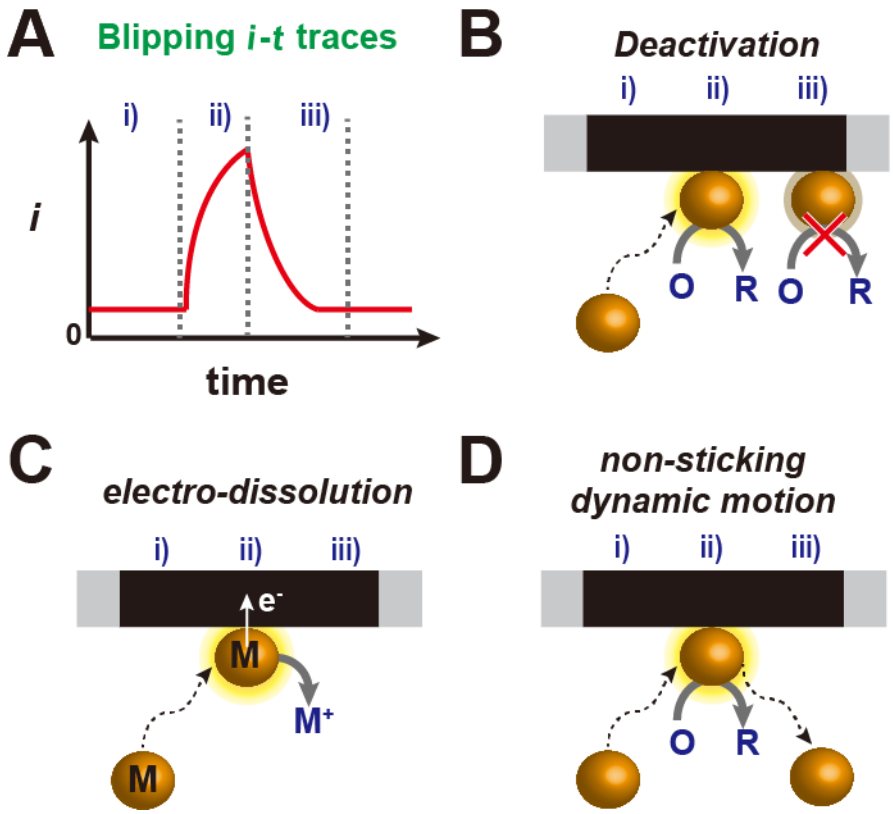

Figure 1.6 (A) Schematic of a typical *i-t* transient for a "blipping" response during a SNEI experiment. Three possible processes giving rise to the response are illustrated: (B) deactivation; (C) electrodissolution; and (D) non-sticking dynamic motion.

This was further investigated by intentionally "poisoning" the surface of Pt NPs with Hg (achieved using a Hg deposited UME) during SNEI with hydrazine oxidation[26], which is otherwise well-known for following the traditional diffusion limited flux process and giving characteristic "staircase" responses with consistent activity during the impact.[16,17] The experimental f_{NP} was reasonably close to that predicted by eq (1.21), meaning that the NP impact on the collector electrode is following the traditional diffusion-limited route. However, *i-t* traces displayed the "blipping" rather than "staircase" morphology, as the hydrazine oxidation process is gradually "switched off" by the contamination of the Pt NP surface with Hg during the impact.[26,39] A similar observation was made during Au NP impact with borohydride or hydrazine oxidation, except instead of NP surface poisoning with Hg, the Au NPs were passivated by forming a catalytically inert AuO_x monolayer during the impacts (*vide infra*).[24] This is work of the author of this thesis, but is not included in the results chapters. It has also been suggested that surface deactivation is

attributable to gas bubble formation (arising from the electrocatalytic reaction) on the surface of NPs, which physically blocks the catalytic reaction. Indeed, nano-bubble formation physically blocking further electrochemical processes during the hydrogen evolution reaction (HER) ($2H^+ + 2e^- \rightarrow H_2$) and hydrazine oxidation ($N_2H_4 \rightarrow N_2 + 4H^+ + 4e^-$) on Pt nano-electrodes has been well established.[40–42] There are possible examples of this phenomenon in SNEI, where IrO_x NPs oxidise water during the impact,[31] generating oxygen gas as a product of the reaction, or Pt NPs oxidise hydrazine on a catalytically inert Ni UME at more positive E_{app}, driving higher N_2 generation.[32] However, it needs to be noted that the nano-bubble formation on NPs during SNEI is expected to be a dynamic and complicated process and thus more direct evidence needs to be provided.

The "blipping" *i-t* transient may also be attributable to non-sticking interaction dynamics of the NP in the vicinity of the collector electrode surface. In this case, the current is diminished as the NPs leave the electron tunnelling region in the vicinity of collector electrode surface. Thus, the motion of the NP is governed by reversible ("non-sticking") collisions with the collector electrode, rather than a diffusion limited flux process, as established above. As a result, the collector electrode no longer acts as a "NP sink" and thus f_{NP} cannot be predicted by eq (1.21). In addition, the NP-collector electrode interaction time is expected to be very short. For instance, it is typically on the order of tens of ns for a nm step motion of a NP within the tunnelling region when purely stochastic Brownian motion of NPs is assumed,[30,43] making the experimental SNEI measurements more challenging. Nevertheless, it is important to note that the temporal step estimation of NP collision does not include interaction (*e.g.*, physical and chemical adsorption/desorption) between NP and the collector electrode surface and thus the "reversible" collision process needs to be investigated in more detail. Recent developments in instrumentation, including high bandwidth electrometers (10 - 100 kHz) and nanoscale electrode geometries, as well as new electrochemical regimes for SNEI probing (see Chapter 3 and 4 for further discussions) have improved the temporal resolution of these measurements, making experimental observation of non-sticking dynamics of NPs in the vicinity of a collector electrode surface possible.[44,45] In these studies, a single NP collision occurs on the order of ms and the average f_{NP} was orders of magnitude higher than f_{NP} estimated by

eq (1.21), due to multiple collisions of a single NP that have been observed for the first time and provide a new impetus to this field.

Lastly, electrodissolution of the NP during the impact also gives rise to a "blipping" *i-t* transient, as the NP physically dissolves while residing on the collector electrode surface. The overall electrodissolution of a metallic NP can be expressed as:

$$\mathrm{M_{NP}} \rightarrow \mathrm{M_{NP}^{n+}} + ne^{-} \qquad \text{eq (1.23)}$$

where *n* is the number of electrons per metal atom in the NP. Thus, using this approach, the number of moles of metal atoms dissolved from a NP (N_M) can be estimated from the area of a single *i-t* trace (*i.e.*, charge, $Q = it$) during the NP impact via Faraday's law:

$$N_M = \frac{Q}{nF} \qquad \text{eq (1.24)}$$

Hence, when a NP is completely dissolved during a single impact, the size of the NP can be estimated through analysis of a single *i-t* transient, assuming that the NP is spherical, using the following:

$$r_{NP} = \sqrt[3]{\frac{3N_M A_M}{4\pi\rho}} \qquad \text{eq (1.25)}$$

where A_M is relative atomic mass and ρ is the bulk density of the metal of NP.

Compton *et al*. have demonstrated *in-situ* size analysis of Ag[46,47] and Cu[48] NPs with nm resolution and addressed colloidal stability and aggregation phenomena[49,50] using the SNEI-electrodissolution approach. Although recent studies, carried out with improved SNEI measurement systems and in combination with complementary techniques, have revealed that the electrochemical dissolution of Ag NPs is a somewhat more complex process. Firstly, improvement of the temporal resolution has allowed the *i-t* transients to be analysed in greater depth, revealing multiple partial electrodissolution "events" associated with a single Ag NP after initially making contact with the collector electrode. This implies that the blipping *i-t* responses are attributable to both electrodissolution of Ag and the non-sticking dynamics of Ag NPs on the collector electrode surface.[51–55] The non-sticking dynamics of Ag NPs with the collector electrode is material-dependent as the affinity of Ag towards surfaces varies.[51,56] Additionally, this was further elaborated upon by introducing spectroscopic

microscopy in tandem with SNEI measurements of Ag NP electrodissolution, providing images during Ag NP electrodissolution on the collector electrode surface.[57–60] A few possible reasons for multiple electrodissolution processes were suggested, including near-wall hindered diffusion in the vicinity of the collector electrode[51,55] and charge accumulation on the Ag NP surface during dissolution to Ag^+.[54] Although interpretation of Ag NP electrodissolution is undoubtedly complicated, general coulometric SNEI methodology is empirically more straightforward and has now been extended to *in-situ* size analysis of Mo[61], C-60[62], Au[24,63] and other systems, such as NP alloys[64] and bioanalysis[65].

1.2.3 Micro-Droplet Electrochemical Cell

Instead of immersing the entire electrode in bulk solution, a droplet probe can be brought to ("landed" on) the surface of interest, forming a confined electrochemical cell. Using this methodology, charge transfer at a localized area of the surface can be measured directly. Figure 1.7A illustrates early examples of the micro-droplet electrochemical cell setup for static measurements. A capillary, the tip end opening diameter varying from 1-1000 μm, filled with electrolyte, electrochemical reactants and a quasi-reference counter electrode (QRCE) is mounted on a mechanical micro-positioner and positioned over the surface of interest.[66–72] A silicone or rubber gasket (Figure 1.7B) is fixed onto the end of the capillary to reduce evaporation and leaking of the solution, as well as ensuring a well-defined WE area when the droplet is contacted with the (semi)conducting surface of interest.[67] As a result, in this configuration, the dimensions of the WE are determined by the geometry of the capillary end and there is no direct contact of the capillary with the surface of interest. The contact of the confined droplet onto the surface can be made mechanically using micro-positioners with concurrent optical and contact force monitoring when the droplet is large enough to be visualized optically.[66,67] Feedback of some signal, reported in the most recent advances [from the Warwick Electrochemistry and Interfaces Group (WEIG)],[73] can be utilized to provide more fine control of the positioning of a micro-droplet on the surface. This will be further discussed in the dynamic measurement section (1.3.4). Once the droplet is in contact with the substrate surface, electrochemical measurements are made as a function of time or potential, by

applying a bias between the QRCE in the capillary and the WE defined by the footprint of the droplet cell.

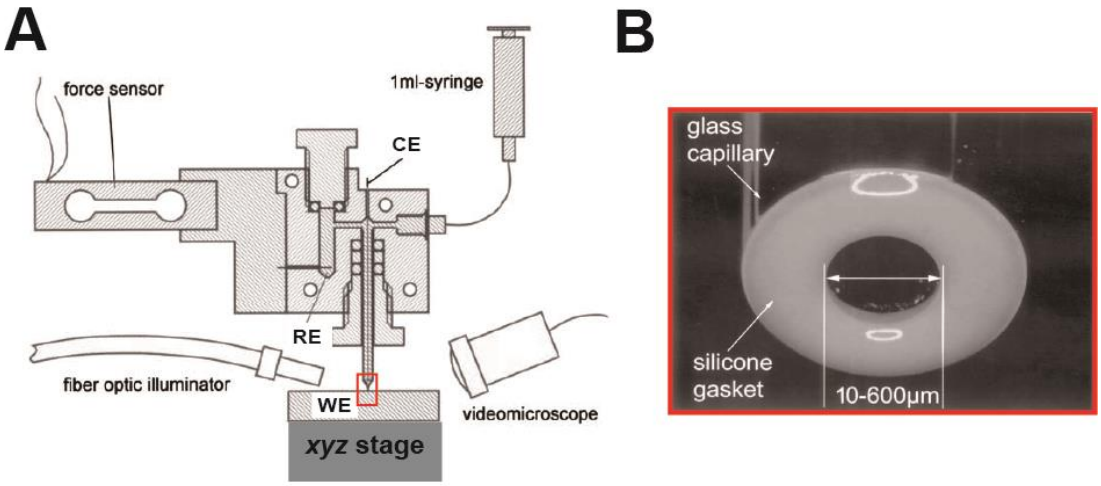

Figure 1.7 (A) A schematic of the early stage of micro-droplet electrochemical cell setup with optical and contact force monitoring. (B) Optical image of a glass capillary with an applied silicone gasket. Figure 1.7 was adapted from Lohrengel *et al*. (2001).[67]

The micro-droplet electrochemical cell method enables the investigation of electrochemical properties in small, confined areas of the substrate surface, as well as expanding the range of materials which can be studied to those which cannot be fabricated into a conventional WE. This technique was initially implemented for static single-point measurements in corrosion studies on a stainless steel to study localized (pitting) corrosion initiation.[66] It was further utilized for local surface modification with surface oxide layers and to characterise grains and grain boundaries on alloy materials.[67,68,70–72] This was advanced from the microscale to the nanoscale, with the use of a 150 nm diameter opening capillary and shear-force positional feedback mode, demonstrating nanolithography through the electrodeposition of copper lines (200 nm thickness) on gold and silicon surfaces.[69]

In addition to the advantages highlighted above, the droplet contact method eliminates that part of C_{stray} that can result from incomplete sealing between the metal electrode and insulating sheath in UME fabrication.[14] This is beneficial in reducing the background noise associated with C_{stray}, improving the temporal resolution of current measurements for SNEI.

1.2.4 SNEI Experiments Using the Micro-Droplet Electrochemical Cell Method

The addition of colloidal NPs into the capillary probe in the micro-droplet electrochemical cell method enables SNEI measurements to be carried out (Figure 1.8A). It needs to be highlighted, again, that contactless electrochemical measurement using the micro-droplet electrochemical cell method opens up the possibility to work with a wide range of substrate materials including delicate samples such as a carbon film on a transmission electron microscopy (TEM) grid,[56,74,75] and materials generating low background current such as highly oriented pyrolytic graphite (HOPG)[44,76] and self-assembled monolayers (SAMs) on Au.[77] The use of a TEM grid as a substrate for SNEI measurements was first demonstrated by electrocatalytic hydrazine oxidation at Au NPs, which showed a good agreement with previous SNEI studies using UMEs.[76] After the initial sticking collision of the Au NP on the TEM grid, the size and shape of the reacting particle was subsequently analysed in TEM and compared to the *i-t* impact signal. This is the first example of a true structure-function study using the SNEI approach.

The addition of high bandwidth current measurement systems to the micro-droplet electrochemical cell setup also allows the morphology of the *i-t* traces to be related to the amplification condition (*i.e.*, time constant of the instruments measuring the current), as well as the detection of rapid impact events that are often overlooked by other studies with conventional instrumentation.[49,78]

This approach was utilized to study the impact of Au NPs on Au surfaces functionalized with self-assembled monolayers (SAMs) of alkanethiols with different functional groups (*i.e.*, -OH, -COOH, $-CH_3$) (Figure 1.8B).[77] The strong effect of the surface chemistry on the residence time and electron transfer (ET) kinetics of the NPs was explored through the outer sphere oxidation of $Fe(CN)_6^{4-}$ to $Fe(CN)_6^{3-}$ during NP impact events.[77] Moreover, it was also shown that the bandwidth of the current amplifier effects the apparent residence time of the NP on the substrate surface and influences the transient signal recorded, especially when an NP resides for a short-time on a collector electrode.[51,77] For instance, when the residence time of NPs on a

collector electrode surface is shorter than the rise time of the current amplifier, an attenuated electrochemical (*i-t*) response is observed.[77]

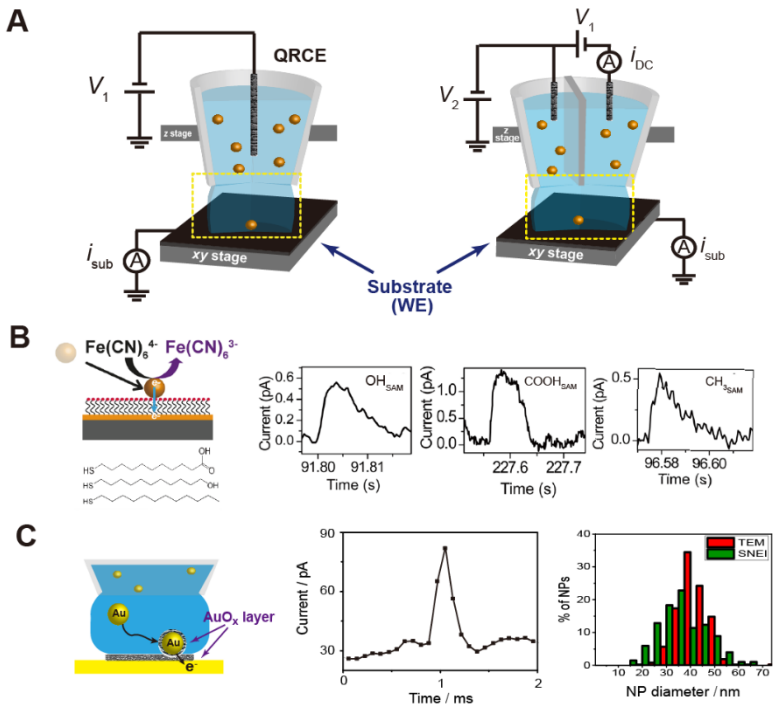

Figure 1.8 (A) Schematics of the micro-droplet electrochemical cell setup for SNEI experiments using a single channelled probe (left)[24,51] and a double channelled probe (right).[44,76,77] Confined droplet contact on the substrate is achieved through monitoring signals (*i.e.*, currents) induced by the circuit completion (i_{sub}) and the deformation of the droplet (i_{DC}). More operation details are provided in Section 1.3.4. (B) Principle of a single Au NP electrochemical impact on SAM-modified Au electrodes and typical *i-t* responses with, −OH, −COOH, and $-CH_3$ terminated SAMs. (B) was adapted from Chen *et al*. (2015).[77] (C) Illustration of an AuO_x layer formation on an Au NP through electron tunnelling between the Au NP and passivated Au electrode surface, with a typical *i-t* response of the process followed by comparisons of size analysis between TEM analysis and SNEI. (C) is adapted from Bentley *et al*. (2016).[24]

As mentioned above and in Section 1.2.2, high temporal resolution in the *i-t* transient measurement allows considerable insight into NP motion and dynamic (non-sticking) surface interactions, providing evidence of a single NP undergoing multiple interactions with a collector electrode surface. Studies of the electrocatalytic oxidation

of H_2O_2 at RuO_x NPs with a high bandwidth current measurement system demonstrated in-depth statistical analysis of characteristic current rise time distributions (< 700 μs), attributable to the NP hindered diffusion in the vicinity of a collector electrode surface, supported by 3D random walk simulations.[44] Improved temporal resolution was also applied to Ag NP electrodissolution studies (also mentioned in Section 1.2.2), showing a complex process involving size-dependent (r_{NP} = 5 to 50 nm) partial dissolution based on various distinctive *i-t* traces and the residence time of the NPs.[51] Both works are presented in more detail in Chapters 3 and 4, respectively. In a later study, with similar experimental regime, *i-t* traces with high temporal resolution allowed the observation of rapid surface oxidation (*ca.* 500 μs) at single Au NPs (to form a monolayer of AuO_x) during impact with an Au/AuO_x collector electrode (Figure 1.8C). The charge passed during the surface oxidation process was used for NP sizing analysis and the results were shown to be comparable to what was measured using TEM (Figure 1.8C). Furthermore, direct empirical evidence of the suppression in the (electro)catalytic activity of the Au NPs was shown, effectively "switching off" the borohydride and hydrazine oxidation processes due to formation of a passivating oxide layer on the surface of the NPs.[24]

1.3 Electrochemical Techniques for Single NP Detection: Dynamic measurements

In dynamic measurements, the probe is translated ("scanned") across the surface of interest (*e.g.*, catalytic NPs on a support), during the measurement, to collect spatially resolved electrochemical information. Methods in this category are generally termed scanning electrochemical probe microscopy (SPEM). Recent advances have been reviewed by the author.[79] When the probe can provide positional feedback, topographical information is also obtained, thus allowing structure to be correlated to function (*e.g.,* electrochemical activity). Herein, recent studies demonstrating the visualisation of individual NP activity with nanoscale spatial resolution using advanced SEPM techniques are highlighted and discussed.

1.3.1 Scanning Electrochemical Microscopy

Scanning electrochemical microscopy (SECM) was introduced in 1989 by A. J. Bard[80] followed by the first demonstration from Engstrom *et al*. in 1987,[81] employing an UME as a probe to investigate heterogeneous electrochemical activities at an electrode/electrolyte interface. Since this first demonstration of SECM, due to the fast adoption of this robust technique in the field of electrochemistry, it has been employed in a wide range of the applications in the fields of chemistry, biology, and material science.[15] Disk-UMEs are the most commonly utilised SECM probe as they are relatively easy to fabricate and commercially available.[8]

The electrochemical feedback (*i.e.*, current) at the SECM probe (i_{tip}) provides information on the composition of the solution, distance between the probe and substrate ($d_{t\text{-}s}$) and the electrochemical nature of the substrate (Figure 1.9). When the tip (RG > 10) is positioned over a substrate surface at a distance far enough to not be affected by any processes on the substrate interface (*i.e.*, in bulk), and a fixed potential is applied at the tip, which is sufficient to convert species A to B at the diffusion-controlled rate, i_{tip} is predicted to be constant, as described by eq (1.16) (where $\underline{i}_{ss} = i_{tip\infty}$). i_{tip} changes as the probe is brought near the substrate surface due to perturbation of the diffusion profile at the tip. When the substrate is electrochemically inert (*e.g.*, an insulator), the diffusion at the tip is hindered by the substrate and i_{tip} decreases as the tip approaches to the substrate surface (Figure 1.9B), which is known as "negative feedback". On the other hand, at an electrochemically active surface (*e.g.*, a conductor), which is biased at a potential which converts species B back to A (B is generated at the tip), i_{tip} increases as the tip approaches to the substrate surface (Figure 1.9B), which is known as "positive feedback". Typical approach curves in both cases are presented in Figure 1.9, with i_t, which is i_{tip} normalised with $i_{tip\infty}$, versus L, which is $d_{s\text{-}t}$ normalised with the radius of the tip (r_{tip}). A multitude of operation modes have been reported, including generation-collection mode, where the $d_{t\text{-}s}$ is very small (within a few tip radii) and the substrate is biased at a potential which generates B from A and the tip detects B or vice versa, where the substrate detects B which is generated at the tip.[82] More importantly, using these approaches, quantitative analysis of electrochemical activity and kinetic heterogeneities at the surface can be

investigated as i_{tip} varies with k^0 as it is scanned across the surface of interest (Figure 1.10).

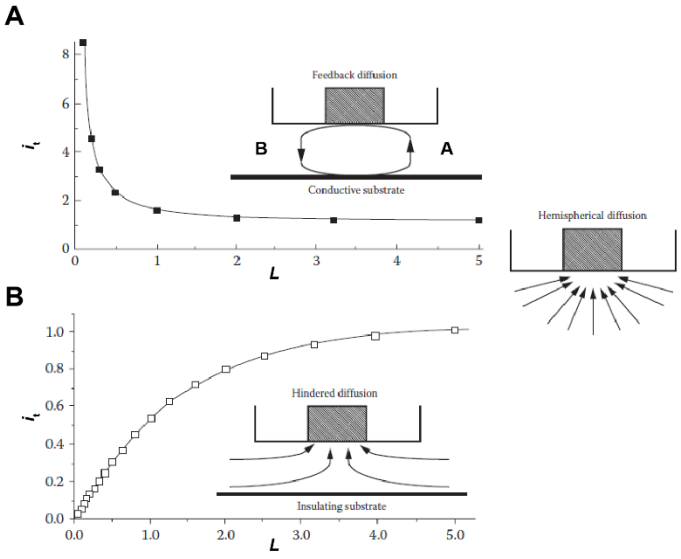

Figure 1.9 i_t as a function of tip–substrate separation, L ($d_{t\text{-}s}$ normalised with r_{tip}) where the substrate is (A) a conductor ("positive feedback") and (B) an insulator ("negative feedback"), with illustrations of the diffusion profile at the tip in each case, in bulk (hemispherical), on a conductor (feedback) and on an insulator (hindered). Figure 1.9 was adapted from Bard *et al*. (2012).[82]

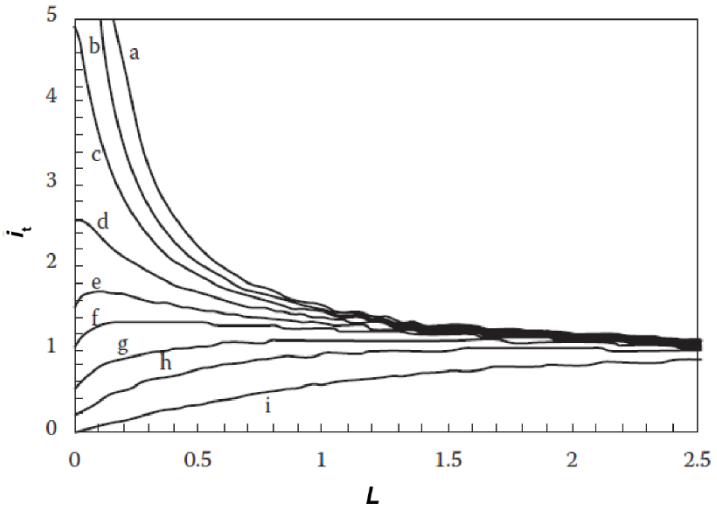

Figure 1.10 Approach curves as a function of k^0 for electron transfer (redox) reaction at the substrate. From top to bottom, k^0 (cm s^{-1}) is (a) 1, (b) 0.5, (c) 0.1, (d) 0.025, (e) 0.015, (f) 0.01, (g) 0.005, (h) 0.002, and (i) 0.0001. Curve (a) is identical to that for

mass transfer controlled (electrochemically reversible) reaction and curve (i) for an insulating substrate in Figure 1.9. Figure 1.10 was adapted from Bard *et al*. (2012).[82]

Since the conception of SECM, countless studies have been reported using different feedback modes for different purposes (*e.g.*, kinetic studies, surface manipulation, mass-transport studies on thin membranes, etc.).[83,84] Among those studies, the most significant highlight of SECM is the direct dynamic mapping of a surface, which can provide either topographical or electrochemical activity information. Fabrication and characterization procedures of nanoscale probes have been reported in a number of recent studies,[85–87] and for this reason, the highest possible mapping resolution achievable from conventional SECM has become a key focus.[87–89] For instance, SECM has been used to study electrocatalytic nanomaterials (*e.g.*, NPs) adhered to an electrocatalytically inert support, with sizes ranging from 20 nm to a few hundreds of nm.[87–89] However, it is important to point out that the SECM technique operates on a constant height scanning mode with no positional feedback, and there is no possibility of simultaneous topographical and heterogeneous reactivity mapping unless dual mediators are used, one for topography and one for activity, which is very restrictive.[90] Furthermore, in constant height scanning mode, surface height and surface activity can become convoluted for rough surfaces, and there is a significant problem of tip crash further limiting the applicability of this technique at the nanoscale.

1.3.2 SECM Hybrid Techniques

As alluded to above, most applications of SECM suffer from difficulty in maintaining and knowing the probe-to-substrate separation as there is no positional feedback during "constant height" imaging.[91] This is especially true at the nanoscale, where small changes in the working distance caused by sample tilt, topographical features, and the effects of the thermal drift of piezoelectric positioners[92] can severely affect the fidelity of spatially resolved electrochemical reactivity data. SECM, for this reason, has been amalgamated with other scanning probe techniques such as atomic force microscopy (AFM)[93] and scanning ion conductance microscopy (SICM)[94–96], which help to provide a more robust means of positioning the probe near a sample substrate.

AFM operates by monitoring the force between a sharp tip located at the end of a reflective cantilever arm and the substrate, providing information on probe-to-substrate separation (Figure 1.11A). In brief, the force depends on the spring constant of the cantilever and the distance between the tip probe and the substrate (Figure 1.11B), which is measured by a laser reflected off the back of the cantilever arm. In imaging mode, the tip is moved laterally across the surface of interest and deflection of the cantilever is detected from the position of the laser by a photodiode detector, thus providing topographical information on the atomic scale. Integration of AFM to SECM (SECM-AFM) (Figure 1.11C) was successfully demonstrated in 2000 using manually fabricated dual-functioning (SECM and AFM) probes, showing spatially well-resolved and simultaneously obtained topography and electrochemical reactivity maps.[97] It was further utilized at various surfaces, such as micro-scale patterns on mixed conducting/insulating surfaces, including UMEs,[98–100] well-defined 2D surfaces,[101,102] immobilised enzymes,[101,102] and artificial membranes.[101,102] SECM-AFM was also implemented to study more dynamic surface processes, such as dissolution[103] and corrosion.[104] More recently, the spatial resolution of SECM-AFM has been improved to image individual NPs adhered on a surface (Figure 1.11D).[105] The NPs, in this work, perform both as a scaffold and as a nanoelectrode, mediating electron transfer between the gold substrate, underlying a SAM, and the redox labels (ferrocene, Fc) anchored to the NP surface. Simultaneously obtained topography and electrochemical activity maps in Figure 1.11D reveal that the electrochemical properties of individual NPs can be resolved by SECM-AFM. As probe fabrication and characterization procedures have rapidly advanced,[106] there have recent demonstrations of SECM-AFM[107,108] being used to probe nanostructures, which opens up the possibility of undertaking dynamic studies of electrochemical activity at a single NP. It needs to be further noted that commercial systems for SECM-AFM are now available from Bruker[109] and Keysight Technology.[110]

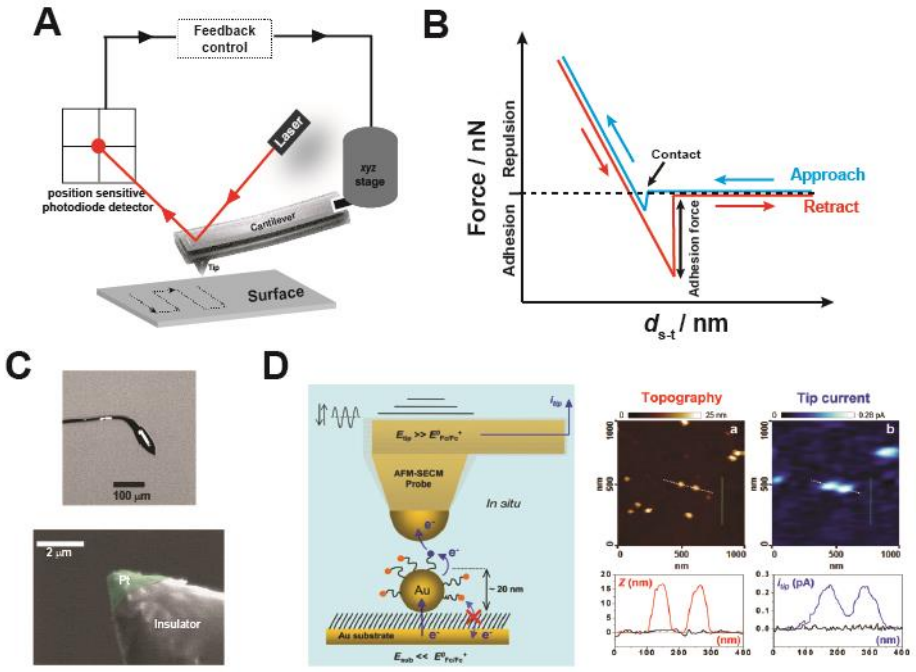

Figure 1.11 (A) Schematic showing the basic principles of AFM operation and (B) force-$d_{s\text{-}t}$ relationships at approach and retract of the AFM tip. (C) Optical and scanning electron microscopic (SEM) images of manually fabricated Pt wire SECM-AFM probe. (C) was adapted from Macpherson *et al*. (2000).[97] (D) Principle of the SECM-AFM technique for the interrogation of PEGylated ferrocene (PEG = polyethyleneglycol) anchored on individual gold NPs (left). Simultaneously obtained topography and tip current images (right). Cross sections of the topography and tip current images (dotted white lines) are respectively plotted in red and blue. Corresponding cross sections taken in a zone where NPs are absent (solid green line in the plots) are plotted as black traces. (D) was adapted from Huang *et al*. (2013).[106]

Position control in SICM is achieved by monitoring ionic current (i_{ion}) at the probe (Figure 1.12A). In brief, the probe is filled with electrolyte solution and a QRCE, immersed in electrolyte solution containing an identical/similar QRCE and then a constant potential bias is applied between the two QRCEs to induce an i_{ion} through the SICM probe end. When the probe is positioned in bulk (*i.e.*, distant from the surface of interest), the magnitude of the i_{ion} is governed by the resistance of the SICM probe end (due to its geometry, ranging from micro- to nano-scale) and conductivity of the solution. As the SICM probe is approached to the surface of interest, the ionic current becomes increasingly dominated by the high resistance in

the probe-surface gap, thus resulting in a decrease in the magnitude of the i_{ion}, which can be used as a feedback signal to maintain constant distance between the probe and the substrate. SICM, thus, has traditionally been used for non-contact topographical imaging[111], although recent work has shown that it can be used as a multifunctional tool capable of elucidating a variety of surface properties, as the ionic current is sensitive to changes in the local ionic atmosphere near to surfaces.[112–116] This aspect of SICM is addressed in further detail below (Section 1.3.3) and further expanded upon in Chapter 5.

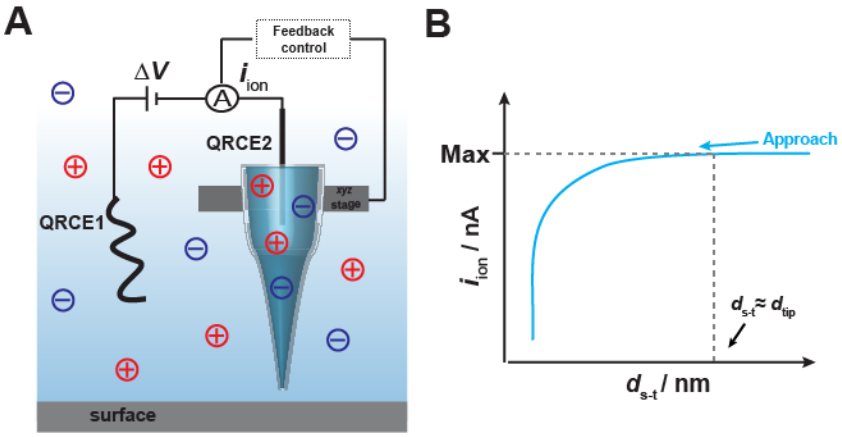

Figure 1.12 (A) Basic principle of SICM operation, where a potential bias between two QRCEs and the induced ionic current is noted as ΔV and i_{ion}, respectively. (B) i_{ion}-$d_{s\text{-}t}$ relationship during approach of a SICM probe to a surface. The magnitudes of i_{ion} begins to decrease where $d_{s\text{-}t}$ is similar to the diameter of the probe (d_{tip}).

When SICM is combined with SECM (SECM-SICM), both topography and electrochemical reactivity maps can be obtained simultaneously by employing dual-functional SECM-SICM probes (Figure 1.13). SECM-SICM probes are varied from single-channelled[117,118] to double-channelled probes,[86,119] however, the double channelled probes are more widely used in recent studies due to the less complicated probe fabrication process. The SECM channel in double-channelled probes are initially fabricated with carbon as a result of pyrolysis processes of a carbon containing gas in an argon atmosphere (Figure 1.13A).[119] As carbon is relatively inert in most electrocatalytic reactions, SECM probes are further functionalised through electrodeposition to allow the probing of activity on catalytic surfaces.[85,95,119–121]

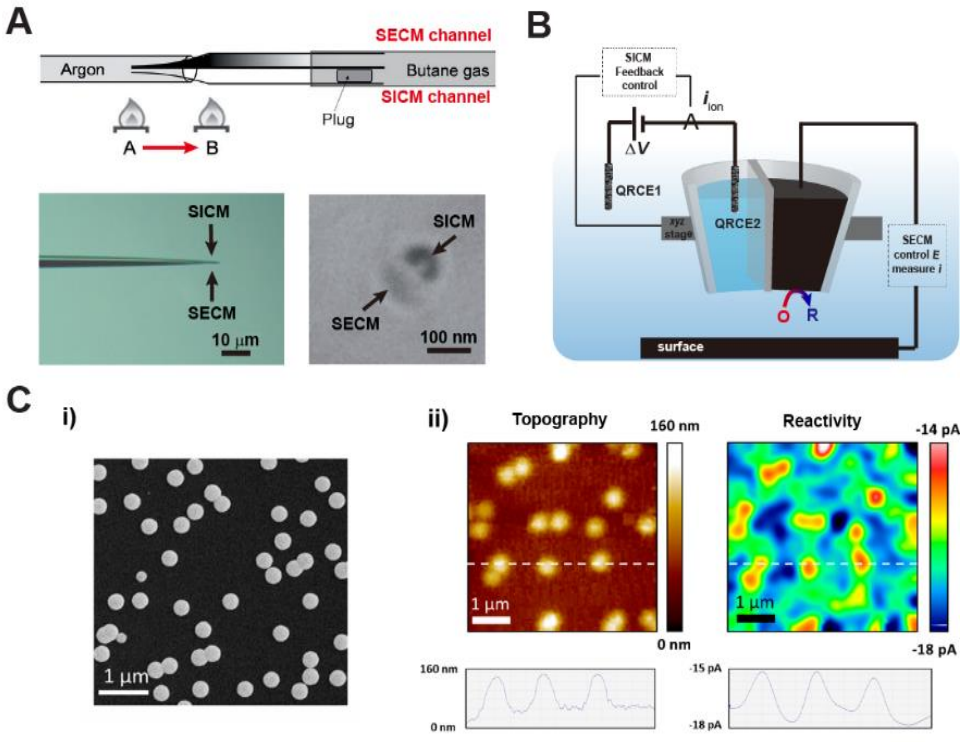

Figure 1.13 (A) Schematic illustration of double-channelled SECM-SICM probe fabrication (top) with optical (bottom left) and SEM (bottom right) images of the probes. (A) was adapted from Takahashi *et al*. (2011).[119] (B) Schematic showing the basic principles of SECM-SICM operation. (C) (i) A SEM image of spherical Pt NPs electrochemically decorated on a GC surface and (ii) corresponding topography and ORR reactivity maps of the surface, simultaneously obtained by the SECM-SICM technique. (C) was adapted from O'Connell *et al*. (2014).[121]

SECM-SICM has been utilized to study biological cells,[119,120] local ion flux studies[118,120,121], as well as to visualize both the topography and electrocatalytic activity of NPs.[95,121] The electocatalytic activity of spherical Pt NPs (r_{NP} = 50 – 200 nm) on a glassy carbon (GC) support was visualized by investigating the oxygen reduction reaction (ORR) in alkaline media, with a spatially resolved electrochemical map correlated with the location of the NPs obtained from a topography map.[121] Similar experiments were performed on AuNPs (r_{NP} ≈ 200 nm) with more complex shape and structure within NPs in an attempt to correlate the reactivity to the topography and crystalline structure of ensembles of AuNPs.[95] Also, this work

highlights different reactivity between individual AuNPs with similar shape, possibly related to the difference in crystalline structure of the NPs.[95]

Combination of these complementary techniques, together with SECM, can help to enhance the quality of the obtained electrochemical/topographical images because of the more precise control over the substrate-probe distance. These multifunctional techniques have also helped expand electrochemical measurements to the study of nonconductive biological specimens[94,96,122] and can also provide additional information through analysing the data recorded from the complimentary technique. For instance, AFM is capable of providing mechanical properties at the nanoscale[107,108] and SICM allows local delivery of the analyte (Chapter 6).[96] However, the already difficult task of quickly producing reproducible, nanoscale SECM probes becomes more challenging when dual-functional probes are to be employed.[106]

1.3.3 Scanning Ion Conductance Microscopy

Most recently, SICM alone has emerged as *a multifunctional tool* capable of elucidating surface properties, in addition to high-resolution topographical scanning.[79,123] It has been shown that in addition to being sensitive to the resistance induced by the small separation between the (nanopipette) tip and sample substrate (as in conventional SICM), the ion conductance current is also sensitive to changes in the local ionic atmosphere near the surface induced by either heterogeneous surface charges[112–115,124] or the result of an electrochemical reaction[116] taking place at the surface, to which the author contributed but is not included in the thesis chapters. Electrochemical mapping with SICM is possible because the majority of electrochemical reactions cause a measurable change in the overall ion composition in the vicinity of the electrode surface, opening up further possible applications of SICM for studying different electrocatalytic materials, especially at the nanoscale. The major advantage of SICM for this application is that the experimental setup and procedure is relatively simple, with the probe fabrication much more robust when compared to the other SEPM imaging techniques outlined above.

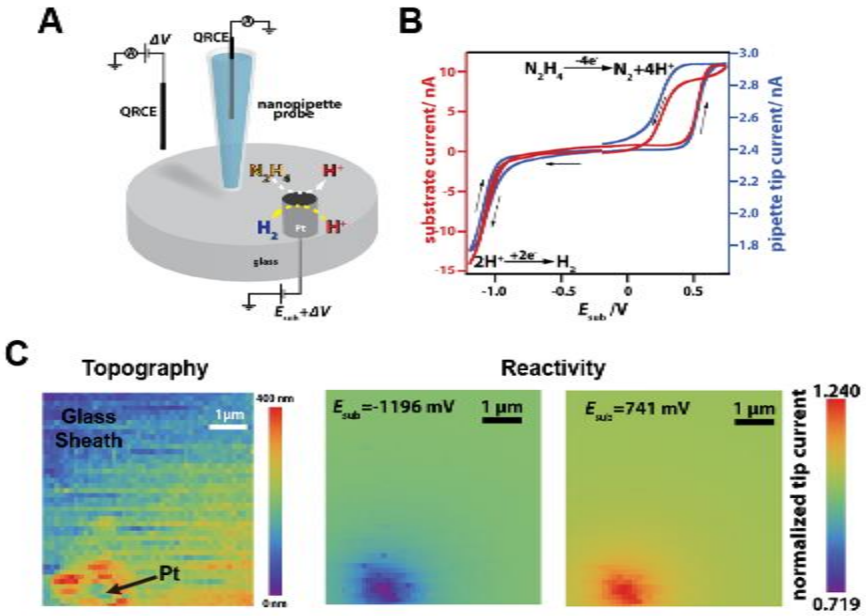

Figure 1.14 (A) Basic operating principle for electrochemical reaction mapping with SICM. (B) Cyclic voltammograms acquired from the substrate (Pt UME, red) and concurrently monitored current at the SICM probe (blue) which is positioned at the central part of the substrate electrode during the potential sweep. (C) Topography (left) and reactivity (middle, HER; right, hydrazine oxidation) maps obtained from dynamic reaction imaging with SICM. Figure 1.14 was adapted from Momotenko *et al.* (2016).[116]

By adopting different scan regimes, it therefore becomes possible to perform electrochemical reactivity mapping,[116] whilst simultaneously acquiring topographical information. Notably, Figure 1.14 shows an example of the results collected with SICM nanoprobes (d_{tip}= 300-500 nm).[116] Dynamic reaction mapping was demonstrated in this work, where cyclic voltammetry is performed at each position (pixel) of the probe ($d_{s\text{-}t} < d_{tip}$) in an acidic electrolyte solution containing hydrazine. When the potential is swept positively, protons are generated as a result of hydrazine oxidation, resulting increase of i_{tip} due to increase of conductivity in the vicinity of the electrode (Figure 1.14B and C). When the potential is swept in negative direction, on the other hand, protons are consumed as a result of HER, resulting in a decrease in i_{tip} due to a decrease of conductivity in the vicinity of the electrode (Figure 1.14B and C). As the topographical information is simultaneously recorded throughout the

experiments, the corresponding topography image can be acquired, showing a Pt electrode surrounded with an insulating glass sheath. Simultaneous topography and electrochemical activity mapping with SICM has been further improved in terms of scanning time and sensitivity by utilising smaller SICM nanoprobes ($d_{tip} \approx 30$ nm), allowing the visualisation of individual NPs rather than a microscale electrode. A detailed description of the experimental design and results are presented in Chapter 5.

1.3.4 Scanning Electrochemical Cell Microscopy

The static micro-droplet electrochemical cell technique (see Section 1.2.3) has been advanced to the dynamic imaging technique scanning electrochemical cell microscopy (SECCM) through the implementation of a double-channelled glass micro/nano-pipette. The SECCM system provides highly sensitive feedback for probe-to-substrate separation and greater versatility in terms of the substrate materials that can be studied and operating protocols.[73,125] As the probe can maintain constant probe-to-substrate separation, SECCM also allows simultaneous topographical and electrochemical activity mapping during scanning of the surface of interest.[73,125]

The schematic shown in Figure 1.15A illustrates the SECCM setup. A double-channelled glass pipette (tip end diameter varies from 100 nm to a few μm) filled with electrolyte solution (including analytes) and a QRCE in each channel, is mounted on a piezoelectric nano-positioner for precise positioning of the SECCM probe. A potential bias (V_2) is applied between the QRCEs to induce an ionic current (i_{dc}) across the meniscus formed at the end of the pipette, and changes in i_{dc} are used as a feedback signal to control probe-to-substrate separation. During operation, a small harmonic (mechanical) oscillation of probe (in the *z*-direction) is added through a lock-in amplifier. Once the meniscus makes contact the surface of interest (there is no direct contact between glass pipette and the surface), the ion current across the meniscus will show a periodic modulation (*ac* component, i_{ac}) at the same frequency of harmonic oscillation due to reversible deformation of the meniscus. i_{ac} is highly sensitive, as its background signal before the contact is very small (Figure 1.15B) and the magnitude of i_{ac} informs on probe-to-substrate separation. If the substrate is a (semi)conductor, the meniscus contact area is defined as WE at the potential of $-(V_1+V_2/2)$ and electrochemical reactivity (i_{WE}) can be measured directly within the localised area of the meniscus cell.[73,125]

The small WE area and absence of direct physical contact between electrode and insulating sheath in SECCM regime lead to low background currents and relatively low capacitance (during potential scanning or transient phenomena) compared to fabricated UME with a comparable electrode area.[51] Also, setup allows the study of a wide range of substrate materials (*vide supra*), including polycrystalline metal foils,[126–128] semiconductors,[129–131] and battery materials.[132] Beyond electrochemically active surfaces, it needs to be highlighted that phenomena on insulating materials can also be studied with SECCM, such as the dissolution of crystals[133] and the titration of static charge.[134]

The spatial resolution SECCM has been shown to be sufficient to resolving electrocatalytic activities of individual nanomaterials on surfaces. The electrocatalytic activity of single Pt NPs (r_{NP}= 50 nm - 100 nm) electrochemically deposited on a single-wall carbon nanotube (SWCNT) was successfully visualized for the ORR and HER.[135] Similarly, SECCM has been utilised to show kinks/defects in SWCNTs facilitate the electro reduction of O_2 to H_2O_2.[136] As electrochemical data obtained through SECCM is spatially resolved, the surface can be further analysed, with the additional use of other microscopic techniques [*e.g.*, scanning electron microscopy (SEM) based techniques, TEM, AFM, and Raman microscopy] in a *correlative multi-microscopy approach*. This approach allows micro/nanoscopic structure to be directly correlated to electrochemical function of the surface of interest.

In more recent studies, SECCM has been advanced by combining it with potential-sweep voltammetry, one of the most commonly used classical electrochemical techniques.[137] Potential-sweep voltammetry is performed at every point of meniscus contact (*i.e.,* voltammetric SECCM), providing the wealth of information at a confined area. Hopping mode, where the probe is vertically positioned at the set probe-to-substrate separation at each approach and retracted followed by lateral movement for the next point, is more commonly used to eliminate overlap between adjacent liquid meniscus contact[127,131,138] The spatio-temporal resolution can be manipulated through hop distance and the scan rate of voltammetry, respectively. This allows the electrochemical reaction to be visualised across the surface of interest with spatially resolved equipotential images at multiple different potentials that can be used to construct electrochemical reaction movies.[127,131,138] In-depth kinetic analysis

can be performed at each confined area through Tafel analysis[1,131] or FEM simulations, which opens up opportunities to study electrocatalytic nanomaterials.

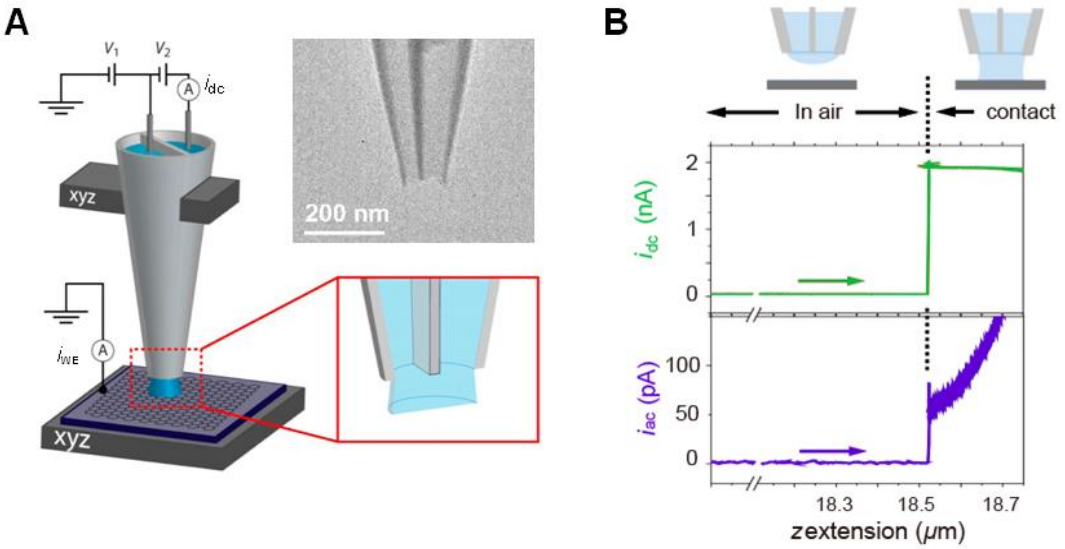

Figure 1.15 (A) Schematic of the SECCM setup, with a TEM image of a double-chanelled quartz nanopipette ($d_{tip} \approx 100$ nm) inset. (B) Approach curves of an SECCM probe with i_{dc} and i_{ac} as a function as z extension towards the substrate. Shown above the plots are illustrations delineating three regions; in air, where no contact has been made with the substrate; jump-to-contact (dashed line); and contact. Figure 1.15 was adapted from Mirkin and Amemiya (2015).[139]

1.3.5 Super-Resolution Optical Imaging Techniques.

The SEPM techniques explained thus far have successfully visualised electrochemical activity of individual NPs,[89,91,105,107,121,135] yet sub-particle activity mapping has not been achieved. The recent developments in super high resolution imaging techniques combining optical measurements with plasmonic nanomaterials (*e.g.* surface-enhanced Raman scattering (SERS) and surface-enhanced fluorescence) has allowed for single molecule level detection induced by electrochemical control using optically active probe molecules.[140] The spatial resolution that has been achieved is as low as 5-20 nm, allowing the sub-entity level (electro)chemical activity of nanomaterials to be probed.[141–146] By integrating electrochemical cells, controlling the applied potential

on plasmonic nanomaterials, into SERS, the SERS signals can be switched on and off electrochemically, allowing the origin of the SERS emission to be localized.[140] Indeed, local hot spots were probed with the use of optically/electrochemically active Nile Blue on Au and Ag NPs aggregates and correlated with the structures of the aggregates, as characterized by electron microscopy.[143,144] High sensitivity and spatial resolution provide an in-depth understanding of the (electro)chemical reaction within a nanomaterial, and how it relates to defects[142], crystallographic facet[145] and structure[146] (*i.e.* structure-function relationship). However, this approach separately requires supplementary techniques, such as electron microscopy, to study the morphology of the nanomaterials, with simultaneous topographical imaging not possible.[141,144]

1.4 Aims of the Thesis

The study of catalytic nanomaterials has become an important area in modern science, as they often possess superior (electro)catalytic activity compared to the bulk material, making them highly desirable for a range of practical real-world applications.[147–150] Evidence presented through numerous studies, using ensembles of (nano)catalysts, has revealed that subtle changes in the shape, size, and structure of the studied nanomaterial can significantly affect (electro)catalytic activity.[151–153] Consequently, in-depth understanding of nanocatalysts at the single entity level has emerged as a new area in electrochemistry, despite the fact that it is fundamentally challenging from both experimental and theoretical standpoints.[154,155] The main aim and interest of this thesis, thus, is to observe and quantify the heterogeneous (electro)activity of catalytic nanoparticles (NPs) at the single entity level through the use of a diverse range of electrochemical micro-/nano-probe techniques.

In the work presented in Chapters 3 and 4, a micro-droplet electrochemical cell has been deployed in a static regime to electrochemically observe the impacts of individual NPs with a collector electrode surface. Chapter 3 demonstrates an in-depth analysis of the dynamics of individual NPs in the vicinity of a catalytically inert carbon electrode surface through the observation of electrocatalytic H_2O_2 oxidation on RuO_x NPs, coupled with 3D random walk simulations. It also addresses the importance of high temporal resolution in this type of measurement, where the NP impact time on the collector electrode surface is on the millisecond timescale. Chapter 4 investigates

the electrodissolution of individual Ag NPs using an analogous measurement system to that utilized in Chapter 3, demonstrating multiple steps during a single Ag NP electrodissolution event (*i.e.*, consecutive partial dissolution processes). An in-depth analysis of current-time (*i*-*t*) transients (*i.e.*, consumed charge, impact duration, event frequency) has revealed detailed information about the complex Ag NP stripping process. In addition, the nature of the surface interaction between the dissolving Ag NP and the collector electrode has been shown to be strongly material dependent, with distinctly different *i*-*t* morphologies observed at carbon and gold surfaces.

Through the use of the Warwick Electrochemistry & Interfaces Group (WEIG) operating system,[137] which provides a versatile platform for the implementation of a diverse range of scanning electrochemical probe microscopy techniques, Chapter 5 and 6 introduce new nano-probe techniques in a dynamic regime for nanoscale studies. In Chapter 5, scanning ion conductance microscopy (SICM), a single channel nano-probe technique traditionally employed solely for topographical mapping, has been shown to be a powerful technique for simulatneous electrochemical and topographical mapping at the nanoscale, which can reveal a wealth of information when combined with finite element method (FEM) simulations. Chapter 6 applies dual channel nano-probes, known as scanning electrochemical microscopy (SECM)-(SICM) probes, again for simultaneous topographical and electrochemical mapping, where in this case, the SICM probe serves an additional function by delivering the analyte to the surface of interest through controlling the polarity of the applied bias.

Overall, this thesis has contributed to significant advances in the spatio-temporal resolution of electrochemical measurements performed on single NPs, using a diverse range of electrochemical techniques at the nanoscale. In a later study by the author of this thesis (not included in the results chapters), high temporal resolution current measurements of 260 μs per data point (i.e., sampling rate = 250 kHz) was performed with a single channelled nanopipette probe (d ≈ 30 nm) to achieve an *xy* spatial resolution of ~50 nm, which is comparable to super resolution optical imaging techniques (Section 1.3.5).[156] In addition, in that study, the *z*-height resolution achieved in the topography map was ≤ 2 nm, which is comparable to what is possible with an AFM integrated SEPM technique (Section 1.3.2).

1.5 References

(1) Bard, Allen J. Faulkner, L. R. *Electrochemical Methods: Fundamentals and Applications*, 2nd ed.; Wiley: New York, 2001.

(2) Erdey-Grúz, T. *Kinetics of Electrode Process*; Wiley-Interscience: New York, 1972.

(3) Vetter, K. J. *Electrochemical Kinetics*; Academic: New York, 1967.

(4) Delahay, P. *Double Layer and Electrode Kinetics*; Wiley-Interscience: New York, 1965.

(5) Oldham, K. B.; Myland, J. C. *Fundamentals of Electrochemical Science.*; Academic Press: San Diego, 1994.

(6) Malek, K.; Coppens, M. O. *J. Chem. Phys.* **2003**, *119* (5), 2801–2811.

(7) Bae, J., Han, J., Chung, T. *Phys. Chem. Chem. Phys.* **2012**, *14* (2), 448–463.

(8) Forster, R. J. *In Encyclopedia of Electrochemistry*, Volume3.; Bard, A. J., Stratmann, M., Unwin, P. R., Eds.; Wiley VCH: Weinheim, Germany, 2003.

(9) Newman, J. *Ind. Eng. Chem.* **1968**, *60* (4), 12–27.

(10) Malmsten, R. A.; Smith, C. P.; White, H. S. *J. Electroanal. Chem.* **1986**, *215* (1–2), 223–235.

(11) Morris, R. B.; Fischer, K. F.; White, H. S. *J. Phys. Chem.* **1988**, *92* (18), 5306–5313.

(12) Saito, Y. *Rev. Polarogr.* **1968**, *15* (6), 177–187.

(13) Zoski, C. G.; Mirkin, M. V. *Anal. Chem.* **2002**, *74* (9), 1986–1992.

(14) Wipf, D. O.; Michael, A. C.; Wightman, R. M. *J. Electroanal. Chem. Interfacial Electrochem.* **1989**, *269* (1), 15–25.

(15) Amemiya, S.; Bard, A. J.; Fan, F. F.; Mirkin, M. V; Unwin, P. R. **2008**.

(16) Xiao, X.; Bard, A. J. *J. Am. Chem. Soc.* **2007**, *129* (31), 9610–9612.

(17) Xiao, X.; Fan, F.-R. F.; Zhou, J.; Bard, A. J. *J. Am. Chem. Soc.* **2008**, *130* (49), 16669–16677.

(18) Zhou, H.; Park, J. H.; Fan, F. F.; Bard, A. J. **2012**, 8–11.

(19) Xiao, X.; Pan, S.; Jang, J. S.; Fan, F. R. F.; Bard, A. J. *J. Phys. Chem. C* **2009**, *113* (33), 14978–14982.

(20) Wakerley, D.; Guell, A. G.; Hutton, L. A.; Miller, T. S.; Bard, A. J.; Macpherson, J. V. *Chem. Commun.* **2013**, *49* (50), 5657–5659.

(21) Zhou, H.; Fan, F. R. F.; Bard, A. J. *J. Phys. Chem. Lett.* **2010**, *1* (18), 2671–2674.

(22) Wakerley, D.; Güell, A. G.; Hutton, L. A.; Miller, T. S.; Bard, A. J.; Macpherson, J. V. *Chem. Commun.* **2013**, *49* (50), 5657.

(23) Kim, J.; Kim, B. K.; Cho, S. K.; Bard, A. J. *J. Am. Chem. Soc.* **2014**, *136* (23), 8173–8176.

(24) Bentley, C. L.; Kang, M.; Unwin, P. R. *J. Am. Chem. Soc.* **2016**, *138* (39), 12755–12758.

(25) Bobbert, P. A.; Wind, M. M.; Vlieger, J. *Physica A* **1987**, *141*, 58–72.

(26) Dasari, R.; Robinson, D. A.; Stevenson, K. J. *J. Am. Chem. Soc.* **2013**, *135* (2), 570–573.

(27) Percival, S. J.; Zhang, B. *J. Phys. Chem. C* **2016**, *120* (37), 20536–20546.

(28) Guo, Z.; Percival, S. J.; Zhang, B. *J. Am. Chem. Soc.* **2014**, *136* (25), 8879–8882.

(29) Quinn, B. M.; Van 'T Hof, P. G.; Lemay, S. G. *J. Am. Chem. Soc.* **2004**, *126* (27), 8360–8361.

(30) Kwon, S. J.; Zhou, H.; Fan, F.-R. F.; Vorobyev, V.; Zhang, B.; Bard, A. J. *Phys. Chem. Chem. Phys.* **2011**, *13* (12), 5394.

(31) Kwon, S. J.; Fan, F.-R. F.; Bard, A. J. *J. Am. Chem. Soc.* **2010**, *132* (38), 13165–13167.

(32) Jung, A. R.; Lee, S.; Joo, J. W.; Shin, C.; Bae, H.; Moon, S. G.; Kwon, S. J. *J. Am. Chem. Soc.* **2015**, *137* (5), 1762–1765.

(33) Boika, A.; Thorgaard, S. N.; Bard, A. J. *J. Phys. Chem. B* **2013**, *117* (16), 4371–

4380.

(34) Fosdick, S. E.; Anderson, M. J.; Nettleton, E. G.; Crooks, R. M. *J. Am. Chem. Soc.* **2013**, *135* (16), 5994–5997.

(35) Dick, J. E.; Hilterbrand, A. T.; Boika, A.; Upton, J. W.; Bard, A. J. *Proc. Natl. Acad. Sci. U. S. A.* **2015**, *112* (17), 5303–5308.

(36) Dick, J. E.; Renault, C.; Bard, A. J. *J. Am. Chem. Soc.* **2015**, *137* (26), 8376–8379.

(37) Dick, J. E.; Hilterbrand, A. T.; Strawsine, L. M.; Upton, J. W.; Bard, A. J. *Pnas* **2016**, 1605002113-.

(38) Bard, A. J. *J. Am. Chem. Soc.* **2010**, *132* (22), 7559–7567.

(39) Dasari, R.; Tai, K.; Robinson, D. A.; Stevenson, K. J. *ACS Nano* **2014**, *8* (5), 4539–4546.

(40) Luo, L.; White, H. S. *Langmuir* **2013**, *29* (35), 11169–11175.

(41) Chen, Q.; Wiedenroth, H. S.; German, S. R.; White, H. S. *J. Am. Chem. Soc.* **2015**, *137* (37), 12064–12069.

(42) Chen, Q.; Luo, L.; Faraji, H.; Feldberg, S. W.; White, H. S. *J. Phys. Chem. Lett.* **2014**, *5* (1), 3539–3544.

(43) Kätelhön, E.; Compton, R. G. *Chem. Sci.* **2014**, *5* (12), 4592–4598.

(44) Kang, M.; Perry, D.; Kim, Y. R.; Colburn, A. W.; Lazenby, R. A.; Unwin, P. R. *J. Am. Chem. Soc.* **2015**, *137* (34), 10902–10905.

(45) Zhou, M.; Yu, Y.; Hu, K.; Xin, H. L.; Mirkin, M. V. *Anal. Chem.* **2017**, acs.analchem.6b04140.

(46) Batchelor-McAuley, C.; Ellison, J.; Tschulik, K.; Hurst, P. L.; Boldt, R.; Compton, R. G. *Analyst* **2015**, *140* (15), 5048–5054.

(47) Bartlett, T. R.; Sokolov, S. V.; Compton, R. G. *ChemistryOpen* **2015**, *4* (5), 600–605.

(48) Haddou, B.; Rees, N. V; Compton, R. G. *Phys. Chem. Chem. Phys.* **2012**, *14* (39), 13612–13617.

(49) Lees, J. C.; Ellison, J.; Batchelor-Mcauley, C.; Tschulik, K.; Damm, C.; Omanovič, D.; Compton, R. G. *ChemPhysChem* **2013**, *14* (17), 3895–3897.

(50) Sokolov, S. V.; Tschulik, K.; Batchelor-McAuley, C.; Jurkschat, K.; Compton, R. G. *Anal. Chem.* **2015**, *87* (19), 10033–10039.

(51) Ustarroz, J.; Kang, M.; Bullions, E.; Unwin, P. R. *Chem. Sci.* **2017**, *8*, 1841–1853.

(52) Krause, K. J.; Adly, N.; Yakushenko, A.; Schnitker, J.; Mayer, D.; Offenhäusser, A.; Wolfrum, B. *Anal. Chem.* **2016**, *88* (7), 3632–3637.

(53) Peng, Y. Y.; Qian, R. C.; Hafez, M. E.; Long, Y. T. *ChemElectroChem* **2017**, *4* (5), 977–985.

(54) Oja, S. M.; Robinson, D. A.; Vitti, N. J.; Edwards, M. A.; Liu, Y.; White, H. S.; Zhang, B. *J. Am. Chem. Soc.* **2017**, *139* (2), 708–718.

(55) Ma, W.; Ma, H.; Chen, J.-F.; Peng, Y.-Y.; Yang, Z.-Y.; Wang, H.-F.; Ying, Y.-L.; Tian, H.; Long, Y.-T. *Chem. Sci.* **2017**, *8* (3), 1854–1861.

(56) Lai, S. C. S.; Lazenby, R. A.; Kirkman, P. M.; Unwin, P. R. *Chem. Sci.* **2015**, *6* (2), 1126–1138.

(57) Patel, A. N.; Martinez-Marrades, A.; Brasiliense, V.; Koshelev, D.; Besbes, M.; Kuszelewicz, R.; Combellas, C.; Tessier, G.; Kanoufi, F. *Nano Lett.* **2015**, *15* (10), 6454–6463.

(58) Brasiliense, V.; Berto, P.; Combellas, C.; Kuszelewicz, R.; Tessier, G.; Kanoufi, F. *Faraday Discuss.* **2016**, *193*, 339–352.

(59) Brasiliense, V.; Patel, A. N.; Martinez-Marrades, A.; Shi, J.; Chen, Y.; Combellas, C.; Tessier, G.; Kanoufi, F. *J. Am. Chem. Soc.* **2016**, *138* (10), 3478–3483.

(60) Brasiliense, V.; Berto, P.; Combellas, C.; Tessier, G.; Kanoufi, F. *Acc. Chem. Res.* **2016**, *49* (9), 2049–2057.

(61) Giovanni, M.; Ambrosi, A.; Sofer, Z.; Pumera, M. *Electrochem. commun.* **2015**, *56*, 16–19.

(62) Stuart, E. J. E.; Tschulik, K.; Batchelor-Mcauley, C.; Compton, R. G. *ACS*

Nano **2014**, *8* (8), 7648–7654.

(63) Qiu, D.; Wang, S.; Zheng, Y.; Deng, Z. *Nanotechnology* **2013**, *24* (50), 505707.

(64) Saw, E. N.; Grasmik, V.; Rurainsky, C.; Epple, M.; Tschulik, K. *Faraday Discuss.* **2016**, *157* (207890), 243–284.

(65) Sepunaru, L.; Sokolov, S. V.; Holter, J.; Young, N. P.; Compton, R. G. *Angew. Chemie - Int. Ed.* **2016**, *55* (33), 9768–9771.

(66) Suter, T.; Böhni, H. *Electrochim. Acta* **1997**, *42* (20–22), 3275–3280.

(67) Lohrengel, M. M.; Moehring, A.; Pilaski, M. *Electrochim. Acta* **2001**, *47* (1), 137–141.

(68) Woldemedhin, M. T.; Raabe, D.; Hassel, A. W. *Phys. status solidi* **2011**, *208* (6), 1246–1251.

(69) Staemmler, L.; Suter, T.; Böhni, H. *J. Electrochem. Soc.* **2004**, *151* (11), G734–G739.

(70) Hassel, A. W.; Seo, M. *Electrochim. Acta* **1999**, *44* (21), 3769–3777.

(71) Lill, K. A.; Hassel, A. W.; Frommeyer, G.; Stratmann, M. *Electrochim. Acta* **2005**, *51* (5), 978–983.

(72) Mardare, A. I.; Wieck, A. D.; Hassel, A. W. *Electrochim. Acta* **2007**, *52* (28), 7865–7869.

(73) Snowden, M. E.; Güell, A. G.; Lai, S. C. S.; McKelvey, K.; Ebejer, N.; O'Connell, M. a.; Colburn, A. W.; Unwin, P. R. *Anal. Chem.* **2012**, *84* (5), 2483–2491.

(74) Kim, Y. R.; Lai, S. C. S.; McKelvey, K.; Zhang, G.; Perry, D.; Miller, T. S.; Unwin, P. R. *J. Phys. Chem. C* **2015**, *119* (30), 17389–17397.

(75) Zhang, G.; Güell, A. G.; Kirkman, P. M.; Lazenby, R. A.; Miller, T. S.; Unwin, P. R. *ACS Appl. Mater. Interfaces* **2016**, *8* (12), 8008–8016.

(76) Kleijn, S. E. F.; Lai, S. C. S.; Miller, T. S.; Yanson, A. I.; Koper, M. T. M.; Unwin, P. R. *J. Am. Chem. Soc.* **2012**, *134*, 18558–18561.

(77) Chen, C. H.; Ravenhill, E. R.; Momotenko, D.; Kim, Y. R.; Lai, S. C. S.; Unwin,

P. R. *Langmuir* **2015**, *31* (43), 11932–11942.

(78) Zhou, Y.-G.; Rees, N. V; Compton, R. G. *Angew. Chem. Int. Ed. Engl.* **2011**, *50* (18), 4219–4221.

(79) Kang, M.; Momotenko, D.; Page, A.; Perry, D.; Unwin, P. R. *Langmuir* **2016**, *32* (32), 7993–8008.

(80) Bard, A. J.; Fan, F.-R. F.; Kwak, J.; Lev, O. *Anal. Chem.* **1989**, *61* (2), 132–138.

(81) Engstrom, R. C.; Meaney, T.; Tople, R.; Wightman, R. M. *Anal. Chem.* **1987**, *59* (15), 2005–2010.

(82) *Scanning Electrochemical Microscopy*, 2nd ed.; Bard, A. J., Mirkin, M. V, Eds.; CRC Press: New York, 2012.

(83) Wittstock, G.; Burchardt, M.; Pust, S. E.; Shen, Y.; Zhao, C. *Angew. Chemie - Int. Ed.* **2007**, *46* (10), 1584–1617.

(84) Polcari, D.; Dauphin-Ducharme, P.; Mauzeroll, J. *Chem. Rev.* **2016**, *116* (22), 13234–13278.

(85) Actis, P.; Tokar, S.; Clausmeyer, J.; Babakinejad, B.; Mikhaleva, S.; Cornut, R.; Novak, P.; Shevchuck, A. I.; Dougan, J. A.; Schuhmann, W.; Klenerman, D.; Rusakov, O. D. A.; Sviderskaya, E. V; Korchev, Y. E. *ACS Nano* **2014**, *8* (1), 875–884.

(86) Thakar, R.; Weber, A. E.; Morris, C. A.; Baker, L. A. *Analyst* **2013**, *138* (20), 5973–5982.

(87) Blanchard, P. Y.; Sun, T.; Yu, Y.; Wei, Z.; Matsui, H.; Mirkin, M. V. *Langmuir* **2016**, *32* (10), 2500–2508.

(88) Yu, Y.; Sun, T.; Mirkin, M. V. *Anal. Chem.* **2015**, *87* (14), 7446–7453.

(89) Kim, J.; Renault, C.; Nioradze, N.; Arroyo-Currás, N.; Leonard, K. C.; Bard, A. J. *J. Am. Chem. Soc.* **2016**, *138* (27), 8560–8568.

(90) Gonsalves, M.; Barker, A. L.; Macpherson, J. V; Unwin, P. R.; Hare, D. O.; Winlove, C. P. *Biophys. J.* **2000**, *78*, 1578–1588.

(91) Sun, T.; Yu, Y.; Zacher, B. J.; Mirkin, M. V. *Angew. Chemie - Int. Ed.* **2014**, *53* (51), 14120–14123.

(92) Kim, J.; Shen, M.; Nioradze, N.; Amemiya, S. *Anal. Chem.* **2012**, *84* (8), 3489–3492.

(93) Kranz, C.; Friedbacher, G.; Mizaikofft, B.; Lugstein, A.; Smoliner, J.; Bertagnolli, E. *Anal. Chem.* **2001**, *73* (11), 2491–2500.

(94) Takahashi, Y.; Shevchuk, A. I.; Novak, P.; Babakinejad, B.; Macpherson, J.; Unwin, P. R.; Shiku, H.; Gorelik, J.; Klenerman, D.; Korchev, Y. E.; Matsue, T. *Proc. Natl. Acad. Sci. U. S. A.* **2012**, *109* (29), 11540–11545.

(95) O'Connell, M. A.; Lewis, J. R.; Wain, A. J. *Chem. Commun.* **2015**, *51* (51), 10314–10317.

(96) Page, A.; Kang, M.; Armitstead, A.; Perry, D.; Unwin, P. R. *Anal. Chem.* **2017**, *89*, 3021–3028.

(97) Macpherson, J. V; Unwin, P. R. **2000**, *72* (2), 276–285.

(98) Pobelov, I. V; Mohos, M.; Yoshida, K.; Kolivoska, V.; Avdic, A.; Lugstein, A.; Bertagnolli, E.; Leonhardt, K.; Denuault, G.; Gollas, B.; Wandlowski, T. *Nanotechnology* **2013**, *24* (11), 115501.

(99) Gullo, M. R.; Frederix, P. L. T. M.; Akiyama, T.; Engel, A.; F, N.; Staufer, U. *Spectroscopy* **2006**, *78* (15), 5436–5442.

(100) Dobson, P. S.; Weaver, J. M. R.; Holder, M. N.; Unwin, P. R.; Macpherson, J. V. *Anal. Chem.* **2005**, *77* (2), 424–434.

(101) Anne, A.; Cambril, E.; Chovin, A.; Demaille, C.; Goyer, C. *ACS Nano* **2009**, *3* (10), 2927–2940.

(102) Pust, S. E.; Salomo, M.; Oesterschulze, E.; Wittstock, G. *Nanotechnology* **2010**, *21* (10), 105709.

(103) Jones, C. E.; Unwin, P. R.; Macpherson, J. V. *Chemphyschem* **2003**, *4* (2), 139–146.

(104) Davoodi, A.; Pan, J.; Leygraf, C.; Parvizi, R.; Norgren, S. *Mater. Corros.* **2013**, *64* (3), 195–198.

(105) Huang, K.; Anne, A.; Bahri, M. A.; Demaille, C. *ACS Nano* **2013**, No. 5, 4151–4163.

(106) Kranz, C. *Analyst* **2014**, *139* (2), 336–352.

(107) Knittel, P.; Bibikova, O.; Kranz, C. *Faraday Discuss.* **2016**, *193* (0), 353–369.

(108) Knittel, P.; Mizaikoff, B.; Kranz, C. *Anal. Chem.* **2016**, *88* (12), 6174–6178.

(109) PeakForce SECM Overview - Bruker AFM Modes | Bruker https://www.bruker.com/products/surface-and-dimensional-analysis/atomic-force-microscopes/modes/modes/imaging-modes/peakforce-secm/overview.html (accessed Sep 4, 2017).

(110) 5500 Atomic Force Microscope (AFM) (N9410S) | Keysight (formerly Agilent's Electronic Measurement) http://www.keysight.com/en/pd-858475/atomic-force-microscope-afm-n9410s?nid=-33986.426382&cc=GB&lc=eng (accessed Sep 4, 2017).

(111) Chen, C.-C.; Zhou, Y.; Baker, L. A. *Annu. Rev. Anal. Chem.* **2012**, *5* (1), 207–228.

(112) Page, A.; Perry, D.; Young, P.; Mitchell, D. A.; Frenguelli, B. G.; Unwin, P. R. *Anal. Chem.* **2016**, *88*, 10854–10859.

(113) McKelvey, K.; Kinnear, S. L.; Perry, D.; Momotenko, D.; Unwin, P. R. *J. Am. Chem. Soc.* **2014**, *136*, 13735–13744.

(114) Perry, D.; Paulose Nadappuram, B.; Momotenko, D.; Voyias, P. D.; Page, A.; Tripathi, G.; Frenguelli, B. G.; Unwin, P. R. *J. Am. Chem. Soc.* **2016**, *138* (9), 3152–3160.

(115) Sa, N.; Lan, W. J.; Shi, W.; Baker, L. A. *ACS Nano* **2013**, *7* (12), 11272–11282.

(116) Momotenko, D.; McKelvey, K.; Kang, M.; Meloni, G. N.; Unwin, P. R. *Anal. Chem.* **2016**, *88* (5), 2838–2846.

(117) Takahashi, Y.; Shevchuk, A. I.; Novak, P.; Murakami, Y.; Shiku, H.; Korchev, Y. E.; Matsue, T. *J. Am. Chem. Soc.* **2010**, *132* (29), 10118–10126.

(118) Morris, C. a.; Chen, C.-C.; Baker, L. a. *Analyst* **2012**, *137* (13), 2933–2938.

(119) Takahashi, Y.; Shevchuk, A. I.; Novak, P.; Zhang, Y.; Ebejer, N.; MacPherson, J. V.; Unwin, P. R.; Pollard, A. J.; Roy, D.; Clifford, C. A.; Shiku, H.; Matsue, T.; Klenerman, D.; Korchev, Y. E. *Angew. Chemie - Int. Ed.* **2011**, *50* (41), 9638–9642.

(120) Şen, M.; Takahashi, Y.; Matsumae, Y.; Horiguchi, Y.; Kumatani, A.; Ino, K.; Shiku, H.; Matsue, T. *Anal. Chem.* **2015**, *87* (6), 3484–3489.

(121) O'Connell, M. A.; Wain, A. J. *Anal. Chem.* **2014**, *86* (24), 12100–12107.

(122) Frederix, P. L. T. M.; Bosshart, P. D.; Akiyama, T.; Chami, M.; Gullo, M. R.; Blackstock, J. J.; Dooleweerdt, K.; de Rooij, N. F.; Staufer, U.; Engel, A. *Nanotechnology* **2008**, *19* (38), 384004.

(123) Page, A.; Perry, D.; Unwin, P. R. *Proc. R. Soc. A Math. Phys. Eng. Sci.* **2017**, *473* (2200).

(124) Sa, N.; Baker, L. A. *J. Am. Chem. Soc.* **2011**, *133* (27), 10398–10401.

(125) Ebejer, N.; Güell, A. G.; Lai, S. C. S.; McKelvey, K.; Snowden, M. E.; Unwin, P. R. *Annu. Rev. Anal. Chem. (Palo Alto. Calif).* **2013**, *6*, 329–351.

(126) Chen, C.-H.; Meadows, K. E.; Cuharuc, A.; Lai, S. C. S.; Unwin, P. R. *Phys. Chem. Chem. Phys.* **2014**, *16*, 18545–18552.

(127) Chen, C. H.; Jacobse, L.; McKelvey, K.; Lai, S. C. S.; Koper, M. T. M.; Unwin, P. R. *Anal. Chem.* **2015**, *87* (11), 5782–5789.

(128) Aaronson, B. D. B.; Lai, S. C. S.; Unwin, P. R. *Langmuir* **2014**, *30* (7), 1915–1919.

(129) Aaronson, B. D. B.; Garoz-Ruiz, J.; Byers, J. C.; Colina, A.; Unwin, P. R. *Langmuir* **2015**, *31* (46), 12814–12822.

(130) Aaronson, B. D. B.; Byers, J. C.; Colburn, A. W.; McKelvey, K.; Unwin, P. R. *Anal. Chem.* **2015**, *87* (8), 4129–4133.

(131) Bentley, C. L.; Kang, M.; Maddar, F.; Li, F.; Walker, M.; Zhang, J.; Unwin, P. R. *Chem. Sci.* **2017**, DOI: 10.1039/C7SC02545A.

(132) Takahashi, Y.; Kumatani, A.; Munakata, H.; Inomata, H.; Ito, K.; Ino, K.; Shiku, H.; Unwin, P. R.; Korchev, Y. E.; Kanamura, K.; Matsue, T. *Nat.*

Commun. **2014**, *5*, 5450.

(133) Kinnear, S. L.; Mckelvey, K.; Snowden, M. E.; Peruffo, M.; Colburn, A. W.; Unwin, P. R. **2013**, *29* (2013), 247143.

(134) Nadappuram, B. P.; McKelvey, K.; Byers, J. C.; Güell, A. G.; Colburn, A. W.; Lazenby, R. A.; Unwin, P. R. *Anal. Chem.* **2015**, *87* (7), 3566–3573.

(135) Lai, S. C. S.; Dudin, P. V.; MacPherson, J. V.; Unwin, P. R. *J. Am. Chem. Soc.* **2011**, *133* (28), 10744–10747.

(136) Byers, J. C.; Güell, A. G.; Unwin, P. R. *J. Am. Chem. Soc.* **2014**, *136*, 11252–11255.

(137) Bentley, C. L.; Kang, M.; Unwin, P. R. *Curr. Opin. Electrochem.* **2017**.

(138) Sharel, E. P.; Kim, Y. R.; Perry, D.; Bentley, C. L.; Unwin, P. R. *ACS Appl. Mater. Interfaces* **2016**, *8* (44), 30458–30466.

(139) *Nanoelectrochemistry*; Mirkin, M. V, Amemiya, S., Eds.; CRC Press: New York, 2015.

(140) Willets, K. A.; Wilson, A. J.; Sundaresan, V.; Joshi, P. B. *Chem. Rev.* **2017**, *117* (11), 7538–7582.

(141) Sambur, J. B.; Chen, T.-Y.; Choudhary, E.; Chen, G.; Nissen, E. J.; Thomas, E. M.; Zou, N.; Chen, P. *Nature* **2016**, *530* (7588), 77–80.

(142) Zhou, X.; Andoy, N. M.; Liu, G.; Choudhary, E.; Han, K.-S.; Shen, H.; Chen, P. *Nat. Nanotechnol.* **2012**, *7* (4), 237–241.

(143) Wilson, A. J.; Willets, K. A. *Nano Lett.* **2014**, *14* (1), 939–945.

(144) Weber, M. L.; Wilson, A. J.; Willets, K. A. *J. Phys. Chem. C* **2015**, *119*, 18591–18601.

(145) Tachikawa, T.; Yamashita, S.; Majima, T. *J. Am. Chem. Soc.* **2011**, *133* (18), 7197–7204.

(146) Andoy, N. M.; Zhou, X.; Choudhary, E.; Shen, H.; Liu, G.; Chen, P. *J. Am. Chem. Soc.* **2013**, *135* (5), 1845–1852.

(147) Perreault, F.; Fonseca de Faria, A.; Elimelech, M. *Chem. Soc. Rev.* **2015**, *44*

(16), 5861–5896.

(148) Chen, A.; Chatterjee, S. *Chem. Soc. Rev.* **2013**, *42* (12), 5425–5438.

(149) Trogadas, P.; Ramani, V.; Strasser, P.; Fuller, T. F.; Coppens, M. O. *Angew. Chemie - Int. Ed.* **2016**, *55* (1), 122–148.

(150) Raccichini, R.; Varzi, A.; Passerini, S.; Scrosati, B. *Nat. Mater.* **2015**, *14* (3), 271–279.

(151) Kleijn, S. E. F.; Lai, S. C. S.; Koper, M. T. M.; Unwin, P. R. *Angew. Chemie - Int. Ed.* **2014**, *53* (14), 3558–3586.

(152) Wu, J.; Yang, H. *Acc. Chem. Res.* **2013**, *46* (8), 1848–1857.

(153) Rodriguez, P.; Koper, M. T. M. *Phys. Chem. Chem. Phys.* **2014**, *16* (27), 13583–13594.

(154) Sambur, J. B.; Chen, P. *Annu. Rev. Phys. Chem.* **2014**, *65* (1), 395–422.

(155) Oja, S. M.; Fan, Y.; Armstrong, C. M.; Defnet, P.; Zhang, B. *Anal. Chem.* **2016**, *88* (1), 414–430.

(156) Bentley, C. L.; Kang, M.; Unwin, P. R. *J. Am. Chem. Soc.* **2017**, *139*, 16813–16821.

Chapter 2. Experimental Methods

2.1 Chemicals

Details on the chemicals and materials used are included in full in the Materials and Methods section of each results chapter. All chemicals were used as received unless otherwise stated. Synthesis procedures and characterization are also included in the pertinent chapters. All solutions were prepared with de-ionized water (Milli-Q, resistivity of 18.2 MΩ cm at 25 °C). The mass and pH of chemicals and solutions were measured using a four-figure analytical balance (Sartorius A2008) and a pH meter (UltraBASIC pH meter, Denver Instruments), respectively. All experiments were performed at room temperature.

2.2 Pipette Fabrication and Characterisation

All pipettes used in this thesis were (initially) fabricated from glass or quartz capillaries using a CO_2-laser puller (P-2000, Sutter Instruments). The capillary material, pulling parameters and dimensions of the pipettes used in each chapter are listed on Table 2.1.

Table 2.1 Capillary materials, dimensions, suppliers and the pulling parameters of the pipettes utilised in each chapter.

$d_{pipette}$[a]	Capillary material; Dimensions; Supplier	Pulling parameters (HEAT[d];FILAMENT[e];VELOCITY[f];DELAY[g];PULL[h])
Chapter 3 ≈ **3 μm**	borosilicate theta glass; o.d.[b] 1.5 mm, i.d.[c] 1.24 mm; Harvard Apparatus	line1: 400;5;50;128;0 line2: 400;5;50;128;1 line3: 400;5;50;128;0
Chapter 4 ≈ **5 μm**	borosilicate glass; o.d. 1.2 mm, i.d. 0.69 mm; Harvard Apparatus	line1: 430;4;20;121;22
Chapter 5	quartz; o.d. 1 mm, i.d. 0.5 mm; Friedrich & Dimmock	line1: 750;4;30;150;80

≈ **30 nm**		line2: 650;3;40;135;150
Chapter 6	quartz theta; o.d. 1.2 mm, i.d. 0.9 mm, ; Friedrich and Dimmock	line1: 900;4;20;140;100
≈ **150 nm**		line2: 850;3;20;140;150

[a]d_{pipette}, diameter of the pipette; [b]o.d., outer diameter of the capillary; [c]i.d., inner diameter of the capillary; [d]HEAT, the output power of the laser; [e]FILAMENT, the scanning pattern of the laser beam onto the capillary; [f]VELOCITY, the velocity at which a puller bar moves prior to a hard pull; [g]DELAY, the time of the start of the hard pull relative to the deactivation of the laser; [h]PULL, the force of the hard pull.[1]

In Chapter 6, double-channelled quartz theta pipette probes were further modified for multifunctional applications (*i.e.*, SECM-SICM) through the deposition of pyrolysed carbon (from butane) in one of the channels.[2–5] The experimental set up for the process is shown in Figure 2.1A. In brief, one of the barrels was blocked with 'Blu-Tack' (Bostik), while butane was passed through the other barrel at a constant pressure of 0.6 – 0.8 bar (Figure 2.1B). The tapered end (tip) was then carefully aligned and placed inside a wider, single-channelled quartz capillary (*i.e.*, i.d. 1.2 mm), through which a constant flow of argon was passed (0.1 L min^{-1}) and then heated with a micro torch to deposit a layer of pyrolysed carbon in the "unblocked" channel. The heating time at the end (tip) of pipette was varied from 1 to 15 s and was eventually optimised to 3 s. This results in a double-channelled multifunctional nanopipette, one filled with a solid carbon electrode for SECM and the other open, to be filled with electrolyte solution for SICM (Figure 2.1C). These probes were further tailored through focussed ion beam (FIB) milling with a JEOL 4500 (Chapter 6).

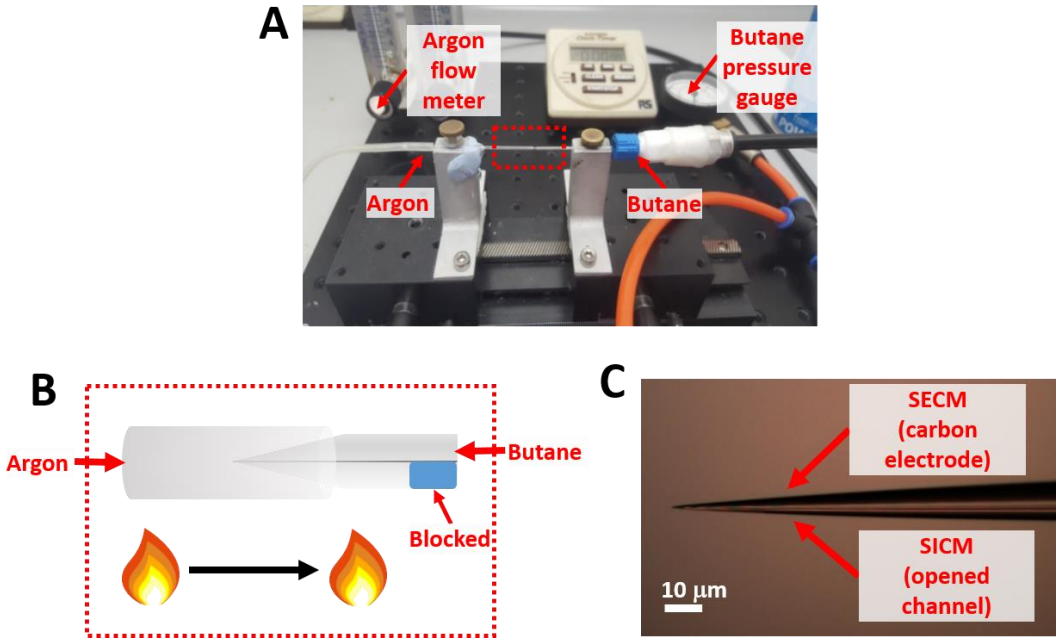

Figure 2.1 (A) A photograph and (B) schematic depicting the experimental set up for the butane pyrolysis process during fabrication of double-channelled SECM-SICM probes. (C) Optical image of a fabricated SECM-SICM probe.

Micropipette and large nanopipette (hundreds of nm scale) probes were characterised by FE-SEM (Zeiss SUPRA 55 FE-SEM, at from 3 to 5 kV). SEM images provide details on the geometry of the end ('tip') of the pipettes. However, for small nanopipettes (tens of nm scale), it can be challenging to resolve the geometry with SEM. Also, SEM is unable to provide information on the internal geometry of the pipette probes, as it utilizes a relatively low energy electron beam, usually below 20 kV (Figure 2.2A). For this reason, a transmission electron microscope (Jeol 2000FX TEM, at 200 kV), equipped with a GATAN ORIUS 11-megapixel digital camera, was used for the full characterisation (*i.e.*, inner/outer geometry) of fine nanopipette probes (Figure 2.2B). Figure 2.3 shows an example of a pipette sample prepared for TEM characterisation. During this process, the end of the pipette (tip) was carefully cut with a diamond pen, placed on a carbon-taped brass TEM holder and fixed in place with conductive silver paint (RS). Electron microscopy images used for the analysis of the micro/nanopipette probes utilised in the thesis are presented in the each chapter.

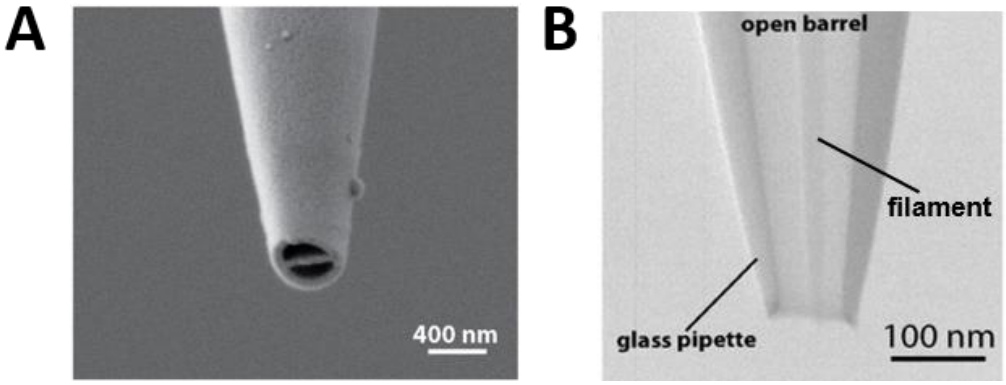

Figure 2.2 Electron microscopy images of the nanopipette probes used for high-resolution electrochemical imaging. (A) SEM image of a double-channelled theta nanopipette. (B) TEM image of a single-channelled nanopipette. Figure 2.2 was adapted from Kang *et al.* (2016).[6]

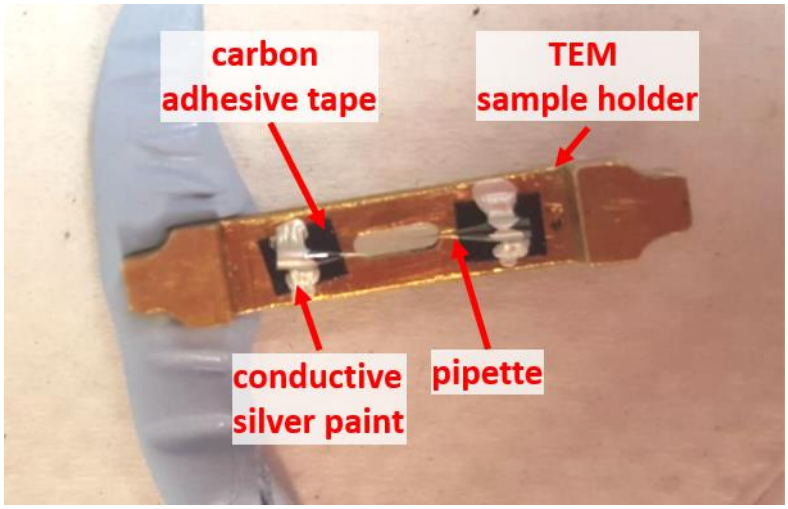

Figure 2.3 Photograph of nanopipette probes mounted on a brass holder for TEM characterization.

2.3 SEPM Operating System

SEPM encompasses a range of techniques (*vide supra*) that make use of a dynamic probe containing an electrochemical sensor to measure the local flux or concentration of an electroactive/charged species at, or near, a surface or interface. WEIG provides a new SEPM operating system to the public, the Warwick Electrochemical-Scanning Probe Microscopy (WEC-SPM) software, written in the LabVIEW programming language (National Instruments) to control, and measure,

signals from the hardware through a field-programmable gate array (FPGA) card (PCIe-7852R, National Instruments).[7] The instrumentation was optimised for the static/dynamic operation of nanoscale probes in a stable environment (Figure 2.4), incorporating a feedback response that was used to control the distance between the probe and a surface. The use of an FPGA card allowed fast output/input through multiple channels, achieving fast and ultrasensitive operation. Furthermore, as the operating system is flexible and shared through a common remote server, new SEPM techniques can be developed, implemented and distributed with a range of probe positioning configurations.

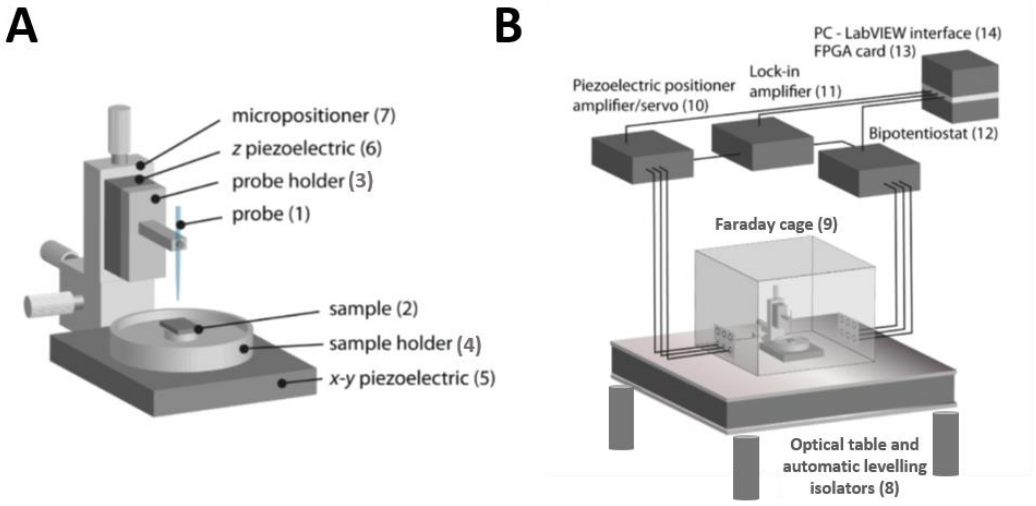

Figure 2.4 Schematic of a typical SEPM set up, for use with the WEC-SPM software. (A) Illustrates the positioning system and (B) shows the general control of the SEPM system. Figure 2.4 was adapted from the WEC-SPM Control Software User Guide (2017).[8]

The components that make up a typical SEPM set up for use with the WEC-SPM software, as carried out in this thesis, are shown schematically in Figure 2.4. The probe (*e.g.*, micro/nanopipette) [(1), Figure 2.4A], vertically mounted on the probe holder [(3), Figure 2.4A], was positioned above the sample surface [(2), Figure 2.4A], which was fixed on the sample holder [(4), Figure 2.4A]. The probe holder was fixed on a *z*-piezoelectric nanopositioner (various models from Physik Instrumente), allowing movement of the probe normal to the sample surface, while the sample holder

was carefully mounted on *xy*- piezoelectric nanopositioners (various models from Physik Instrumente and Mad City Labs Inc.). Coarse positioning of the probe/sample was achieved using mechanical micropositioners (Newport, M-461-XYZ-M) [(7), Figure 2.4A] or more recently, picomotors (Newport, 8303 Picomotor Actuator)[9], while fine movement (*nm* spatial resolution) was achieved using the *xy*- and *z*-piezoelectric nanopositioners described above [(5) and (6), Figure 2.4A, maximum translation varies from 30×30 μm to 100×100 μm and from 15 μm to 38 μm, respectively].

The positioning system (Figure 2.4A) was placed in a custom-built Faraday cage [(9), Figure 2.4B], located on an optical table (Newport, RS2000) with automatic levelling isolators (Newport, S-2000A-423.5) [(8), Figure 2.4B], minimising external mechanical vibration at low frequencies. Acoustic foam was attached to the inside of the Faraday cage to reduce acoustic vibration. Vacuum insulation panels (Kevothermal) and aluminium heat sinks were also installed in the Faraday cage to improve thermal insulation, while the temperature was held constant in the laboratory (24 ± 1°C) with a 24 hour air-conditioning system. It is important to note that these environmental controls play an extremely significant role in the nanoscale system, as the position of the probe can be perturbed by externally induced mechanical/physical noise.[10]

The piezoelectric nanopositioners were controlled by amplifiers/servos [(10), Figure 2.4B] through analog control signals. Each amplifier/servo was calibrated to an individual piezoelectric positioner by the supplier, and the control signal (0 – 10 V on the systems in WEIG, although it can be varied) was amplified to move the piezoelectric positioner the desired amount, while simultaneously monitoring the position with the servos. An external lock-in amplifier (SR830, Stanford Research Systems) was used to generate the oscillating signal for the modulated feedback control modes (*i.e.*, an oscillating probe and the oscillating electrochemical signal),[11–13] and to extract the oscillating component in the induced signal [(11), Figure 2.4B]. Currents were measured with customized (bi)potentiostats [(12), Figure 2.4B], which were built in house by Dr. Alex Colburn. This equipment was controlled, and the signals measured, also using analog signals.

An FPGA card, mounted directly into the motherboard of the PC using a PCI express interface [(13), Figure 2.4B], was used to collect the data and control the instrumentation [*e.g.*, position of the probe and potential of the (bi)potentiostats]. An unified analog interface was used to control the instrumental components and collect eight different signals (*e.g.*, *xyz* position, two individual channels of potential, three individual channels of current), measured synchronously through the FPGA card, at rates up to 750 kHz. A home built break out box, with BNC connectors (total 16 channels, Table 2.2), was used connect the analog input (AI) and output (AO) lines of the FPGA card to the instrumental components. In addition, the FPGA card allowed complex calculations, such as data filtering and probe position control logic (*e.g.*, self-referencing, Chapter 5 and Chapter 6). A PC running Windows 7 and the latest version of LabVIEW 2013 or LabVIEW 2016 was used throughout this thesis [(14), Figure 2.4B]. The system was utilised for a range of SEPM techniques, including SECCM (Chapter 3 and 4), SICM (Chapter 5) and SICM-SECM (Chapter 6), as presented in the following results chapters.

Table 2.2 The BNC channels from the breakout box (AO = Analog Output, AI = Analog Input).

AO-0	**AO-1**	**AO-2**	**AO-3**	**AO-4**	**AO-5**	**AO-6**	**AO-7**
x piezo output	y piezo output	z piezo output	Potential 1	Potential 2	Picomotor control 1	Picomotor control 2	Picomotor control 3
AI-0	**AI-1**	**AI-2**	**AI-3**	**AI-4**	**AI-5**	**AI-6**	**AI-7**
x piezo input	y piezo input	z piezo input	Current 1	Current 2	Lock-in amplitude	Current3	Lock-in phase

2.4 References

(1) Sutter Instrument. 2012.

(2) Takahashi, Y.; Shevchuk, A. I.; Novak, P.; Zhang, Y.; Ebejer, N.; MacPherson, J. V.; Unwin, P. R.; Pollard, A. J.; Roy, D.; Clifford, C. A.; Shiku, H.; Matsue, T.; Klenerman, D.; Korchev, Y. E. *Angew. Chemie - Int. Ed.* **2011**, *50* (41), 9638–9642.

(3) Takahashi, Y.; Shevchuk, A. I.; Novak, P.; Murakami, Y.; Shiku, H.; Korchev, Y. E.; Matsue, T. *J. Am. Chem. Soc.* **2010**, *132* (29), 10118–10126.

(4) O'Connell, M. A.; Lewis, J. R.; Wain, A. J. *Chem. Commun.* **2015**, *51* (51), 10314–10317.

(5) Nadappuram, B. P.; McKelvey, K.; Byers, J. C.; Güell, A. G.; Colburn, A. W.; Lazenby, R. A.; Unwin, P. R. *Anal. Chem.* **2015**, *87* (7), 3566–3573.

(6) Kang, M.; Momotenko, D.; Page, A.; Perry, D.; Unwin, P. R. *Langmuir* **2016**, *32* (32), 7993–8008.

(7) Bentley, C. L.; Kang, M.; Unwin, P. R. *Curr. Opin. Electrochem.* **2017**.

(8) Warwick Electrochemistry and Interfaces Group. The University of Warwick 2017.

(9) Kang, M.; Perry, D.; Bentley, C. L.; West, G.; Page, A.; Unwin, P. R. *ACS Nano* **2017**.

(10) Byers, J. C.; Paulose Nadappuram, B.; Perry, D.; McKelvey, K.; Colburn, A. W.; Unwin, P. R. *Anal. Chem.* **2015**, *87* (20), 10450–10456.

(11) Perry, D.; Paulose Nadappuram, B.; Momotenko, D.; Voyias, P. D.; Page, A.; Tripathi, G.; Frenguelli, B. G.; Unwin, P. R. *J. Am. Chem. Soc.* **2016**, *138* (9), 3152–3160.

(12) McKelvey, K.; Kinnear, S. L.; Perry, D.; Momotenko, D.; Unwin, P. R. *J. Am. Chem. Soc.* **2014**, *136*, 13735–13744.

(13) Ebejer, N.; Güell, A. G.; Lai, S. C. S.; McKelvey, K.; Snowden, M. E.; Unwin, P. R. *Annu. Rev. Anal. Chem. (Palo Alto. Calif).* **2013**, *6*, 329–351.

Chapter 3. Time-Resolved Detection and Analysis of Single Nanoparticle Electrocatalytic Impacts

3.1 Abstract

There is considerable interest in understanding the interaction and activity of single entities, such as (electro)catalytic nanoparticles (NPs), with (electrode) surfaces. Through the use of a high bandwidth, high signal/noise measurement system, NP impacts on an electrode surface are detected and analyzed in unprecedented detail, revealing considerable new mechanistic information on the process. Taking the electrocatalytic oxidation of H_2O_2 at ruthenium oxide (RuO_x) NPs as an example, the rise time of current–time transients for NP impacts is consistent with a hydrodynamic trapping model for the arrival of a NP with a distance-dependent NP diffusion-coefficient. NP release from the electrode appears to be aided by propulsion from the electrocatalytic reaction at the NP. High-frequency NP impacts, orders of magnitude larger than can be accounted for by a single pass diffusive flux of NPs, are observed that indicate the repetitive trapping and release of an individual NP that has not been previously recognized. The experiments and models described could readily be applied to other systems and serve as a powerful platform for detailed analysis of NP impacts.

3.2 Introduction

An important frontier in electrochemistry is measuring the behavior of individual nanoentities such as nanoparticles (NPs), nanowires, and nanorods and relating this to other properties such as size, structure, and electronic characteristics, so as to develop fundamental understanding and rational applications.[1–3] An interesting approach for observing the electrochemical properties of catalytic NPs is to monitor their impact (or landing) from solution onto a collector electrode, as introduced by Bard *et al.*,[4,5] and developed by several groups.[6–12] In order to resolve

such impacts, the use of a small-sized ultramicroelectrode (UME) is mandatory to reduce both background currents and the impact frequency. To enhance the impact signal to background current, electrode surfaces have been modified with Hg or Bi,[9] and boron-doped diamond[12] has also been used as an UME material. Alternatively, scanning electrochemical cell microscopy (SECCM) functioning as an ultramicro-electrochemical cell system offers particularly low background currents by reducing the area of the collector electrode as well as offering the widest range of support electrodes. This is because the electrochemical cell is formed by meniscus confinement, rather than electrode encapsulation (Figure 3.1).[13] Despite these innovations, detailed analysis of the form of the current–time profile which is the primary signal for the landing (and detachment) of a single NP on an electrode has not yet been forthcoming but would represent a huge advance toward understanding the impact process. Herein, it is possible to analyze this process as never before and deduce key information on the NP arrival and release process from individual impact transients. Moreover, this chapter shows that impact frequencies can be orders of magnitude higher than expected based on single pass diffusion due to the repetitive impact and release of a single NP.

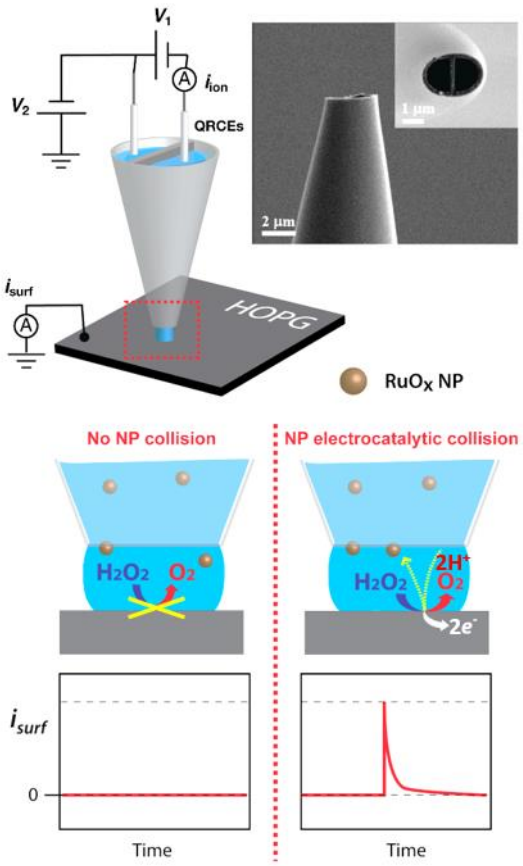

Figure 3.1 RuO_x NP landing experiments in an ultramicro-electrochemical cell, showing the cell setup (top), with a typical theta pipet for meniscus contact and NP delivery to a working electrode (HOPG) substrate. There is no oxidation of H_2O_2 at the HOPG electrode surface, *i.e.*, no surface current (i_{surf}), as shown on the bottom left, unless a NP impacts with the surface and sets off the electrocatalytic oxidation of H_2O_2 at the NP (bottom right).

3.3 Materials and Methods

3.3.1 Chemicals

$RuCl_3 \cdot xH_2O$ (99.98 %), H_2O_2 (30 wt %) solutijon, and sodium citrate were purchased from Sigma-Aldrich (St. Louis, MO) and NaOH, $NaH_2PO_4 \cdot xH_2O$, and Na_2HPO_4 were supplied by Fisher Scientific. 0.1 M phosphate buffer solution (pH 7.4) was prepared for electrolyte solutions with high purity water (Milli-Q, 18.2 MΩ cm resistivity at 25 °C), as also used for other solutions.

3.3.2 Electrochemical Landing Experiment

A dual-barrelled glass theta pipette with a diameter of 3 μm was prepared from a borosilicate theta glass capillary (TGC150-10, Harvard Apparatus) using a CO_2-laser puller (P-2000, Sutter Instruments) and the outer wall of the end of the pipette was silanized with dichlorodimethylsilane ($Si(CH_3)_2Cl_2$, Acros Organics, 99+ %) to aid meniscus confinement when the meniscus came into contact with the substrate of interest. An AgCl-coated Ag wire was placed in each barrel of the pipette to act as a quasi-reference counter electrode (QRCE) and highly oriented pyrolytic graphite (HOPG) was used as the substrate working electrode.

The instrumentation for SECCM has been described in full elsewhere, including for fast electrochemical measurements.[14,15] The pipette and HOPG (ZYB-grade, Aztech Trading, UK, http://www.2spi.com) were mounted on a *z*-piezoelectric positioner (P-753.3CD LISA, PhysikInstrumente) and *xy*-piezoelectric stage (P-621.2CL PIHera, PhysikInstrumente), respectively, in a Faraday cage. A bias potential of 0.1 V was applied between two QRCEs, and the resulting conductance current was measured to confirm that a meniscus had formed and to monitor its stability before it approached towards the HOPG surface. Once in meniscus contact, the inter-QRCE bias was set to zero. The current from the substrate was recorded as a function of time to identify the contact of meniscus with the HOPG and to detect RuO_x NPs landing on the HOPG surface at various potentials. For the experiments herein, the instrumentation time constant was 10 μs and data were obtained at a rate of 165 μs per data point acquisition rate (each point from the average of 33 points acquired every 5 μs).[13] The data from the home-built current amplifier were acquired by a FPGA card (PCIe-7852R) with Labview 2013 interface.

Figure 3.2 shows typical CVs on HOPG with meniscus contact in the absence of NPs, with no H_2O_2 and with 0.5 mM H_2O_2 present. These data show that there is very little current for H_2O_2 oxidation in the potential range of interest at HOPG alone.

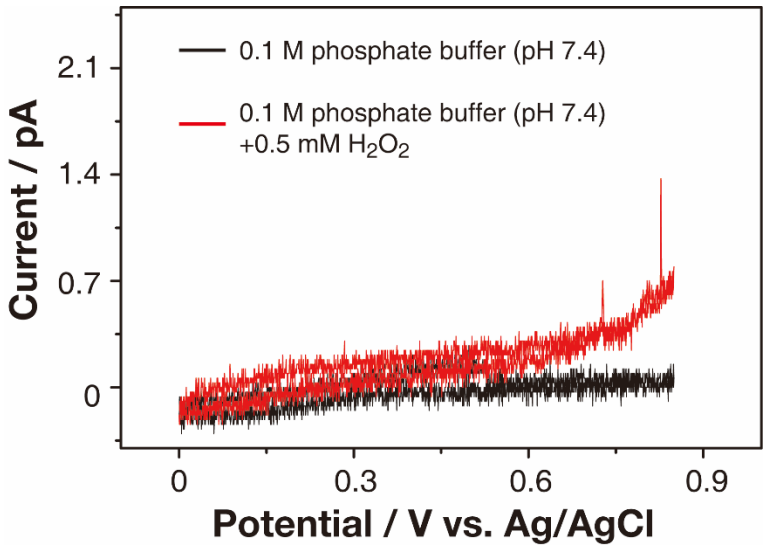

Figure 3.2 Cyclic voltammograms, with and without H_2O_2 present, on HOPG in 0.1 M phosphate buffer (pH 7.4) at a scan rate of 0.1 V s^{-1}.

3.3.3 Preparation and Characterization of Ruthenium Oxide Nanoparticles (RuO_x NPs)

Amorphous RuO_x NPs were synthesized by injecting 30 mM NaOH solution into 1 mM $RuCl_3 \cdot xH_2O$.[16,17] To stabilize the RuO_x NPs,[18] 34 mM sodium citrate was added with vigorous magnetic stirring and the solution was washed three times with high purity water, with repeated centrifugation and sonification to remove excessive sodium citrate in solution. In the case of RuO_x NPs synthesized without sodium citrate, the additional step of sodium citrate capping was simply omitted. Field emission-scanning electron microscopy (FE-SEM) and transmission electron microscopy (TEM) were used to characterize the size of RuO_x NPs. FE-SEM was performed with a Zeiss SUPRA 55 FE-SEM at 5 kV and TEM images were obtained with a Jeol 2000FX TEM at 200 kV. A Malvern Zetasizer Nano ZS (Malvern Instruments Ltd., UK) was used to measure ζ-potentials of RuO_x NPs in aqueous solutions and RuO_x NP size in the solution used for impact studies. The concentration of RuO_x NPs was estimated as 15 pM after drying steps, considering the average size of the RuO_x NPs (56 ± 16 nm), molecular weight (169.07 g mol^{-1}), and bulk density (2.46 g cm^{-3}) of hydrous RuO_x.[17]

3.3.4 Three-Dimensional (3D) Random Walk Simulations

To explore the nature of the current-time transients obtained during NP landing experiments, three-dimensional (3D) random walk simulations were performed of a single NP in a box of size 3 μm (*x*) × 3 μm (*y*) × 0.3 μm (*z*, height) (close to the dimensions of the SECCM meniscus).[19] A time-step, *dt*, of 1 ns was used with distance-step, *ds*, that was calculated according to:[20]

$$ds(z) = \sqrt{2D(z)dt} \quad (1)$$

$D(z)$ is the diffusion coefficient of the NP, which varies with distance, *z*, from the collector electrode:[21]

$$D(\mathrm{z}) = \frac{6z^2 + 2r_{\mathrm{NP}}z}{6z^2 + 9r_{\mathrm{NP}}z + 2r_{\mathrm{NP}}^2} D_{\mathrm{NP}} \quad (2)$$

where *z* is the electrode-NP separation, r_{NP} is the NP radius, assumed to be 28 nm which is the average value in the experiments reported. D_{NP} is the bulk diffusion coefficient of NP that can be reasonably estimated from the Stokes-Einstein equation:[13]

$$D_{\mathrm{NP}} = \frac{k_{\mathrm{B}}T}{6\pi\eta r_{\mathrm{NP}}} \quad (3)$$

where k_{B} is the Boltzmann constant (1.381×10^{-23} J K^{-1}), *T* is the temperature (298 K), η is the dynamic viscosity of the solution (8.90×10^{-4} Pa s for dilute aqueous solution), and r_{NP} is 28 nm. D_{NP} herein is estimated as 8.8×10^{-8} cm^2 s^{-1}.

At each time-step, the NP was allowed to move, *ds*, with equal probability in the ± *x*, ± *y* or ± *z* direction. 3,000,000 steps were used in each simulation giving a total simulation time of 3 ms for each run.

In each simulation, the initial position of the NP was set to be 5 nm above the collector electrode surface in the center of the *x*-*y* plane. Whenever the NP was within 1 nm of the surface during the simulation, an occupancy of 1 was assigned at that time, as this is sufficiently close for there to be electronic coupling for electrochemistry (electrocatalysis) to occur at the NP.[22,23] To capture the effect of the electrometer

response time, the occupancy was convoluted with the electrometer response function:[20]

$$f(t,\tau) = \frac{2\pi}{\tau} e^{-\frac{2\pi t}{\tau}} \quad (4)$$

where τ is the time constant of the electrometer (10 μs in these experiments and simulations), and t is time. This time constant was roughly 10,000 times larger than the time-step used and so the effect of the electrometer response function is that the NP has to remain occupant within the tunneling distance for a few sequential time-steps to see a response. In order to give the simulated data the same treatment as in experiments, samples were taken from this convolved current signal every 5 μs and 33 of these were averaged to give each point, resulting in one data point every 165 μs.

200 simulations were run, each of 3 ms, starting with the NP having the same initial position (see above). For a typical landing event, the response signal and occupancy are shown in Figure 3.3A and the corresponding height of the NP above the collector electrode is shown in Figure 3.3B, along with an *x*-*y* coordinate trace in Figure 3.3C. It can be seen that once the simulation starts, the NP moves above the surface, but that there is ultimately a tendency for the NP to come into close contact with the collector electrode, primarily as a result of the distance-dependent diffusion coefficient, *D*(z), which hydrodynamically traps the NP. A further consequence of this effect is that the lateral movement of the NP is also hindered, resulting in the NP, residing close to its initial position at (0,0) in the *x*-*y* plane as shown in Figure 3.3C. The distance-dependent diffusion coefficient (eq. 2), used in this model applies for any spherical particle near a (comparatively) infinite wall in solution refer to the original papers,[21,24] where the Reynolds number is low (as applicable herein). This will be a reasonable approximation for many NP systems, but analogous relationships – if needed – could be used for NPs with other shapes. It should further be pointed out that additional contributions to NP adsorption beyond hydrodynamic trapping could easily be incorporated as required, including electric field and double layer effects (at low electrolyte concentration).

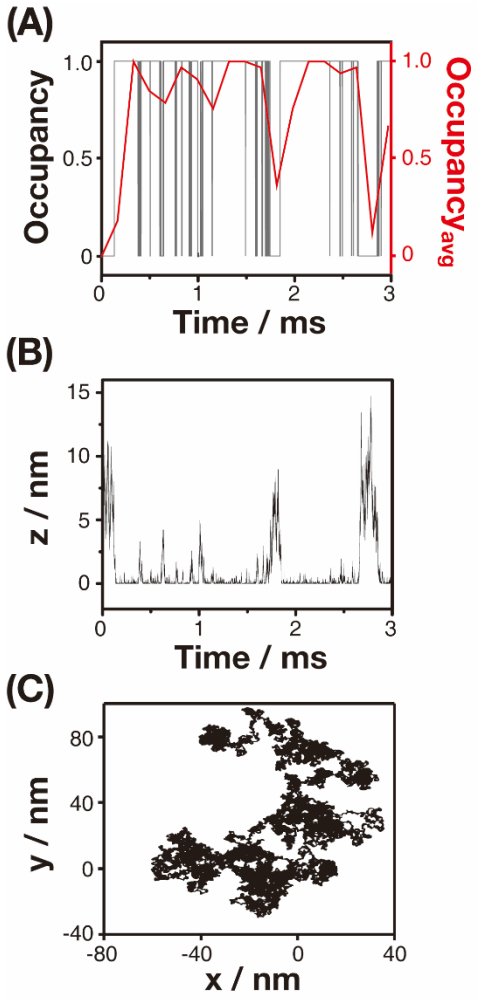

Figure 3.3 (A) Comparisons of the occupancy (black) and the average occupancy of the NP considering the experimental conditions (red). (B) The height (*z*) of the NP above the collector electrode during the interaction of a NP with the collector electrode and (C) lateral trajectory of the NP.

3.4 Results and Discussion

In this chapter, SECCM[13] was utilised to investigate H_2O_2 oxidation at ruthenium oxide (RuO_x) NPs, determining the NP landing characteristics and the distribution of kinetics currents for individual impacts within an ensemble of colliding NPs, with unprecedented time resolution. The heterogeneous kinetics of H_2O_2 electro-oxidation has been studied extensively at a variety of nanomaterials,[13] among which several metal oxides appear to be promising, particularly for bioanalytical applications, due to the biocompatibility and robust electrocatalytic performance.[25–

[28] RuO_x is especially interesting as it electrochemically catalyzes H_2O_2 electro-oxidation at relatively low overpotentials in physiological environments.[26,27] The experiments reported herein allow us to measure the residence time and interaction of RuO_x NPs with an electrode during electroctalysis.

The ultramicro-electrochemical cell was made by meniscus contact of a highly oriented pyrolytic graphite (HOPG) collector electrode from a tapered dual-barrelled borosilicate theta pipet (end diameter 3 μm), filled with a solution of RuO_x NPs and 0.5 mM H_2O_2 in 0.1 M phosphate buffer (pH 7.4) and containing a Ag/AgCl quasi-reference counter electrode (QRCE) in each channel (Figure 3.1).[13] The pipet was approached toward the HOPG with a *z*-piezoelectric positioner while monitoring the ion-conductance current between the barrels (i_{ion}) with a potential bias of 0.1 V between the two Ag/AgCl QRCEs (V_1). Once the meniscus was in contact with the HOPG, sensed as an abrupt change in i_{ion},[13] V_1 was set to 0 V and current–time (*i*–*t*) traces were recorded from the HOPG substrate (i_{surf}). HOPG was selected as the collector electrode as it exhibits exceptionally low background currents,[29,30] and is relatively insensitive to H_2O_2 oxidation over the potential range where RuO_x is an effective electrocatalyst (Figure 3.2). Moreover, many types of NPs exhibit weak interaction with HOPG,[31,32] and this enabled us to monitor H_2O_2 oxidation on the RuO_x NPs with glancing collisions rather than sticking landings where the NP would remain and accumulate on the support electrode.

RuO_x NPs were synthesized with sodium citrate and characterized by field emission-scanning electron microscopy (FE-SEM) and transmission electron microscopy (TEM), Figure 3.4A and B. Sodium citrate was used as a capping agent as it promoted the formation of well-dispersed RuO_x NPs with a reasonably regular size and shape (Figure 3.4) but would not lead to much inhibition of electron transfer in collision experiments unlike some alternative organic capping agents.[33] The apparent NP radius, r_{NP}, was estimated from the analysis of TEM images of NPs, with a mean value of 28 ± 8 nm (N = 200) and from dynamic light scattering (DLS) for the same solution conditions as for the electrochemical measurements (26 ± 5 nm), with the results of both analyses shown in Figure 3.4C. The capping step also enhanced the colloidal stability of RuO_x NPs in aqueous solution, as a result of a larger absolute ζ-potential value than without capping agent (Table 3.1).[34] RuO_x NPs synthesized without sodium citrate, in contrast, showed uneven structures with a broad distribution

of both apparent size (Figure 3.5) and the current signal in landing experiments, due to a predominance of agglomerates (Figure 3.6).

Table 3.1 ζ -potential measurements of RuOx NPs with or without the sodium citrate capping step.

	w/o sodium citrate	w/ sodium citrate
ζ-potential (mV)	-29.7±4.1	-43.7±6.2

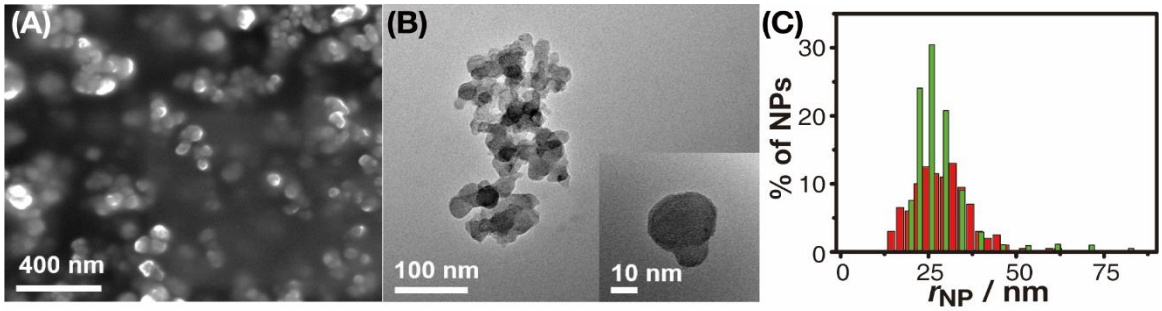

Figure 3.4 (A) FE-SEM and (B) TEM images of RuO_x NPs synthesized with sodium citrate. (C) Size distribution from the analysis of TEM images (red) and from DLS (green), in terms of the particle radius, r_{NP}.

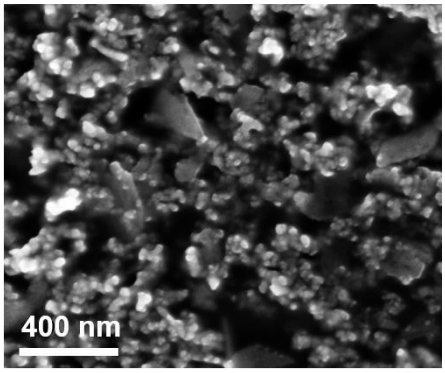

Figure 3.5 SEM images of RuO_x NPs synthesized without sodium citrate.

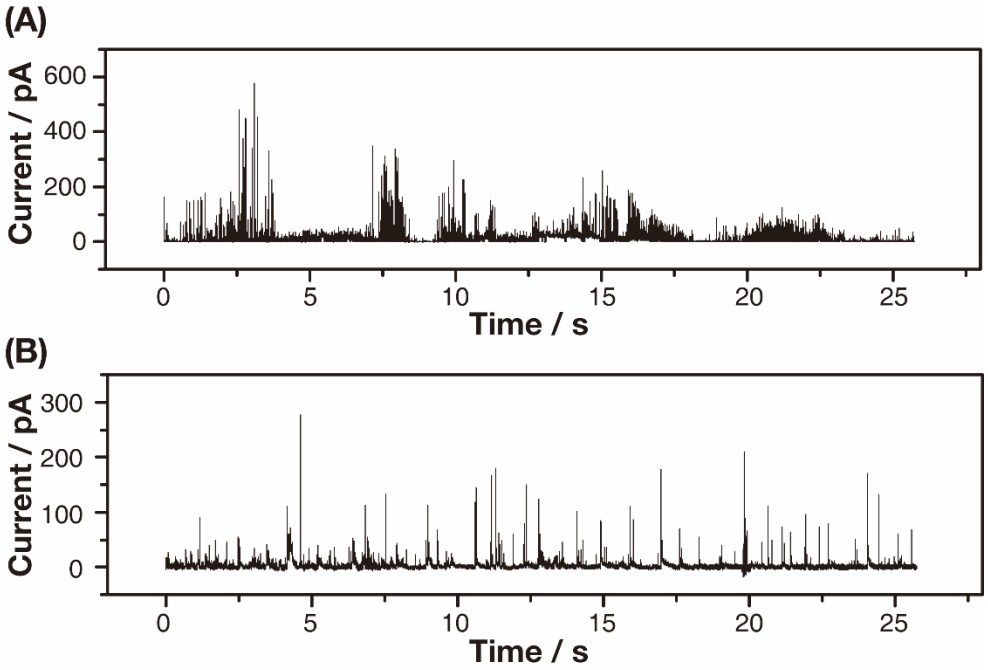

Figure 3.6 Current responses of RuO_x NP impacts at HOPG in the presence of 0.5 mM H_2O_2, at a potential of 0.55 V vs. Ag/AgCl QRCE. This figure compares NPs synthesized (A) without or (B) with a sodium citrate capping step. Note the difference in the current scales.

RuO_x NP impacts with the collector electrode were observed only in the presence of 0.5 mM H_2O_2in 0.1 M phosphate buffer solution (pH 7.4) due to H_2O_2 oxidation on RuO_x NPs when they made the contact with the HOPG support (Figure 3.7). These data are representative of more than 8 experimental runs carried out on this system. Control measurements, with and without H_2O_2 present (at a collector electrode potential of 0.55 V), are given in Figure 3.8. Results at different applied potentials (E_{app}) (0.15, 0.25, 0.35, 0.45, 0.55, 0.65, and 0.75 V) showed that in the presence of H_2O_2 distinct features in the *i–t* trace started to appear at 0.25 V (Figure 3.7A). The individual *i–t* response shape (Figure 3.7B) was characterized by a fast rise to a peak (i_{peak}) and a slower decay back to the baseline, within 3 ms, during the single NP impacts on the collector electrode. i_{peak} tended to increase with more positive E_{app}. At 0.25 V, events with i_{peak} of just 7 ± 1 pA and charge of 11 ± 4 fC could be seen (corresponding to the two-electron oxidation of just 35 (±14) × 10^3 molecules of H_2O_2).

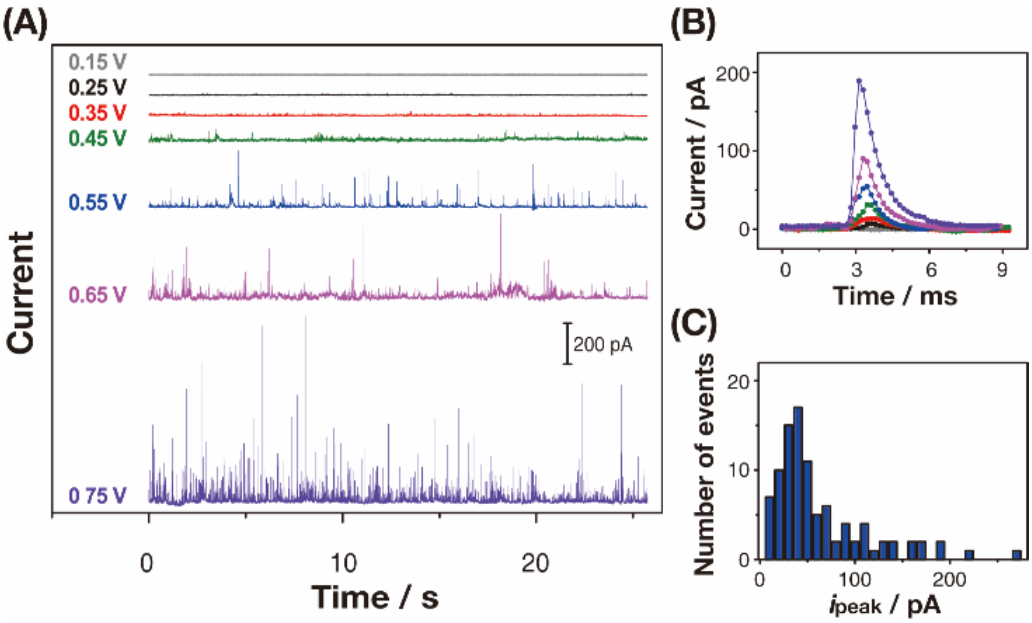

Figure 3.7 (A) Current (isurf) responses for 0.5 mM H_2O_2 oxidation with 15 pM RuO_xNPs in 0.1 M phosphate buffer solution (pH 7.4) at different E_{app} at the HOPG collector electrode (0.15 V, 0.25 V, 0.35 V, 0.45 V, 0.55 V, 0.65 and 0.75 V vs Ag/AgCl QRCE). (B) Example current responses of individual impacts of RuO_xNPs at the different E_{app} with the color matched with part A; the bigger the current magnitude the higher the E_{app}. (C) Distribution of peak currents, i_{peak}, from collision experiments at 0.55 V.

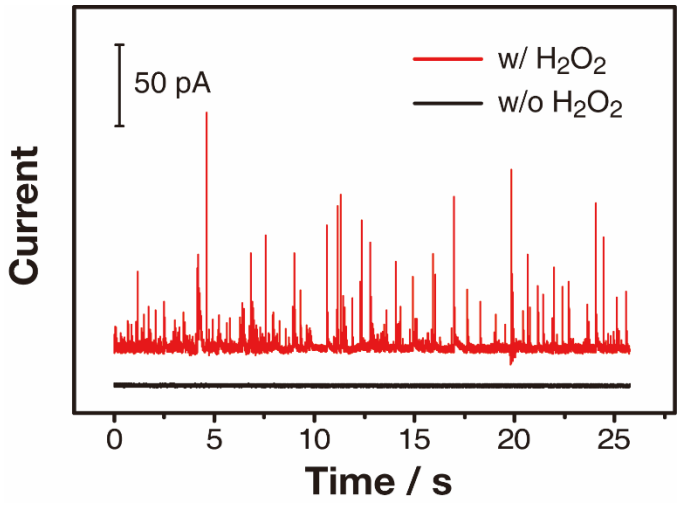

Figure 3.8 Comparison of current responses in RuO_x NP landings with 0.5 mM H_2O_2 and without 0.5 mM H_2O_2 at 0.55 V.

A potential of 0.55 V was chosen as an optimized value for further studies to obtain a sufficiently large current response for H_2O_2 electro-oxidation to be made with good signal-to-noise and bandwidth (Figure 3.7A), while minimizing side reactions such as water splitting that can occur on RuO_x NPs at excessively positive potential (Figure 3.9).[26,35] The mean value of i_{peak} at 0.55 V (Figure 3.7C) was 46 ± 16 pA corresponding reasonably well to that expected for the diffusion-controlled steady-state current (i_{ss}) predicted for a NP on a surface, based on the NP size distribution (Figure 3.4C):[20,36]

$$i_{ss} = 4\pi(ln2)nFD_{H_2O_2}C_{H_2O_2}r_{NP} \quad (1)$$

where n is the number of electrons transferred per H_2O_2 (2), F is the Faraday constant (96 485 C mol^{-1}), D_{H2O2} is the diffusion coefficient of H_2O_2 in 0.1 M phosphate buffer solution (1.46 × $10^{-5}$$cm^2$ s^{-1}),[37] C_{H2O2} is the concentration of H_2O_2 (0.5 mM). This simple analysis yields i_{ss} = 38 ± 10 pA.

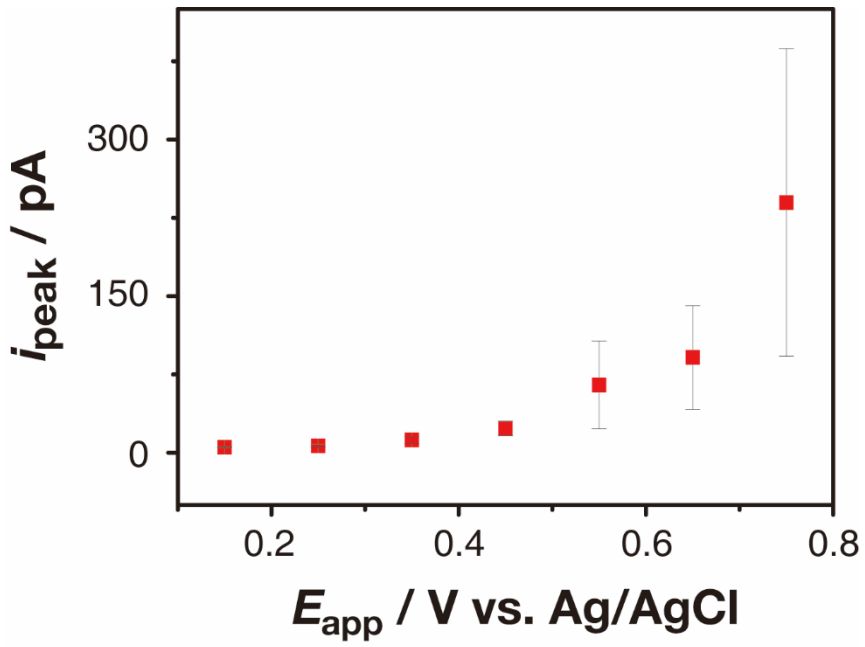

Figure 3.9 Plot of average i_{peak} against different E_{app} from Figure 3.7.

The high rates of mass transport to NPs of this size means that the characteristic steady-state diffusion time, 0.5 μs (≈ r_{NP}^2/D_{H2O2}), is rapid and much faster than the response time of the electrochemical measurement system. The electrochemical current at any time (taking into account the instrument response function for the

current measurement (Section 3.3.4) is thus determined by the occupancy of the NP with the electrode surface. Since i_{peak} is close to that expected for a diffusion-limited process (see above), i_{peak} represents an occupancy of one of the NP with the surface, and $i(t)/i_{peak}$ is thus the relative occupancy at time t.

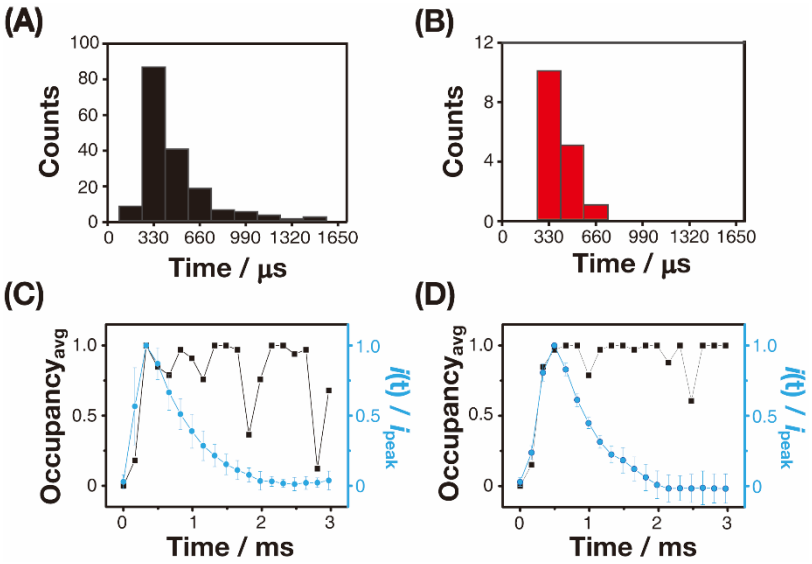

Figure 3.10 Histograms of the rise time from (A) 200 simulations and (B) 16 experimental transients. Experimental *i*–*t* traces (blue lines) are presented in parts C and D. These are the average (one standard deviation) of (C) 10 individual transients that had a rise time of 330 µs and (D) 5 individual traces that had a rise time of 500 µs. Shown alongside are simulated occupancy traces (black lines), which displayed a similar rise time for comparison.

The excellent signal-to-noise and high bandwidth in our experiment allowed us to examine individual transients in unprecedented detail and compare the results to three-dimensional (3D) random walk simulations of NP landing, details of which are presented in Section 3.3.4. Although the model has been developed for a spherical NP, to which most systems will approximate, it would be possible to consider nonspherical NPs (variable direction-dependent diffusion coefficient). Furthermore, it has been shown that NP aggregation is relatively unimportant in this system, but if such effects occurred, they could be incorporated into the model, *e.g.*, through a time-dependent particle size and population, representing the aggregation and deaggregation kinetics. In brief, for the simulations, an electrolyte zone above the collector electrode was considered of a similar size to the SECCM meniscus. Electron transfer between the

electrode and NP was reasonably assumed to occur when the NP was within 1 nm of the electrode.[22] 200 simulations each of 3 ms duration were performed, with the NP having the same initial position at the start (5 nm above the electrode, over the center). As the NP moved from the start position and began to encounter the electrode, the simulations showed a distribution of rise times, defined as the time taken for the occupancy to change from an average of 0.1 to 0.9, centered around 465 μs, as summarized in Figure 3.10A. This distribution is seen to be consistent with the current–time transients observed experimentally (Figure 3.10B). A key factor determining the rise time is a distance-dependent diffusion coefficient, expected for a spherical particle near a wall in solution, which slows the NP speed of motion, the closer the NP moves to the electrode, leading to hydrodynamic trapping (Section 3.3.4).

In fact, the model simulations predict the NP to remain, on average, near the electrode surface due to the hindered diffusion of the NP, resulting in a occupancy close to 1 for an extended period.[21] However, in the experiments, after reaching a peak, the current shows a decay with time over a few milliseconds. This difference in behavior between the experiment and model simulation can be seen in Figure 3.10C,D which each show the occupancy extracted from single example simulation runs plotted with current–time profiles obtained experimentally, as the average of 10 transients (C) and 5 transients (D). The experimental transients and example simulation plots were grouped by the rise time, with the rise time centered about 330 μs (C) and 500 μs (D). The difference between experiment (colored traces) and the model (black traces) indicates that the hydrodynamic trapping is ultimately overcome, and this can reasonably be attributed to the propulsion of the NP due to the release of oxygen as part of H_2O_2 electro-oxidation (e.g., 1.2×10^5 O_2 molecules per RuO_x NP), as seen at larger "swimmer particles" in solution.[38] In essence, spatially and temporally nonuniform oxygen generation on the asymmetrical NP (Figure 3.4B) after trapping on the collector electrode could accelerate the movement of the NP[39] and overcome the hindered diffusion of the NP near the surface, reducing the average occupancy (current) and ultimately leading to the particle moving completely outside the electron transfer region. Further evidence for this mechanism comes from the analysis of responses at 0.75 V where water oxidation was also initiated, causing higher currents and propulsion effects (Figure 3.9). The decay time, defined as the time period

from i_{peak} to the time when the current was 10% of i_{peak} following the peak was 1.95 (±0.15) ms (N = 38) compared to 3.08 (±0.58) ms at 0.55 V (N = 29), indicating that NPs tend to depart from the electrode quicker at higher bias. Other possible (alternative) reasons for the current–time decay that need to be considered include some deactivation process,[9,28] although this is unlikely, first, because such particles are highly active (on average) for long periods when adsorbed on other electrode surfaces[26] and, second, due to the subsequent electrochemical events observed that involve the same NP (*vide infra*). Moreover, the low concentration of H_2O_2 used is insufficient for the NP surface to become supersaturated with O_2 and for all of the sites on the NP to be deactivated.[40]

As well as explaining the time scale of the observed current transients, the mechanism of hydrodynamic trapping and electrochemical release also accounts for the high frequency of NP impacts (f_{NP}) observed. Hitherto, a model based on a diffusion-limited flux of NPs at an UME is often used to analyze f_{NP}, given by[4,5]

$$f_{NP} = 4D_{NP}C_{NP}N_A r_{disc} \quad (2)$$

where D_{NP} is the diffusion coefficient of NPs (8.8×10^{-8} cm^2 s^{-1}), C_{NP} is the concentration of NPs (15 pM), N_A is the Avogadro constant (6.022×10^{23} mol^{-1}), and r_{disc} is the radius of the electrode (1.5 μm herein). For SECCM the diffusional flux is about 10% of that for the same sized disc electrode,[19] and for the experimental conditions herein, this yields a value of 0.05 s^{-1}. This corresponds to a single pass collision with the collector electrode every 20 s or so on average. The f_{NP} of 86 s^{-1} was measured, about 1700-times greater than the f_{NP} value expected based purely on single-pass diffusion. The reason for the much larger f_{NP} value is that once the NP has moved away from the electrode and the electrochemical reactions switches off as a consequence, the NP will tend to come back to the electrode surface (hydrodynamic trapping), resulting in another current transient such as in the case shown in Figure 3.11, where multiple, rapid events are observed. The rapidity of such discrete events would be very difficult to discern with previously employed setups. Indeed, some previous studies have acknowledged that the accuracy of the f_{NP} measurement was low due to instrumental limitations necessitating a slow data acquisition rate.[41] Other studies have reported that the value of f_{NP} was reasonably similar to that expected for a diffusional flux of NPs.[9] However, even without electrochemically driven

propulsion, it is important to point out that the random walk simulations with hydrodynamic trapping evidence a stochastic interaction of the NP with the collector electrode (simulation traces in Figure 3.10C,D and Figure 3.3). Consequently, multiple current events in quick succession are expected for NPs that do not remain affixed (and accumulate) on the electrode surface.

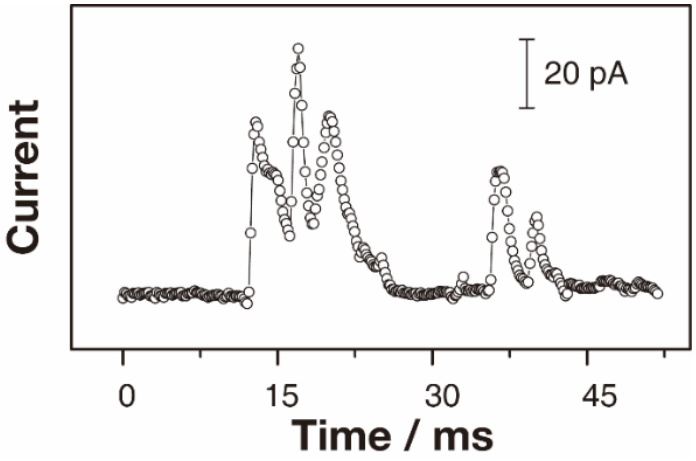

Figure 3.11 Typical multiple RuO_x NP impact events at a collector electrode potential of 0.55 V.

3.5 Conclusions

In conclusion, experiments in the SECCM system have provided profound new insights into the interaction of a NP with an electrode surface during impact, using H_2O_2 oxidation at RuO_x NPs as an illustrative case. The rise time of the current–time transients is consistent with random walk simulations for the diffusion of a NP, but with a bias due to hydrodynamic trapping near the electrode due to a greatly reduced diffusion-coefficient. Multiple, rapid current–time curves with very high frequency indicate successive trapping and release of a single NP, with release proposed to be aided by electrochemical propulsion which switches on when a NP hits the electrode but off again upon NP departure. For the electrochemical fluxes herein, the propulsion is insufficient to completely release the NP at the first attempt and, on average, our measurements show that about 1700 attempts are needed for complete release and loss of the NP from the electrode.

3.6 References

(1) Cox, J. T.; Zhang, B. *Annu. Rev. Anal. Chem.* **2012**, *5* (1), 253–272.

(2) Sambur, J. B.; Chen, P. *Annu. Rev. Phys. Chem.* **2014**, *65* (1), 395–422.

(3) Zhang, B.; Fan, L.; Zhong, H.; Liu, Y.; Chen, S. *J. Am. Chem. Soc.* **2013**, *135* (27), 10073–10080.

(4) Xiao, X.; Bard, A. J. *J. Am. Chem. Soc.* **2007**, *129* (31), 9610–9612.

(5) Kwon, S. J.; Zhou, H.; Fan, F.-R. F.; Vorobyev, V.; Zhang, B.; Bard, A. J. *Phys. Chem. Chem. Phys.* **2011**, *13* (12), 5394.

(6) Fosdick, S. E.; Anderson, M. J.; Nettleton, E. G.; Crooks, R. M. *J. Am. Chem. Soc.* **2013**, *135* (16), 5994–5997.

(7) Dasari, R.; Robinson, D. A.; Stevenson, K. J. *J. Am. Chem. Soc.* **2013**, *135* (2), 570–573.

(8) Kim, B. K.; Kim, J.; Bard, A. J. *J. Am. Chem. Soc.* **2015**, *137* (6), 2343–2349.

(9) Jung, A. R.; Lee, S.; Joo, J. W.; Shin, C.; Bae, H.; Moon, S. G.; Kwon, S. J. *J. Am. Chem. Soc.* **2015**, *137* (5), 1762–1765.

(10) Guo, Z.; Percival, S. J.; Zhang, B. *J. Am. Chem. Soc.* **2014**, *136* (25), 8879–8882.

(11) Stuart, E. J. E.; Tschulik, K.; Batchelor-Mcauley, C.; Compton, R. G. *ACS Nano* **2014**, *8* (8), 7648–7654.

(12) Wakerley, D.; Guell, A. G.; Hutton, L. A.; Miller, T. S.; Bard, A. J.; Macpherson, J. V. *Chem. Commun.* **2013**, *49* (50), 5657–5659.

(13) Kleijn, S. E. F.; Lai, S. C. S.; Miller, T. S.; Yanson, A. I.; Koper, M. T. M.; Unwin, P. R. *J. Am. Chem. Soc.* **2012**, *134*, 18558–18561.

(14) Zhang, G.; Kirkman, P. M.; Patel, A. N.; Cuharuc, A. S.; McKelvey, K.; Unwin, P. R. *J. Am. Chem. Soc.* **2014**, *136* (32), 11444–11451.

(15) Kim, Y. R.; Lai, S. C. S.; McKelvey, K.; Zhang, G.; Perry, D.; Miller, T. S.; Unwin, P. R. *J. Phys. Chem. C* **2015**, *119* (30), 17389–17397.

(16) Chen, Z. G.; Pei, F.; Pei, Y. T.; De Hosson, J. T. M. *Cryst. Growth Des.* **2010**, *10* (6), 2585–2590.

(17) Zheng, J. P.; Cygan, P. J.; Jow, T. R. *J. Electrochem. Soc.* **1995**, *142* (8), 2699–2703.

(18) Pei, L.; Mori, K.; Adachi, M. *Langmuir* **2004**, *20* (18), 7837–7843.

(19) Snowden, M. E.; Güell, A. G.; Lai, S. C. S.; McKelvey, K.; Ebejer, N.; O'Connell, M. a.; Colburn, A. W.; Unwin, P. R. *Anal. Chem.* **2012**, *84* (5), 2483–2491.

(20) Bard, Allen J. Faulkner, L. R. *Electrochemical Methods: Fundamentals and Applications*, 2nd ed.; Wiley: New York, 2001.

(21) Bevan, M. A.; Prieve, D. C. *J. Chem. Phys.* **2000**, *113* (3), 1228–1236.

(22) Zhao, J.; Bradbury, C. R.; Huclova, S.; Potapova, I.; Carrara, M.; Fermín, D. J. *J. Phys. Chem. B* **2005**, *109* (48), 22985–22994.

(23) Kätelhön, E.; Compton, R. G. *Chem. Sci.* **2014**, *5* (12), 4592–4598.

(24) Goldman, A. J.; Cox, R. G.; Brenner, H. *Chem. Eng. Sci.* **1967**, *22* (4), 653–660.

(25) Chen, W.; Cai, S.; Ren, Q.-Q.; Wen, W.; Zhao, Y.-D. *Analyst* **2012**, *137* (1), 49–58.

(26) Kang, M.; Lee, Y.; Jung, H.; Shim, J. H.; Lee, N. S.; Baik, J. M.; Lee, S. C.; Lee, C.; Lee, Y.; Kim, M. H. *Anal. Chem.* **2012**, *84* (21), 9485–9491.

(27) Kim, S. J.; Jung, H.; Lee, C.; Kim, M. H.; Lee, Y. *Sensors Actuators, B Chem.* **2014**, *191*, 298–304.

(28) Sardesai, N. P.; Andreescu, D.; Andreescu, S. *J. Am. Chem. Soc.* **2013**, *135* (45), 16770–16773.

(29) Patel, A. N.; Collignon, M. G.; OConnell, M. A.; Hung, W. O. Y.; McKelvey, K.; MacPherson, J. V.; Unwin, P. R. *J. Am. Chem. Soc.* **2012**, *134* (49), 20117–20130.

(30) Patel, A. N.; Tan, S. Y.; Miller, T. S.; MacPherson, J. V.; Unwin, P. R. *Anal.*

Chem. **2013**, *85* (24), 11755–11764.

(31) Lai, S. C. S.; Lazenby, R. A.; Kirkman, P. M.; Unwin, P. R. *Chem. Sci.* **2015**, *6* (2), 1126–1138.

(32) Yang, D.-Q.; Sacher, E. *Chem. Mater.* **2006**, *18* (7), 1811–1816.

(33) Kleijn, S. E. F.; Lai, S. C. S.; Koper, M. T. M.; Unwin, P. R. *Angew. Chemie - Int. Ed.* **2014**, *53* (14), 3558–3586.

(34) Jiang, J.; Oberdörster, G.; Biswas, P. *J. Nanoparticle Res.* **2009**, *11* (1), 77–89.

(35) Lee, Y.; Suntivich, J.; May, K. J.; Perry, E. E.; Shao-Horn, Y. *J. Phys. Chem. Lett.* **2012**, No. pH 1, 399–404.

(36) Bobbert, P. A.; Wind, M. M.; Vlieger, J. *Physica A* **1987**, *141*, 58–72.

(37) Evans, S. a G.; Elliott, J. M.; Andrews, L. M.; Bartlett, P. N.; Doyle, P. J.; Denuault, G. *Anal. Chem.* **2002**, *74* (6), 1322–1326.

(38) Wang, Y.; Hernandez, R. M.; Bartlett, D. J.; Bingham, J. M.; Kline, T. R.; Sen, A.; Mallouk, T. E. *Langmuir* **2006**, *22* (25), 10451–10456.

(39) Howse, J. R.; Jones, R. A. L.; Ryan, A. J.; Gough, T.; Vafabakhsh, R.; Golestanian, R. *Phys. Rev. Lett.* **2007**, *99* (4), 8–11.

(40) Luo, L.; White, H. S. *Langmuir* **2013**, *29* (35), 11169–11175.

(41) Kwon, S. J.; Fan, F. R. F.; Bard, A. J. *J. Am. Chem. Soc.* **2010**, *132* (38), 13165–13167.

Chapter 4. Impact and Oxidation of Single Silver Nanoparticles at Electrode Surfaces: One Shot versus Multiple Events

4.1 Abstract

Single nanoparticle (NP) electrochemical impacts is a rapidly expanding field of fundamental electrochemistry, with applications from electocatalysis to electoanalysis. These studies, which involve monitoring the electrochemical (usually current-time, *I-t*) response when a NP from solution impacts with a collector electrode, have the scope to provide considerable information on the properties of individual NPs. Taking the widely studied oxidative dissolution of individual silver nanoparticles (Ag NPs) as an important example, this chapter presents measurements with unprecedented noise (< 5 pA) and time resolution (time constant 100 μs) that are highly revealing of Ag NP dissolution dynamics. Whereas Ag NPs of diameter, d = 10 nm are mostly dissolved in a single event (on the timescale of the measurements), a wide variety of complex processes operate for NPs of larger diameter ($d \geq 20$ nm). Detailed quantitative analysis of the *I-t* features, consumed charge, event duration and impact frequency leads to a major conclusion: Ag NPs undergo sequential partial stripping (oxidative dissolution) events, where a fraction of a NP is electrochemically oxidized, followed by the NP drifting away and back to the tunnelling region before the next partial stripping event. As a consequence, analysis of the charge consumed by single events (so-called "impact coulometry") cannot be used as a general method to determine the size of colloidal NPs. However, a proper analysis of the *I-t* responses provides highly valuable information on the transient physicochemical interactions between NPs and polarized surfaces.

4.2 Introduction

Over the last decade, synthetic routes have been refined to the point where nanoparticles (NPs) can be produced with good control over size, shape and composition[1,2]. Yet, developments in understanding the physicochemical and functional properties of NPs are still underway. This is particularly true for the electrochemistry of NPs, which is of fundamental interest and underpins a wide range of energy conversion and sensing devices.[3] Gaining deeper knowledge of the relationship between size, structure and activity of NPs is essential for rational and optimised applications.

Traditionally, electrochemical characterization of NPs has involved measurements on large populations of NP ensembles immobilised on surfaces[4]. However, the properties determined in this way are convoluted by subtle variations in NP size and shape, and potentially complex interactions between neighbouring NPs[4]. As such, the electrochemical properties of *single NPs* and their interaction with different types of substrate electrodes is an important emerging area. A prominent method to study the electrochemistry of single NPs[5], relies on monitoring the electrochemical signal when an electroactive NP impacts from a suspension of NPs in solution onto a collector electrode surface, a rapidly growing area called single NP impact electrochemistry (SNIE). SNIE requires an experimental set up that has low background noise and low NP impact frequency, which has normally been achieved by the use of ultramicroelectrodes (UMEs) of a few microns in diameter[6–9].

Hitherto, there are basically two approaches to monitor NP electrochemical impacts. First, electrocatalytic current amplification, which relies on an electrochemical process that is catalysed by the NP under study, but not the collector electrode (over the applied potential range of interest)[5,7–14]. The recorded current-time (*I*-*t*) transient can provide information on the interaction of the NP with the substrate (elastic collision, adsorption, etc) as well as the kinetics of the reaction under study. If the kinetics are fast and the process is mass transport limited, the size of the colliding NP can also be inferred from the diffusion-limited current[5,15].

Second is electrochemical oxidative dissolution (stripping)[16]. In this case, the measured current-time transient reflects the anodic dissolution of the NP into its constituent ions upon impact. By measuring the charge consumed during each NP

collision, it has been proposed that the size of the colliding NP can be inferred by Faraday's law[16–21]. However, this requires that the *I-t* transient is measured with high accuracy and that the whole particle is oxidized while in contact with the surface in a single impact.

Complete NP dissolution has been claimed for Ag particles with diameters ranging from 6 nm[20] to 100 nm[18], and it has consequently been argued that impact coulometry can be used as a method for in-situ determination of the size, with nm resolution, of colloidal NPs of different materials such as Ag[18–20], Cu[22], Mo[23], C-60[24], Au[25] or to address colloidal stability and aggregation phenomena[17,21]. However, none of these studies provided a thorough analysis of the recorded *I-t* transients nor examined, with the same experimental setup, the landing of NPs with diameters spanning the range claimed. Moreover, recent work shows that the electrochemical dissolution of single NPs is a somewhat more complex process[26–30]. This makes a detailed analysis of NP oxidative impacts imperative, particularly as this methodology is now being extended to other systems, such as NP alloys[31] and bioanalysis[32]. It is further important to note that in many reports on impact coulometry, little information was given about signal amplification, effect of sampling time and the data processing carried out to interpret NP impact current transients; these critical factors have only recently begun to be reported[33,34].

Electrochemical oxidation of single Ag NPs of 10 nm in diameter has produced current magnitudes of 1 to 10 pA and anodic dissolution transient durations of 2-3 ms by using carbon fiber (CF)[20] and Pt[34] UMEs, but the use of a cut-off filter[20] or signal averaging[34] compromised the ability to probe short-time stripping events. In addition, the electrochemical oxidation of Ag NPs of 100 nm in diameter has led to peak currents spanning from 30-200 pA[21], on the one hand, to 0.5-10 nA[18], on the other, with an *identical experimental configuration* save for the use of different equipment to record the transients. This difference of almost 3 orders of magnitude in the peak currents for the anodic stripping of Ag NPs of the same size highlights the potential complexity of the stripping process, but raises significant questions on the sampling rate and data filtering in the faithful acquisition of current transients. This important issue is only just beginning to be considered. For example, the effect on impact transients of the cut-off frequency of a Bessel filter has recently been reported[35]. However, although the charge transferred in an impact process may be conserved

irrespective of the bandwidth of the current follower[33], the features of the *I-t* transient are expected to be affected considerably by the filtering process[36–38]. This is one of the major aspects of SNEI that is considered herein.

As an alternative to the use of UMEs, it has been recently demonstrated that scanning electrochemical cell microscopy (SECCM) offers high sampling rates with low background current levels (Chapter 3)[14]. This is due to the confinement of the electrochemical cell within a meniscus formed by a micropipette and the collector electrode. Hence, the SECCM platform has been used successfully for single-entity electrochemical measurements such as monitoring the electrodeposition of single NPs[39,40], electrochemical detection of single molecules[41] and, most recently, the time-resolved detection of single NP electrocatalytic impacts[14], including surface oxide formation on noble material (Au) NPs.[42] An advantage of the SECCM approach is that there is no need for an encapsulated collector electrode, so that a wide range of electrode materials can be used for this purpose, including materials with low noise characteristics.

In this work, SECCM was utilised to study the electrochemical dissolution of single Ag NPs with diameters ranging from 10 to 100 nm upon impact on glassy carbon (GC) surfaces, as carbon collector electrode surfaces have been used most in previous studies (see Section 4.3.2). For comparison, 100 nm Ag NPs have also been studied on an Au collector electrode. The SECCM setup allows us to obtain a peak-to-peak background noise of 4-5 pA with a current amplification time constant as low as 100 µs. Under these conditions, *I-t* transients are significantly different from, and more complex than, previous reports[18,21]. Oxidative NP impacts are much more complex than considered hitherto. In particular, this chapter shows that individual Ag NPs most typically dissolve through *multiple and repetitive impacts*, in which partial oxidation occurs, and for larger NPs overall *electrodissolution is often incomplete*. The resulting *I-t* traces *can therefore not be used for NP sizing*, as has been proposed. However, thorough examination of the recorded *I-t* curves provides important information on the near wall dynamics of NPs and their interaction with different surfaces during electrochemical dissolution processes, which is potentially highly valuable as an approach for understanding surface chemistry.

4.3 Materials and Methods

4.3.1 Chemicals

$NaNO_3$ (≥ 99.0 %) and silver nanoparticles (Ag NPs) with five different sizes (diameter, d = 10, 20, 40, 60 and 100 nm) dispersed in sodium citrate aqueous solution were purchased from Sigma-Aldrich (St. Louis, MO). An aqueous supporting electrolyte of 50 mM $NaNO_3$ was prepared with high purity water (Milli-Q, 18.2 MΩ cm resistivity at 25 °C). Citrate capped Ag NPs were chosen for this study, since they have been used in most previous single NP electrodissolution studies.[16–21,26,27,29,34] Likewise, most previous studies have been carried out with citrate present in solutions (Table 4.1)

Table 4.1 Summary of Conditions for previous studies of Ag NP electro-oxidation.

Reference number[a]	**Electrodes[b] (μm)**	**NP Size[c] (nm)**	**Capping agent[d] and electrolyte**	**E_{app}[e] vs reference electrode[f]**
Ref [16]	GC-UME (d=N/A)	20-50	Citrate 10 mM Sodium dihydrogen citrate and 90 mM KCl	*I-t* (not specified) Varied E (50-500 mV) for *I-V* curve vs Ag/AgCl
Ref [17]	CF-UME (d=10)	17-48	Citrate 100 mM trisodium citrate	0.6 V vs. Ag wire or 0.3V vs MSE
Ref [18]	GC-UME (d=11.3)	100	Citrate 20 mM KCl	0.6V vs SCE
Ref [19]	CF-UME (d=10)	30	Different capping agents including citrate 20 mM $NaNO_3$	0.6 V vs MSE

Ref [20]	CF-UME (d=7)	12	Citrate 20 mM trisodium citrate	0.6 V vs. MSE
Ref [21]	CF-UME (d=7)-RAM	100	Citrate 0 -2.5 M KCl	0.6 V vs SCE
Ref [27]	Au square UME (50 X 50 μm^2)	100	Citrate 50 mM KNO_3	0.6-0.9 V vs Ag/AgCl QRE
Ref [28]	Au coated glass electrode (7 mm^2)	60 and 100	Capping agent –not specified 30-50 mM KSCN and KNO_3	Various potentials vs Ag/AgCl QRE
Ref [29]	Pt-UME (d=8-20)	20	Citrate KCl (concentration not specified)	0.4 V vs Ag/AgCl
Ref [31]	Array of Pt(d=8)-UME	10	Citrate 120 mM KCl	0.4 vs Ag/AgCl

[a]Reference number is originated from Section 4.2. [b]UME, ultramicroelectrode; RAM, random assembly microelectrode. [c]All NP sizes are presented as diameter. [d]Solutions contain citrate, but the concentration is not always easily determined from the AgNP colloidal solutions being used. [e]E_{app}, applied potential at the collector electrode. [f]Ag/AgCl, commercial Ag/AgCl reference electrode; SCE, saturated calomel electrode; MSE, mercury sulfate electrode; Ag/AgCl QRE, Ag/AgCl quasi reference electrode.

4.3.2 Electrochemical Dissolution of Individual Ag NPs: Experimental Setup

Two different configurations (UME and SECCM) were tested in initial experiments to evaluate the most appropriate experimental setup and instrumentation for single NP impact studies. On the one hand, Au (25 µm diameter) and CF (7 µm diameter) disc UMEs were used in bulk solution to measure the background currents that arose from polarizing the working electrode at a potential (E) sufficiently positive to drive the oxidation of Ag NPs (E = 0.6V vs Ag/AgCl quasi-reference counter electrode, QRCE), in a 2-electrode arrangement. These measurements were performed in supporting electrolyte without Ag NPs. The QRCE has a potential of +188 mV vs saturated calomel electrode (SCE) and is stable to within 3 mV over a 30 minute period (a larger period than the measurement time considered herein). The anodic dissolution process is thus driven strongly, which is the appropriate condition for sizing and analytical applications. The current amplification time constant of the electrometer was varied to study its effect on the measured background currents.

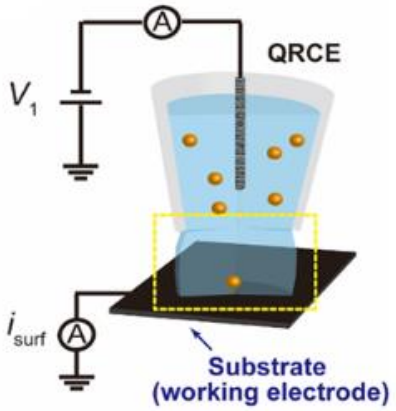

Figure 4.1 Schematic of the set up for SECCM NP impact experiments.

On the other hand, the SECCM setup (see Figure 4.1)[43] consisted of a single-barrelled pipette (aperture diameter of 5 µm) pulled from a borosilicate glass capillary utilizing a CO_2-laser puller (P-2000, Sutter Instruments). The pipette was filled with a 1:1 solution of 50 mM $NaNO_3$ and the as-purchased AgNP solution. A AgCl-coated Ag wire was placed in the capillary and used as a QRCE. The pipette was mounted on

a z-piezoeletric positioner (P-753.1CD LISA, PhysikInstrumente) and positioned on the surface of interest (meniscus-only contact) using an xy-piezoelectrric positioner (P-622.2CD PIHera, PhysikInstrumente). The electrochemical cell and all positioners were placed in a Faraday cage with heat sinks and vacuum panels to minimize noise and thermal drift. Glassy carbon (GC) pieces (HTW-Germany) and Au UMEs (as for UME measurements) were used as the substrates to be comparable with the UME bulk measurements.

A potential of -0.1 V vs Ag/AgCl QRCE was applied to the substrate as the pipette was approached towards it and the current from the substrate was recorded to detect the moment when the meniscus contacted the surface (current spike), but without contact from the pipette[43]. This signal was used to stop the pipette movement. Once the meniscus was in contact with the substrate, the potential was switched to 0.6 V vs Ag/AgCl QRCE, to observe the electrochemical dissolution of impacting Ag NPs. It needs to be noted that there is no electro-oxidation processes of sodium citrate at 0.6 V vs Ag/AgCl QPCE[19].

A home-built potentiostat and electrometer were used throughout all measurements. Two home-built 8th order brick-wall filter units were utilized to vary the time constant of the current amplifier from 100 µs to 50 ms) and the data were recorded with an acquisition rate of 165 µs (sampling rate of 5 µs averaged 33 times). Data acquisition and fine control of all the instruments was achieved by using an FPGA card (PCIe-7852R) controlled by a LabVIEW 2013 interface. Data treatment was carried out with Igor Pro 6.37 (Wavemetrics).

4.3.3 Ag NP Characterization: TEM and DLS

Silver nanoparticles (AgNPs) with nominal diameter of 10, 20, 40, 60 and 100 nm (abbreviated as Ag10NPs, Ag20NPs, Ag40NPs, Ag60NPs and Ag100NPs, respectively) were characterized by dynamic light scattering (DLS, a Malvern Zetasizer Nano ZS, Malvern Instruments Ltd., UK) and transmission electron microscopy (TEM, Jeol 2100, at 200 kV). Representative TEM images are shown in Figure 4.2. The average diameters obtained by both TEM and DLS are shown in Table 4.2. DLS measurements after addition of 25 mM $NaNO_3$ also performed to rule out NP agglomerations induced by the electrolyte (Table 4.2).

The concentrations of Ag NPs were estimated based on weight per volume concentration (provided by the supplier) considering molecular weight (107.86 g mol^{-1}) and bulk density (10.49 g cm^{-3}) of Ag (Table 4.3). The bulk diffusion coefficient of NPs (D_{NP}) was also calculated by the Stokes-Einstein equation:

$$D_{NP} = \frac{k_B T}{6\pi\eta r_{NP}} \quad (1)$$

where k_B is the Boltzmann constant (1.381×10^{-23} J K^{-1}), T is the temperature (298 K), η is the dynamic viscosity of the solution (8.90×10^{-4} Pa s for dilute aqueous solution), and r_{NP} is the NP radius from the TEM results in Table 4.2 (Table 4.3).

For a diffusion-controlled movement of the NPs towards the collector surface, the estimated impact frequency (f_{NP}) can be calculated by the following equation.[5]

$$f_{NP} = 0.52 D_{NP} C_{NP} N_A r_{disc} \quad (2)$$

where D_{NP} is the diffusion coefficient of NPs of the given sizes (Table 4.3), C_{NP} is the concentration of NPs (Table 4.3), N_A is the Avogadro constant (6.022×10^{23} mol^{-1}), and r_{disc} is the radius of the electrode (3.1 µm herein considering the expansion of meniscus after land on the surface (Figure 4.3)). The diffusion flux in the SECCM setup herein was 13 % of a disc UME of the same size, deduced by measuring the steady-state current in 2 mM $Ru(NH_3)_6^{3+}$ including 0.1 M KNO_3 (Figure 4.3).[2] This resulted in using 0.52 in eq (2) instead of a factor of 4. The f_{NP} results of each type of AgNP are presented in Table 4.3.

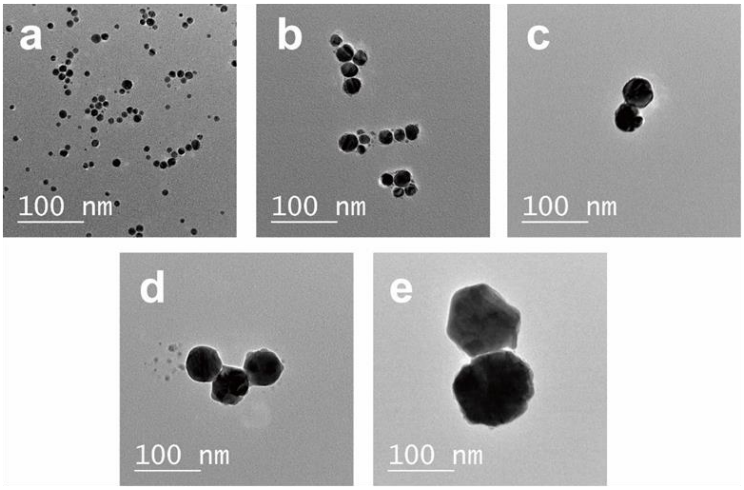

Figure 4.2 Representative TEM images of Ag NPs with nominal diameters of (a) 10 nm, (b) 20 nm, (c) 40 nm, (d) 60 nm and (e) 100 nm (abbreviated as Ag10NPs, Ag20NPs, Ag40NPs, Ag60NPs and Ag100NPs, respectively).

Table 4.2 Average diameters (nm) of Ag NPs as determined from TEM and DLS (in absence and presences of 25 mM $NaNO_3$).

	TEM	**DLS (w/o 25 mM $NaNO_3$)**	**DLS (w/ 25 mM $NaNO_3$)**
Ag10NPs	9.4 ± 0.2	13.2 ± 1.8	12.1 ± 1.0
Ag20NPs	19.4 ± 1.6	22.5 ± 1.6	21.2 ± 1.0
Ag40NPs	39 ± 0.6	40.3 ± 1.0	39.0 ± 1.1
Ag60NPs	58.2 ± 1	72.7 ± 2.2	72.8 ± 6.0
Ag100NPs	93.8 ± 1.4	91.7 ± 5.9	90.5 ± 2.7

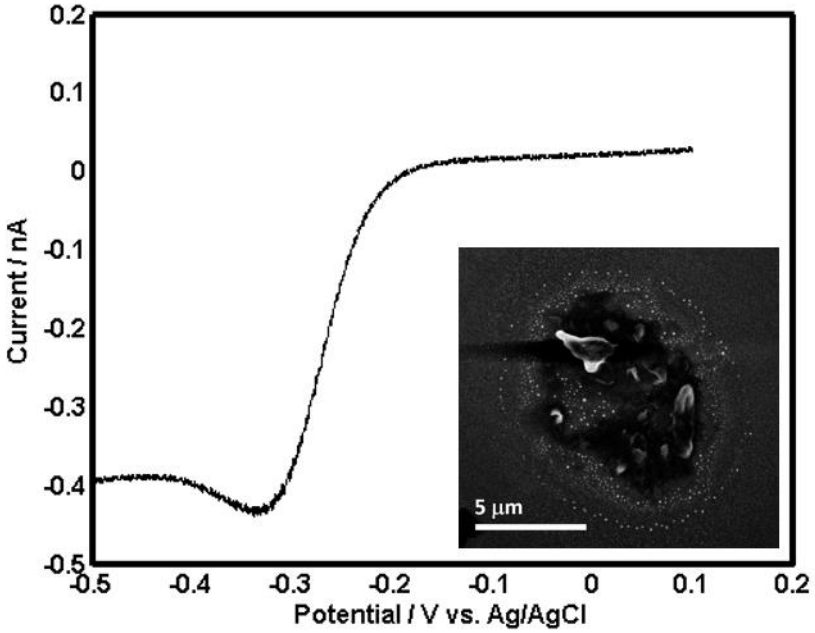

Figure 4.3 Linear sweep voltammogram (LSV) (100 mV s^{-1}) for the reduction of 2 mM $Ru(NH_3)_6^{3+}$ in 0.1 M KNO_3 solution by the meniscus contact on GC using a glass pipette (diameter of 8 μm) and SEM image of the footprint after the meniscus contact (inset). The diameter of the droplet was just 25 % larger than the pipette end diameter. Note that the LSV is not fully at steady-state due to the scan speed used and the fact that SECCM diffusion is from a conical segment rather than fully hemispherical.

Table 4.3 Estimated concentration, diffusion coefficient and impact frequency of distributions of Ag NPs with nominal diameters of 10, 20, 40, 60 and 100 nm.

	Estimated concentration (M)	D_{NP} **(cm^2 s^{-1})**	f_{NP} **(s^{-1})**
Ag10NPs	$6.0\ 10^{-9}$	$5.2\ 10^{-7}$	240
Ag20NPs	$7.6\ 10^{-10}$	$2.5\ 10^{-7}$	15
Ag40NPs	$9.5\ 10^{-11}$	$1.3\ 10^{-7}$	0.94
Ag60NPs	$2.8\ 10^{-11}$	$8.4\ 10^{-8}$	0.19
Ag100NPs	$6.0\ 10^{-12}$	$5.2\ 10^{-8}$	0.025

4.4 Results and Discussion

4.4.1 Influence of the Experimental setup, Instrumentation and Acquisition Parameters on the Background Current (noise) Level

In the absence of Ag NPs in solution, both GC and Au electrodes show little electroactivity with an applied potential of 0.6V vs Ag/AgCl. The current measured is due to background electrical and electrochemical noise inherent in the experimental configuration. These currents depend on the electrode surface area exposed to the electrolyte, cell design, the specifications of the current measuring instrumentation (amplification), the acquisition frequency (sampling rate or bandwidth) and the post-processing of the recorded data (filtering).[44]

As explained in Section 4.2, it is mandatory to reach low background currents (≈ pA) and high sampling rates (≈ 10 KHz), but these parameters are interrelated and there is a trade-off.[36] The time constant (τ_C) of the setup is of high importance, particularly when the transient duration is of the same order of magnitude[33,37,38].

In order to evaluate the background currents for different time constant settings, electrode materials and electrochemical setups (UME and SECCM), *I-t* transients were recorded in solutions without Ag NPs during the application of E = 0.6 V vs Ag/AgCl QRCE to the working electrode. Representative *I-t* transients are displayed in Figures 4.4a, b and c. Peak to peak noise values have been measured and plotted against the amplifier τ_C in Figure 4.4d.

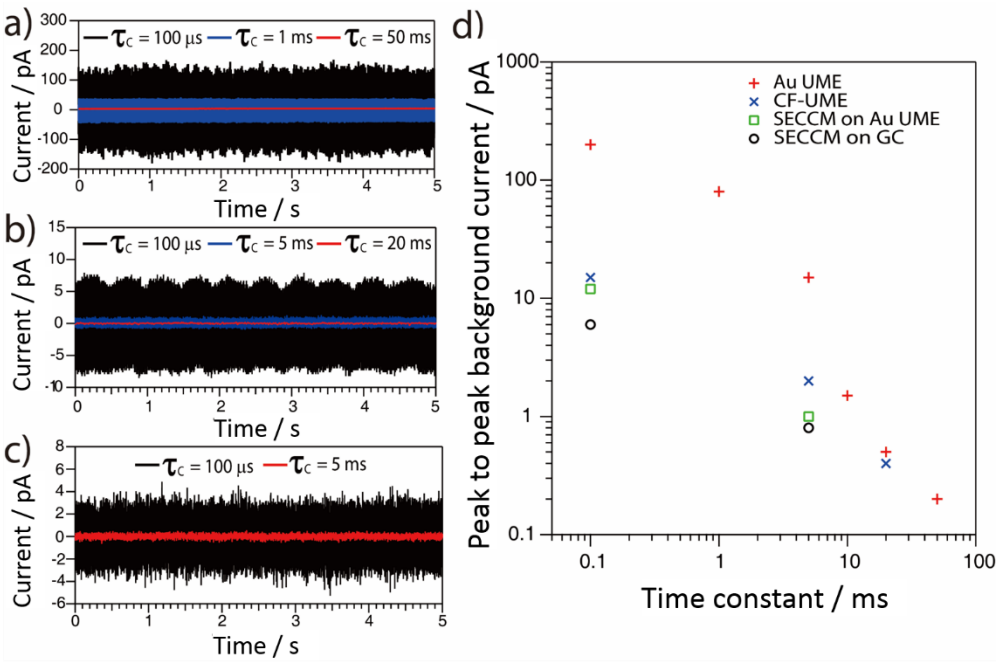

Figure 4.4 Representative *I-t* transients obtained during the polarization at E= +0.6 V *vs* Ag/AgCl of a (a) Au UME, (b) CF-UME and (c) GC electrode in SECCM setup, with different amplification time constants. d) Peak to peak background current *vs* amplification time constant for different electrode materials and setups.

As expected, decreasing τ_C results in an increase of the background current, irrespective of the electrochemical setup employed. Furthermore, and most importantly, it is confirmed that confining the electrochemical cell to a meniscus of several microns diameter (SECCM setup) leads to lower background currents than immersing an UME in a standard electrochemical cell[45]. This is mainly due to the change in the collector electrode area (Figure 4.3). It is also clear that for SECCM cells of similar area, GC gives lower background currents than Au as the collector electrode. In large part, this is due to less wetting (smaller contact area) of the GC substrate. This work thus mainly is focused on GC, although some comparative measurements on Au are also reported.

These data highlight some important considerations concerning the detection and analysis of single Ag NP stripping by impacts. If the *I-t* response of a stripping event is considered as a triangular spike, the charge consumed during such a transient could be approximated by $Q = I_p t_e/2$, with I_p the maximum spike current and t_e the duration of the event. Then, for an Ag NP of d = 10 nm, the charge associated with its

full electrochemical dissolution would be about 5 x 10^{-15} C. So, if a stripping event lasted for 10 ms, the peak current would only be 1 pA. Alternatively, peak currents of 10 pA would be expected if the events spanned just 1 ms. However, in order to accurately resolve such an *I-t* transient, the amplification time constant would need to be smaller than the event duration, otherwise the information of the *I-t* transient would be a convolution of the real process and the electronics of the instrument[33,36–38]. The noise consequences of decreasing the time constant are evident in Figure 4.4. It follows from this analysis that, to resolve events in the ms range, a τ_C of 100 µs would be essential. With these conditions, the SECCM configuration on a GC substrate is optimal.

4.4.2 AgNP Stripping Using SECCM

Unless stated otherwise, the data presented in this section was obtained with a SECCM configuration with a current amplification time constant of 100 µs to allow an accurate resolution of ms to sub-ms stripping events. To examine the effect of the time constant on the analysis of single NP impacts, a comparison between τ_C = 100 µs and τ_C = 5 ms is made in section 4.4.2D.

4.4.2A Qualitative description of I-t transients Figures 4.5, 4.6 and 4.7 provide a summary of the main characteristic features of Ag NP stripping events *based on the analysis of more than 2000 I-t impact transients.*

Figure 4.5 shows the transients during the electrodissolution of Ag NPs of *d* = 10 and 20 nm. The first column (Figure 4.5a) shows characteristic events of the stripping of NPs of *d* = 10 nm. Although a few events with currents up to 40-80 pA can be observed (4.5a.i; *black*), the most representative population of events comprises peak heights less than 15 pA (4.5a.ii; *blue*) and sharp durations of 0.3 to 5 ms. (4.5a.iii, 4.5a.iv, 4.5a.v; *green*).

The second and third columns (Figures 4.5b and 4.5c) show the characteristic features upon stripping of NPs of *d* = 20 nm. The characteristics are similar to *d* = 10 nm: fast and sharp events of duration shorter than 5 ms (4.5b.iii, 4.5b.iv, 4.5b.v), but with slightly higher maximum currents (10-20 pA). However, there are a few longer events (*t* = 5-20 ms) with an irregular, saw-tooth profile (4.5c.iii, 4.5c.iv, 4.5c.v;

brown). Further interpretation of these features is given in Section 4.4.2B. Evidently, the electrodissolution processes on *green* and *brown I-t* transients must be different from each other.

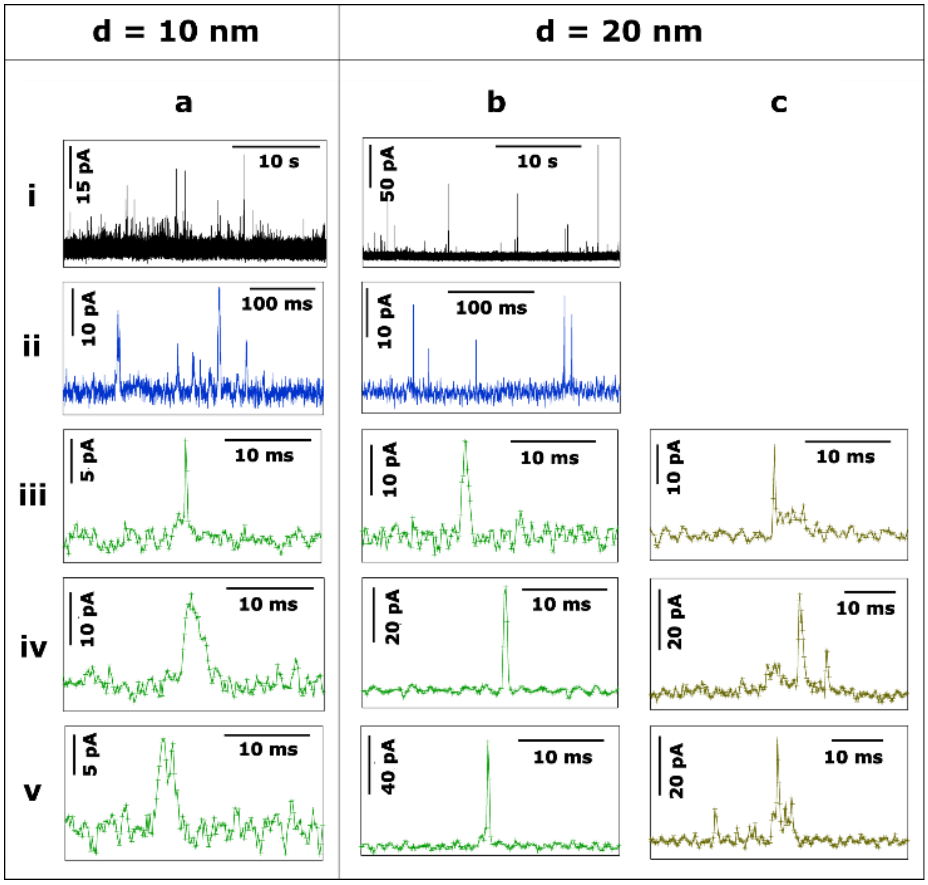

Figure 4.5 Representative current transients obtained by applying E = +0.6 V vs Ag/AgCl to a GC electrode with a solution containing Ag NPs with nominal diameter of (a) 10 nm and (b,c) 20 nm. The numbers i-v refer to different cases discussed in the text.

Figure 4.6 shows the transients during the electrodissolution of Ag NPs of *d* = 40 and 60 nm. In both cases, the appearance of isolated events of much larger maximum current, compared to Figure 4.5, is evident (4.6a.i, 4.6c.i). This response is shown in detail (4.6a.v and 4.6c.v; *orange*) and evidences that the duration of such *orange* events (*t* = 1-3 ms) is similar to that of *green* events (4.6a.iii, 4.6a.iv, 4.6c.iii, 4.6c.iv) but with much higher current (*I* > 100 pA). The charge consumed in these events approaches, but is not, full stripping, corresponding to Ag NPs of *d* = 30 nm (4.6a.v) and *d* = 47 nm (4.6c.v). More interestingly, *green* (*t* < 5 ms; *I* = 5-30 pA) low

current fast events *and brown* (t = 5-10 ms; I = 5-40 pA) low current, saw-tooth, longer events are still prevalent. These events are sometimes isolated (4.6a.ii, 4a.6.iii, 4.6c.iv) and sometimes grouped in bundles (4.6a.iv, 4.6c.ii, 4.6c.iii). Most importantly, in none of these cases does the charge consumed during single events account for the stripping of entire NPs and hence represents only a partial stripping process[27–29]. It should be noted that when the NP diameter increases from 20 to 60 nm, the occurrence of such bundles of low current (*green* and *brown*) events is more frequent (28% and 58% of the total charge for d = 20 nm and d = 60 nm, respectively). Furthermore, contrary to the cases of d = 10 nm and d = 20 nm, for d = 40 and d = 60 nm, *very long saw-tooth events* are also present (Figures 4.6b.v and 4.6d.v; *red*) with durations that span to 100-500 ms and peak currents that span from a few tens to hundreds of pA. In these specific cases, the total charge associated with these events may indicate total stripping of large particles as the inferred diameters are of d = 64 nm (4.6b.v) and d = 70 nm (4.6d.v), respectively. Further quantitative analysis is reported in Section 4.4.2B.

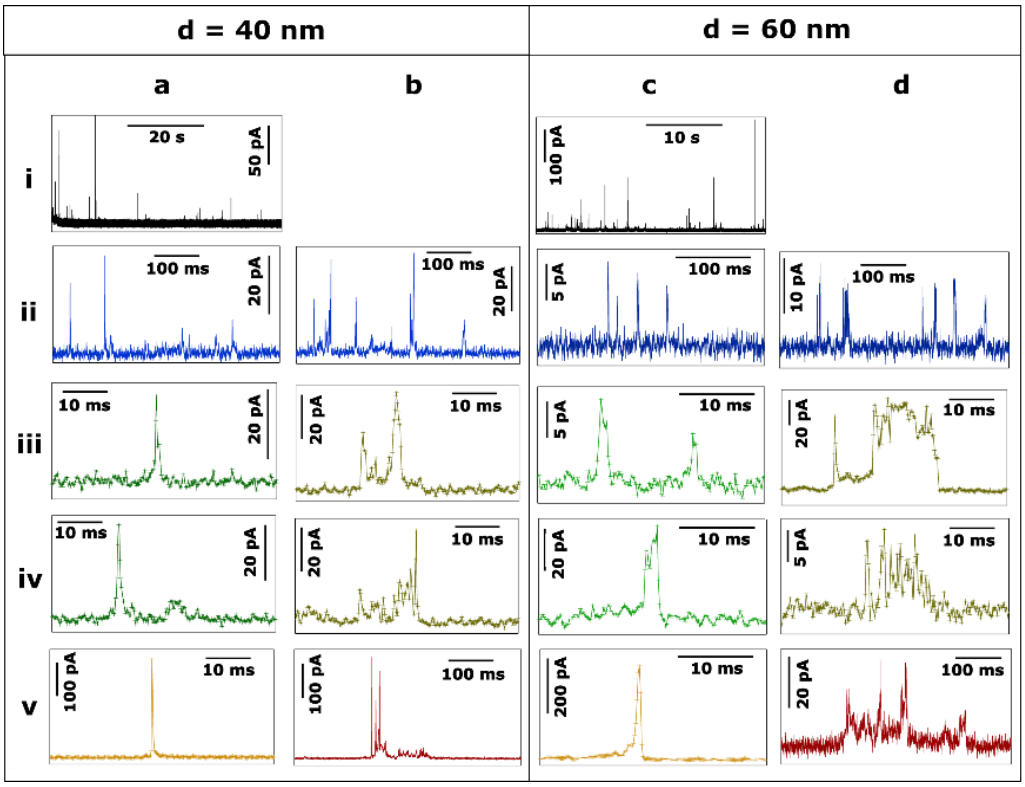

Figure 4.6 Representative current transients obtained by applying E = +0.6 V vs Ag/AgCl to a GC electrode with a solution containing Ag NPs with nominal diameter of (a, b) 40 nm and (c, d) 60 nm. The numbers i-v refer to different cases discussed in the text.

Ag NPs of d = 100 nm were landed on both GC (Figure 4.7(a,b)) and Au (Figure 4.7(c,d)) collector electrodes. With GC as the collector electrode, Figure 5a.i shows 140 seconds of the current response. Peak currents range from 10 to 100 pA. Note that the event frequency is low because the total concentration of Ag was maintained for the different sized particles in these studies (Table 4.3). This was advantageous because the stripping process became increasingly complex –and could be of much longer duration - as the NP size increased. These results thus achieved conditions where the mean primary first pass diffusion frequency, f_{NP}, was small (average time between first impact of NPs of 40 s in the case of d = 100 nm NPs) so that a sequence of complex events on (much) shorter time scales could reasonably be assigned to a single NP (Table 4.3).

A closer examination of the current transients reveals 3 distinct types of events, which suggest 3 underlying stripping processes. On the one hand, bundles of fast events with low currents (≤ 20 pA) are shown in Figures 4.7a.ii and 4.7b.ii (*light blue).* These bundles span for a few seconds in total but are constituted by individual *green* events (details in 4.7a.iii and 4.7a.iv) that last only for a few ms each. The charge consumed in such individual events is of the order of 10^{-15} to 10^{-13} C that would correspond to NPs of d = 10-20 nm. *Such small particles are absent in these measurements* as confirmed by TEM and DLS (Table 4.2). Thus, each of these events represents the *partial stripping* of a small fraction (0.1% -2 %) of the same particle of d = 100 nm. This is most likely due to the temporary detachment of a NP from the surface after partial stripping, followed by re-engagement and a subsequent partial stripping event. A similar interpretation could be drawn for the experiments carried out with NPs of d = 40 and d = 60 nm (Figures 4.6b.ii, 4.6c.ii, 4.6d.ii). The repetitive engagement and detachment of NPs with a collector electrode has been previously demonstrated for ruthenium oxide NPs impacting on HOPG during catalytic amplification of hydrogen peroxide oxidation, and can be revealed provided that the time constant is sufficiently short[14]. Furthermore, the ready detachment of Ag NPs during electrodeposition has also been shown[40].

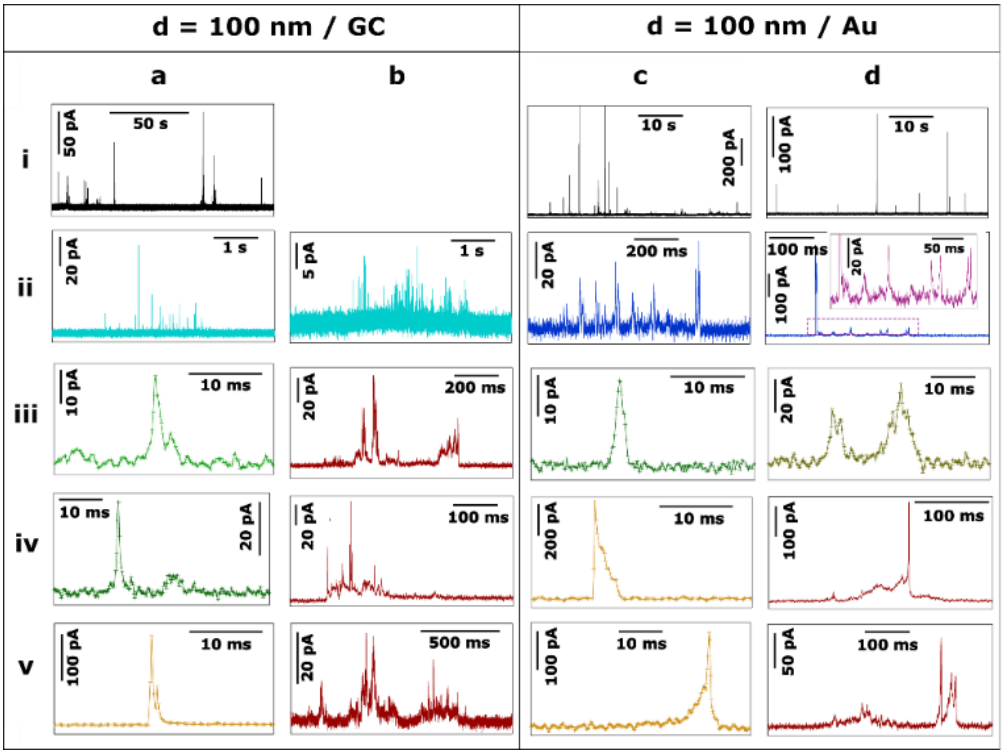

Figure 4.7 Representative current transients obtained by applying E = +0.6 V vs Ag/AgCl to a (a, b) GC and a (c, d) Au electrode with a solution containing Ag NPs with nominal diameter of 100 nm. The numbers i-v refer to different cases discussed in the text.

Additionally, short, sharp, high-current *orange* (4.7a.v) and long low-current, saw-tooth *red* (4.7b.iii, 4.7b.iv, 4.7b.v) events spanning hundreds of milliseconds are found, with a higher occurrence than for smaller NPs. Although large amounts of charge are consumed in these cases, the whole NP is not necessarily oxidized to Ag^+ cations, since the charge consumed on events 4.7b.iii, 4.7b.v, 4.7b.iv and 4.7a.v would correspond to d = 90 nm, d = 98 nm, d = 80 nm, and d = 30 nm, respectively. Whereas full particle stripping probably occurs in the two first cases, only 50% and 3% of a NP of d = 100 nm are dissolved in the latter two examples.

Figures 4.7c and 4.7d show characteristic transients on a Au electrode. At first sight, the features of these transients are similar to d = 100 nm Ag NPs landed on GC (Figures 4.7a and 4.7b), but with some differences discussed here and in Section 4.4.3. On the one hand, the bundles of small charge events are constituted by individual (*green* and *brown*) events, whose duration is slightly longer on Au than on GC. Such individual events span from less than 5 ms (4.7c.iii) up to 30 ms (4.7d.iii). On the other

hand, a typical bundle is a few hundred ms long, which is less than for GC (few seconds).

Similar to GC, the most prevalent types of stripping events on the Au collector electrode are short, sharp, high-current *orange* (4.7c.iv, 4.7c.v) and long low-current, saw-tooth *red* (4.7d.iv, 4.7d.v) events. However, there are some subtle differences. Using a Au electrode, sharp *orange* events span for 5-15 ms, approximately twice the duration as on GC. These sharp events are asymmetric having either a very sharp increase in current followed by a longer decay (4.7c.iv) or *vice-versa* (4.7c.v). The first case represents a NP engaging quickly at the collector electrode and being held back as it attempts to disengage[14]. The second case embodies a NP gradually engaging with the electrode and sticking, and then quickly detaching after partial stripping. It should be noted that the charge consumed in both cases would represent the partial stripping of fractions of 18% and 22% of a particle of d = 100 nm. This asymmetry is not only noticeable on Au, but can also be seen in GC where sharper current increase (4.7a.v) or decrease (4.6c.v) can also be detected, although these events occur more frequently on Au (35%) than on GC (8%).

Saw-tooth *red* (4.7d.iv, 4.7d.v) events spanning hundreds of ms are also found on Au. They represent only 25% of the total charge (54% for GC). Such events attain currents up to hundreds of pA. Again, although large amounts of charge are also consumed in these cases, total stripping cannot always be guaranteed, as while the charge consumed on event 5d.iv corresponds to d = 100 nm, that on 5d.v represents d = 80 nm (or 50% of a Ag NP of d = 100 nm).

4.4.2B Quantitative analysis of I-t transients It is worth reemphasizing that the measurement of the charge associated with the electrochemical dissolution of single NPs upon impact onto a collector electrode has been claimed to allow the sizing (including determining the size distribution) of NPs with diameters from 6 to 100 nm with a resolution comparable to TEM[20,21]. The qualitative analysis of the features of the *I-t* transients reported in Section 4.4.2A suggests otherwise. In this section, a quantitative analysis of the main types of current transients is presented, which confirms the deductions made from our qualitative survey of the wide range of *I-t* morphologies that occur in NP impacts.

Figure 4.8a shows normalized histograms of the charge consumed by each single event (current spike) for the stripping of NPs of *d* = 10, 20, 40, 60 and 100 nm on GC and *d* = 100 nm on Au. The charge data span *5 orders of magnitude* and so histograms are displayed as a log-log plot in order to better visualize all the data. The dashed blue lines correspond to the charge associated to the electrochemical oxidation of Ag NPs of ideal spherical shape with diameters of 10, 20, 40, 60 and 100 nm.

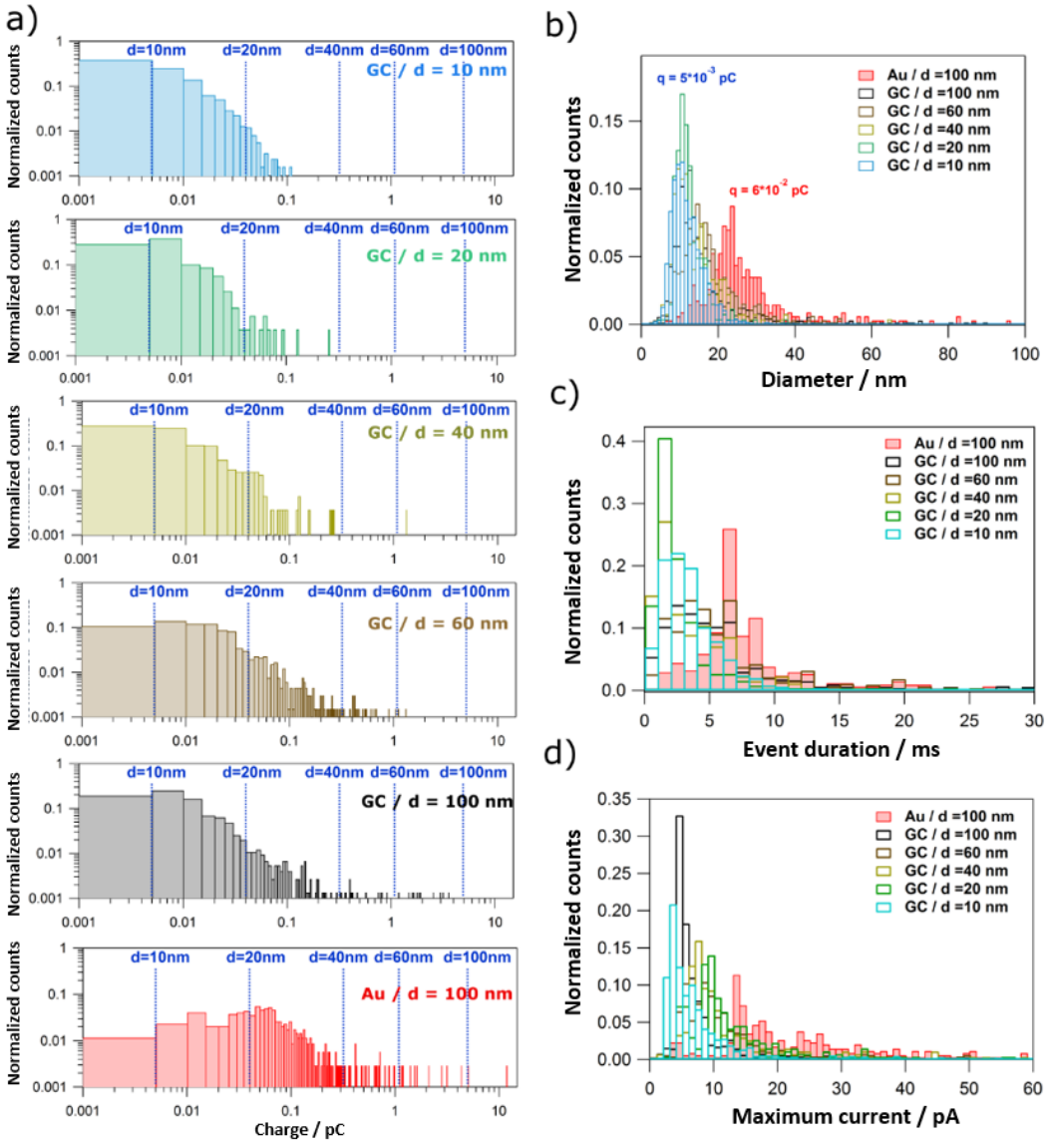

Figure 4.8 (a) Log-log plot of the charge histograms for single events recorded during the stripping of Ag NPs with nominal diameter of 10, 20, 40, 60 and 100 nm on GC and 100 nm Ag NPs on Au electrodes. Histograms of the (b) equivalent NP diameter (assuming dissolution of whole NP), (c) event duration and (d) maximum current.

When using GC as the collector electrode, the great majority of single events consume charges ranging from only 1 x 10^{-15} to 5 x 10^{-14} C, independent of NP size. Such charges would be equivalent to NPs of d = 10-20 nm. Consequently, such events could represent (close to) full NP stripping when $d \leq 20$ nm. However, the upper limit, a charge of 5 x 10^{-14} C, represents only 15%, 5% and 1% of NPs with d of 40, 60 and 100 nm, respectively. This confirms that for particles of this size, most of the *I-t* transients correspond to partial stripping of a small fraction of an impacting NP, followed by the release of the remaining NP. Events associated with the full stripping of large NPs are extremely rare. For the Au collector electrode, the charge histogram peaks around 6 x 10^{-14} C, higher than for GC (5 x 10^{-15} C). Thus, the charge consumed in single events is *more dependent on the collector electrode material than on the NP size*. This difference can be explained by the higher affinity of Ag towards Au[46] than towards GC[47].

The charge consumed can be converted to an equivalent diameter using Faraday's law. Figure 4.8b shows the histograms of equivalent NP diameters inferred from the charge histograms in Figure 4.8a. The same conclusion can be drawn: complete particle stripping on GC occurs *only for particles with d = 10 nm*. The histograms for NPs of larger diameter give an incorrect NP size distribution. Again, the influence of the collector electrode material can be clearly seen as the equivalent diameter histogram peaks at 25 nm for Au, most likely due to the stronger binding affinity and longer duration that Ag NPs spend on the Au surface (Figure 4.7 and associated discussion above).

In Figures 4.5, 4.6 and 4.7, it was shown that many events span over hundreds and thousands of milliseconds (*brown* and *red* events). Such events are consistently longer and more common for larger NP size (from 10% of all events for d = 20 nm to 55% when d = 100 nm). This can be inferred from the complete event duration histograms (Figure 4.8c, with data also shown with a log-log scale in Figure 4.9). In Figure 4.8c, the *x*-axis stops at 30 ms to better visualize the event duration distributions for the shorter times, as these are the most prevalent (*green* and *orange* events in Figures 4.5, 4.6 and 4.7). Figure 4.8c shows a slight increase with NP size in the mode of the histograms for GC, being 1-2 ms for d = 10, 20 and 40 nm, and 3-4 ms for d = 60 and 100 nm. The distinct difference between Au and GC collector electrodes for NPs of d = 100 nm is very clear, with the histogram for Au peaking at around 7-9 ms.

It is worth reemphasizing that such subtle differences can only be attained using sub-ms amplification time constants, as in this study.

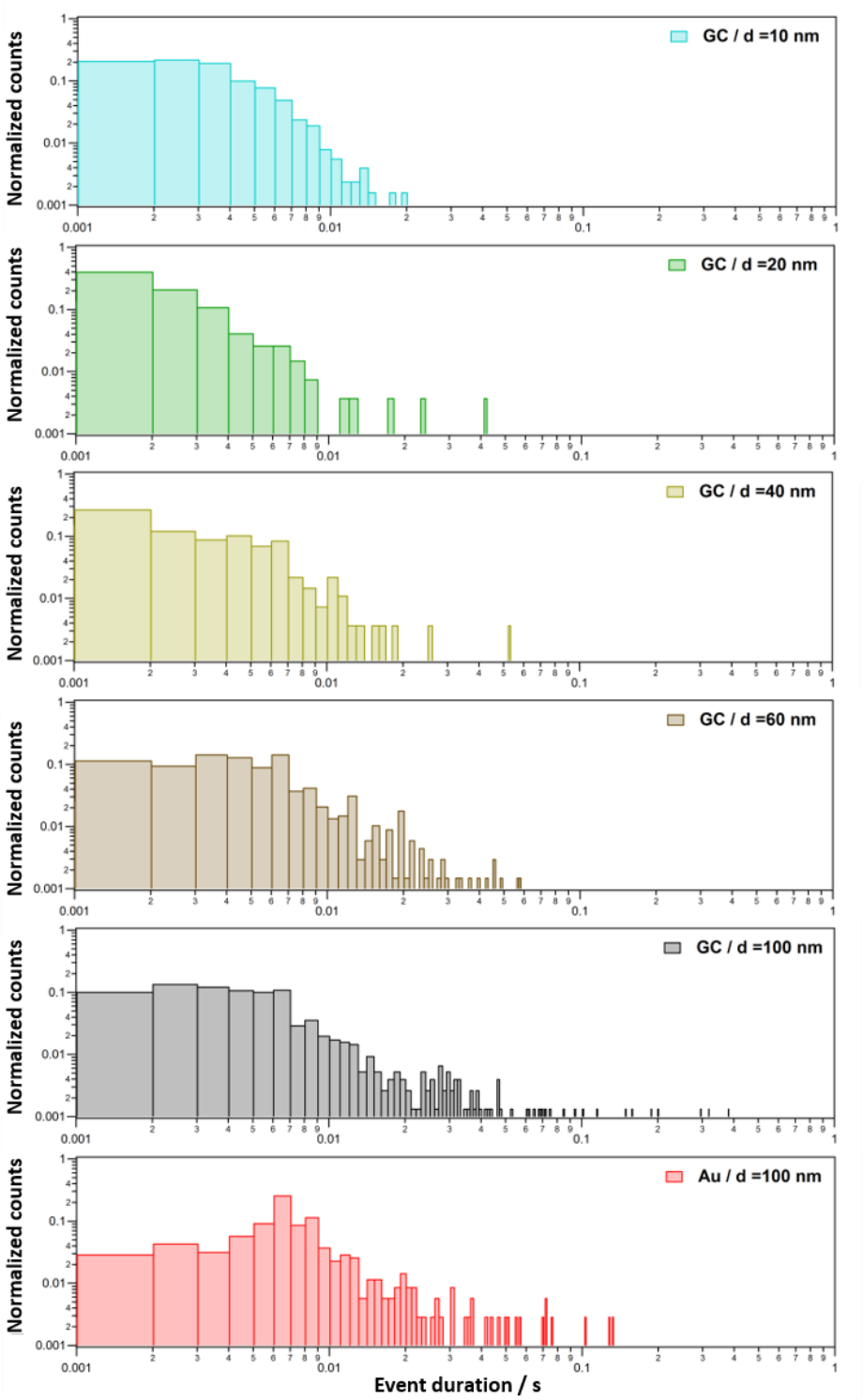

Figure 4.9 Log-log plot of the event duration histograms for single events recorded during the stripping of Ag NPs with nominal diameter of 10, 20, 40, 60 and 100 nm on GC and Au electrodes.

In Figures 4.5, 4.6 and 4.7, it was evident that some events reached hundreds of pA (*orange* and some *red* events), particularly for larger NP sizes, although such events are rather rare. This can be inferred from the complete maximum current histograms, shown with a log-log scale in Figure 4.10. A histogram of the maximum currents recorded for single events is also displayed in Figure 4.8d. The *x*-axis is cut off at 60 pA, as currents up to this value represent the majority of events (*green*, *brown* and some *red* events in Figures 4.5, 4.6 and 4.7). Figure 4.8d highlights that for GC most of the events are between 4 and 10 pA, whereas for Au as the collector electrode, most of the events attain currents between 14 and 30 pA.

Given that the consumed charge (Figure 4.8a), the event duration (Figure 4.8c) and the maximum currents (Figure 4.8d) are all dependent on the collector electrode, electrochemical dissolution of single NPs upon impact can be used to highlight differences in the physicochemical interactions and electron transfer reactions between colloidal NPs and different surfaces. That the electro-oxidation, as manifested in the *I-t* characteristics, is very different on these two electrodes, with further elaboration below, is also very good evidence for the proposed mechanism, involving transient interactions and partial electro-oxidation of Ag NPs at the collector electrode surface. Were the behaviour due to other processes, such as the possible formation of Ag_3Cit (for example), one would expect the same behaviour for the same sized NPs on different collector electrodes, and this is not the case. As shown in the voltammetric data in Figure 4.11, citrate inhibits the electrodissolution of Ag (most likely by adsorption), but there are no discrete passivation events, even in constant potential *I-t* measurements, with high time resolution and under conditions where the near-electrode concentrations of Ag^+ are comparable to, and in excess of, those pertaining to the studies herein and over time scales that are orders of magnitude longer.

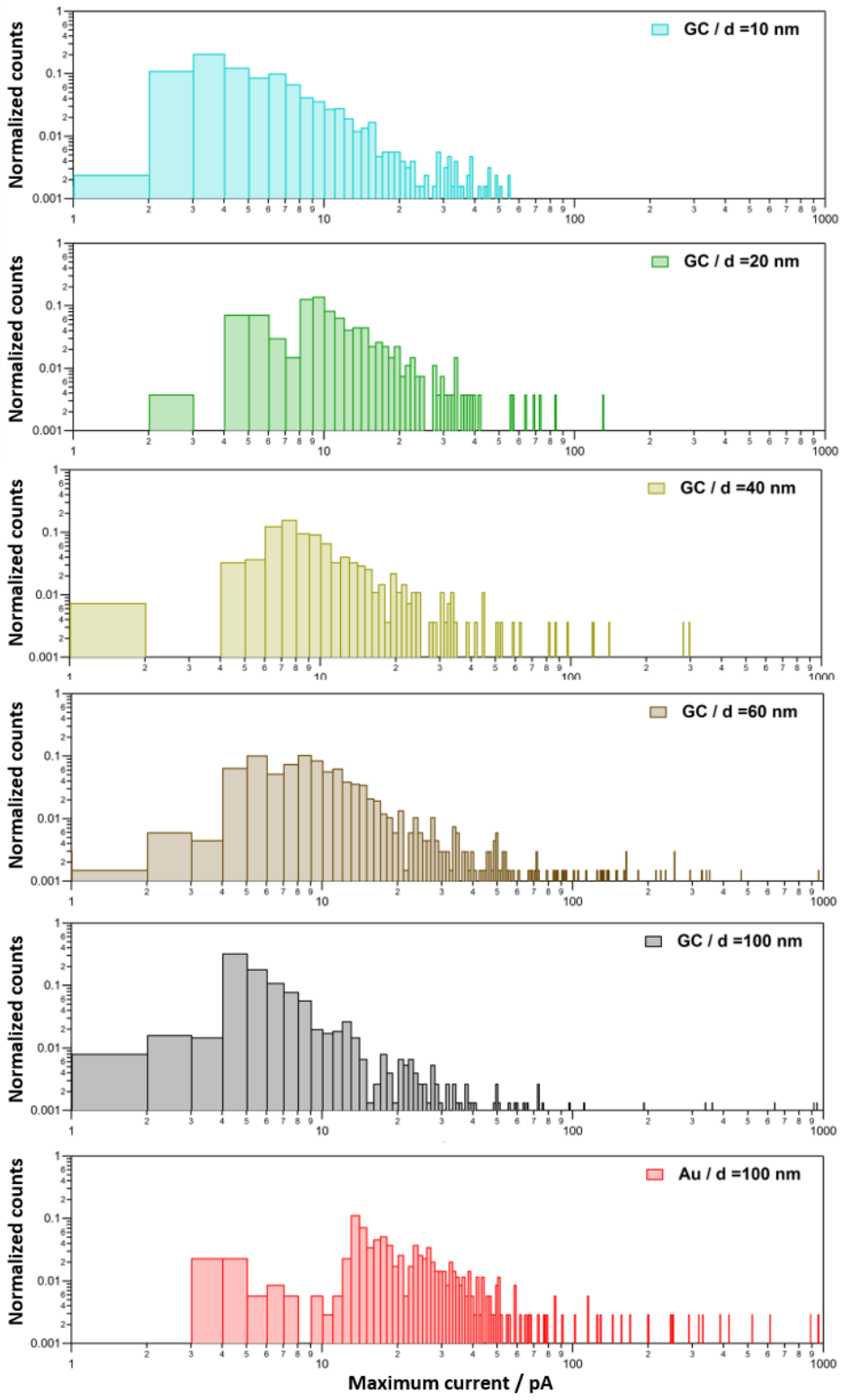

Figure 4.10 Log-log plot of the maximum current histograms for single events recorded during the stripping of Ag NPs with nominal diameter of 10, 20, 40, 60 and 100 nm on GC and Au electrodes.

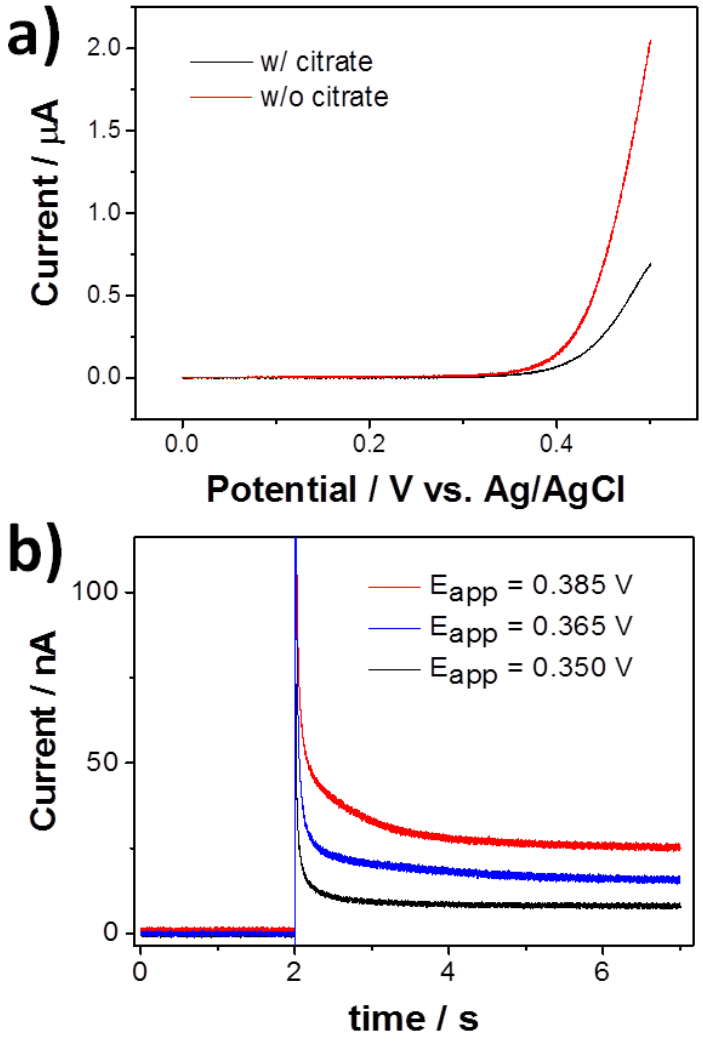

Figure 4.11 (a) LSV (50 mV s^{-1}) for Ag (UME of diameter = 125 μm) electrodissolution in presence (black) and absence (red) of 1 mM trisodium citrate in 25 mM $NaNO_3$. (b) Current-time curves at different applied potentials (E_{app} vs. Ag/AgCl) where the steady-state currents are corresponding to 0.6 (black), 1.3 (blue), and 1.9 (red) mM of Ag^+ concentrations on the Ag UME surface. Citrate inhibits Ag electrodissolution (probably by surface adsorption) but there is no evidence of surface passivation due to Ag_3Cit precipitation.

4.4.2C Quantitative analysis of the time elapsed between consecutive events Another parameter that can be deduced from a quantitative analysis of the *I-t* transients is the event frequency or its inverse - the time between two consecutive events. In previous NP impact studies, the event frequency has been found to be of the order predicted assuming a single pass diffusive flux of NPs[11,16,48] or slightly lower[4,12,49]. However, the author of this thesis recently showed that the measured frequency can actually be *several orders of magnitude larger than expected* based on simple diffusion, due to the rapid and repetitive trapping and release of a single NP upon impact (Chapter 3)[14].

Figure 4.12 shows histograms of the peak to peak time elapsed between two consecutive events for the Ag NPs studied on the 2 different collector electrodes. This magnitude spans over several orders of magnitude, from milliseconds to several seconds and so histograms are shown with a log-log scale. The blue dashed lines correspond to the estimated average time that would be elapsed between two consecutive events, based on the diffusive flux (Table 4.3) if each NP was fully dissolved in one single impact. Such average time is $1/f_{NP}$, with f_{NP} the estimated impact frequency assuming single pass NP diffusion.

If NPs were fully stripped in a single event, these histograms would show a normal distribution centred at the estimated average time between events. However, this is only the case for d = 10 nm. Instead, it can be seen that, for $d \geq 20$ nm there is a much higher proportion of events that occur with a frequency that is higher (shorter time between) than expected for single pass diffusion and that the higher frequency of impacts becomes more significant as the NP size increases. This is a confirmation that, except for NPs of d = 10 nm, larger NPs undergo multiple partial stripping impacts with the collector electrode. This is in line with the equivalent diameter histograms shown in Figure 4.8b and with the fact that only for d = 10 nm, is there a single type of *I-t* response (Figure 4.5a, only *green* events).

For $d \geq 20$ nm, it is evident that, on the one hand, most of the events are separated in time by less than 50 ms. On the other hand, the separation between some events may span up to 100 s. It is reasonable to propose that the first distribution corresponds to repetitive partial stripping events of the same NP, in which the NP size is reduced in a series of 'bites' which may, or may not, ultimately lead to complete dissolution (see Section 4.4.3, below)[14,50]. This mechanism corresponds to the event

bundles depicted in Figures 4.6b.iv, 4.6d.ii, 4.6d.iii, 4.7a.ii, 4.7b.ii, 4.7c.ii, 4.7d.ii and 4.7d.iii. The longer timescale events relate to the time that elapses between two separate NPs diffusing from the bulk solution towards the electrode.

For d = 20 and d = 40 nm, the expected time between two NPs impinging on the electrode falls reasonably in the centre of the second distribution, corresponding to the first impact that a NP makes with the collector electrode. Hence, this would also mean that, although undergoing several partial events, NPs of this size could eventually be fully stripped, in several discrete stripping events. However, for NPs of d = 60 and d = 100 nm, because the overwhelming majority of the inter-event times are much shorter than the diffusion flux time, a NP moves back and forth many times from the solution to the near-wall region, and undergoes a series of partial stripping events on each arrival.

A further striking feature is the difference in impact times between the two collector electrodes for 100 nm Ag NPs. When Au is the collector electrode, the time between events is > 7 ms, but on the GC collector electrode, many events have a much shorter timescale. This is because Ag NPs make much weaker (shorter time) contact with GC[40,51,52], leading to a higher frequency of attachment (impact)-detachment events compared with Au as the collector electrode.

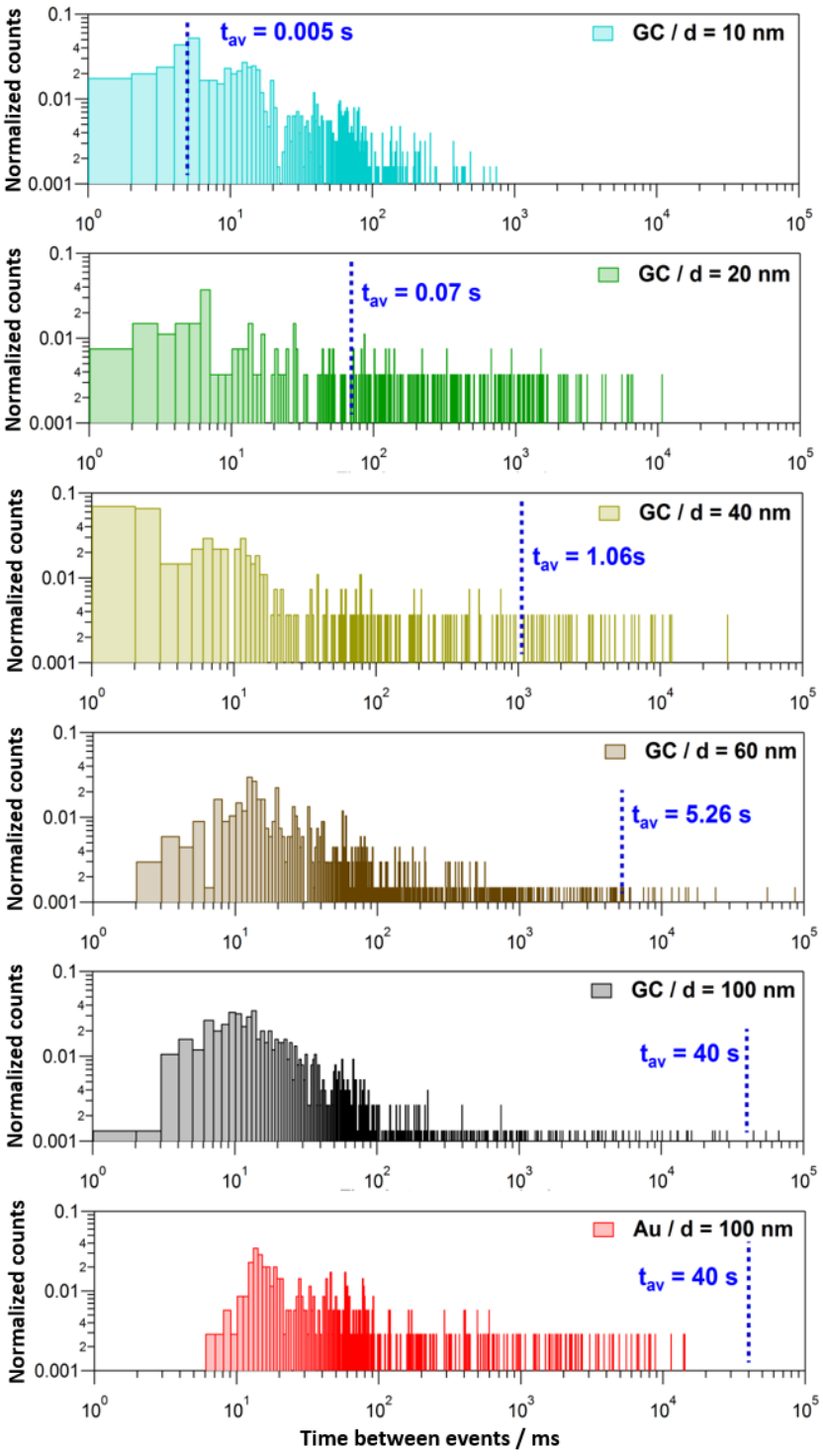

Figure 4.12 Log-log plot of the time elapsed between consecutive events recorded during the stripping of Ag NPs with nominal diameter of 10, 20, 40, 60 and 100 nm on GC and Au electrodes. The blue dashed line represents the estimated average time between two events if each NP was fully stripped in one single event.

4.4.2D Effect of the amplification time constant in the analysis of stripping events

The effect of the time constant on the current response was briefly examined for two reasons: (i) a number of studies in the literature, carried out with commercial potentiostats, appear to have employed a much longer time constant than considered for our studies[17–19,24,53]; and (ii) a long time constant will lead to a merging (summing) of discrete events, and it was worth testing if this allows the NP size to be recovered. Figure 4.13a shows selected *I-t* transients, recorded with τ_C = 100 µs, that display distinctive features (taken from Figures 4.5, 4.6, and 4.7 and discussed in Section 4.4.2A). For comparison, Figure 4.13b shows representative *I-t* signals taken under the same conditions, but with τ_C = 5 ms. The events correspond to 60 nm Ag NPs (left hand side) and 100 nm Ag NPs (centre) on GC, and to 100 nm Ag NPs on Au (right hand side). Increasing the time constant results in the signal being smoothed and is detrimental to the correct interpretation of NP landing events, which have been discussed in detail above. On the left hand side, it can be seen that the bundles of *green* events and saw-tooth *brown* transients become indistinguishable with τ_C = 5 ms. When the size of the impacting NP is larger, longer *red* saw-tooth events and *blue* event bundles are clearly distinguished with τ_C = 100 µs, whereas it is not possible to distinguish them from each other when τ_C = 5 ms, as displayed in the centre of Figure 4.13b. Furthermore, on the right hand side, it is seen that when *orange* sharp events are detected with τ_C = 100 µs, an asymmetry is evident, allowing us to differentiate between fast current increase – gradual current decrease and *vice-versa*, discussed above. A higher τ_C results in an altered measured transient[37,38] that does not allow this discrimination.

The quantitative analysis of more than 4000 events recorded with τ_C = 5 ms is summarized in Figures 4.13c and 4.13d. On the one hand, the equivalent particle size distribution, assuming that NPs are anodically dissolved in one impact, is shown in Figure 4.13c and is very similar to that for τ_C = 100 µs (see Figure 4.8b). This similarity is due to the fact that increasing the amplification time constant results in an altered *I-t* profile (much smaller current and longer duration) but the charge transferred is well conserved.[33] The computed average diameters increase slightly for τ_C = 5 ms because events that are separated by very short times ($t_{sep} < \tau_C$) would be identified as one single event of larger charge. Figure 4.13d shows the histogram of the duration of single events. The mode of the histograms is between 9 and 12 ms, and is independent

of NP size and collector electrode material. This is in contrast with data reported for τ_C = 100 µs (see Figure 6c) that showed a clear difference between the average event duration for GC (1-4 ms) and Au (7-9 ms). It is worth reemphasizing that these apparently subtle differences are of great importance in understanding the dynamics of NPs in the vicinity of polarized surfaces. Studies with the 5 ms time constant would conclude that the collector electrode surface chemistry was not important, whereas the shorter time constant reveals the significance of the surface chemistry in determining the nature of the impact event. It is further important to note that, even using slow time constants, similar to the ones in previous reports[20,21], NPs of $d \geq 20$ nm *do not undergo complete dissolution upon impact* [27–29], and such data cannot be used reliably for NP sizing.

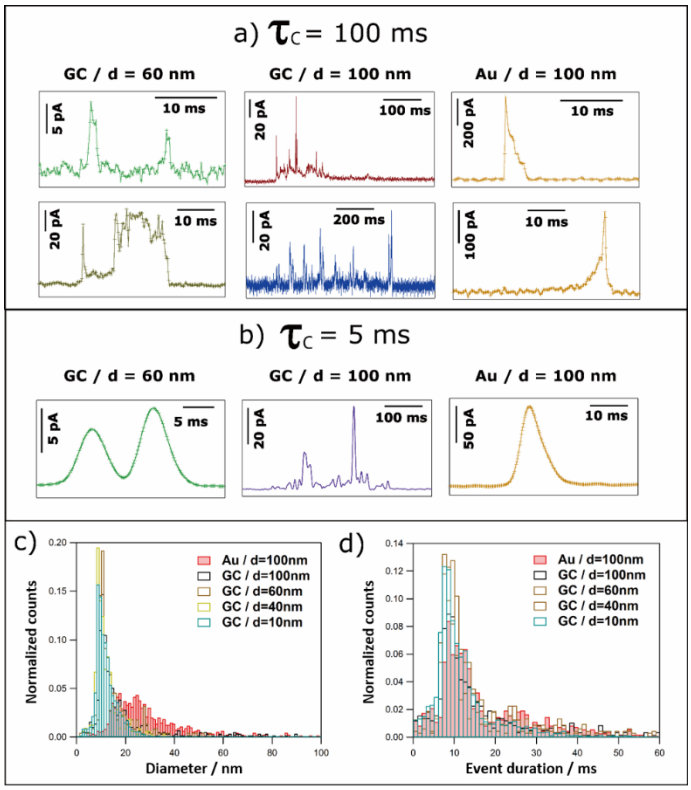

Figure 4.13 Representative current transients obtained with (a) τ_C = 100 µs and (b) τ_C = 5 ms, by applying E=+0.6 V vs Ag/AgCl to a GC electrode with a solution containing Ag NPs with nominal diameter of (left) 40 nm and (middle) 100 nm, and to a Au electrode with a solution containing Ag NPs with nominal diameter of 100 nm (right). Histograms of (c) equivalent NP diameter (assuming complete dissolution of NPs) and (d) event duration, both for τ_C = 5 ms.

4.4.3 Electrochemical Dissolution Mechanisms of Individual NPs

Since both Au and GC surfaces are heterogeneous and there is certain dispersion in size and shape of NPs of a nominal size, variability in the *I-t* responses within a particular experiment is expected, as each event probes the interaction of a single NP with the region(s) of the collector electrode where it lands. Surface chemistry has been shown to have a significant effect on the residence time (and hence interaction) of NPs with collector electrode surfaces (overall comparison of the response on GC and Au collector electrodes), although it should be noted that electron tunnelling between an electrode and an adsorbed NP is relatively immune to passive layers (*e.g.* adsorbed impurities), unless the layer becomes too thick, with a dependence on the NP size[54]. Figure 9 shows the most recurrent morphologies for *I-t* transients, from which aspects of the dissolution mechanisms can be inferred (as a function of NP size). The percentage next to each scheme marks the proportion of that type of event, calculated as the ratio of the charge passed for events with that particular characteristic to the total charge consumed by events of all types.

For particles of d = 10 nm, virtually 100% of the recorded events have maximum currents between 4 and 40 pA, and durations between 1 and 10 ms (80% have durations between 2 and 4 ms). This type of event has been coded as *green* event in earlier sections of the article. The charge consumed in these events is in very good agreement with that required for the electrodissolution of a NP of d = 10 nm (see Figures 4.8a and 4.8b). Hence, on the timescale accessible for these measurements, the electro-oxidation of small NPs of d = 10 nm, upon impact on GC, essentially occurs in a single event (Figure 4.14a).

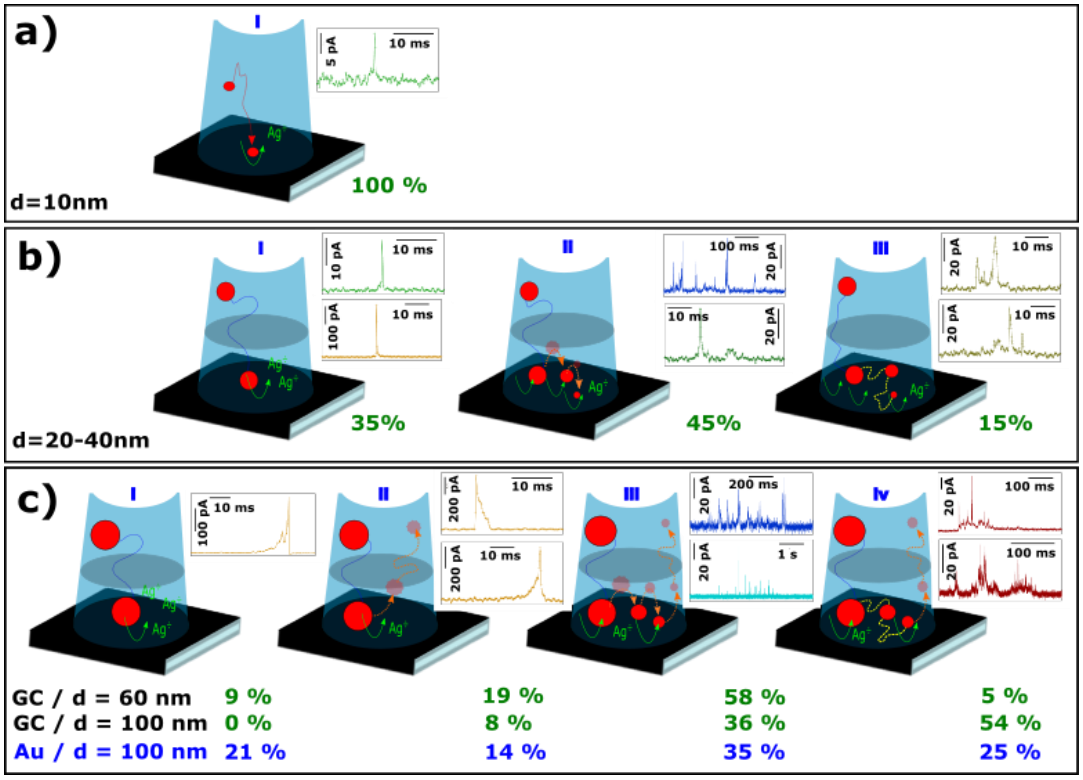

Figure 4.14 Schematic of different processes of electrochemical dissolution of Ag NPs with nominal diameters of (a) 10, (b) 20, 40 and (c) 60, 100 nm.

For particles of d = 20 and 40 nm, there are at least three scenarios. The charge passed in some *green* and *orange* events is consistent with the stripping of an entire NP, but occurs in only 35% of the cases (Figure 4.14b.i). The most common scenario for *green* events (Figure 4.14b.ii) is that the charge accounts for just a fraction of that needed to fully dissolve the impacting NP. This is also evident when one considers the time elapsed between consecutive events, which is much shorter than expected if each NP were to impact only once by diffusion (see Section 4.4.2C). In the main, NPs of $d \geq 20$ nm require several impacts to be dissolved completely. A possible scenario is that, after a first partial stripping event, the NP leaves the tunnelling (charge transfer) region, but remains in the vicinity of the surface due to near-wall hindered diffusion[14,50]. There is then a high chance for such a partially dissolved NP to impact on the collector surface again and undergo another (partial) stripping event. The analysis of the time between consecutive events (see Section 4.4.2C, Figure 4.12) points towards NPs in this size range being eventually stripped in multiple events before leaving the near-wall region.

A third scenario is displayed in Figure 4.14b.iii. Although less frequent, 15% of the charge consumed during the stripping of NPs of d = 20 or 40 nm occurs in longer events that display a saw-tooth shape, i.e, several current maxima and minima instead of a single current peak. These events have been coded *brown* and have durations of tens of ms, with the current never dropping to zero. However, it must be noted that each data point represents the average current transferred during 165 μs, and the NP could move away from the electrode and back again in this time period. In essence, a saw-tooth *I-t* profile indicates that the NP is not firmly attached to the substrate during the stripping process. For this scenario, and for NPs of this size range, the charge consumed during these long *brown* events appears to be consistent with the electrochemical dissolution of entire NPs.

For larger diameters (d = 60 and 100 nm), the *I-t* transients also show several different scenarios. On the one hand, there are short and isolated current transients that reach several hundreds of pA and last less than 30 ms (*orange* events), but these events only account for 28% and 8%, respectively. The bundles of the total charge for 60 nm and 100 nm Ag NPs on GC. This scenario is displayed in Figures 9c.i and 9c.ii. In relatively few cases (9% for d = 60 nm) is the amount of charge consumed during these events close to that required for entire NP electrodissolution (4.14c.i). In most cases, the charge passed corresponds to only a fraction of the landing NP, with no pre- or post-transient signal. This means that after partial stripping, the NP drifts away into the bulk solution (Figure 4.14c.ii). Such a NP could impact with the electrode again after a longer time has passed, generating another *I-t* transient. This scenario is in agreement with the conclusions from the analysis of the time between consecutive events (Figure 4.12 and discussion above). Still, if only these events (I_{Peak} > 100 pA) were taken into account, the calculated average NP diameter would be 39 nm and 47 nm for Ag NPs of nominal diameters of 60 nm and 100 nm, respectively, landing on GC. Alternatively, on Au, an estimated diameter of 60 nm would be obtained for Ag NPs of 100 nm nominal diameter. This reemphasizes that impact coulometry cannot provide an accurate measurement of the size of NPs in solution.

Inspection of the *orange* transients leads to further insights into the stripping processes. Independent of NP size, and of whether partial or full stripping takes place, such sharp events are asymmetric and can be classified in two sub-types. In some cases, a very sharp increase in current is followed by a longer decay (Figures 4.7a.v,

4.7c.iv) and *vice-versa* (4.6c.v, 4.7c.v), (see Section 4.4.2A). These events last approximately twice as long on Au as on the GC collector, indicating that Ag NPs tend to stay for longer time in the tunnelling region close to Au than to a GC electrode due to a stronger binding affinity between Ag and Au[46].

The majority of *I-t* traces for 60 and 100 nm diameter NPs are comprised of short, low-current events (4.14c.iii) or long, irregular and saw tooth events (4.14c.iv). These cases are analogous to those shown in Figure 4.14b.ii and 4.14b.iii respectively, the bundles of short events span up to few seconds whereas saw-tooth events can last up to hundreds of ms. Larger NPs with smaller diffusion coefficients are less likely to leave the near-wall region after partial stripping (4.14.c.iii) and tend to stay within the tunnelling region (4.14c.iv) for longer times.

To reiterate, the relative occurrence of the different scenarios (Figure 4.14c) depends on the collector electrode material. For d = 100 nm, the proportion of 9c.i and 9c.ii scenarios is higher for Au (35%) than for GC (8%). On the other hand, longer saw-tooth events (scenario 4.14c.iv), which reflect weak interaction between the NP and collector electrode, are more frequent on GC (54%) than on Au (25%).

4.4.4 Special Case: Periodic Current Transients

In some occasions, isolated current profiles displaying a periodic pattern were found. Figure 4.15 shows three examples obtained for NPs of d = 40 nm (a, b), d = 60 nm (c, d) on GC and d = 100 nm on Au (e, f).

In the case of GC, for both d = 40 and d = 60 nm, the periodicity of the current profile is so ideal (within the resolution of the measurement) that the separation between current peaks is 1.3 ± 0.2 ms (8 data points). The possibility that this could be an electronic artefact can be discarded as such events are recorded during long *I-t* acquisitions that mainly display events as shown in Figures 4.5, 4.6 and 4.7. It must be noted that the charge consumed during the whole duration of these periodic events is equivalent to NPs of d = 44 nm and d = 60 nm, respectively, which indicates that the NPs are more or less completely consumed in a series of ‘bites’.

When the substrate is Au instead of GC, the repeated feature for d = 100 nm is not a single peak but a doublet, which repeats every 75 ± 7 ms. The two peaks that constitute the doublet are separated by 13 ± 2 ms. Interestingly, the charge consumed

during the whole duration of this periodic event is equivalent to a NP of d = 94 nm, indicating that close to full NP stripping also occurs.

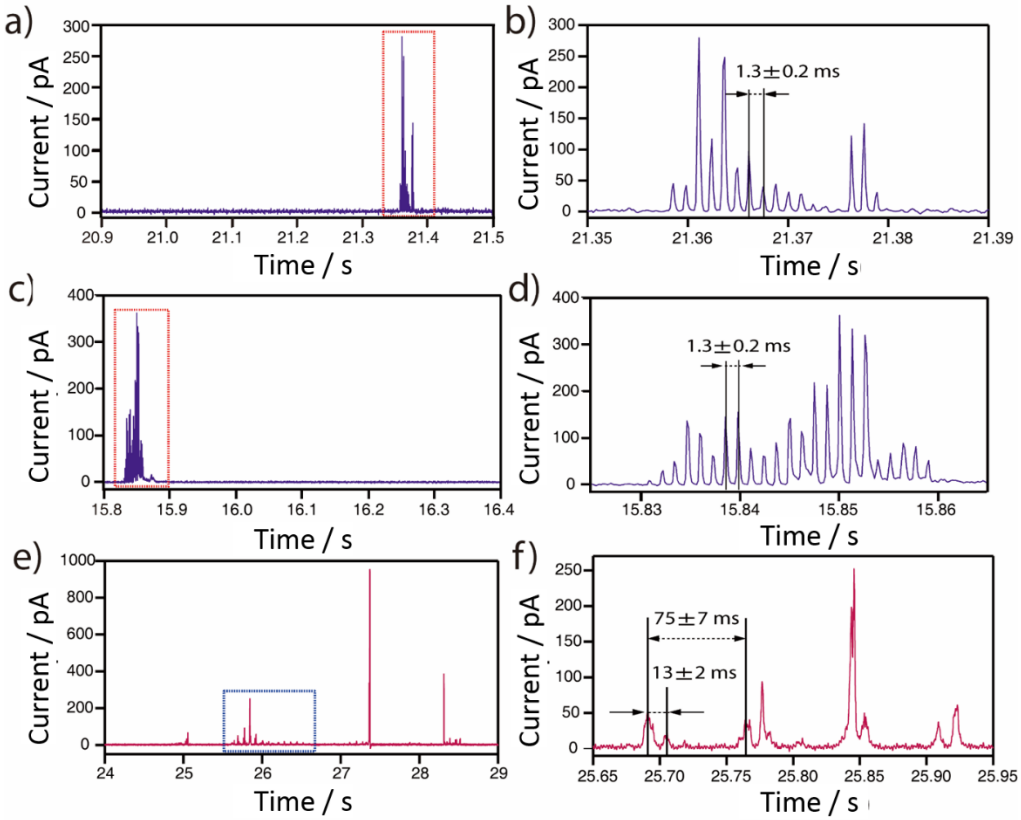

Figure 4.15 Representative periodic *I-t* transients obtained by applying E=+0.6 V vs Ag/AgCl to a GC with a solution containing Ag NPs with nominal diameter of (a,b) 40 nm and (c,d) 60 nm, and to Au with a solution containing Ag NPs with nominal diameter of (e,f) 100 nm.

The fact that these oscillatory phenomena are very infrequent (< 1%), implies that rather special conditions need to be fulfilled to give rise to this *I-t* behaviour. The NP is cycled to and from the collector electrode with a close to constant periodicity, which is different on Au and GC substrates. These specific NP dynamics near the electrode cannot be caused by diffusional trapping as this would imply the time between events to have a larger dispersion, to change as the NP size decreased during dissolution and to be independent of the collector material. Figure 4.16 shows a schematic representation of the periodic stripping process recorded using GC (Figure 4.16a) and Au (Figure 4.16b) as collector electrode. In the first case, the NP enters the tunnelling region and electro-oxidation of Ag atoms from the part of the NP in closer

contact with the collector electrode occurs. As a result, the interaction between the NP (which could be pushed away by electrochemical propulsion[14]), due to a non-uniform electrochemical flux, and the substrate is momentarily broken. This absence of current lasts for just 0.5 ms. The process starts again and is repeated until the NP is completely consumed. For the Au collector electrode, the periodic stripping mechanism appears more complex, comprising two consecutive stripping events that occur within 25 ms that are followed by 50 ms without electrochemical current before repetition of the *I-t* motif.

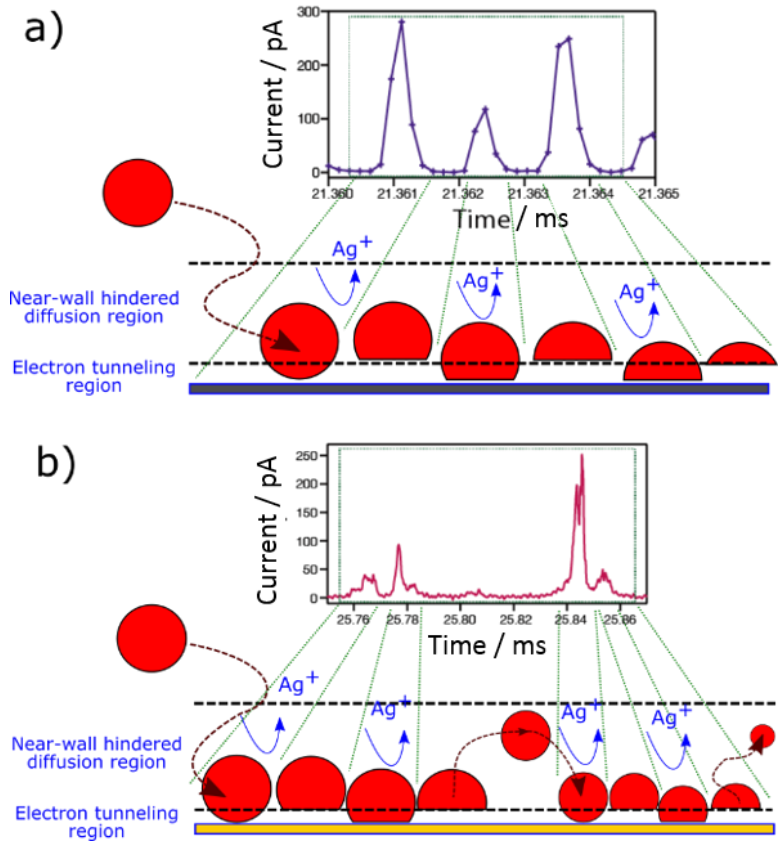

Figure 4.16 Periodic *I-t* patterns (from Figure 4.15) and Schematic representation of the electrochemical dissolution mechanism of Ag NPs on a (a) GC and on (b) Au substrate.

The observation of a distinctly different periodic pattern on each of the two collector electrodes reflects some surface-specific features that can also be inferred from the analysis of the more prevalent irregular peak bundles (4.14.c.iii). These latter events occur on GC with a higher frequency and shorter duration than on Au (see Figures 4.8c and 4.12). It is clear that the collector electrode material has a great

influence on the stripping mechanism of impacting Ag NPs, as well as on the near-wall dynamics during partial stripping processes, and the investigation of these periodic patterns could be worthwhile in the future as a means of deepening understanding of NP-substrate interactions.

4.5 Conclusions

The detection of electrochemical reactions that occur upon impact of single NPs with an electrode surface - a growing field that is termed 'single NP impact electrochemistry' - requires that small signals can be measured quickly, necessitating low background currents (pA) and fast current amplifiers. Otherwise, the *I-t* signal becomes highly distorted, making it extremely difficult to interpret the underlying phenomena. These requirements have been met for the comprehensive time-resolved study presented herein on the electrochemical dissolution of single Ag NPs of different sizes by means of NP impacts in an SECCM configuration, using GC and Au as collector electrodes.

In contrast to previous work, it has been found that NP stripping leads to a wide range of very different and distinctive current transients (*I-t* morphologies), even during impacts of NPs of the same nominal size with the same substrate. Whereas most of the NPs of diameter, d = 10 nm dissolve electrochemically in single events (on the timescale of the measurement technique) that lasts a few milliseconds, this is not true of NPs with larger diameters. In this case, between 60% and 85% of the total consumed charge occurs in event bundles or saw-tooth current profiles that may span from tens of milliseconds up to several seconds for a single NP.

A quantitative analysis of the *I-t* features, consumed charge, event duration and impact frequency leads to a major conclusion: Ag NPs undergo consecutive partial stripping events in which a fraction of the NP is electrochemically oxidized, followed by the NP drifting away and then back to the tunnelling region for further (partial) dissolution. Whereas for NPs of d = 20 nm and 40 nm, the whole NP tends to be electrochemically dissolved after several consecutive (discrete) stripping events, the analysis of the associated *I-t* transients as individual events leads to the wrong estimation of the NP size distribution. Furthermore, for particles of d = 60 nm or 100 nm, most of the NPs are released from the near-wall region back into the bulk solution

after incomplete stripping. Hence, the analysis of the charge consumed by single events ('impact coulometry') *is not appropriate as a general method to determine the size of colloidal NPs.*

On the other hand, it needs to be emphasized that a proper analysis of *I-t* transients provides very valuable information on the physicochemical interactions between NPs and polarized surfaces. This work has shown that the relatively stronger interaction between Ag NPs and Au results in larger charges consumed per event, and longer residence time of the Ag NPs in the vicinity of the surface. In addition, an interesting, but rare, observation has been the detection of periodic *I-t* patterns with frequencies as high as 1 kHz, recorded for most of the NP sizes studied on both GC and Au. Whereas understanding the physical origin of such patterns requires further study, they serve to highlight the complexity of electrochemical dissolution phenomena via single NP impacts and the need for sub-ms time resolution (or, in the future, better) to properly study such processes.

4.6 References

(1) Burda, C.; Chen, X.; Narayanan, R.; El-Sayed, M. A. *Chem. Rev.* **2005**, *105* (4), 1025–1102.

(2) Tao, A. R.; Habas, S.; Yang, P. *Small* **2008**, *4* (3), 310–325.

(3) Aricò, A.; Bruce, P.; Scrosati, B. *Nat. Mater.* **2005**, *4* (May), 366–377.

(4) Kleijn, S. E. F.; Lai, S. C. S.; Koper, M. T. M.; Unwin, P. R. *Angew. Chem. Int. Ed. Engl.* **2014**, 3558–3586.

(5) Xiao, X.; Bard, A. J. *J. Am. Chem. Soc.* **2007**, *129* (31), 9610–9612.

(6) Heinze, J. *Angew. Chemie Int. Ed.* **1993**, *32* (9), 1268–1288.

(7) Kwon, S. J.; Bard, A. J. *J. Am. Chem. Soc.* **2012**, *134* (16), 7102–7108.

(8) Alligrant, T. M.; Nettleton, E. G.; Crooks, R. M. *Lab Chip* **2013**, *13* (3), 349–354.

(9) Alligrant, T. M.; Dasari, R.; Stevenson, K. J.; Crooks, R. M. *Langmuir* **2015**, *31* (42), 11724–11733.

(10) Bard, A. J.; Zhou, H.; Kwon, S. J. *Isr. J. Chem.* **2010**, *50* (3), 267–276.

(11) Robinson, D. A.; Yoo, J. J.; Castañeda, A. D.; Gu, B.; Dasari, R.; Crooks, R. M.; Stevenson, K. J. *ACS Nano* **2015**, *9* (7), 7583–7595.

(12) Xiao, X.; Fan, F.-R. F.; Zhou, J.; Bard, A. J. *J. Am. Chem. Soc.* **2008**, *130* (49), 16669–16677.

(13) Dick, J. E.; Bard, A. J. *J. Am. Chem. Soc.* **2016**, *138* (27), 8446–8452.

(14) Kang, M.; Perry, D.; Kim, Y. R.; Colburn, A. W.; Lazenby, R. A.; Unwin, P. R. *J. Am. Chem. Soc.* **2015**, *137* (34), 10902–10905.

(15) Kleijn, S. E. F.; Lai, S. C. S.; Miller, T. S.; Yanson, A. I.; Koper, M. T. M.; Unwin, P. R. *J. Am. Chem. Soc.* **2012**, *134*, 18558–18561.

(16) Zhou, Y.-G.; Rees, N. V; Compton, R. G. *Angew. Chem. Int. Ed. Engl.* **2011**, *50* (18), 4219–4221.

(17) Lees, J. C.; Ellison, J.; Batchelor-Mcauley, C.; Tschulik, K.; Damm, C.; Omanovič, D.; Compton, R. G. *ChemPhysChem* **2013**, *14* (17), 3895–3897.

(18) Bartlett, T. R.; Sokolov, S. V.; Compton, R. G. *ChemistryOpen* **2015**, *4* (5), 600–605.

(19) Toh, H. S.; Jurkschat, K.; Compton, R. G. *Chem. - A Eur. J.* **2015**, *21* (7), 2998–3004.

(20) Batchelor-McAuley, C.; Ellison, J.; Tschulik, K.; Hurst, P. L.; Boldt, R.; Compton, R. G. *Analyst* **2015**, *140* (15), 5048–5054.

(21) Sokolov, S. V.; Tschulik, K.; Batchelor-McAuley, C.; Jurkschat, K.; Compton, R. G. *Anal. Chem.* **2015**, *87* (19), 10033–10039.

(22) Haddou, B.; Rees, N. V; Compton, R. G. *Phys. Chem. Chem. Phys.* **2012**, *14* (39), 13612–13617.

(23) Giovanni, M.; Ambrosi, A.; Sofer, Z.; Pumera, M. *Electrochem. commun.* **2015**, *56*, 16–19.

(24) Stuart, E. J. E.; Tschulik, K.; Batchelor-Mcauley, C.; Compton, R. G. *ACS Nano* **2014**, *8* (8), 7648–7654.

(25) Qiu, D.; Wang, S.; Zheng, Y.; Deng, Z. *Nanotechnology* **2013**, *24* (50), 505707.

(26) Brasiliense, V.; Berto, P.; Combellas, C.; Kuszelewicz, R.; Tessier, G.; Kanoufi, F. *Faraday Discuss.* **2016**, *193*, 339–352.

(27) Brasiliense, V.; Patel, A. N.; Martinez-Marrades, A.; Shi, J.; Chen, Y.; Combellas, C.; Tessier, G.; Kanoufi, F. *J. Am. Chem. Soc.* **2016**, *138* (10), 3478–3483.

(28) Patel, A. N.; Martinez-Marrades, A.; Brasiliense, V.; Koshelev, D.; Besbes, M.; Kuszelewicz, R.; Combellas, C.; Tessier, G.; Kanoufi, F. *Nano Lett.* **2015**, *15* (10), 6454–6463.

(29) Krause, K. J.; Adly, N.; Yakushenko, A.; Schnitker, J.; Mayer, D.; Offenhäusser, A.; Wolfrum, B. *Anal. Chem.* **2016**, *88* (7), 3632–3637.

(30) Brasiliense, V.; Berto, P.; Combellas, C.; Tessier, G. *Acc. Chem. Res.* **2016**, *49*, 2049–2057.

(31) Saw, E. N.; Grasmik, V.; Rurainsky, C.; Epple, M.; Tschulik, K. *Faraday Discuss.* **2016**, *157* (207890), 243–284.

(32) Sepunaru, L.; Sokolov, S. V.; Holter, J.; Young, N. P.; Compton, R. G. *Angew. Chemie - Int. Ed.* **2016**, *55* (33), 9768–9771.

(33) Kätelhön, E.; Tanner, E. E. L.; Batchelor-McAuley, C.; Compton, R. G. *Electrochim. Acta* **2016**, *199*, 297–304.

(34) Krause, K. J.; Yakushenko, A.; Wolfrum, B. *Anal. Chem.* **2015**, *87* (14), 7321–7325.

(35) Kätelhön, E.; Compton, R. G. *Chem. Sci.* **2014**, *5* (12), 4592–4598.

(36) Kang, M.; Momotenko, D.; Page, A.; Perry, D.; Unwin, P. R. *Langmuir* **2016**, *32* (32), 7993–8008.

(37) Chen, C. H.; Ravenhill, E. R.; Momotenko, D.; Kim, Y. R.; Lai, S. C. S.; Unwin, P. R. *Langmuir* **2015**, *31* (43), 11932–11942.

(38) Zhao, L.-J.; Qian, R.-C.; Ma, W.; Tian, H.; Long, Y.-T. *Anal. Chem.* **2016**, *88* (17), 8375–8379.

(39) Kim, Y. R.; Lai, S. C. S.; McKelvey, K.; Zhang, G.; Perry, D.; Miller, T. S.; Unwin, P. R. *J. Phys. Chem. C* **2015**, *119* (30), 17389–17397.

(40) Lai, S. C. S.; Lazenby, R. a.; Kirkman, P. M.; Unwin, P. R. *Chem. Sci.* **2015**, *6* (2), 1126–1138.

(41) Byers, J. C.; Paulose Nadappuram, B.; Perry, D.; McKelvey, K.; Colburn, A. W.; Unwin, P. R. *Anal. Chem.* **2015**, *87* (20), 10450–10456.

(42) Bentley, C. L.; Kang, M.; Unwin, P. R. *J. Am. Chem. Soc.* **2016**, *138* (39), 12755–12758.

(43) Edwards, M. A.; Williams, C. G.; Whitworth, A. L.; Unwin, P. R. *Anal. Chem.* **2009**, *81* (11), 4482–4492.

(44) Morgan, D. M.; Weber, S. G. *Anal. Chem.* **1984**, *56* (13), 2560–2567.

(45) Nomura, S.; Nozaki, K.; Okazaki, S. *Anal. Chem.* **1991**, *63* (22), 2665–2668.

(46) Lee, H. M.; Ge, M.; Sahu, B. R.; Tarakeshwar, P.; Kim, K. S. *J. Phys. Chem. B* **2003**, *107*, 9994–10005.

(47) Khomyakov, P. A.; Giovannetti, G.; Rusu, P. C.; Brocks, G.; Van Den Brink, J.; Kelly, P. J. *Phys. Rev. B - Condens. Matter Mater. Phys.* **2009**, *79* (19), 1–12.

(48) Kwon, S. J.; Fan, F. R. F.; Bard, A. J. *J. Am. Chem. Soc.* **2010**, *132* (38), 13165–13167.

(49) Kwon, S. J.; Zhou, H.; Fan, F.-R. F.; Vorobyev, V.; Zhang, B.; Bard, A. J. *Phys. Chem. Chem. Phys.* **2011**, *13* (12), 5394.

(50) Bevan, M. A.; Prieve, D. C. *J. Chem. Phys.* **2000**, *113* (3), 1228–1236.

(51) Ustarroz, J.; Ke, X.; Hubin, A.; Bals, S.; Terryn, H. *J. Phys. Chem. C* **2012**, *116* (3), 2322–2329.

(52) Ustarroz, J.; Hammons, J. A.; Altantzis, T.; Hubin, A.; Bals, S.; Terryn, H. *J. Am. Chem. Soc.* **2013**, *135*, 11550–11561.

(53) Chen, C.-C.; Zhou, Y.; Baker, L. A. *ACS Nano* **2011**, *5* (10), 8404–8411.

(54) Chazalviel, J. N.; Allongue, P. *J. Am. Chem. Soc.* **2011**, *133* (4), 762–764.

Chapter 5. Simultaneous Topography and Reaction Flux Mapping At and Around Electrocatalytic Nanoparticles

5.1 Abstract

The characterization of electrocatalytic reactions at individual nanoparticles (NPs) is presently of considerable interest but very challenging. Herein, we demonstrate how simple-to-fabricate nanopipette probes with diameters of approximately 30 nm can be deployed in a scanning ion conductance microscopy (SICM) platform to simultaneously visualize *electrochemical reactivity* and *topography* with high spatial resolution at electrochemical interfaces. By employing a self-referencing hopping mode protocol, whereby the probe is brought from bulk solution to the near-surface at each pixel, and with potential-time control applied at the substrate, current measurements at the nanopipette can be made with high precision and resolution (30 nm resolution, 2600 pixels μm^{-2}, < 0.3 seconds/pixel) to reveal a wealth of information on the substrate physicochemical properties. This methodology has been applied to image the electrocatalytic oxidation of borohydride at ensembles of AuNPs on a carbon fiber support in alkaline media, whereby the depletion of hydroxide ions and release of water during the reaction results in a detectable change in the ionic composition around the NPs. Through the use of finite element method simulations, these observations are validated and analyzed to reveal important information on heterogeneities in ion flux between the top of a NP and the gap at the NP-support contact, diffusional overlap and competition for reactant between neighboring NPs, and differences in NP activity. These studies highlight key issues that influence the behavior of NP assemblies at the single NP level and provide a platform for the use of SICM as an important tool for electrocatalysis studies.

5.2 Introduction

The study of catalytic nanomaterials has become an important research area, due to a range of significant real-world applications, as well as fundamental interest.[1–4] Numerous studies, using ensembles of catalytic nanoparticles (NPs), have revealed that changes in NP shape, size, and structure can significantly affect (electro)catalytic activity,[5–7] but investigations of activity at the individual NP level are challenging.[8,9] Among a rather limited set of tools that have been applied for single NP electrochemical characterization,[9–14] scanning electrochemical probe microscopy (SEPM) techniques are particularly attractive, and can be highly sensitive.[15] In this chapter, it is demonstrated how a simple glass nanopipette can serve as a powerful and highly sensitive probe of NP size, shape and activity, with a spatial resolution of the order of the probe size (30 nm herein).

Advances in nanoprobe fabrication and characterization procedures[16–18] have led to significant advances in several SEPMs. The widely used scanning electrochemical microscopy (SECM) technique has recently been applied to electrocatalytic nanomaterials adhered to an electrocatalytically inert support.[18–20] However, this technique usually operates in a constant plane scanning mode with no positional feedback of the probe with respect to the surface and no topographical information obtained. Alternatively, scanning electrochemical cell microscopy (SECCM) offers integrated probe positional feedback and direct electrochemical measurements and has recently been used for the electrochemical characterization of nanomaterials (*e.g.* sp^2 carbon nanomaterials[21] and nanoparticles[22,23]). When applied in a correlative multi-microscopy approach,[24,25] it provides a means of directly relating structure (*i.e.* surface structure/properties) and function (*i.e.* electrocatalytic activity), at the nanoscale, which is a long term aspiration in electrochemical science and catalysis.

To overcome the lack of positional feedback, SECM has been successfully integrated with other scanning probe techniques such as atomic force microscopy (AFM),[26,27] scanning ion conductance microscopy (SICM)[28–30] and scanning tunneling microscopy (STM),[31,32] as well as using dual redox mediators,[33] to enable electrochemical and topographical images to be obtained. However, making reproducible nanoscale SECM probes is non-trivial and time-consuming, and this can

be even more challenging when multi-channel probes are to be employed.[34] Further, the SECM tip response needs to be stable for long time periods and the tip current has to quantitatively detect the reactant, product or intermediates, which becomes more challenging with the intrinsic high diffusion/migration rates at the nanoscale.

SICM is a well-established contactless topographical probe imaging technique, capable of characterizing delicate samples with nanometer scale resolution, using nanoscale glass or quartz probes that can be made very easily and quickly using a laser capillary puller. These probes are filled with electrolyte and a contacting electrode is inserted.[35–38] There has been significant progress to improve the time resolution of SICM through the use of high bandwidth electrometers and the introduction of versatile scanning regimes.[35,39–41] Moreover, SICM has very recently expanded beyond its major use for topographical imaging to become a multifunctional tool capable of elucidating a variety of surface properties, beyond topography.[15,35–38,42] Notably, the ion conductance current is sensitive to changes in the local ionic atmosphere near to surfaces induced by either surface charge[39,40,43] or as the result of electrochemical reactions[44]. Since all electrochemical processes result in a change in ionic composition, SICM is potentially a very powerful general probe for visualizing nanoscale electrocatalysis.

Herein, it is demonstrated how SICM with fine nanopipettes (diameter, $d_{tip} \approx$ 30 nm) can be used to perform simultaneous electrochemical flux and topographical imaging with high spatial resolution, commensurate with the probe size. Using the electrocatalytic oxidation of borohydride (BH_4^-) at Au NPs on a carbon support as an exemplar system, it is shown that it is possible to study and compare electrocatalytic activity of individual NPs within an ensemble. Complementary finite element method (FEM) simulations provide insight into several critically important phenomena such as the competition between neighboring NPs for reactant and heterogeneities in ion fluxes around a single NP. This study highlights SICM as a key tool for mapping nanoscale electrochemical processes and provides a road map for future applications of SICM in this area.

5.3 Materials and Methods

5.3.1 Chemicals

Sodium borohydride ($NaBH_4$, 99.99 %, Sigma-Aldrich), sodium hydroxide (NaOH, > 97 %, Fisher Scientific), perchloric acid ($HClO_4$, 70 %, ACS reagent, Sigma-Aldrich), chloroauric acid trihydrate ($HAuCl_4 \cdot 3H_2O$, ≥ 99.9 %, Sigma-Aldrich), were used as provided by the supplier. All solutions were prepared with Milli-Q reagent grade water (resistivity *ca.* 18.2 MΩ cm at 25°C). Electrodeposition of Au nanostructures was carried out with 0.5 mM $HAuCl_4$ in 0.1 M $HClO_4$ aqueous solution. SICM electrochemical imaging was carried out with 3 mM $NaBH_4$ in 30 mM NaOH aqueous solution.

5.3.2 Nanopipette and Sample Preparation

Nanopipettes (diameter ≈ 30 nm) were fabricated from quartz capillaries (o.d. 1 mm, i.d. 0.5 mm, Friedrich & Dimmock) using a laser puller (P-2000, Sutter Instruments) and characterized by transmission electron microscopy (TEM) (Jeol 2000X, HT = 200 eV), after SICM measurements. Two different types of UME sealed in a glass sheath, CF (diameter = 7 μm, XAS Grade, Goodfellow) and Au (diameter = 10 μm, 99.99+%, Goodfellow), were prepared as substrates. UMEs were polished with microcloth (Buehler) immersed in alumina powder solution (MicroPolish™ Alumina, 0.05 μm, Buehler) followed by mechanical polishing step using diamond lapping films (UltraPrep™ Diamond Lapping Films, 0.1 μm, Buehler). CF UMEs were further used as a supporting substrate for electrodeposited Au nanostructures or Au nanoparticles (AuNPs). Au nanostructures were prepared by applying a constant potential of 0.5 V *vs*. Ag/AgCl for 14 s to the CF UME in 0.5 mM $HAuCl_4$ with 0.1 M $HClO_4$, and AuNPs were prepared by applying 0 V *vs.* Ag/AgCl for 1 s to the CF UME, in the same plating solution. The size and shape of the nanostructured Au on the CF UMEs was characterized with scanning electron microscopy (SEM) (Zeiss Sigma FE-SEM, Carl Zeiss AG). Sample preparation for cross-sectional analysis of the AuNPs was performed using focused-ion beam (FIB)-SEM (Scios DualBeam, FEI) and the sample was characterized with TEM (Talos F200X, FEI).

5.3.3 Scanning Ion Conductance Microscopy (SICM)

A quartz nanopipette was mounted on a custom-designed holder and positioned over the area of interest using a mechanical micropositioner (Newport, M-461-XYZ-M) and 3MP digital camera (PixelLink, PL-B776U) with a 6× magnification lens. Vertical coarse movement of the nanopipette was achieved with a picomotor (Newport, 8303 Picomotor Actuator), utilized to bring the nanopipette within the travel range of the single-axis nanopositioner. A 15 μm range single axis nanopositioner (Physik Instrumente, P-753.1CD; positional error = 0.05 nm) was used for precise vertical movement of the nanopipette with the protocol described in the main text, with fine lateral moment of the sample achieved using a highly precise XY pieozoelectric stage (Physik Instrumente, P-733.2DD). The SICM system was installed on an optical table (Newport, RS2000) equipped with automatic levelling isolators (Newport, S-2000A-423.5).

A direct current (DC) feedback hopping mode was used.[39,45] A Faraday cage enclosed the SICM system with vacuum insulation panels (Kevothermal) and aluminium heat sinks to reduce thermal drift of the piezoelectric positioners. A home-built potentiostat and electrometer were used for electrochemical measurements. Two Pd wires saturated with hydrogen (Pd-H_2), prepared as reported in elsewhere[25,46,47], served as quasi-reference counter electrodes (QRCEs). Control of instrumentation and data acquisition was conducted with a custom-developed LabVIEW (2016, National Instruments) program through an FPGA card (NI PCIe-7852e). Data were acquired at a rate of *ca.* 516 μs per point (resulting from a 4 μs sampling time and averaging of 129 sample points). The nanopipette was approached to the surface at a rate of 3 μm s^{-1} at each pixel until the desired set point of I_{tip} was achieved (*i.e.* a decrease of 4.1 % between the bulk and surface, herein) and immediately pulled back to the desired distance. After holding in this position for 40 ms, during which time the substrate potential was switched, the tip was retracted away from the surface and moved to the next pixel where the process was repeated.

5.3.4 FEM Simulations

Finite element method (FEM, COMSOL Multiphysics v5.2a) simulations were employed to explore the experimental observations, where SICM was applied for the

electrochemical mapping of single Au nanoparticles (NPs) within an ensemble, to explain the influence of tip bias on I_{tip} and the halo effect discussed in the Results and Discussion. Simulations of an array of 9 equally spaced NPs with varying spacing distances were also performed in order to gauge how the particles separation affects the ionic current response. A schematic of an example simulation domain is shown in Figure 5.1.

For the case shown in Figure 1A, the boundary conditions applied are shown in Table 5.1. The nanopipette geometry, used in the FEM simulations, was determined by TEM imaging of nanopipettes utilized in the experiments (Figure 5.2).[48] 30 mM NaOH and 3 mM $NaBH_4$ was present in both the nanopipette domain and the bulk solution. In all simulations, a representation of the reaction was applied by applying the following fluxes to the NP boundaries:

$$\boldsymbol{j_{OH^-} = -8k[OH^-][BH_4^-]}$$

$$\boldsymbol{j_{BH_4^-} = -k[OH^-][BH_4^-]} \qquad \text{eq (5.1)}$$

$$\boldsymbol{j_{BO_2^-} = k[OH^-][BH_4^-]}$$

where k is the (potential-dependent) apparent heterogeneous electron transfer rate constant, and $[OH^-]$ and $[BH_4^-]$ are the near interface concentrations of OH^- and BH_4^- ions respectively. The aim was not to determine the potential-dependence of k, but to provide a tool for explaining the behavior seen experimentally. For simplicity, simulations were carried out in a time-independent (steady-state) regime, which was appropriate given the aim. While a 7 μm diameter disk UME, the geometry of the CF support used herein, would not strictly achieve a steady-state on the 15 to 20 ms timescale (*i.e.* the time at which I_{tip} was calculated),[49] the reaction tends to this situation. In FEM simulations the NPs were represented as an ellipsoid, with radius (80 nm) and height (81 nm) taken to be typical values extracted from experimental SICM data.

The first simulation involved a 2D axisymmetric geometry to estimate the surface charge of the glass nanopipette in bulk solution (no influence of the surface). A parametric sweep of the charge applied to boundary, B2, of Figure 5.1A, was performed, with simulated current-voltage (*I*-*V*) data presented in Figure 5.1B.[48] It can

be seen that a surface charge, σ, of around -40 mC m^{-2}, on the glass walls, gave a good agreement with the experimental *I-V* data.

FEM simulations also allowed for the experimental working distance to be estimated. Steady-state simulations were performed to predict the ionic current response at different probe-substrate separations (Figure 5.1C) and this yielded a separation of 6 nm. The substrate was assumed to be held at approximately the potential of zero charge of the substrate upon approach and so the effects of this could be ignored.

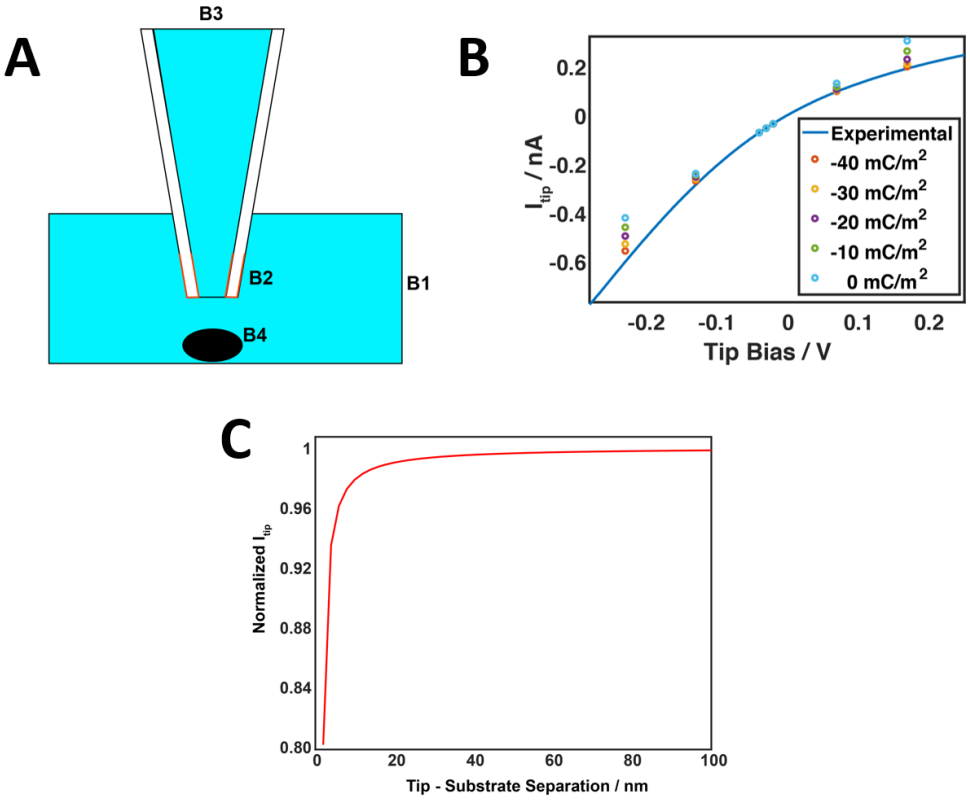

Figure 5.1 (A) A 2D Schematic representation of the FEM simulation domain with boundary descriptions shown in Table 5.1. All other boundaries not explicitly labeled were set as no flux boundaries. (B) Simulated *I-V* curved with varying surface charge on the nanopipette walls together with the experimental data for the nanopipette used for reaction mapping experiments, with the nanopipette positioned in bulk solution. Note that the geometry of the nanopipettes were consistent according to the TEM characterization of multiple nanopipettes, and the average current magnitude at V_{tip} of +0.15 V yielded 188 pA with a standard deviation of 7 pA (N = 4). (C) Simulated

SICM approach curve (tip-substrate separation *versus* normalized I_{tip}) with the solution conditions as in the experiments.

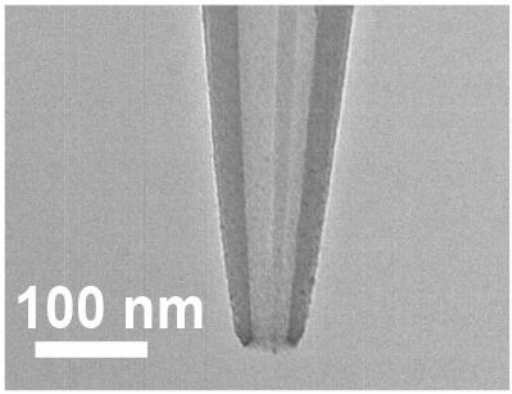

Figure 5.2 Transmission electron microscopy (TEM) image of a representative nanopipette with a tip diameter of approximately 30 nm.

Table 5.1 FEM boundary conditions for simulation geometry depicted in Figure 5.1.

Boundary	Conditions
B1	V = 0, $[OH^-]$ = 30 mM, $[Na^+]$ = 33 mM, $[BH_4^-]$ = 3 mM
B2	σ = -40 mC/m^2
B3	V = 0.1 V, $[OH^-]$ = 30 mM, $[Na^+]$ = 33 mM, $[BH_4^-]$ = 3 mM
B4	$\boldsymbol{j}_{OH^-}$, $\boldsymbol{j}_{BH_4^-}$,$\boldsymbol{J}_{BO_2^-}$, $\boldsymbol{j}_{H_2O}$
B5	inert substrate and its boundary condition

5.4 Results and Discussion

5.4.1 Electrochemical SICM Operating Principles

Salient experimental details are given in a section at the end of the paper, but to understand the approach, it is necessary to outline key features of the SICM protocol developed. The strategy implemented allows a detailed correlation between structure (topography) and function (electrochemical reactivity) at the nanoscale. Figure 5.3A provides a schematic illustration of the experimental setup.[44] Briefly, electrochemical control of the substrate (working) electrode potential was achieved with a potential V_{sub} (variable) applied with respect to a quasi-reference counter electrode (QRCE) in the bulk electrolyte/reactant solution, denoted QRCE1, producing the substrate current (I_{sub}). QRCE1 was biased at a potential of $-V_{tip}$ with respect to ground, for the ion-conductance measurements with the SICM tip, *via* QRCE2 (at ground) inside a quartz nanopipette (filled with the same solution as the bulk; *vide infra*). The bias, V_{tip}, resulted in an ion conductance current (I_{tip}), which was monitored throughout the scanning process and was used to both position the tip above the substrate (*i.e.* to obtain topographical data) and probe ion fluxes in the vicinity of the surface induced by an electrochemical reaction (*i.e.* electrocatalytic activity data). A representative TEM image of a nanopipette probe is shown in Figure 5.2. It has an inner diameter of ≈30 nm.

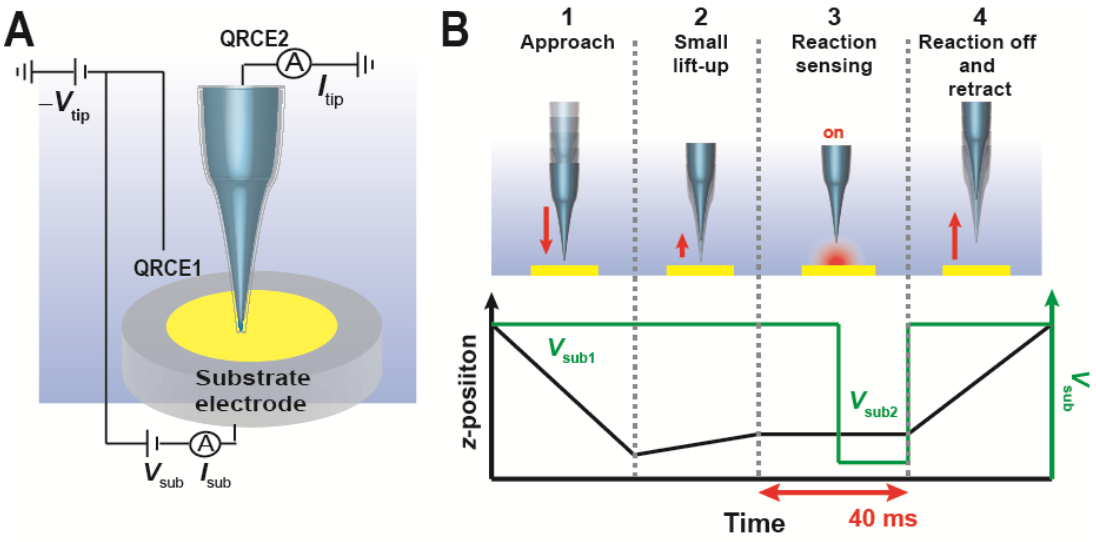

Figure 5.3 (A) Schematic of the experimental setup used for simultaneous topographical/electrochemical mapping of a substrate electrode using SICM. (B) Shown at the top are schematics of the main features of the imaging procedure during the hop motion of the probe (numbered 1 to 4) at each pixel. A trace of *z*-position and V_{sub} during each step is shown at the bottom. The overall procedure can be summarized as follows: (1) approach towards the substrate surface under DC ionic current feedback to reach the set point distance; (2) small retract ("small lift-up"); (3) waiting time of 20 ms followed by potential step by jumping V_{sub} from V_{sub1} to V_{sub2}; and (4) full retract before the hop procedure is repeated at the next pixel, typically 20 nm lateral displacement from the previous one. The tip current, measured throughout, was analyzed as discussed in the text.

A direct current (DC) hopping mode with self-referencing was implemented. I_{tip} was measured throughout the entire imaging process every 4 μs with 129 points averaged to give a data point every 516 μs, as the probe was approached from bulk solution to the surface at each lateral position (pixel).[29,39] When surface charge (double layer) effects are negligible, I_{tip} decreases appreciably as the tip is approached within a distance of about one tip diameter from the surface.[38] This was a reasonable consideration for the studies herein, given the electrolyte concentration, tip/substrate separation and V_{sub} of 0.00 V *vs.* Pd-H_2 QRCE on approach, which is close to the potential of zero charge of Au at high pH.[50] A feedback threshold, or set point, of I_{tip} corresponding to a decrease of 4.1 % between the bulk and surface was set, and the tip-substrate separation distance on approach estimated from the measured I_{tip} value

(Figure 5.4), which was used in FEM simulations to estimate the actual separation distance. For surfaces that were planar on the scale of the nanopipette probe opening, *i.e.* over the UME and even over the top of nanostructures, the final I_{tip} value herein, during approach, corresponded to a closest tip-substrate separation distance of approximately 6 nm, slightly closer to the surface than the target due to the intrinsic response latency of the piezo and control system.[35] This end position of the nanopipette at each approach (*z*-extension) was used to construct high resolution 3D topographical maps (*e.g.* Figure 5.3B, part (1)). It is important to note that SICM approach curves to a curved or tilted surface, *e.g.* over a NP edge, would yield a different separation distance to those performed over a flat surface. Such a situation is quite rare in an image, but still taken into account in FEM simulations performed, as the working distance is calculated based on the experimental final value of I_{tip}. For clarity, where probe-substrate separation distances are quoted herein, these correspond to the distance, which would be achieved above the top of a nanostructure and planar surface.

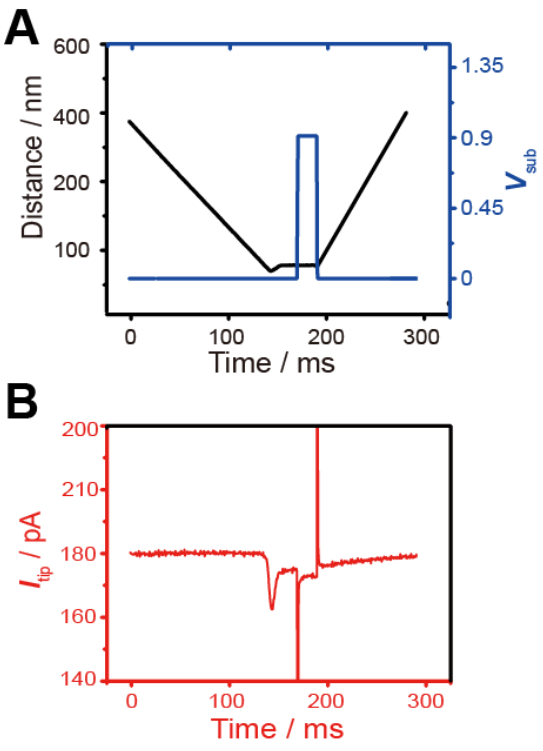

Figure 5.4 (A) Plots of *z*-position (black trace) and substrate electrode potential (V_{sub}) (blue trace) vs. time, showing the protocol utilized during each hop (pixel-level measurement) of a typical imaging experiment. (B) The corresponding tip current (I_{tip}) *vs* time plot, recorded simultaneously with (A).

Upon detecting the near surface (reaching the target set point), the nanopipette immediately retracted a fixed distance (*vide infra*), which is called as a "small lift-up" (typically 20 nm, but varied in some experiments) herein, a distance at which the measurements of electrochemical activity were obtained (Figure 5.3B, part (2)). This step was implemented to: (i) minimize the impact of the probe on mass-transport at the substrate (*i.e.* physical blockage of the surface reaction flux by the tip); (ii) minimize any effects of the electrical double layer on the recorded response, especially when rapidly changing the substrate potential with time (*vide infra*); while (iii) maintaining high spatial and time resolution for electrochemical image acquisition, by measuring electrocatalytic ion fluxes at sufficiently close distances to the surface (*vide infra*). The distance between the tip and the substrate during the electrochemical measurement ($d_{s\text{-}t}$) is the sum of the estimated tip distance from the initial approach curve (*i.e.* 6 nm) and the distance of "small lift-up" set by the operating program.

After lift-up, a potential step of the V_{sub} was applied after a waiting period of 20 ms. The substrate potential was jumped from V_{sub1}, where no (electrochemical) reaction occurred at the substrate, to V_{sub2}, where the electrocatalytic reaction was "switched on", typically for just 20 ms at each pixel (see Figure 5.3B, part (3)). This is an advantageous feature of this technique, serving to reduce any possible deterioration in the surface activity that could be caused by prolonged turnover of the reactant on the catalyst surface.[51,52] For the maps of electrochemical activity presented herein, up to 3136 pixels were recorded, meaning that the reaction was only "on" for about one minute (62.72 seconds). On this timescale, there was typically only 4 % random variation in I_{sub} with respect to the average I_{sub} when the reaction was "on". For the data presentation in the images herein, I_{tip} measured when the substrate reaction was "on" was normalized with respect to I_{tip} when reaction was "off". This is denoted by $I_{tip}(V_{sub2})/I_{tip}(V_{sub1})$ and referred to as "normalized I_{tip}" throughout. $I_{tip}(V_{sub1})$ was the average value of the last 5 ms at V_{sub1} before the step in potential to V_{sub2} and $I_{tip}(V_{sub2})$ was measured over the last 5 ms of the 20 ms potential step, so as to minimize any influence of non-faradaic (charging) and non-steady state effects at short times. Note that the substrate reaction is not at true steady-state during this period, but tends towards this situation (*vide infra*). Some transient tip current data are also presented, such as in Figure 5.4, which gives an example I_{tip}-time trace, together

with the corresponding change in tip-substrate distance and V_{sub} during a single pixel measurement.

Prior to approach at the next pixel, the nanopipette was rapidly withdrawn into bulk to a distance between 400 nm and 1.2 μm, depending on the sample roughness (Figure 5.3B, part (4)). Overall, the procedure resulted in a pixel acquisition time of around 0.3 s pixel^{-1} (Figure 5.4), allowing relatively high electrochemical (and topographical) image acquisition (mapping) rates: typical scans of 2600 pixels μm^{-2} (3136 pixels in a scan area ≈ 1.2 μm^2) took approximately 15 minutes. It is important to note that, while higher imaging scan rates are certainly possible in SICM experiments,[35,44,53] these typically only consider SICM for topographical measurements. The inherent nature of making functional (electrochemical) measurements with SICM means that in most cases, longer exposure times of the tip near the surface are required.

5.4.2 Electrochemical Mapping on UMEs

BH_4^- electro-oxidation on an Au surface in alkaline media was selected as the model electrocatalytic process. 3 mM $NaBH_4$ with 30 mM NaOH (pH 12.5) electrolyte solution was used for the experiments to ensure that the pH was greater than 12 and that the $[OH^-]/[BH_4^-]$ ratio was greater than 4.4, which has been shown to suppress the chemical hydrolysis process, which consumes BH_4^- and releases H_2.[54,55] The net reaction for borohydride electro-oxidation is as follows:

$$BH_4^- + 8OH^- \rightarrow BO_2^- + 6H_2O + 8e^- \qquad \text{eq (5.2)}$$

where for each BH_4^- oxidized, 8 OH^- ions are consumed from the electrolyte in an overall 8-electron process. This model inner-sphere reaction is known to be sensitive to the type[51,56] and surface crystallographic orientation of the metal electrode.[7,57] Additionally, it is worth noting that this reaction is of practical importance, as it is the anodic process in direct borohydride fuel cells.[51,56]

Linear sweep voltammetry in the configuration shown in Figure 5.3, performed at an Au ultramicroelectrode (UME) substrate (≈ 10 μm, diameter), with Pd-H_2 QRCE1, showed the characteristic BH_4^- electro-oxidation response expected in alkaline media (Figure 5.5A and B, black solid line). In agreement with previous

studies,[47,58] the substrate current begins to increase near a potential of 0.1 V due to the oxidation of BH_4^-, reaching a plateau in the potential range from 0.6 V to 1.1 V. Note that the linear sweep voltammograms (LSVs) shown in Figure 5.5A and B were measured on different Au UMEs at different times, resulting in the slight difference in the magnitude of the oxidation current. At a potential of 1.1 V, an AuO_x monolayer starts to form on Au, passivating the surface and "switching off" the BH_4^- oxidation reaction, resulting in a rapid decrease in current with the ongoing anodic potential scan.[47,58] As the voltage was swept further positive (from 1.4 V to 1.8 V), the substrate current again began to slowly increase, attributable to the gradual formation of an AuO_x multilayer.[59]

I_{tip} was also monitored simultaneously during the voltage sweep at two different tip electrode potential biases (QRCE2), V_{tip}, with respect to QRCE1. For this purpose, a nanopipette was centered on the Au electrode with $d_{s\text{-}t}$ of 26 nm (Figure 2A and B, blue and red solid lines). When the QRCE2 (in the tip) was biased *positively* at 0.15 V (relative to QRCE1 in bulk) throughout the substrate voltage sweep, I_{tip} was found to be extremely sensitive to the substrate electrochemical reaction (Figure 5.5A). The consumption of OH^- at the Au substrate leads to a significant change in ionic strength near the surface that is manifested as a decrease in normalized I_{tip}, which tracks the changes in I_{sub} very faithfully. In contrast, when the tip was biased *negatively* at -0.35 V, I_{tip} was seen to be insensitive to the substrate reaction (Figure 5.5B).[60] Note that the bias on the tip has little influence on the substrate UME voltammetric characteristics. This was also confirmed by measuring the voltammetric behavior without the SICM tip present, which were as reported by us earlier.[47] Note that although QRCE2 could, in principle, act as a counter electrode for the substrate reaction (especially when biased negative with respect to QRCE1), the narrow dimensions of the nanopipette means that this is a very resistive path and so the counter current for the substrate reaction flows through QRCE1. These initial experiments demonstrate that the SICM tip is a relatively non-invasive probe of the substrate reaction, but one whose sensitivity depends on the tip bias.

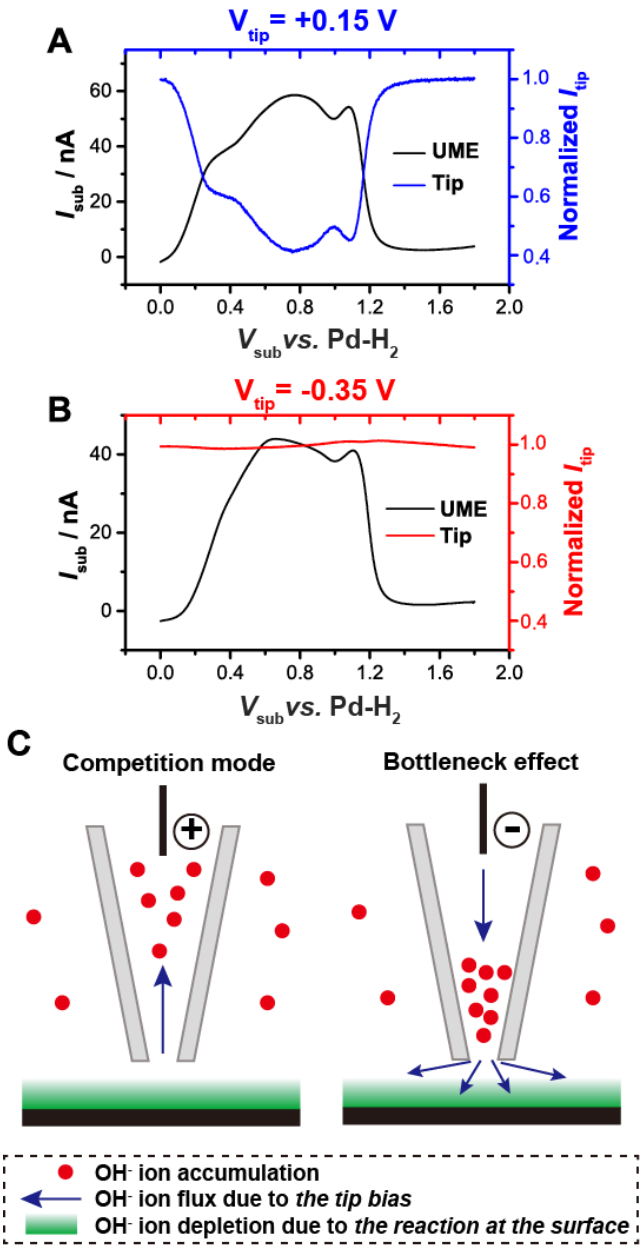

Figure 5.5 LSVs (potential sweep at V_{sub}) obtained at two individual Au UMEs (diameter ≈ 10 μm) in a solution containing 3 mM $NaBH_4$ and 30 mM NaOH with scan rate of 0.2 V s^{-1}. The substrate current (I_{sub}) and tip current (I_{tip}) were concurrently measured at fixed tip bias potentials (V_{tip}) of (A) +0.15 V and (B) -0.35 V. The SICM probe was positioned at the center of the Au UME at a vertical distance of 26 nm (*vide infra*) during the measurements. For normalization, the magnitude of I_{tip} without the substrate reaction was (A) 180 pA and (B) -850 pA. (C) Schematics (not to scale) illustrating OH^- ion accumulation and changes in the OH^- flux near the end of the nanopipette at positive (left) and negative (right) tip biases during BH_4^- oxidation.

FEM simulations were carried out to rationalize the experimental observation that I_{tip} was most sensitive to the substrate reaction with a positively biased tip. The surface charge on the nanopipette was estimated to be approximately -40 mC m^{-2}, due to the high solution pH (Figure 5.1).[48] As summarized in the schematic in Figure 5.5C, when the tip is positively biased (Figure 5.5C, left), OH^- ions (the major current carrying ion) are depleted near the end of the tip due to migration towards QRCE2 in the tip, a process that is in competition with the depletion in OH^- that occurs in the vicinity of the substrate when the electrochemical reaction is switched on. By contrast, with a negatively biased tip (Figure 5.5C, right), OH^- ions accumulate near the end of the tip, due to an asymmetry in mass-transport through the tip (slower) and away from the end (faster). This produces a "bottleneck effect", so that the conductance of the tip end (most resistive part of the circuit) is similar whether the substrate reaction is on or off. Consequently, the normalized I_{tip} value is close to unity during the scan of the substrate electrode potential as seen in Figure 5.5B.

The FEM simulation results presented in Figure 5.6 and Figure 5.7, confirm these findings: at positive tip bias, the [OH^-] profile and overall ion current reaction in the tip (and hence current in the SICM circuit) changes between a slow and fast substrate reaction, whereas at negative tip bias, the ionic concentration at the tip end is enhanced, but is essentially invariant with the rate of the substrate reaction. For reaction imaging, a positive tip bias was thus used herein, unless stated otherwise.

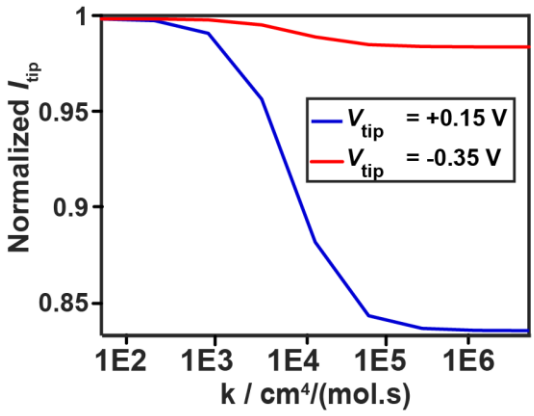

Figure 5.6 FEM simulations of normalized I_{tip} at different fixed biased potential at the tip (V_{tip}) with an increase in k at the substrate, showing higher sensitivity of I_{tip} to the reaction at *positive* V_{tip} in correspondence with the experimental results in Figure 2A and B of the main manuscript.

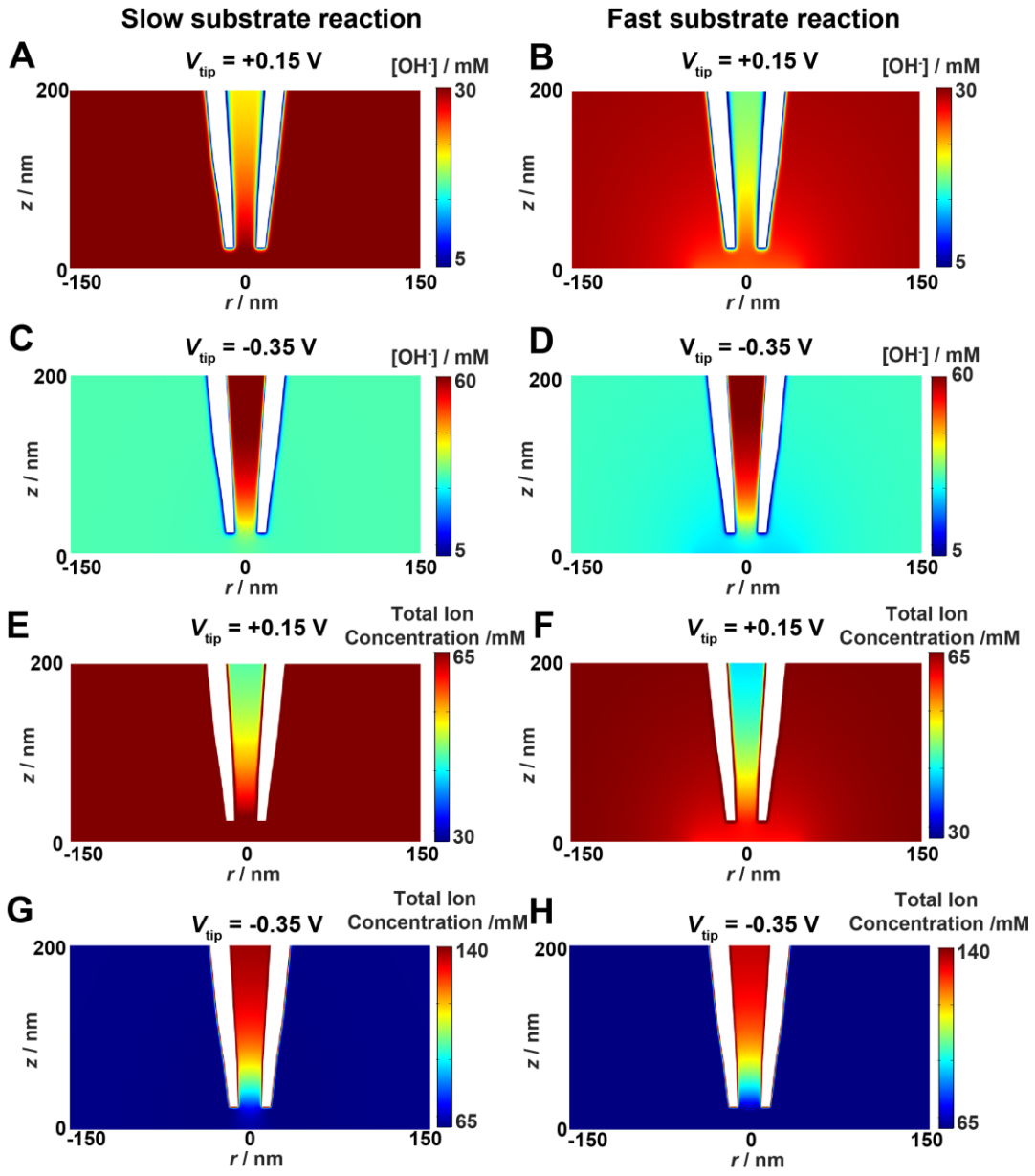

Figure 5.7 FEM simulation results of OH^- concentrations near the end of the nanopipette and above a reactive substrate at biased potential at the tip (V_{tip}) of + 0.15 V (A and B) and -0.35 V (C and D) with 'slow' and 'fast' substrate reaction, defined by k = 70 cm^4 mol^{-1} s^{-1} and $k = 1.2\times10^6$ cm^4 mol^{-1} s^{-1} respectively. Corresponding total ionic concentrations shown in E-H.

5.4.3 Tip Distance Effects in Reaction Mapping.

It was important to assess what the tip measures at different distances from the substrate and to establish the region where the tip is mainly sensitive to the substrate electrode reaction. In addition to the reactive ion fluxes as considered herein, the ionic current in SICM may be sensitive to the electrical double layer at charged substrates.[39,40,43] For electrochemical imaging, a large positive bias is applied at the substrate electrode to drive BH_4^- electro-oxidation, and therefore, the surface charge will be more positive than when the reaction is off (V_{sub} = 0 V relative to the bulk QRCE). Based on previous SICM surface charge studies,[39,40,43,61,62] at positive tip bias, this would be expected to result in an enhanced tip current, whereas the tip current decreases when the substrate reaction is on (Figure 5.5A). The effect of surface charge is further extinguished the greater the tip-substrate separation.[61,62] In contrast, the change in ionic composition due to the substrate reaction extends over the concentration (diffusion) boundary layer, which is orders of magnitude larger. Thus, one can set a "near interface distance" for reaction imaging where there is a significant change in ionic strength from the substrate reaction but where the tip is insensitive to surface charge effects. Furthermore, situating the tip a little further from the substrate is also advantageous in minimizing the extent to which mass transport to the substrate is blocked by the tip.[63]

To investigate the effect of $d_{s\text{-}t}$ on the SICM response, electrochemical and topographical images of an Au UME and surrounding glass sheath were obtained at $d_{s\text{-}t}$ values of 11, 26, and 106 nm, with the resulting maps for V_{sub2} = 0.9 V (pixel density of 165 pixels μm^{-2}) shown in Figure 5.8A, B and C, respectively. The topographical maps are remarkably consistent and highlight an Au electrode that is recessed by about 300 nm compared to the surrounding glass sheath, resulting from the polishing process during UME fabrication/conditioning. In contrast, the activity maps are much more distance-dependent. Notably the activity map obtained at a $d_{s\text{-}t}$ of 11 nm (Figure 5.8A) shows a much diminished change in normalized I_{tip} between the Au substrate and glass sheath, when compared to the larger $d_{s\text{-}t}$ values of 26 nm and even 106 nm (Figure 5.8B and C). This could, in part, be due to the tip partly sensing the electrical double layer at such small probe-substrate separations (as discussed above), and/or physical blockage of the reaction flux at the surface by the

tip, as is well known in other local probe measurements of electrochemical interfaces.[63,64] In contrast, when $d_{s\text{-}t}$ is relatively large (Figure 5.8C), there is a much shallower lateral gradient in I_{tip} between the active electrode and glass insulator compared to $d_{s\text{-}t}$ = 26 nm. Consequently, a balance needs to be struck between $d_{s\text{-}t}$ being small enough to provide the desired resolution but large enough to avoid the effects seen in Figure 5.8A. As a result, $d_{s\text{-}t}$ was fixed at 26 nm for the experiments discussed further below. Additional simultaneously recorded electrochemical images and topographical obtained at $d_{s\text{-}t}$ = 26 nm, with V_{sub2} set to be either 0.3 V or 0.6 V (Figure 5.9), further demonstrate how the proposed SICM approach is sensitive to the reaction rate at the UME substrate, an aspect that the author of this thesis developed next for single NP mapping.

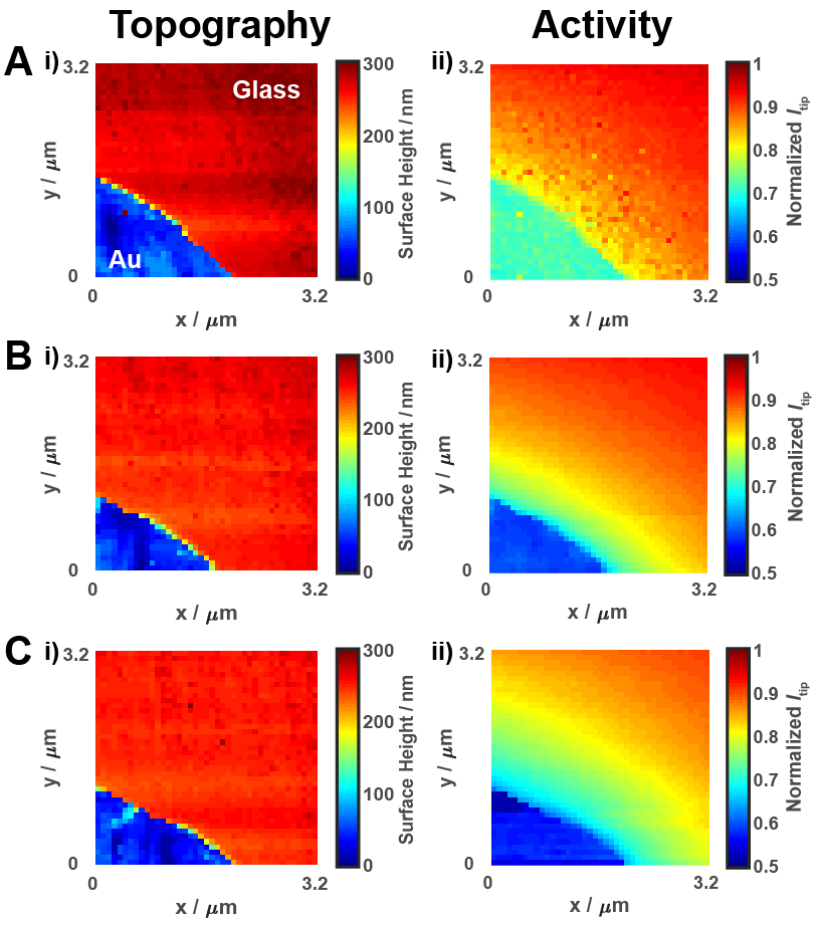

Figure 5.8 (i) SICM topography and (ii) electrochemical activity maps of an Au UME (diameter ≈ 10 μm), obtained simultaneously, in a solution containing 3 mM $NaBH_4$ and 30 mM NaOH, recorded with V_{sub2} = 0.9 V, V_{tip} = +0.15 V and $d_{s\text{-}t}$ values of (A) 11 nm, (B) 26 nm and (C) 106 nm. There is no interpolation of the data and each of the images contains 1681 pixels.

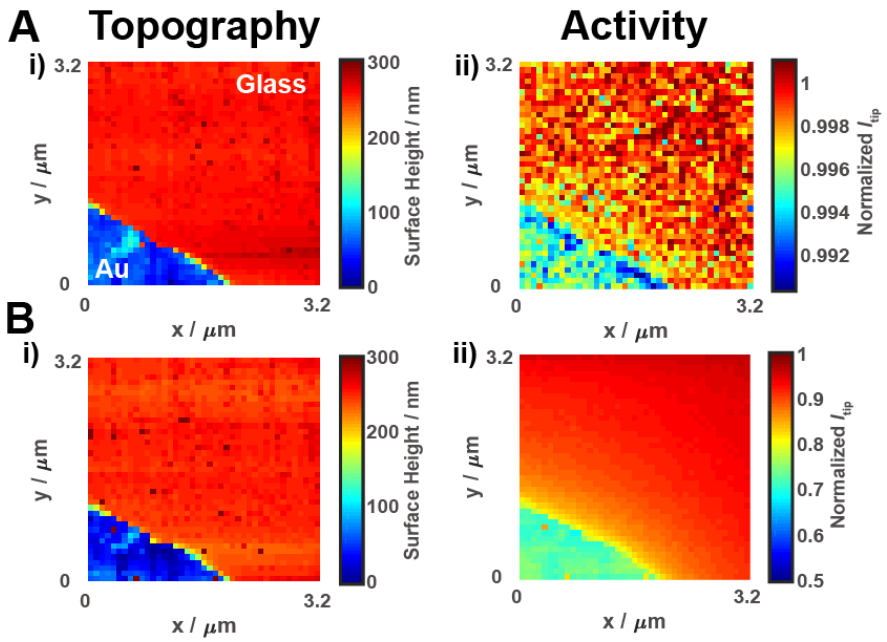

Figure 5.9 (i) SICM topography and (ii) electrochemical activity maps of a segment of an Au UME (diameter ≈ 10 μm) sealed in glass, obtained in a solution containing 3 mM $NaBH_4$ and 30 mM NaOH, recorded with $d_{t\text{-}s}$ = 26 nm, V_{tip} = +0.15 V and V_{sub2} values of (A) 0.3 V and (B) 0.6 V. There is no interpolation of the data and the images contain 1681 pixels.

5.4.4 Single NP Mapping

In contrast to Au electrodes, carbon fiber (CF) is an electrocatalytically inert material for BH_4^- electro-oxidation[52,65] (Figure 5.10A). I_{tip} (V_{tip} = +0.15V) maps of a CF UME showed no contrast between the carbon and glass surfaces, with uniform values of normalized I_{tip} close to one, in the potential range of interest, as expected for an inert substrate (Figure 5.10B and C). CF was thus a suitable support material to explore electrocatalytically active individual Au NPs and nanostructures. A CF UME with Au nanostrutures was prepared as described in Section 5.3.2. The SEM images in Figure 5.11A show that Au nanostructures were mostly deposited at the boundary between the CF and the glass sheath of the UME and that the size of the nanostructures varied from 150 nm to 800 nm, with different shapes resulting from the aggregation of small (10 - 50 nm) Au clusters. Comparison of the topographical maps [Figure 5.11B and C(i)], obtained as part of the SICM protocol, with the SEM images [Figure 5.11A(ii)] show that SICM topographical imaging (pixel density of 2600 pixels μm^{-2})

provides size information *in-situ* at a resolution and accuracy that is comparable to electron microscopy for the range of scale of nanostructures studied herein.

Two typical electrochemical activity images with V_{sub2} of 0.65 V and 0.9 V are shown in Figure 5.11B(ii) and C(ii), respectively. These maps are just 1×1.2 μm^2 and comprise 3111 pixels. The magnitude of the change in normalized I_{tip} during the electrochemical reaction on the Au nanostructures is much smaller than observed on the Au UME under comparable conditions, evident by comparing the normalized I_{tip} values in Figure 5.8B and Figure 5.11C. This is because the mass transport rate to the Au nanostructures is considerably higher than for the Au UME and so there are greater kinetic limitations at the nanostructures at the same driving force. This aspect is further evident from Figure 5.11B and C, where it can be seen that the larger Au nanostructures (bottom, approximately 800 nm largest dimension) gives rise to a more significant decrease in I_{tip} compared to two smaller Au nanostructures (middle and top, approximately 150 and 200 nm) as a result of greater depletion of the interfacial ion concentration of BH_4^- and OH^- at the larger structure.

It is important to highlight that considerable detail on local nanostructure activity can be obtained due to the high pixel density. Although there is overlap of diffusion between neighboring nanostructures, particularly at higher substrate potential, such that the activity of the large lower nanostructure dominates, it is still possible to pinpoint the active top NP, for example, [part of Figure 5.11C(ii) shown in Figure 5.11C(iii)] and its activity quite easily seen at lower substrate driving force [part of Figure 5.11B(ii) shown in Figure 5.11B(iii)].

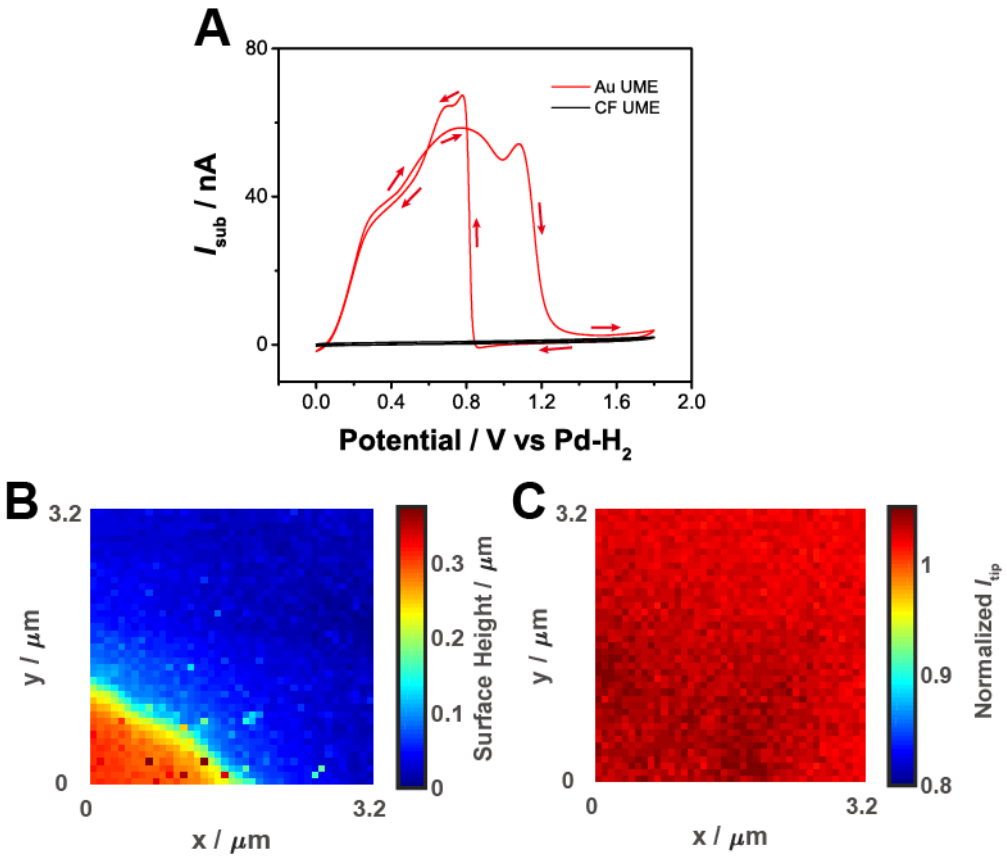

Figure 5.10 (A) Cyclic voltammograms (CVs) obtained at Au (diameter ≈ 10 μm, red trace) and CF (diameter ≈ 7 μm, black trace) UMEs in an aqueous solution containing 3 mM $NaBH_4$ and 30 mM NaOH with a scan rate of 0.2 V s^{-1}. (B) SICM topography map and (C) corresponding electrochemical activity image, obtained at the CF UME in the solution defined above with $d_{t\text{-}s}$ = 26 nm, V_{tip} = + 0.15 V and V_{sub2} = 0.9 V, showing the inactive carbon surface for BH_4^- electro-oxidation. The topography map of the UME shows that the CF (red) extends from the end of the glass support (blue), arising from the polishing process during UME fabrication/conditioning. There is no interpolation of the data and the images contain 1681 pixels.

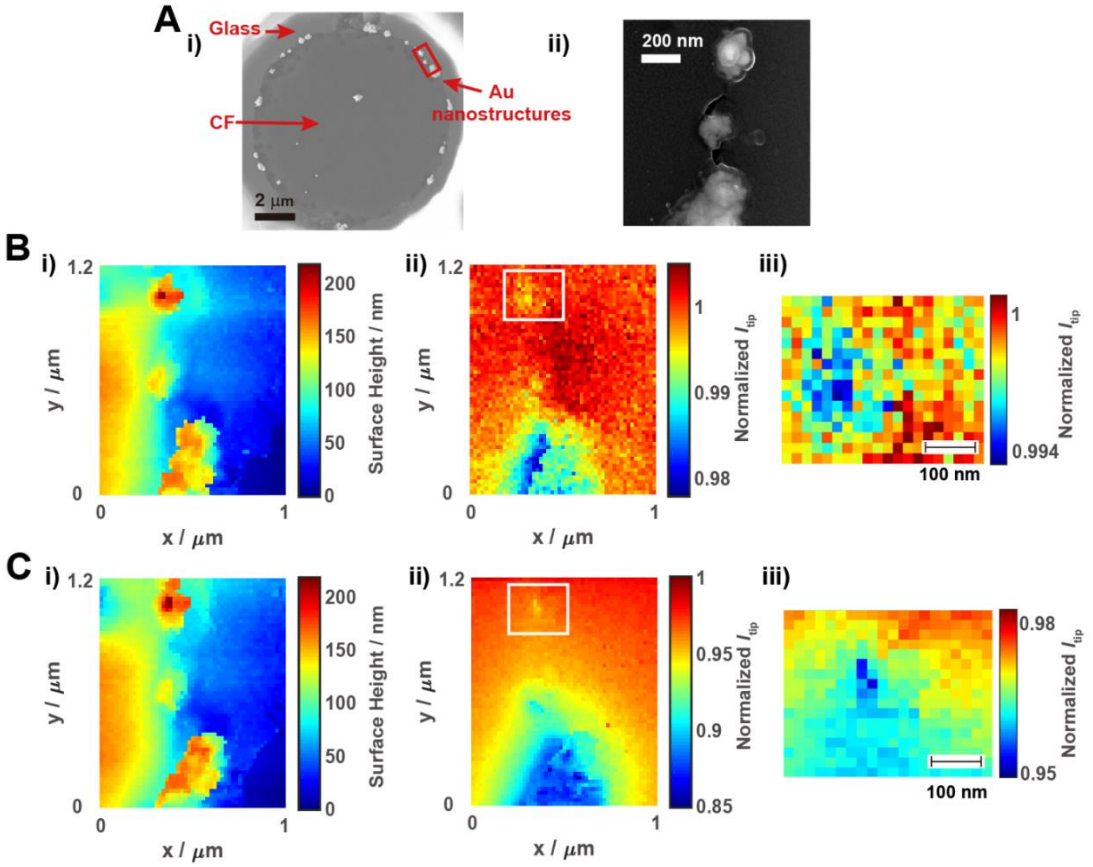

Figure 5.11 (A) SEM images of Au nanostructures on a CF UME: (i) an electron micrograph of the CF UME with deposited Au nanostructures and (ii) magnified view of the red box in (i), indicating the area imaged with SICM. (B) (i) SICM topography map and (ii) corresponding electrochemical activity image of Au nanostructures at V_{sub2} = 0.65 V. (iii) is a replotted electrochemical image of selected area in Figure 5.11B (ii); with the scale bar indicating 100 nm. (C) is identical to (B), except the data were obtained at a V_{sub2} of 0.9 V. Data were obtained in a solution containing 3 mM $NaBH_4$ and 30 mM NaOH at V_{tip} of +0.15 V, recorded with a $d_{s\text{-}t}$ value of 26 nm (when the nanopipette is positioned above the top of the particle). There is no interpolation of the data and the full SICM images each contain 3111 pixels in total. Note that the SICM image shows the CF to protrude from the glass surround (raised areas in the left of the topographical images).

A more homogenous distribution of AuNPs on a CF UME was produced as outlined in Section 5.3.2. SEM and SICM images of the resulting AuNPs are shown in Figure 5.12. Cross-sectional TEM images of individual AuNPs confirmed an ellipsoidal 3-D shape (Figure 5.13), such that there was a small gap between the AuNP

and the CF substrate support. The average height of the AuNPs (h_{NP}) characterized by cross-sectional TEM imaging was 76 ± 16 nm (N = 7). Analysis of the size distribution of the AuNPs by SEM imaging [Figure 5.12A(i)], yielded average diameters (d_{NP}) of 125 ± 15 nm (N = 160). The size distribution in the area of interest (N = 11) (*vide infra*) yielded an average d_{NP} of 128 ± 17 nm [SEM image in Figure 5.12A(ii), AuNPs in red box]. Individual particles are annotated (Figure 5.12B) for further analysis and discussion below. For comparison, SICM topographical data of the same NPs yielded an average value of d_{NP} = 136 ± 22 nm and h_{NP} = 72 ± 11 nm (N = 11) (Figure 5.12C), in excellent agreement with electron microscopy. Further, the d_{NP} values from electron microscopy within the scanned area were individually compared NP by NP with the results from SICM (Table 5.2) and, on average, the values derived from the SICM data were only slightly larger than determined by electron microscopy. It is worth highlighting that the spatial resolution achievable by SICM is such that closely spaced adjacent NPs, as shown by Au NPs "8" and "9" as well as "10" and "11" (Figure 5.12B and C), are readily resolved.

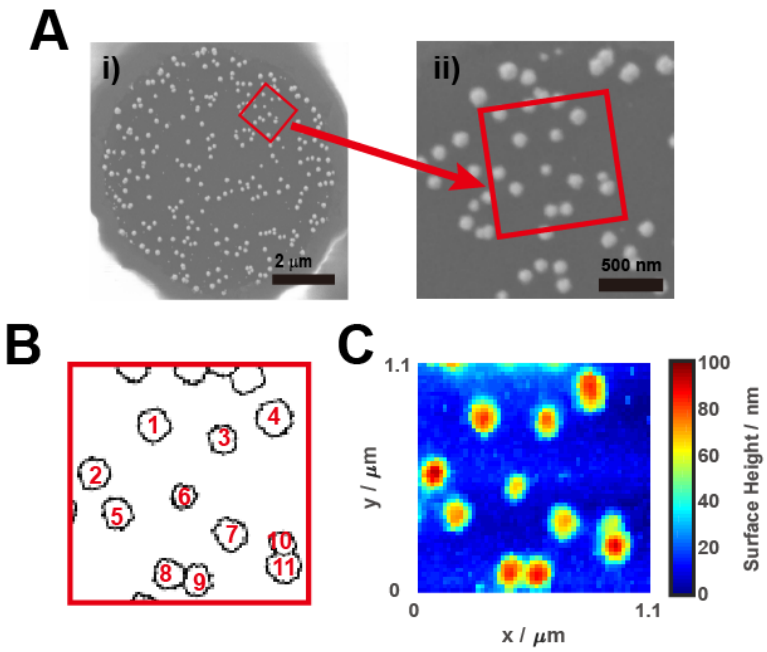

Figure 5.12 (A) SEM images of AuNPs on a CF UME: (i) a full picture of the CF UME with AuNPs and (ii) a magnified view of the red box in (i), indicating the area scanned with SICM. (B) Annotation of individual NPs from the SEM map and (C) corresponding topographical SICM data (pixel density: 2600 pixels μm^{-2}) in a solution

containing 3 mM $NaBH_4$ and 30 mM NaOH at a V_{tip} of +0.15 V. There is no interpolation of the data and the SICM image contains 3136 pixels.

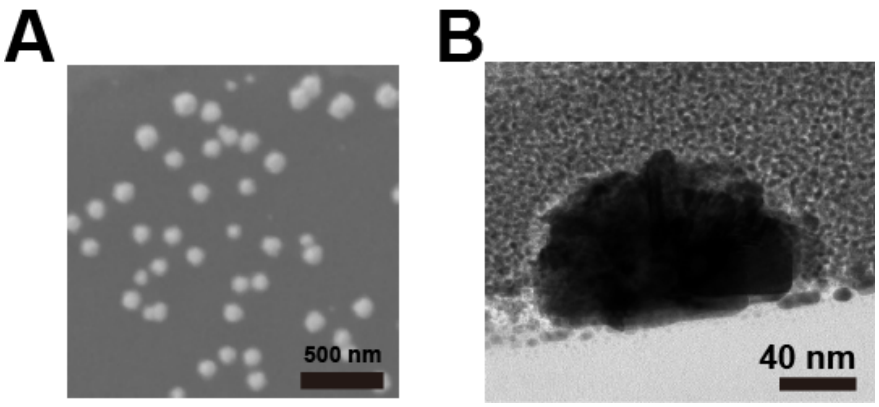

Figure 5.13 (A) SEM images of AuNPs on a CF UME, shown in the main manuscript, Figure 5. (B) A representative TEM image of the cross-section of a single AuNP. The TEM samples were prepared using FIB-SEM from the sample shown in (A).

Table 5.2 Comparison of size analysis results between SEM and SICM from Figure 5 in the main manuscript: NP numbers are annotated in Figure 5B. The particle boundary in SICM topographical data to create Table S2 was defined as a height threshold of 10 nm above the support electrode.

Particle number	NP diameter from SEM /nm	NP diameter from SICM / nm
1	141	140
2	130	140
3	118	120
4	157	160
5	114	140
6	107	100
7	130	160
8	138	140
9	126	140

10	101	100
11	145	160

Figure 5.14 shows topography (i) and activity (ii) images obtained at V_{sub2} values of (A) 0.65 V, (B) 0.75 V, (C) 0.9 V and (D) 0.95 V. Values of V_{sub2} were chosen to span a range of activity, deduced by measuring a CV (3 mM $NaBH_4$ in 30 mM NaOH aqueous solution) at the same CF UME with adhered AuNPs (Figure 5.15). Although there is a small amount of drift between each image, it is clear that a similar area is scanned at each V_{sub2} and that there is good agreement between the topographical and electrochemical activity maps (pixel density was 2600 pixel μm^{-2}) which pinpoint the NPs in different ways.

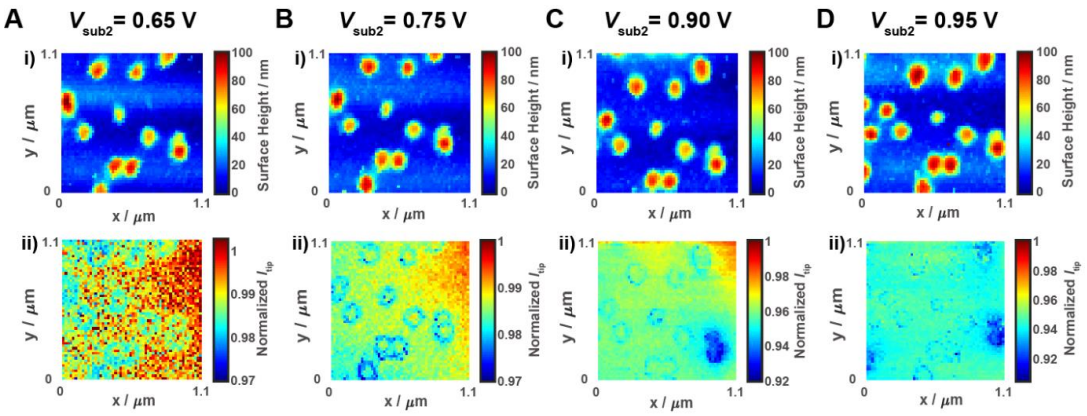

Figure 5.14 (i) SICM topography maps and (ii) simultaneously recorded activity images of AuNPs on a CF UME (diameter = 7 μm) (pixel density: 2600 pixels μm^{-2}), obtained in a solution containing 3 mM $NaBH_4$ and 30 mM NaOH, at V_{sub2} values of (A) 0.65 V, (B) 0.75 V, (C) 0.9 V and (D) 0.95 V. During mapping, V_{tip} and $d_{s\text{-}t}$ were fixed at +0.15 V and 26 nm, respectively. There is no interpolation of the data and the images contain 3136 pixels.

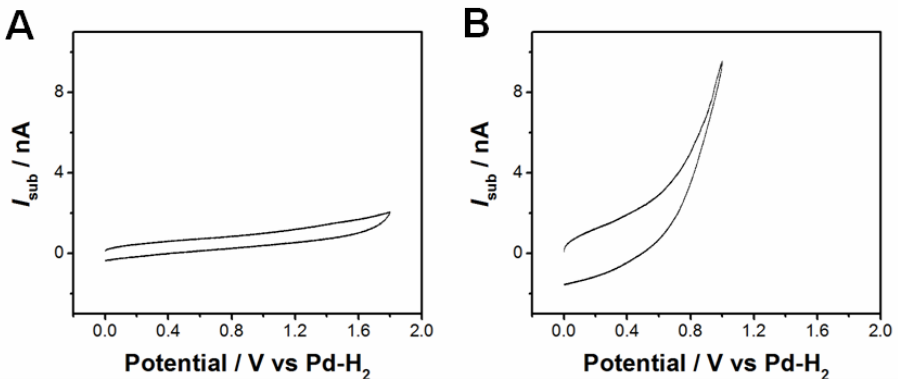

Figure 5.15 CVs obtained at (A) a CF UME (diameter ≈ 7 μm) and (B) a CF UME with electro-deposited AuNPs (Figure 5.12A) in a solution containing 3 mM $NaBH_4$ and 30 mM NaOH with a scan rate of 0.1 V s^{-1}. The CVs were obtained before the SICM mapping and the potential, for Figure 5.15B, was not fully swept to 1.7 V to avoid surface oxidation/reduction of Au, which would modify the surface of the AuNPs.[59]

Considering the diffusion coefficient of BH_4^- ($D_{BH_4^-} = 1.6 \times 10^{-5}$ cm^2 s^{-1})[55] and that I_{tip}, values are the average of the last 5 ms of a 20 ms V_{sub2} pulse, the corresponding diffusion length is *ca.* 6-8 μm [$\approx (2Dt)^{1/2}$].[66] This is of the order of the diameter of the UME substrate, which as a rule of thumb is a reasonable approximation for the characteristic diffusion-layer thickness under steady-state conditions. On this timescale, the diffusion-limited current at a UME of this size is only about 20 % higher than the true steady-state value.[49] There is thus significant overlap between the concentration boundary layers of neighboring NPs. Nonetheless, contrast between individual AuNPs can still be observed in the activity images, especially those obtained at lower overpotentials, due to the uneven particle distribution over the CF surface (see Figure 5.11A and 5.11B). Toy simulations of arrays of NPs, with varying separation distances (Figure 5.16) bear out the expectation: for the same NP reaction kinetics, with arrays of particles that are more bunched (higher NP density), a stronger

depletion of ionic reactants occurs, and hence a lower normalized I_{tip} is expected, as is seen in Figure 5.14.

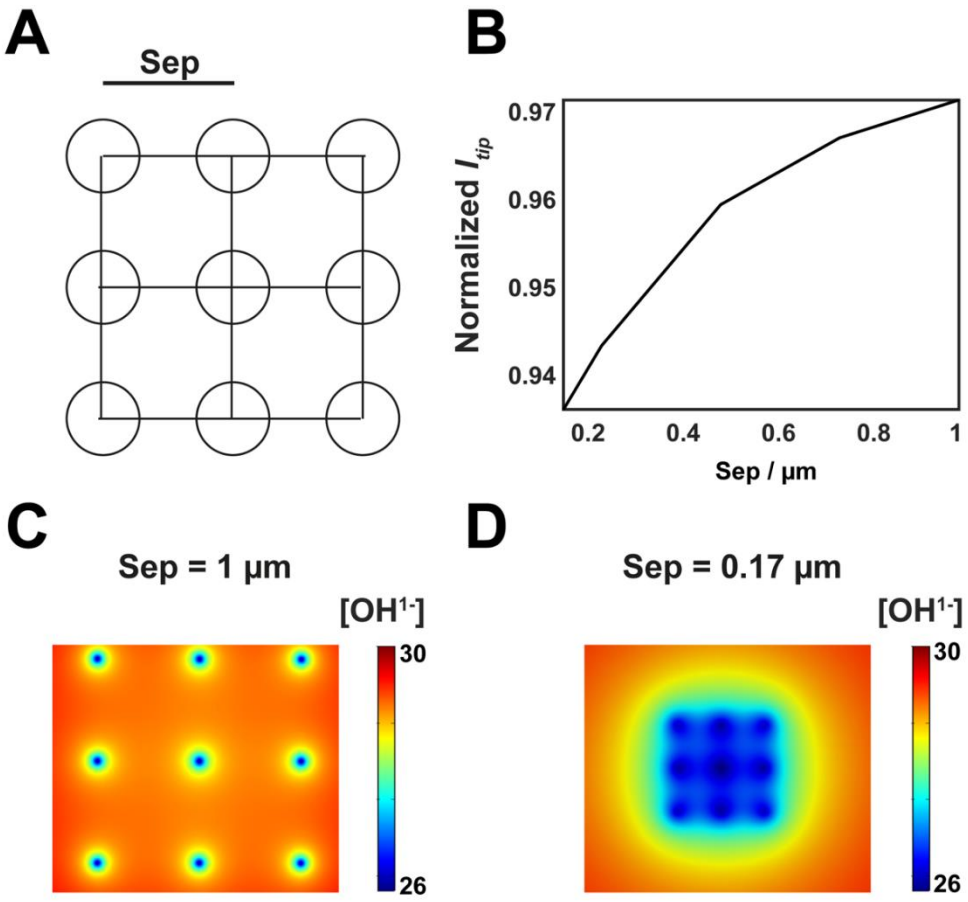

Figure 5.16 (A) Array of NPs on surface separated by distance *Sep*. (B) Effect of separation distance on predicted normalized current above the central particle. (C) OH^- concentration along the bottom plane of the simulation domain showing little overlap between the particles when separated by 1 µm. (D) OH^- concentration along the bottom plane of the simulation domain showing a strong overlap between the particles when separated by 0.17 µm. The value of k was 2.4×10^4 cm^4 mol^{-1} s^{-1} in each simulation.

It should also be noted that at applied potentials of 0.9 and 0.95 V, the AuNPs annotated as "10" and "11" (Figure 5.12B) were seen to have a distinctly high apparent electrochemical activity (*i.e.* low measured normalized I_{tip}) when compared to the other AuNPs ("1-9"). It is unlikely this is simply attributable to their size (Figure 5.16), as similarly sized and spaced Au NPs "8" and "9", adjacent to each other did not show such an enhancement of activities. As the electro-oxidation of BH_4^- on Au is surface

sensitive, it is possible that surface sites that are more favorable to the reaction are more exposed on particles "10" and "11" (*i.e.* there is a legitimate difference in electrocatalytic activity).[7,57] In the future, it could be interesting to further resolve the crystallographic structure/orientation of these surfaces, *e.g.*, using *in-situ* electrochemical STM,[32] although such measurements are challenging, or *ex-situ* using selected area electron diffraction of well-defined crystalline NPs.[67]

At the lower values of applied V_{sub2} (Figure 5.14A and B-ii), there is a noticeable ring shape of lower tip current around the NPs than on the NP top surfaces. To understand this prominent effect, FEM simulations were performed on a single NP, assuming a uniform rate constant (and a first order reaction in both [OH^-] and [BH_4^-] for simplicity) over the NP surface (assumed to be ellipsoidal). Full details of the performed simulations are presented in the Materials and Methods, and some of the key results are shown in Figure 5.17. Figure 5.17A and B present profiles of the total ionic concentration around a NP at slower and faster kinetics, respectively. Analogous to what is seen experimentally (Figure 5.14), there is an increased depletion of the local ion concentration observed as the system switches from low to high driving force, which would be manifested as a decreased normalized I_{tip} as seen experimentally (Figure 5.14).

Notably, when the kinetics of BH_4^- oxidation are slow at the NP (Figure 5.17A), there is more depletion of ionic reactants in the narrow gap between the NP and the surface, compared to the top surface of the NPs, as also seen experimentally at lower potentials (*i.e.* the ring shapes in the electrochemical activity maps in Figure 5.14). The ring effect is less apparent at higher driving force as depletion around the entire particle becomes more significant (Figure 5.17B, D and F), as also seen experimentally (Figure 5.14). The effect observed around the NP at lower overpotential is a mass transport/geometry effect: the narrow gap between the NP and surface restricts mass transport and so there is more depletion of reactants. These results provide direct visual demonstration supporting previous studies of similar effects proposed for hierarchically structured nanomaterials,[68–70] and serve to highlight major perspectives on the different overall activity that prevails on different parts of a NP.

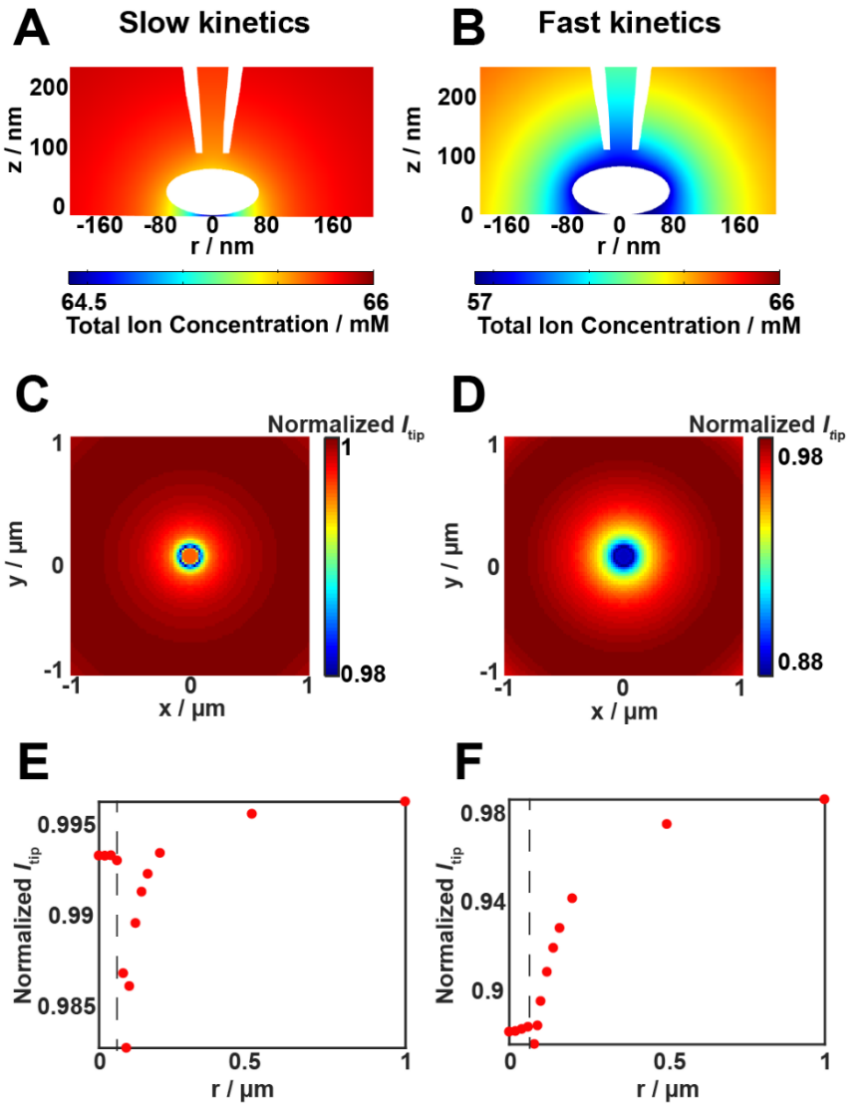

Figure 5.17 FEM simulations of an isolated NP with BH_4^- oxidation at two different heterogeneous rate constant (*k*) (*i.e.* 3.4×10^3 cm^4 mol^{-1} s^{-1} (low) and 1.2×10^6 cm^4 mol^{-1} s^{-1} (high)). Total ion concentration profiles (A and B) showing how the ion concentration around a NP (and at the end of the tip) changes with the reaction rate. (C and D) predicted tip current profiles around the NP showing the same ring effect observed experimentally at low *k*, in particular. (E and F) show simulated tip current *versus* radial direction profiles with the nanopipette tracing the NP or substrate at a distance corresponding the approach current threshold and the small lift up (*i.e.* 26 nm when over the particle centre) at low and high *k*, respectively. (C-F) highlight the 'ring effect' in the activity around the NP, notably at low *k*.

5.5 Conclusions

A procedure for electrochemical (reaction) imaging at the nanoscale has been introduced by using a simple single channel SICM tip. Through careful control of the substrate potential-time profile, and continuous recording of the SICM tip current at high frequency during the imaging process, it is possible to map *topography and electrochemical activity simultaneously*. The small nanopipette probe (30 nm diameter used herein) has enabled high resolution imaging at the sub-particle level, revealing how reactive flux is distributed among groups of NPs depending on the spacing and intrinsic NP activity. An important feature observed in this work, which has not been seen previously, is that the geometry of the nanomaterial with respect to the substrate (for example the narrow gap formed between AuNPs and the CF support compared to the more accessible NP top surface) plays an important role in the distribution of ion fluxes around reactive nanoentities, most noticeable at low overpotentials. These issues have been explored and explained with FEM simulations that support the experimental results.

The studies herein demonstrate SICM as an important technique to study electrochemical activity and ion fluxes, and the correlation of activity to the structure and morphology of nanomaterials. One could envisage future wide applications to study nanomaterials used for rechargeable/renewable energy and in electrochemical sensors, among other applications. The SICM regime described herein is easily implemented and has a number of advantages compared to other SEPMs, not least: (i) a very simple tip fabrication and characterization procedure; (ii) a tip response that is very stable and whose status is checked at *each and every pixel* (and self-referenced); and (iii) the possibility of obtaining images on a reasonably fast timescale.

5.6 References

(1) Perreault, F.; Fonseca de Faria, A.; Elimelech, M. *Chem. Soc. Rev.* **2015**, *44* (16), 5861–5896.

(2) Chen, A.; Chatterjee, S. *Chem. Soc. Rev.* **2013**, *42* (12), 5425–5438.

(3) Trogadas, P.; Ramani, V.; Strasser, P.; Fuller, T. F.; Coppens, M. O. *Angew. Chemie - Int. Ed.* **2016**, *55* (1), 122–148.

(4) Raccichini, R.; Varzi, A.; Passerini, S.; Scrosati, B. *Nat. Mater.* **2015**, *14* (3), 271–279.

(5) Kleijn, S. E. F.; Lai, S. C. S.; Koper, M. T. M.; Unwin, P. R. *Angew. Chemie - Int. Ed.* **2014**, *53* (14), 3558–3586.

(6) Wu, J.; Yang, H. *Acc. Chem. Res.* **2013**, *46* (8), 1848–1857.

(7) Rodriguez, P.; Koper, M. T. M. *Phys. Chem. Chem. Phys.* **2014**, *16* (27), 13583–13594.

(8) Sambur, J. B.; Chen, P. *Annu. Rev. Phys. Chem.* **2014**, *65* (1), 395–422.

(9) Oja, S. M.; Fan, Y.; Armstrong, C. M.; Defnet, P.; Zhang, B. *Anal. Chem.* **2016**, *88* (1), 414–430.

(10) Xiao, X.; Bard, A. J. *J. Am. Chem. Soc.* **2007**, *129* (31), 9610–9612.

(11) Li, Y.; Cox, J. T.; Zhang, B. *J. Am. Chem. Soc.* **2010**, *132* (9), 3047–3054.

(12) Wilson, A. J.; Willets, K. A. *Nano Lett.* **2014**, *14* (1), 939–945.

(13) Sambur, J. B.; Chen, T.-Y.; Choudhary, E.; Chen, G.; Nissen, E. J.; Thomas, E. M.; Zou, N.; Chen, P. *Nature* **2016**, *530* (7588), 77–80.

(14) Willets, K. A.; Wilson, A. J.; Sundaresan, V.; Joshi, P. B. *Chem. Rev.* **2017**, *117* (11), 7538–7582.

(15) Kang, M.; Momotenko, D.; Page, A.; Perry, D.; Unwin, P. R. *Langmuir* **2016**, *32* (32), 7993–8008.

(16) Actis, P.; Tokar, S.; Clausmeyer, J.; Babakinejad, B.; Mikhaleva, S.; Cornut, R.; Novak, P.; Shevchuck, A. I.; Dougan, J. A.; Schuhmann, W.; Klenerman, D.;

Rusakov, O. D. A.; Sviderskaya, E. V; Korchev, Y. E. *ACS Nano* **2014**, *8* (1), 875–884.

(17) Thakar, R.; Weber, A. E.; Morris, C. A.; Baker, L. A. *Analyst* **2013**, *138* (20), 5973–5982.

(18) Blanchard, P. Y.; Sun, T.; Yu, Y.; Wei, Z.; Matsui, H.; Mirkin, M. V. *Langmuir* **2016**, *32* (10), 2500–2508.

(19) Yu, Y.; Sun, T.; Mirkin, M. V. *Anal. Chem.* **2015**, *87* (14), 7446–7453.

(20) Kim, J.; Renault, C.; Nioradze, N.; Arroyo-Currás, N.; Leonard, K. C.; Bard, A. J. *J. Am. Chem. Soc.* **2016**, *138* (27), 8560–8568.

(21) Unwin, P. R.; Güell, A. G.; Zhang, G. *Acc. Chem. Res.* **2016**, *49* (9), 2041–2048.

(22) Lai, S. C. S.; Dudin, P. V.; MacPherson, J. V.; Unwin, P. R. *J. Am. Chem. Soc.* **2011**, *133* (28), 10744–10747.

(23) Momotenko, D.; Byers, J. C.; McKelvey, K.; Kang, M.; Unwin, P. R. *ACS Nano* **2015**, *9* (9), 8942–8952.

(24) Güell, A. G.; Meadows, K. E.; Dudin, P. V.; Ebejer, N.; Macpherson, J. V.; Unwin, P. R. *Nano Lett.* **2014**, *14* (1), 220–224.

(25) Chen, C. H.; Jacobse, L.; McKelvey, K.; Lai, S. C. S.; Koper, M. T. M.; Unwin, P. R. *Anal. Chem.* **2015**, *87* (11), 5782–5789.

(26) Kranz, C.; Friedbacher, G.; Mizaikofft, B.; Lugstein, A.; Smoliner, J.; Bertagnolli, E. *Anal. Chem.* **2001**, *73* (11), 2491–2500.

(27) Macpherson, J. V; Unwin, P. R. **2000**, *72* (2), 276–285.

(28) O'Connell, M. A.; Lewis, J. R.; Wain, A. J. *Chem. Commun.* **2015**, *51* (51), 10314–10317.

(29) Page, A.; Kang, M.; Armitstead, A.; Perry, D.; Unwin, P. R. *Anal. Chem.* **2017**, *89*, 3021–3028.

(30) Takahashi, Y.; Shevchuk, A. I.; Novak, P.; Zhang, Y.; Ebejer, N.; MacPherson, J. V.; Unwin, P. R.; Pollard, A. J.; Roy, D.; Clifford, C. A.; Shiku, H.; Matsue, T.; Klenerman, D.; Korchev, Y. E. *Angew. Chemie - Int. Ed.* **2011**, *50* (41), 9638–9642.

(31) Sklyar, O.; Treutler, T. H.; Vlachopoulos, N.; Wittstock, G. *Surf. Sci.* **2005**, *597* (1–3), 181–195.

(32) Meier, J.; Friedrich, K. A.; Stimming, U. *Faraday Discuss.* **2002**, *121*, 365–372.

(33) Takahashi, Y.; Shevchuk, A. I.; Novak, P.; Babakinejad, B.; Macpherson, J.; Unwin, P. R.; Shiku, H.; Gorelik, J.; Klenerman, D.; Korchev, Y. E.; Matsue, T. *Proc. Natl. Acad. Sci. U. S. A.* **2012**, *109* (29), 11540–11545.

(34) Kranz, C. *Analyst* **2014**, *139* (2), 336–352.

(35) Novak, P.; Shevchuk, A.; Ruenraroengsak, P.; Miragoli, M.; Thorley, A. J.; Klenerman, D.; Lab, M. J.; Tetley, T. D.; Gorelik, J.; Korchev, Y. E. *Nano Lett.* **2014**, *14* (3), 1202–1207.

(36) Lipson, A. L.; Ginder, R. S.; Hersam, M. C. *Adv. Mater.* **2011**, *23* (47), 5613–5617.

(37) Lipson, A. L.; Puntambekar, K.; Comstock, D. J.; Meng, X.; Geier, M. L.; Elam, J. W.; Hersam, M. C. *Chem. Mater.* **2014**, *26* (2), 935–940.

(38) Chen, C.-C.; Zhou, Y.; Baker, L. A. *Annu. Rev. Anal. Chem.* **2012**, *5* (1), 207–228.

(39) Page, A.; Perry, D.; Young, P.; Mitchell, D. A.; Frenguelli, B. G.; Unwin, P. R. *Anal. Chem.* **2016**, *88*, 10854–10859.

(40) Perry, D.; Paulose Nadappuram, B.; Momotenko, D.; Voyias, P. D.; Page, A.; Tripathi, G.; Frenguelli, B. G.; Unwin, P. R. *J. Am. Chem. Soc.* **2016**, *138* (9), 3152–3160.

(41) Ida, H.; Takahashi, Y.; Kumatani, A.; Shiku, H.; Matsue, T. *Anal. Chem.* **2017**, acs.analchem.7b00584.

(42) Page, A.; Perry, D.; Unwin, P. R. *Proc. R. Soc. A Math. Phys. Eng. Sci.* **2017**, *473* (2200).

(43) McKelvey, K.; Kinnear, S. L.; Perry, D.; Momotenko, D.; Unwin, P. R. *J. Am. Chem. Soc.* **2014**, *136*, 13735–13744.

(44) Momotenko, D.; McKelvey, K.; Kang, M.; Meloni, G. N.; Unwin, P. R. *Anal. Chem.* **2016**, *88* (5), 2838–2846.

(45) Novak, P.; Li, C.; Shevchuk, A. I.; Stepanyan, R.; Caldwell, M.; Hughes, S.; Smart, T. G.; Gorelik, J.; Ostanin, V. P.; Lab, M. J.; Moss, G. W. J.; Frolenkov, G. I.; Klenerman, D.; Korchev, Y. E. *Nat. Methods* **2009**, *6* (4), 279–281.

(46) Chen, C.-H.; Meadows, K. E.; Cuharuc, A.; Lai, S. C. S.; Unwin, P. R. *Phys. Chem. Chem. Phys.* **2014**, *16*, 18545–18552.

(47) Bentley, C. L.; Kang, M.; Unwin, P. R. *J. Am. Chem. Soc.* **2016**, *138* (39), 12755–12758.

(48) Perry, D.; Momotenko, D.; Lazenby, R. A.; Kang, M.; Unwin, P. R. *Anal. Chem.* **2016**, *88* (10), 5523–5530.

(49) Shoup, D.; Szabo, A. *J. Electroanal. Chem.* **1982**, *140* (2), 237–245.

(50) Bode, D. D.; Andersen, T. N.; Eyring, H. *J. Phys. Chem.* **1967**, *71* (4), 792–797.

(51) Gyenge, E. *Electrochim. Acta* **2004**, *49* (6), 965–978.

(52) Atwan, M. H.; Macdonald, C. L. B.; Northwood, D. O.; Gyenge, E. L. *J. Power Sources* **2006**, *158* (1), 36–44.

(53) Ida, H.; Takahashi, Y.; Kumatani, A.; Shiku, H.; Matsue, T. *Anal. Chem.* **2017**, *89*, 6015–6020.

(54) Gardiner, J. A.; Collat, J. W. *J. Am. Chem. Soc.* **1965**, *87* (8), 1692–1700.

(55) Mirkin, M. V; Yang, H.; Bard, A. J. *J. Electrochem. Soc.* **1992**, *139* (8), 2212–2217.

(56) Pasqualeti, A. M.; Olu, P. Y.; Chatenet, M.; Lima, F. H. B. *ACS Catal.* **2015**, *5* (5), 2778–2787.

(57) Escaño, M. C. S.; Arevalo, R. L.; Gyenge, E.; Kasai, H. *J. Physics. Condens. Matter* **2014**, *26* (35), 353001.

(58) Iotov, P. I.; Kalcheva, S. V.; Bond, A. M. *Electrochim. Acta* **2009**, *54* (28), 7236–7241.

(59) Burke, L. D. *Gold Bull.* **2004**, *37*, 125–135.

(60) Momotenko, D.; Page, A.; Adobes-Vidal, M.; Unwin, P. R. *ACS Nano* **2016**, *10* (9), 8871–8878.

(61) Sa, N.; Baker, L. A. *J. Am. Chem. Soc.* **2011**, *133* (27), 10398–10401.

(62) Sa, N.; Lan, W. J.; Shi, W.; Baker, L. A. *ACS Nano* **2013**, *7* (12), 11272–11282.

(63) Burt, D. P.; Wilson, N. R.; Janus, U.; Macpherson, J. V; Unwin, P. R. *Langmuir* **2008**, *24* (17), 12867–12876.

(64) Matsushima, H.; Lin, S.-W.; Morin, S.; Magnussen, O. M. *Faraday Discuss.* **2016**, *193* (0), 171–185.

(65) Dong, H.; Feng, R.; Ai, X.; Cao, Y.; Yang, H.; Cha, C. *J. Phys. Chem. B* **2005**, *109* (21), 10896–10901.

(66) Bard, Allen J. Faulkner, L. R. *Electrochemical Methods: Fundamentals and Applications*, 2nd ed.; Wiley: New York, 2001.

(67) Qin, Y.; Zhang, X.; Dai, X.; Sun, H.; Yang, Y.; Li, X.; Shi, Q.; Gao, D.; Wang, H.; Yu, N. F.; Sun, S. G. *Small* **2016**, *12* (4), 524–533.

(68) Han, J. H.; Lee, E.; Park, S.; Chang, R.; Chung, T. D. *J. Phys. Chem. C* **2010**, *114* (21), 9546–9553.

(69) Bae, J., Han, J., Chung, T. *Phys. Chem. Chem. Phys.* **2012**, *14* (2), 448–463.

(70) Walcarius, A. *Chem. Soc. Rev.* **2013**, *42* (9), 4098–4140.

Chapter 6. Quantitative Visualization of Molecular Delivery and Uptake at Living Cells with Self-Referencing Scanning Ion Conductance Microscopy (SICM) – Scanning Electrochemical Microscopy (SECM)

6.1 Abstract

A multifunctional dual-channel scanning probe nanopipette that enables simultaneous scanning ion conductance microscopy (SICM) and scanning electrochemical microscopy (SECM) measurements is demonstrated to have powerful new capabilities for spatially mapping the uptake of molecules of interest at living cells. One barrel of the probe is filled with electrolyte and the molecules of interest and is open to the bulk solution for both topographical feedback and local delivery to a target interface, while a solid carbon electrode in the other barrel measures the local concentration and flux of the delivered molecules. This setup allows differentiation in molecular uptake rate across several regions of single cells with individual measurements at nanoscale resolution. Further, operating in a 'hopping mode', where the probe is translated towards the interface (cell) at each point allows self-referencing to be employed, in which the carbon electrode response is calibrated at each and every pixel for comparison to the bulk measurement. This is particularly important for measurements in living systems where an electrode response may change over time. Finite element method (FEM) modeling places the technique on a quantitative footing to allow the response of the carbon electrode and local delivery rates to be quantified. The technique is extremely versatile, with the local delivery of molecules highly tuneable via control of the SICM bias to promote or restrict migration from the pipette orifice. It is expected to have myriad applications from drug delivery to screening catalysts.

6.2 Introduction

All living cells, irrespective of whether they are plant, animal or bacterial, are continuously exchanging molecules with their extracellular environment. These molecules can range from the small diatomic oxygen (O_2) used in cellular respiration,[1–3] to cytokines,[4] signalling proteins used for intercellular communication that can be 20 kDa or larger in size. The passage of any species from the extracellular to the intracellular domain or vice-versa is dependent on a host of factors, including molecule size and charge,[5,6] physiological conditions and environment,[7] relative concentrations inside and outside of the cell[8] and the presence of suitable membrane proteins if assisted transport is necessary.[9,10] The dependence of uptake on such a wide variety of factors, and the fact that uptake is a complex process involving mass transport (diffusion) and interfacial (membrane) processes, imposes critical requirements on analytical techniques if key details on uptake are to be revealed. Although cell uptake measurements are an essential aspect of new drug development, current methods often use bulk cytotoxicity assays and, at best, whole single cell measurements to ascertain the efficacy of a drug.[11–14]

Scanning electrochemical probe microscopies (SEPMs) have great potential to increase the precision of cellular uptake measurements, particularly as the production of functional nanoscale probes is becoming easier.[15] Hitherto, scanning electrochemical microscopy (SECM)[16] and scanning ion conductance microscopy (SICM)[17] have been the main SEPMs used for cell imaging. SICM has mainly being used for high resolution topographical imaging,[18,19] while SECM has found considerable application for imaging a variety of processes at living cells.[20,21] However, measurements of cell permeability with SECM are somewhat scarce[22,23] and challenging, because existing detection schemes, such as the induced transfer mode,[24] require careful deconvolution of topography and induced transfer (interfacial kinetics). Furthermore, this mode involves the ‘extraction’ of analyte by diffusion from within a cell or tissue, which may not give an accurate measurement of permeability if the analyte is consumed or irreversibly bound inside the cell.

Here, we report a new method combining SICM and SECM probes to determine the topography of a substrate, and cell permeability (molecular uptake) simultaneously and in real time. While integrated electrodes have previously been

used to monitor the efflux from micropipettes,[25,26] they have not been used to monitor uptake at cells and our work greatly develops the capability of SICM-SECM,[27–30] which has recently been applied to model substrates[27,28,31] and electrocatalysis at nanoparticles.[32,29]

The approach makes use of SICM-SECM as a multifunctional tool to spatially resolve the uptake of a molecule of interest to a single cell (SECM channel), whilst reliably positioning the probe at a defined distance from the interface for delivery and topography mapping (SICM channel). The analyte of interest is delivered to the cell in a defined and local manner. This is advantageous compared to the analyte being in bulk solution, because: (i) it allows the detection of *uptake*; (ii) the cell is only dosed transiently with the analyte, which *reduces potential toxicity issues*; and (iii) the response of the SECM and SICM channels can be calibrated *at each and every pixel*. Furthermore, the migration and thus delivery of molecules can be controlled by the polarity and magnitude of the applied SICM bias. As a proof of concept the uptake of the well-characterized redox mediator hexaammineruthenium(III), $[Ru(NH_3)_6]^{3+}$, into *Zea mays* root hair cells has been studied. The technique is comfortably able to differentiate between uptake over the cell and the lack of uptake over glass, and is further able to distinguish heterogeneities in uptake rates across different regions of cells. Interestingly, the rates correlate qualitatively to earlier measurements of membrane surface charge.[33] This sub-cellular resolution is a significant improvement on previous uptake assays and provides a roadmap to further refine the spatial and kinetic resolution. An important aspect of the method is that the probe response can be predicted with finite element modeling (FEM) to provide a robust platform on which the cellular uptake of any electroactive molecule of interest could potentially be studied at the nanoscale, and the method could be applied to many other types of interfaces in addition to cells.

6.3 Materials and Methods

6.3.1 Chemicals

Milli-Q reagent grade water (resistivity *ca.* 18.2 MΩ cm at 25 °C) was used for all solutions. 10 mM KCl (Sigma-Aldrich, pH 6.5) was prepared and used for the bulk solution in all experiments. A solution of 10 mM hexaammineruthenium(III) chloride (Sigma-Aldrich) and 10 mM KCl was prepared and used in the SICM barrel for all experiments.

6.3.2 Substrate Preparation

Zea mays seeds (Avenir, Syngenta) were germinated between two layers of damp paper towel at 25 °C for 4 days. This provided a root of approximately 20 mm length with a dense layer of root hair cells. The corn roots were then attached to a glass-bottomed Petri dish (3512, WillcoWells) using SPM adhesive tabs (Agar Scientific) away from the area being imaged.

6.3.3 Probe Fabrication

The fabrication of the nanoprobes used for SICM-SECM uptake mapping involved a multi-stage process. First, a dual-barrel quartz 'theta' capillary (o.d. 1.2 mm, i.d. 0.9 mm, Friedrich and Dimmock) was pulled to a sharp point of ~150 nm total diameter using a laser puller (P-2000, Sutter Instruments). One of the barrels was sealed with 'Blu-Tack' (Bostik) before butane was flowed down the other barrel in an argon atmosphere (Figure 6.1a). The probe was heated to pyrolytically deposit carbon within the barrel,[31,34] with the butane torch moved laterally, starting from beyond the end of the probe, over the tip and along the probe body. The burn time was typically 3 s at the tip and 10 s on the probe body to ensure that a thick layer of carbon was deposited.

An electrical connection to the SECM electrode was established by inserting a copper wire through the top end of the pipette barrel to make a back contact with the carbon layer. A transmission electron microscope (TEM, JEOL 2000FX) was used to investigate the carbon deposit (see inset micrographs, Figure 6.1a). The carbon deposit could be conformal to the end (left side image) or result in a recessed layer (right hand

image). To avoid complications for an irregular SECM tip geometry, the overall probe diameter was increased to 500 nm using focused ion beam (FIB) milling (JEOL 4500) to ensure consistent probe geometry with a flush carbon electrode (Figure 6.1b), the response of which could be more accurately modeled. Ag/AgCl quasi-reference counter electrodes (QRCEs), comprising AgCl-coated Ag wire,[35,36] were used in the open barrel of the probe and in the bulk solution for SICM feedback (topographical imaging).

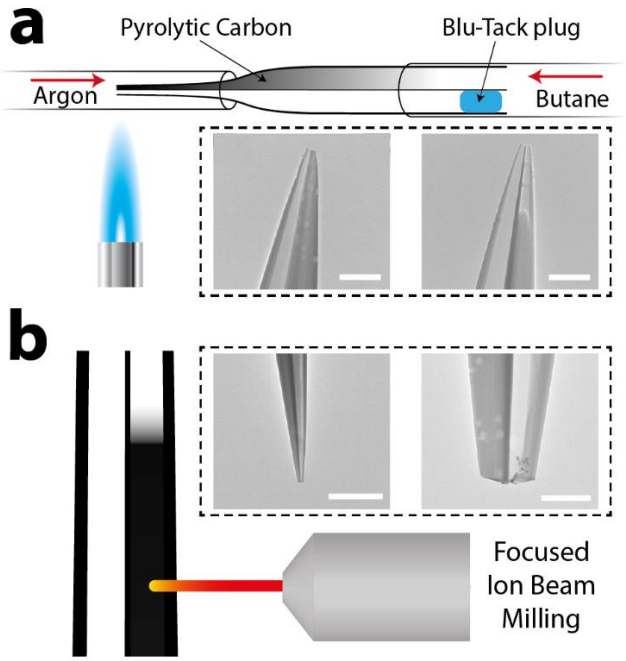

Figure 6.1 Fabrication of dual-barrel nanoprobes for use in SICM-SECM. (a) Carbon was deposited in one barrel of the probe via the pyrolysis of butane (SECM) while the other was kept open (SICM). Inset transmission electron microscopy (TEM) images show an example of both complete (left) and incomplete (right) carbon deposition. Scale bar in both micrographs is 500 nm. (b) The probe diameter was regulated using focused ion beam (FIB) milling. Inset TEM images show a probe with scale bars of 5 μm (left) and 500 nm (right) after FIB milling.

6.3.4 Instrumentation

The SICM-SECM setup was built on the stage of an inverted optical microscope (Axiovert 40 CFL, Zeiss) to facilitate the positioning of the nanoprobe

relative to the substrate. Probe movement normal to the substrate was controlled using a piezoelectric positioning stage with a travel range of 38 μm (P-753-3CD, Physik Instrumente), while fine lateral movement of the substrate for XY positioning was achieved using a two-axis piezoelectric positioning system with a travel range of 300 μm (Nano-BioS300, Mad City Laboratories, Inc.). Instrumentation control and data collection was achieved using a custom-written LabVIEW (2013, National Instruments) program through an FPGA card (NI PCIe-7852R, National Instruments) and custom-built current amplifiers.

6.3.5 Simultaneous Topography and Uptake Mapping

To simultaneously image topography and uptake, the SICM-SECM probe was approached towards the surface at 2 μm s^{-1} (for small area scans) and 3 μm s^{-1} for larger scans (specified herein) until the ionic (SICM) current dropped by 1.5%, compared to the bulk value at each pixel. This was the feedback threshold used throughout. A hopping regime[28,37] was used to permit a quantifiable measurement to be taken at each pixel. The bias between the two QRCEs used for SICM feedback was 0.2 V with the positive bias applied at the QRCE in the SICM barrel. A bias of -0.4 V was applied to the carbon electrode with respect to the QRCE in bulk solution so as to reduce $[Ru(NH_3)_6]^{3+}$ to $[Ru(NH_3)_6]^{2+}$ at a transport-limited rate. The height of the substrate at each pixel was taken from the z-position at the point of closest approach based on the SICM response. The normalized SECM current response was calculated by dividing the faradaic reduction current value at the surface by that in bulk at the same pixel. The use of self-referencing data collection was extremely powerful, allowing the response of the probe to be recalibrated at every point in the scan.

6.3.6 Finite Element Model (FEM) Simulations

3D FEM simulations were performed in COMSOL Multiphysics (v5.2) using the transport of diluted species and electrostatics modules. The dimensions of the probe for the simulation were taken from TEM micrographs.[38] The pipette was simulated as a double-barrel eccentric extruded cone with a total semi-major axis of 250 nm at the end of the pipette, and a semi-major axis of 160 nm for each of the two barrels. The height of the pipette simulated was 5 μm with an inner cone angle of 4.9°.

A 3D axisymmetric domain of the nanopipette with dimensions extracted from TEM images was constructed, a schematic 2D slice of which is depicted in Figure 6.2 below, with boundary conditions in Table 6.2. All boundaries that are not specifically labeled with conditions are set as no flux boundaries with [KCl] = 10 mM. No potential is applied at boundary B1 as the electric field from the probe does not appreciably intercept the surface and any electric boundary condition applied at B1 would necessarily be conjecture. No potential is applied at boundary B4 as the electric field from the electrode will have a negligible effect and was thus not included to reduce the complexity of the simulation. The system of differential equations solved was as follows. Ionic transport is reasonably assumed to follow the classical Nernst-Planck relationship, where the flux J_i of species i is given as:

$$J_i = -D_i \nabla c_i - z_i \frac{F}{RT} D_i c_i \nabla \phi \qquad \text{eq (6.1)}$$

and the Poisson equation describes the electrical potential ϕ:

$$\nabla^2 \phi = -\frac{F}{\varepsilon \varepsilon_0} \sum_i z_i c_i \qquad \text{eq (6.2)}$$

where c_i denotes the concentration of species i, while D_i, z_i, F, R, T, ε and ε_0 specify constants: diffusion coefficient of i, its charge number, the Faraday constant, gas constant, temperature, relative permittivity and vacuum permittivity, respectively.

The initial conditions in the SICM barrel were 10 mM KCl and 10 mM hexaammineruthenium(III) chloride while the initial conditions in bulk solution were 10 mM KCl. A concentration of 0 mM $[Ru(NH_3)_6]^{3+}$ was set as the boundary condition at the end of the SECM barrel (diffusion-limited detection) and the flux was monitored and converted into current. There was no treatment of $[Ru(NH_3)_6]^{2+}$; it is generated in small amounts and is not expected to affect the flux of $[Ru(NH_3)_6]^{3+}$ across the cell membrane. However, the generated species in SECM could sometimes affect the flux of other species, and for a system where this is the case this could readily be treated.

Simulations were first performed to find the point of closest approach from the SICM feedback with a tip potential of +0.2 V. The threshold value used experimentally was a drop in current of 1.5 % compared to the bulk value. Steady-state simulations were carried out at a variety of probe-substrate separations to build an approach curve, from which a separation of 120 nm was determined for this set

point. Having determined the working distance, a series of steady-state simulations were carried out at this probe-substrate separation with surfaces of differing uptake rate constant, k, ranging from 0 cm s^{-1} to 1000 cm s^{-1}. Throughout these simulations the SICM bias of +0.2 V was still applied to mimic the experimental setup.

Surface charge was not included in the simulations herein. While interesting phenomena have been demonstrated as a result of surface charge on a nanopipette/glass substrate,[39] these phenomena are shown to be manifest with significantly smaller probes, and at closer probe-substrate separations than those used herein. However, if future experiments required smaller probe-substrate separations then the effect of surface charge could be incorporated into the simulations. Relatedly, these simulations were carried out in the absence of electroosmotic flow (EOF), as such effects are expected to be negligible under the conditions of the experiments herein,[40] and the self-referencing technique would compensate for the additional flux. The effects of EOF may be different between surface and bulk at very small probe-substrate separations and thus it would be possible to include EOF should this be necessary.[41]

The justification for carrying out steady-state as opposed to time-dependent simulations for the quantification of uptake rate is given in section 6.3.6A, while the justification of the determination of the probe-substrate separation is discussed in section 6.3.6B.

Table 6.1 Diffusion coefficients of the species simulated.

Species	$\boldsymbol{D_i}$, $\times 10^{-5}$ cm^2 s^{-1}
$\mathbf{K^+}$	1.96
$\mathbf{Cl^-}$	2.05
$\mathbf{[Ru(NH_3)_6]^{3+}}$	0.96

Table 6.2 Boundary conditions for the FEM model with boundaries corresponding to Figure 6.2 below.

Boundary	Concentration/Flux	Potential
B1	$flux = -k[\mathrm{Ru(NH_3)_6}]^{3+}$	No electric boundary condition applied
B2	[KCl] = 10 mM	V = 0 V
B3	[KCl] = 10 mM, $[\mathrm{Ru(NH_3)_6Cl_3}]$ = 10 mM	V = + 0.2 V
B4	$[\mathrm{Ru(NH_3)_6}]^{3+}$ = 0 mM	No electric boundary condition applied

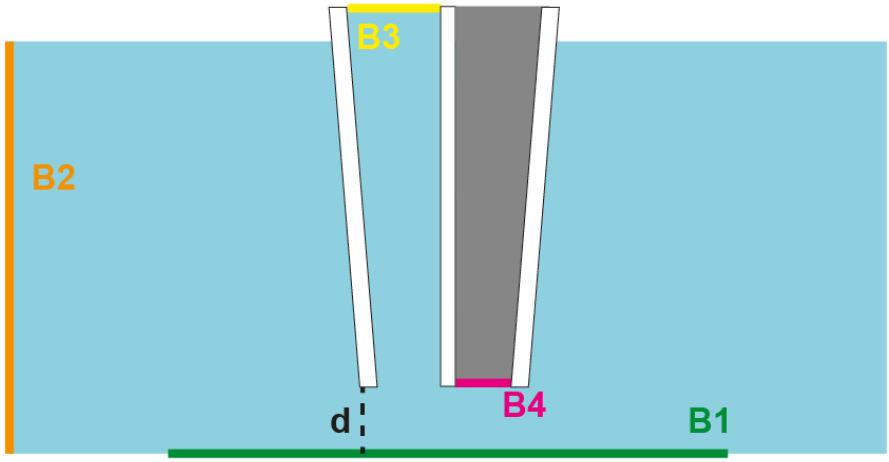

Figure 6.2 Schematic (not to scale) of a 2D slice from the 3D FEM simulation of a dual-channel nanopipette above a surface of variable uptake rate constant, *k*. Boundary conditions at B1-4 in Table 6.2 above.

6.3.6A Justification of tip-substrate separation. The determination of the probe-substrate separation of 120 nm was reached via a simulated approach curve over a surface of no uptake. That separation distance was then used for the steady-state simulations to calibrate the normalized SECM current with a range of uptake rate constants. The SICM current from those steady-state simulations is considered here to determine the influence of uptake rate constant on the SICM approach feedback.

Shown below (Figure 6.3) is the percentage difference in SICM current of the simulations over surfaces of various uptake rate constants (at a probe-separation of 120 nm) when compared to the simulation used to determine the separation distance (surface with an uptake rate constant of zero). It can be seen that for the uptake rate constants encountered in this study (~0.25 cm s^{-1}) the effect on the SICM current is about 0.5%, and similar to the noise level in the SICM current, thus justifying the method used. However, for interfaces with a higher uptake rate constant the effect of the uptake on the SICM feedback would need to be considered. This would not be problematic, but would require analysis of the SICM and SECM data simultaneously (and iteratively) to determine both the approach distance and uptake rate.

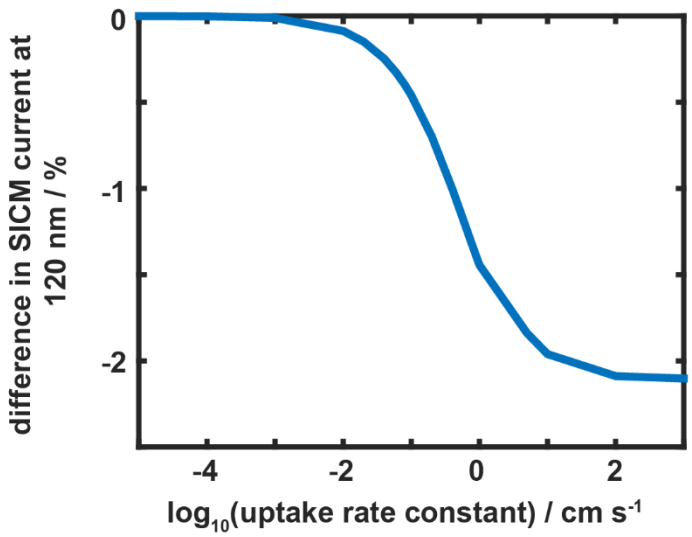

Figure 6.3 Difference in the simulated SICM current at a probe-substrate separation distance (*d*, see above) of 120 nm over substrates of differing uptake rates when compared to the SICM current at 120 nm over a surface with an uptake rate constant of 0 cm s^{-1}.

In order to further justify the probe-substrate separation distance used herein, we now consider the agreement of the theoretical approach curve with a typical experimental approach curve. Figure 6.4 shows the two approach curves in both the SICM channel (over a range of 500 nm) and the SECM channel (over a range of 1000 nm). Both sets of curves show a strong agreement across the entire range, thus fully validating the method presented herein. It should be noted in both figures that the

probe-substrate separation is that taken from the model. Clearly, for an experimental approach the point of closest approach is some way from the surface and thus a shift of 120 nm was applied to the raw experimental data to more easily compare the full approach.

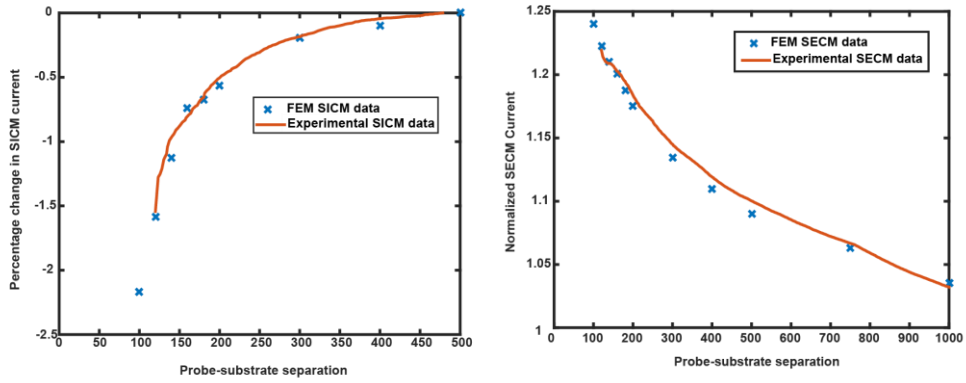

Figure 6.4 Comparison between approach curves in both the SICM and SECM channels from FEM simulations and from a typical experimental approach. In both figures the zero point is that taken from the simulations where the probe-substrate separation is known precisely. The experimental approach curves have been shifted by 120 nm from the point of closest approach.

6.3.6B Approach data justifying steady-state simulations. As the probe approaches the surface it only remains at the point of closest approach for a short period of time (~1 ms), the period of time during which the current reading used to calculate the normalized current at that pixel is collected. In order to ensure that the approach rate to the surface did not influence the response of the probe (and thus justifying the use of steady-state simulations for quantification) a series of approaches were performed at different approach rates to a cell surface, the results of which are shown in Table 6.3. It can be seen that the normalized SECM current at the distance of closest approach does not change at approach velocities up to 10 μm s^{-1}, comfortably justifying an experimental approach rate of 2-3 μm s^{-1}. Above 10 μm s^{-1} it becomes questionable as to whether or not the system is at steady state as the normalized current values increase.

Table 6.3 Normalized SECM current values at the distance of closest approach from a series of approach curves to a *Zea mays* root hair cell at different approach rates. Each value given is the mean of three approaches and an error of one standard deviation is also given.

Approach Speed / μm s^{-1}	Normalized Current
0.5	0.91 ± 0.006
1	0.91 ± 0.008
2	0.90 ± 0.011
5	0.90 ± 0.009
10	0.91 ± 0.010
15	0.93 ± 0.011
20	0.94 ± 0.014

6.4 Results and Discussion

6.4.1 Operational Principle

The use of a dual-barrel nanoprobe for the quantitative detection of cellular uptake is conditional on an intimate understanding of two well established scanning probe techniques: SICM and SECM. As highlighted in the Introduction, SICM utilizes the ionic current between two Ag/AgCl QRCEs, one in the probe and one in the bulk solution, as a feedback signal.[42] This current is dependent on the resistance in the system, which in bulk solution is determined almost exclusively by the aperture of the nanopipette, as the most resistive component.[43] However, as the probe approaches a surface (closer than one probe diameter) the system resistance increases as ion migration between the pipette and bulk solution is hindered by the surface. The corresponding decrease in current can therefore be used to set, and determine, the

probe-substrate separation, and hence measure the topography of the substrate with a resolution on the same scale as the probe opening.[43] Note that for the probe sizes, distances, and electrolyte concentrations used herein the SICM current is immune to rectification effects.[39,44,45] SECM uses a solid micro- or nanoelectrode to probe the local concentration (or flux) of an electroactive species of interest. A potential is applied to the electrode to either oxidize or reduce the desired molecule, with the resulting faradaic current used to obtain flux information.

One QRCE was in the open (electrolyte-filled) barrel of the probe while another was in bulk, with a potential, V_1, applied between the two. The carbon electrode was connected to an offset electrometer that allowed the variation of the applied potential, V_2 - V_1, without affecting the bias used for SICM (Figure 6.5a). Both the bulk solution and the electrolyte channel of the probe contained 10 mM KCl. The molecule of interest (henceforth known as the 'analyte'), was hexaammineruthenium(III) ($[Ru(NH_3)_6]^{3+}$) as the chloride salt at a concentration of 10 mM, which was only in the electrolyte-filled barrel of the nanopipette. There was thus a concentration gradient of this species established around the tip of the probe and the transport of analyte from the open channel to the face of the carbon electrode determined the SECM current signal observed. It is worth noting that while there are interdependent electrochemical and transport processes at the two channels, this interdependence is also treated in the simulations, with all simulations carried out with both the SICM and SECM channels 'on' and both V_1 and V_2 held constant throughout.

Figure 6.5b is a schematic of an SICM-SECM probe near to a root hair cell. As $[Ru(NH_3)_6]^{3+}$ molecules are taken across the membrane it can be seen that, for a fixed probe-substrate separation, the SECM signal would be lower at this substrate than at a completely solid (impermeable) surface, where $[Ru(NH_3)_6]^{3+}$ would be partly trapped (hindered diffusion/migration) between the electrode and the surface. A specific normalized SECM current value (the ratio of the SECM current at the point of closest approach and the SECM current in bulk) thus corresponds to a specific level of uptake at the interface, as discussed in the next section.

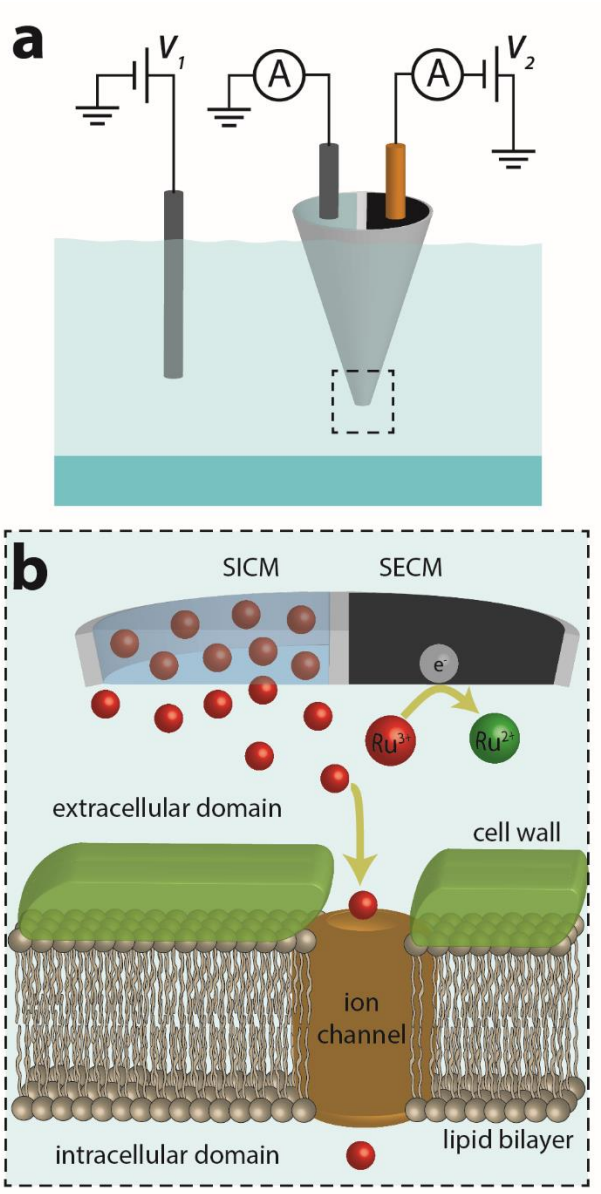

Figure 6.5 SICM-SECM experimental setup for the investigation of cellular uptake. (a) The current flowing between two Ag/AgCl QRCEs, one in bulk and one in the open channel of the probe, with an applied bias, V_1, used for topographical feedback in an SICM configuration. The carbon electrode used to measure the local concentration of the species is at a bias V_2 - V_1. (b) Schematic showing the diffusion-migration of $[Ru(NH_3)_6]^{3+}$ from the SICM barrel into the near cell region. The current due to the reduction of $[Ru(NH_3)_6]^{3+}$ at the SECM channel is monitored on approach of the probe to the surface and compared to the steady-state bulk current response to quantify uptake rates. It should be noted that transport via an ion channel is just one of many possible membrane transport mechanisms and is depicted herein for illustrative purposes.

6.4.2 FEM Simulations

FEM simulations of an SICM-SECM nanopipette (see Materials and Methods for a full detail) approaching a surface of zero uptake allowed the determination of a probe-substrate separation of 120 nm based on the 1.5% decrease of SICM current as the threshold used for the studies herein (Figure 6.6a). Further simulations were carried out with the probe at 120 nm above surfaces with varying analyte uptake rates, ranging from no uptake to a rate constant, *k*, of 1000 cm s^{-1} (see equation 1 above). Normalizing the steady-state SECM current values from these simulations to the value with the probe in bulk solution, 10 μm away from the surface, generated a calibration curve of normalized SECM current versus uptake rate constant for the quantitative estimation of uptake kinetics to a given surface (Figure 6.6b). It can be seen that this technique has a wide dynamic window, and is sensitive to rate constants from about 0.01 cm s^{-1} to 10 cm s^{-1}. This is a positive feature of the method. On the other hand, accurate measurements require that the SECM channel current can be determined with high precision, which is why self-referencing is important, as we show herein.

An investigation was carried out into whether or not the uptake rate constant at the surface would influence the SICM current signal, and thus the probe-substrate separation, the results of which are presented in Section 6.3.6A of Materials and Methods. For the uptake rate constants observed in this study, and the tip-substrate separation used, the flux of $[Ru(NH_3)_6]^{3+}$ did not have a significant effect on the SICM current, with a small decrease predicted that was comparable to the noise of the SICM current measured experimentally. However, for a system where the uptake rate constant was higher (above 1 cm s^{-1}), the probe-substrate separation could be influenced by the uptake of the analyte. This issue could be countered by employing an iterative approach in which both the separation and the uptake rate constant would be determined simultaneously over several rounds of simulations.

Experimentally the probe was retracted 15 μm and this tip-substrate separation and that used in the simulations (10 μm) are sufficient to represent bulk solution. The use of steady-state simulations is justified as the SECM response was the same at approach rates at least five times faster than those used experimentally, meaning that at any given point in the approach, the SECM current can be assumed to be at steady state. This is because the time to steady state at a nanoscale electrode is very short (see Section 6.3.6B of Materials and Methods). It should be noted that for all simulations

of the SECM current, the SICM bias (+0.2 V at the QRCE in the probe) was applied, to imitate precisely the migration (as well as diffusion) of the $[Ru(NH_3)_6]^{3+}$ that occurs in the experiments.

Figure 6.6c shows the steady-state concentration profile of $[Ru(NH_3)_6]^{3+}$ with initial conditions mimicking those used experimentally, with the probe in bulk solution, and bias of +0.2 V vs. the bulk QRCE applied in SICM tip. The concentration at the nanopipette orifice is around 2 mM, one fifth of the bulk nanopipette concentration of 10 mM. This difference is noteworthy when using nanopipettes for local delivery, particularly drug delivery, as it is important to carefully dose the sample with a well-defined quantity (flux). A close-up of the end of the probe (Figure 6.6d) shows a departure from the expected hemispherical concentration profile at the end of the SICM barrel,[46] with the reduction of the $[Ru(NH_3)_6]^{3+}$ to $[Ru(NH_3)_6]^{2+}$ at the carbon electrode modifying the shape on the side closest to the solid amperometric sensor.

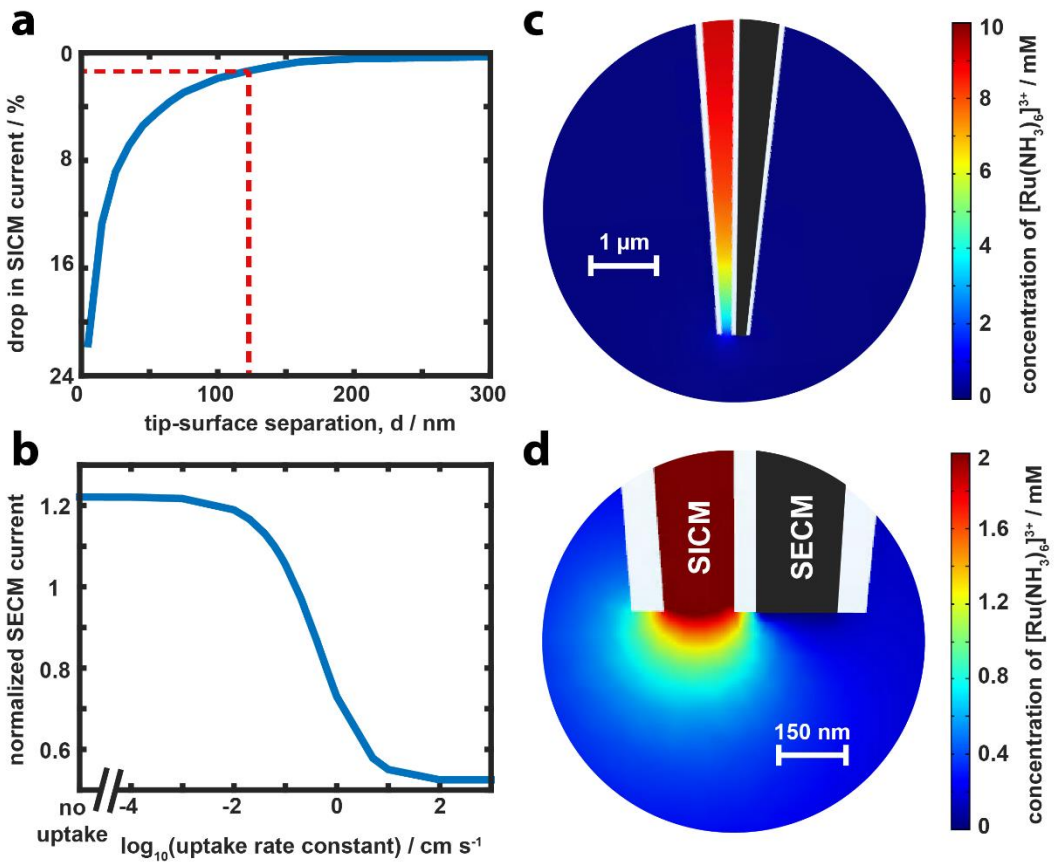

Figure 6.6 Finite element method (FEM) modeling of the SICM-SECM uptake system. (a) Simulated SICM approach curve (current vs. distance) to a surface of zero uptake with a probe of the same geometry as used experimentally, with electrochemistry switched on at the SECM channel. The current data are plotted as the percentage drop in ionic current from the bulk value (~850 pA). The experimental threshold (red line in (a)) was used to determine a working distance at which steady-state simulations (b) were carried out to calibrate the normalized SECM current as a function of the uptake rate constant at the surface. The normalized SECM current is the value at d = 120 nm divided by that with the probe in bulk solution (~10 pA). (c) and (d) show the concentration of $[Ru(NH_3)_6]^{3+}$ at steady state with initial concentrations of 10 mM in the SICM barrel and 0 mM in bulk.

6.4.3 Validation of SICM-SECM for Uptake Mapping

As a proof-of-concept system for spatially-resolved uptake mapping, a surface of reasonably high expected uptake (*Zea mays* root hair cells, see optical micrograph in Figure 6.7a) was imaged on a glass substrate (no expected uptake) in 10 mM KCl (pH 6.5). Figures 6.7b and 6.7c show a typical pair of simultaneously collected topography and normalized SECM current maps of a root hair cell on a glass substrate. The height of the cell varies from 7-10 μm, as it is not fully adhered to the surface,[33] and the steep drop off at the edges of the cell suggests a cylindrical morphology, consistent with previous work.[33]

The normalized SECM current map (Figure 6.7c) displays a very clear distinction between the behavior of the SECM channel over the root hair cell and the glass, with a pixel-perfect correlation with the topography map in Figure 6.7b, *i.e.* at every pixel the SECM response was consistent with the probe approaching the glass or cell (as indicated by topography). As mentioned above (Figure 6.6c), normalized SECM current values greater than 1 mean that the SECM current is higher close to the surface than in bulk. This is always observed over the glass substrate (typical value ~1.25) and is caused by the hindered diffusion/migration of ions away from the end of the probe. A value of normalized SECM current lower than 1.25 corresponds to uptake by the sample. The values across the cell are similar, with an average value of 0.91 ± 0.02, suggesting a high uptake rate constant of 0.31 ± 0.03 cm s^{-1} over the cell surface (Figure 6.6c). Individual approach curves of the SECM current taken from the scan in Figure 6.7c are shown in Figure 6.7d, to illustrate the consistency of the measurements in different areas of the cell and different areas of the glass, and the contrasting behaviour in the approach curve between the cell and glass substrate.

A scan of this size has an acquisition time of approximately 30 minutes. Figures 6.7e,f show the change in SICM and SECM currents, respectively, across the entire scan. The ionic current (SICM, Figure 6.7e) drifts from 835 pA to 810 pA, a change of less than 1 pA min^{-1}. This has a negligible effect on SICM topography imaging as a percentage feedback value, compared to bulk, is used. Proportionally, there is a more pronounced drift (deterioration) of the SECM current (Figure 6.7f) with time, from 10 pA to 6 pA. This makes the self-referencing method described above crucial to the reasonable interpretation of the SECM current data. It should be noted that the spikes both above and below the main trend in Figure 6.7f are

approaches over glass and the root hair cell respectively; the bulk current is given by the red line.

No interpolation has been applied to the data in Figures 6.7b,c and each pixel represents a quantified measurement of the interfacial uptake rate on the nanoscale. Furthermore, it should be noted that much of the scan time is spent in the probe retracting over a sufficient distance to map out topography of the root hair cell on the glass substrate. Many adherent mammalian cells are less than 1 μm in height and thus the scan could be acquired significantly faster in future experiments. Moreover, faster piezoelectric positioning systems would further reduce the scan time and increase pixel density.

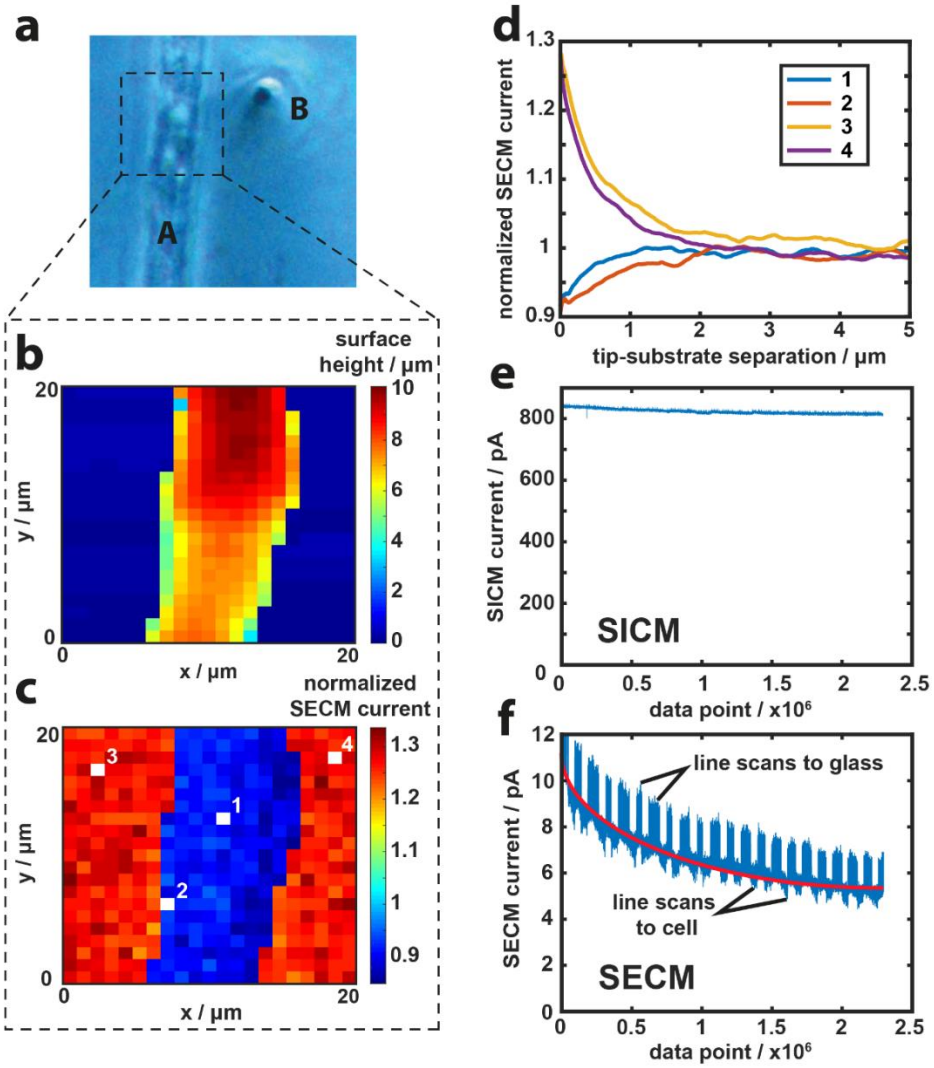

Figure 6.7 SICM-SECM topographical and $[Ru(NH_3)_6]^{3+}$ uptake mapping of a *Zea mays* root hair cell on a glass substrate. (a) Optical image of the scanned root hair cell (A) on a glass support with the end of the probe also visible (B); scan area denoted by the dashed rectangle. (b) Substrate topography extracted from the z-position at the point of closest approach. (c) Normalized SECM current map showing the difference in uptake between glass substrate (zero uptake) and the root hair cell. 'Normalized current' is the ratio of the $[Ru(NH_3)_6]^{3+}$ steady-state limiting reduction current at the point of closest approach to the reduction current in bulk. Individual experimental approach curves from the scan in (c) are shown in (d), at the four positions numbered. SICM (e) and SECM (f) currents across the entirety of the scan (400 separate approach curves) demonstrate minor current drift for SICM, but some effect for SECM, making the self-referencing approach essential. The red line in (f) shows the trend in bulk SECM current, ignoring the approaches to either the cell or the glass.

6.4.4 Differentiation of Subcellular Uptake Heterogeneities

While the ability to distinguish between uptake and no uptake was an important validation of the method, the technique was also applied to differentiate between the uptake rates across a single cell. Figure 6.8a shows a single *Zea mays* root hair cell, curved in a hairpin shape (bend outside of the optical micrograph) such that the root hair body and root hair tip could be imaged concurrently. The topography from the scan area denoted by the dashed white box in Figure 6.8a is shown in Figure 6.8b. The two areas of the cell are at different heights above the glass substrate but both suggest the cylindrical shape seen in Figure 6.7.

The normalized SECM current map (Figure 6.8c, response over the background glass slide grayed out to emphasize contrast; Figure 6.9) shows two clearly defined regions, labelled 'tip' and body' on Figure 6.8b, that have different normalized SECM current value ranges. The body of the cell generally has higher normalized SECM current values (mean = 0.956, standard deviation (s.d.) = 0.033) than at the cell tip (mean = 0.922, s.d. = 0.034), suggesting a faster uptake rate at the root hair tip than at the cell body. This difference between the two regions is emphasized when the data are displayed as a histogram (Figure 6.8d), where the bell-shaped spread of the normalized SECM current values at the tip is shifted from that of the body. The function of the root hair cell is to uptake nutrients that can then be distributed to the rest of the plant[47] and the higher level of uptake at the tip of the cell could potentially be a result either of a higher density of membrane transport proteins, or a generally looser membrane in this region. However, the higher uptake could also be caused by the charge density, arising as a result of charged proteins and lipids at the cell surface. Recent work with SICM for charge mapping[33] has shown that the tip of a root hair cell carries a significant negative charge when compared to the cell body and this could play an important role in the uptake of the positively charged $[Ru(NH_3)_6]^{3+}$ analyte used.

Despite the difference in overall uptake rates between the two regions, there is a spread of uptake values that can be attributed to several factors. First, heterogeneities in protein or charge lipid distribution on the cell surface would cause a distribution of uptake rates (normalized SECM current). A second reason is that the SECM currents measured during the experiment are rather small (~10 pA) and thus there will be a natural variation as a result of electrical noise. With these limitations in mind, it is

possible to quantify the normalized SECM current values measured at both the tip and the body using the simulated calibration curve (Figure 6.6c). The mean values stated above correspond to an uptake rate of 0.27 ± 0.05 cm s^{-1} for the cell tip and 0.22 ± 0.05 cm s^{-1} for the cell body.[47] The ability to distinguish between two regions with similar uptake rates suggests this technique has great promise going forward.

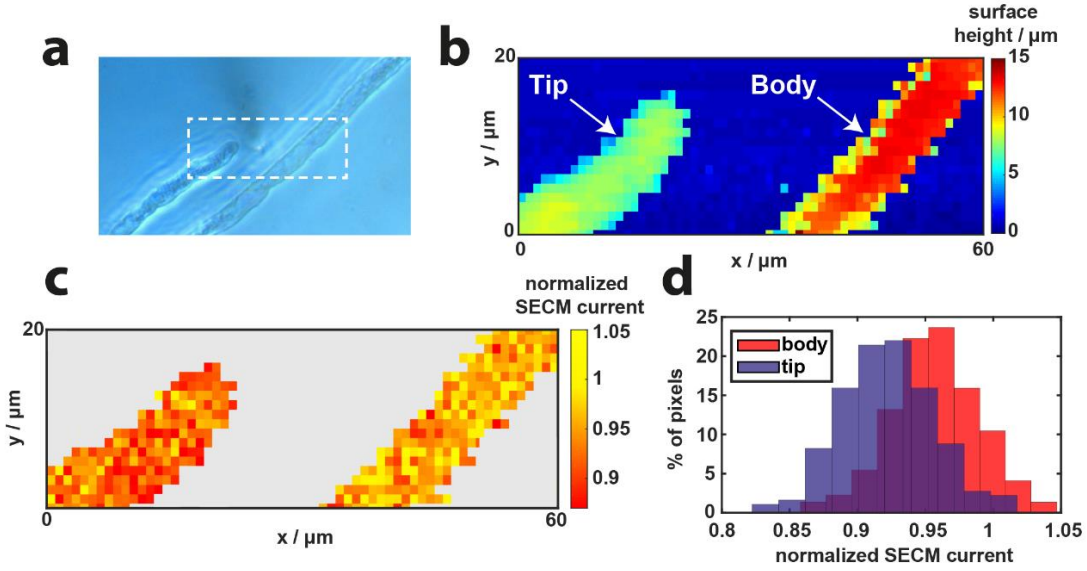

Figure 6.8 SICM-SECM topographical and $[Ru(NH_3)_6]^{3+}$ uptake mapping of two regions of a single *Zea mays* root hair cell. **(**a) Optical image of the scanned root hair cell; scan area denoted by the dashed rectangle. (b) Substrate topography extracted from the z-position at the point of closest approach from the SICM channel. (c) Normalized SECM current map showing a clear difference in uptake between the root hair cell body (higher current, lower uptake) and the root hair cell tip (lower current, higher uptake). 'Normalized current' is the ratio of the $[Ru(NH_3)_6]^{3+}$ reduction current at the point of closest approach to the same reduction current in bulk. (d) Histograms of the normalized SECM current across the two different regions of the root hair cell, 'tip' and 'body' (see (b)).

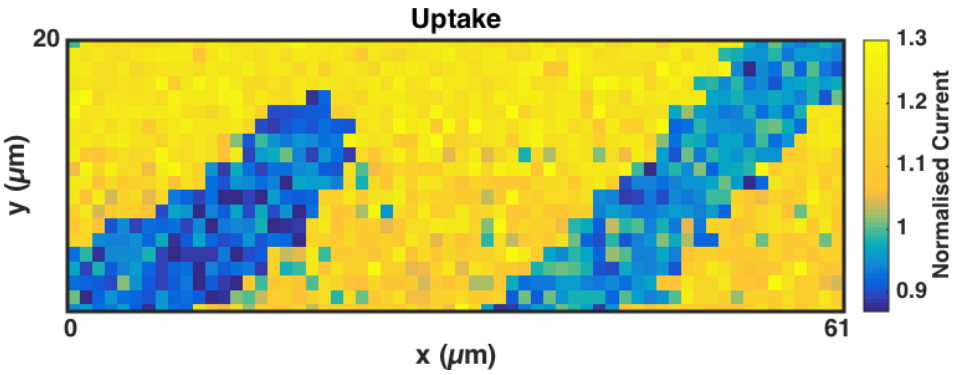

Figure 6.9 Raw data normalized current image of the root hair cell scan presented in Figure 6.8.

6.5 Conclusions

We have demonstrated the use of dual-barrel SICM-SECM nanoprobes to simultaneously measure the topography and spatially-resolve the uptake rate of a molecule of interest delivered from the probe across an interface. As a proof of concept, the uptake of hexaammineruthenium(III) to *Zea mays* root hair cells was studied, highlighting heterogeneities in uptake rate across a single cell, with a slightly higher rate of analyte uptake at the cell tip than at the cell body based on the probe current response. These qualitative differences were then quantified using FEM simulations of the experimental setup to provide a powerful platform for mapping and quantifying the uptake rate of electroactive species across an interface. A key feature of the approach has been pixel-level self-referencing of both the SICM and SECM response at each point in a map to overcome any drift in the response of the two channels.

This new technique could aid the screening of drug molecules; for example, using this assay in tandem with cytotoxicity experiments to inform the user of the efficacy of the drug once it had crossed the cell membrane. The technique could also be used to study electrocatalysis and other materials reactivity problems. This work adds significant new functionality to the family of scanning electrochemical probe techniques and could be combined with laser-scanning confocal microscopy and other microscopies to investigate a wide range of processes, from biological (living) systems to materials and catalysis.

6.6 References

(1) Alberts, B.; Johnson, A.; Lewis, J.; Morgan, D.; Raff, M.; Roberts, K.; Walter, P. *Molecular Biology of the Cell*; Garland Science, 2014.

(2) Lobritz, M. A.; Belenky, P.; Porter, C. B. M.; Gutierrez, A.; Yang, J. H.; Schwarz, E. G.; Dwyer, D. J.; Khalil, A. S.; Collins, J. J. *Proc. Natl. Acad. Sci. U. S. A.* **2015**, *112* (27), 8173–8180.

(3) Wikström, M.; Sharma, V.; Kaila, V. R. I.; Hosler, J. P.; Hummer, G. *Chem. Rev.* **2015**, *115* (5), 2196–2221.

(4) Hunter, C. A.; Jones, S. A. *Nat. Immunol.* **2015**, *16* (5), 448–457.

(5) Calatayud, M. P.; Sanz, B.; Raffa, V.; Riggio, C.; Ibarra, M. R.; Goya, G. F. *Biomaterials* **2014**, *35* (24), 6389–6399.

(6) Zhou, J.; Li, D.; Su, C.; Wen, H.; Du, Q.; Liang, D. *Phys. Chem. Chem. Phys.* **2015**, *17* (14), 8653–8659.

(7) Cho, E. C.; Zhang, Q.; Xia, Y. *Nat. Nanotechnol.* **2011**, *6* (6), 385–391.

(8) Hasegawa, P. M. *Environ. Exp. Bot.* **2013**, *92*, 19–31.

(9) Stein, W. D.; Litman, T. *Channels, carriers, and pumps: an introduction to membrane transport*; Elsevier, 2014.

(10) Grewer, C.; Gameiro, A.; Mager, T.; Fendler, K. *Annu. Rev. Biophys.* **2013**, *42*, 95–120.

(11) Passarelli, M. K.; Newman, C. F.; Marshall, P. S.; West, A.; Gilmore, I. S.; Bunch, J.; Alexander, M. R.; Dollery, C. T. *Anal. Chem.* **2015**, *87* (13), 6696–6702.

(12) Rezgui, R.; Blumer, K.; Yeoh-Tan, G.; Trexler, A. J.; Magzoub, M. *Biochim. Biophys. Acta - Biomembr.* **2016**, *1858* (7), 1499–1506.

(13) Wang, T.; Bai, J.; Jiang, X.; Nienhaus, G. U. *ACS Nano* **2012**, *6* (2), 1251–1259.

(14) Tsang, C. N.; Ho, K. S.; Sun, H.; Chan, W. T. *J. Am. Chem. Soc.* **2011**, *133* (19), 7355–7357.

(15) Kang, M.; Momotenko, D.; Page, A.; Perry, D.; Unwin, P. R. *Langmuir* **2016**, *32* (32), 7993–8008.

(16) Kwak, J.; Bard, A. J. *Anal. Chem.* **1989**, *61*, 1794–1799.

(17) Hansma, P.; Drake, B.; Marti, O.; Gould, S.; Prater, C. *Science (80-.).* **1989**, *243* (4891), 641–643.

(18) Shevchuk, A. I.; Frolenkov, G. I.; Sanchez, D.; James, P. S.; Freedman, N.; Lab, M. J.; Jones, R.; Klenerman, D.; Korchev, Y. E. *Angew. Chemie - Int. Ed.* **2006**, *45* (14), 2212–2216.

(19) Happel, P.; Thatenhorst, D.; Dietzel, I. D. *Sensors* **2012**, *12* (11), 14983–15008.

(20) Bergner, S.; Vatsyayan, P.; Matysik, F. *Anal. Chim. Acta* **2013**, *775*, 1–13.

(21) Schulte, A.; Nebel, M.; Schuhmann, W. *Annu. Rev. Anal. Chem. (Palo Alto. Calif).* **2010**, *3*, 299–318.

(22) Filice, F. P.; Li, M. S. M.; Ding, Z. *Anal. Chim. Acta* **2016**, *908*, 85–94.

(23) Bondarenko, A.; Lin, T.-E.; Stupar, P.; Lesch, A.; Cortes-Salazar, F.; Girault, H. H.; Pick, H. M. *Anal. Chem.* **2016**, *88* (23), 11436–11443.

(24) Gonsalves, M.; Barker, A. L.; Macpherson, J. V; Unwin, P. R.; Hare, D. O.; Winlove, C. P. *Biophys. J.* **2000**, *78*, 1578–1588.

(25) Armstrong-James, M.; Millar, J.; Kruk, Z. L. *Nature* **1980**, *288*, 181–183.

(26) Herr, N. R.; Kile, B. M.; Carelli, R. M.; Wightman, R. M. *Anal. Chem.* **2008**, *80* (22), 8635–8641.

(27) Comstock, D. J.; Elam, J. W.; Pellin, M. J.; Hersam, M. C. *Anal. Chem.* **2010**, *82* (4), 1270–1276.

(28) Takahashi, Y.; Shevchuk, A. I.; Novak, P.; Murakami, Y.; Shiku, H.; Korchev, Y. E.; Matsue, T. *J. Am. Chem. Soc.* **2010**, *132* (29), 10118–10126.

(29) O'Connell, M. A.; Wain, A. J. *Anal. Chem.* **2014**, *86* (24), 12100–12107.

(30) Morris, C. a.; Chen, C.-C.; Baker, L. a. *Analyst* **2012**, *137* (13), 2933–2938.

(31) Takahashi, Y.; Shevchuk, A. I.; Novak, P.; Zhang, Y.; Ebejer, N.; MacPherson, J. V.; Unwin, P. R.; Pollard, A. J.; Roy, D.; Clifford, C. A.; Shiku, H.; Matsue, T.; Klenerman, D.; Korchev, Y. E. *Angew. Chemie - Int. Ed.* **2011**, *50* (41), 9638–9642.

(32) O'Connell, M. A.; Lewis, J. R.; Wain, A. J. *Chem. Commun.* **2015**, *51* (51), 10314–10317.

(33) Perry, D.; Paulose Nadappuram, B.; Momotenko, D.; Voyias, P. D.; Page, A.; Tripathi, G.; Frenguelli, B. G.; Unwin, P. R. *J. Am. Chem. Soc.* **2016**, *138* (9), 3152–3160.

(34) Nadappuram, B. P.; McKelvey, K.; Al Botros, R.; Colburn, A. W.; Unwin, P. R. *Anal. Chem.* **2013**, *85* (17), 8070–8074.

(35) Ebejer, N.; Güell, A. G.; Lai, S. C. S.; McKelvey, K.; Snowden, M. E.; Unwin, P. R. *Annu. Rev. Anal. Chem. (Palo Alto. Calif).* **2013**, *6*, 329–351.

(36) Güell, A. G.; Cuharuc, A. S.; Kim, Y. R.; Zhang, G.; Tan, S. Y.; Ebejer, N.; Unwin, P. R. *ACS Nano* **2015**, *9* (4), 3558–3571.

(37) Takahashi, Y.; Murakami, Y.; Nagamine, K.; Shiku, H.; Aoyagi, S.; Yasukawa, T.; Kanzaki, M.; Matsue, T. *Phys. Chem. Chem. Phys.* **2010**, *12* (34), 10012–10017.

(38) Perry, D.; Momotenko, D.; Lazenby, R. A.; Kang, M.; Unwin, P. R. *Anal. Chem.* **2016**, *88* (10), 5523–5530.

(39) Sa, N.; Lan, W. J.; Shi, W.; Baker, L. A. *ACS Nano* **2013**, *7* (12), 11272–11282.

(40) McKelvey, K.; Kinnear, S. L.; Perry, D.; Momotenko, D.; Unwin, P. R. *J. Am. Chem. Soc.* **2014**, *136*, 13735–13744.

(41) Luo, L.; Holden, D. A.; White, H. S. *ACS Nano* **2014**, *8* (3), 3023–3030.

(42) Chen, C.-C.; Zhou, Y.; Baker, L. A. *Annu. Rev. Anal. Chem.* **2012**, *5* (1), 207–228.

(43) Edwards, M. A.; Williams, C. G.; Whitworth, A. L.; Unwin, P. R. *Anal. Chem.* **2009**, *81* (11), 4482–4492.

(44) Sa, N.; Baker, L. A. *J. Am. Chem. Soc.* **2011**, *133* (27), 10398–10401.

(45) Perry, D.; Al Botros, R.; Momotenko, D.; Kinnear, S. L.; Unwin, P. R. *ACS Nano* **2015**, *9* (7), 7266–7276.

(46) Chen, C.-C.; Baker, L. A. *Analyst* **2011**, *136* (1), 90–97.

(47) Foster, K. J.; Miklavcic, S. J. *Front. Plant Sci.* **2016**, *7*, 914.

Chapter 7. Summary

Electrochemical probing at the nanoscale, although experimentally challenging, is a fast-growing field of research, spurred on by the unique properties of nanomaterials, which are continuing to find countless real-world applications. As subtle changes within a nanomaterial (*e.g.*, structure, shape and size) can strongly influence (electro)chemical activity, it is important to develop robust and versatile techniques for making nanoscopic (electro)chemical measurements. In this thesis, multiple techniques using micro-/nano- pipettes are considered, with new measurement regimes introduced to study (electro)chemical phenomena at the nanoscale.

Firstly, Chapter 3 has provided a new insight into the dynamics of a NP on an electrode surface during SNEI, observing the electrocatalytic oxidation of H_2O_2 on RuO_x NPs in a static SECCM setup (*i.e.*, micro-droplet electrochemical cell) with high temporal resolution. The distribution in rise time, obtained from *i-t* traces in the experiments, corresponded to the results predicted from 3D random walk simulations. The simulations were combined with distance-dependent diffusivity of the NP in the vicinity of the electrode, where the diffusion coefficient decreases as the NPs approach the electrode surface, resulting hydrodynamic trapping of NPs near the electrode/electrolyte interface, within the confined droplet cell. The current decay observed in the blipping *i-t* response is attributable to the propulsion of the NP away from the electrode surface as a result of O_2 gas generated during H_2O_2 oxidation, "switching off" the reaction as the NP departs from the near-electrode electron tunnelling region. The high impact frequency (86 Hz) further has supported the distance-dependent diffusivity of the NP, which resulted in multiple impacts of a single NP as it was confined in the near-surface region. This has demonstrated that high temporal resolution plays an important role in understanding NP-electrode interaction dynamics during SNEI detection, as careful analysis of *i-t* traces can provide a wealth of information.

The experimental system in Chapter 4 was adapted from Chapter 3, simplified by the use of single channel probe, utilized to study the electrodissolution processes of individual Ag NPs on an electrode surface. The high temporal resolution achieved using the high-bandwidth measurement system allowed a wide range of *i-t*

morphologies to be observed during the impact of individual NPs. Using this approach, single Ag NP electrodissolution processes have been studied with a wide range of particle sizes (from 10 nm to 100 nm diameter) and different collector electrode surfaces (*i.e.*, carbon and Au). In-depth quantitative analysis of the *i-t* traces (*i.e.*, consumed charge, event duration and impact frequency) lead to the conclusion that in most cases, Ag NPs undergo multiple, consecutive partial electrodissolution events rather than a single complete electrodissolution event, as previously reported. Additionally, the Ag NPs showed a stronger interaction with an Au surface compared to a carbon surface, evidenced through higher charges consumed per Ag NP partial dissolution event and longer event duration. Interestingly, periodic *i-t* patterns with frequencies near 1 kHz have also been observed for most of the NP sizes on both GC and Au, although understanding the physical origin of such patterns requires further study. Overall, this chapter highlights that electrochemical dissolution processes of individual Ag NPs are rather complex, with careful attention to both experimental design and data analysis needed to fully understand the process.

Chapter 5 introduces a new SICM scanning protocol for robust electrochemical (reaction) imaging at the nanoscale using single channel nanopipette. Potential-time control for electrochemical measurements within this regime allowed the simultaneous mapping of topography and electrochemical reactivity on a reasonable time scale. The electrocatalytic oxidation of borohydride on Au was chosen as the model redox system and was probed at both the micro- and nanoscale. At the microscale, an Au UME was used as a proof-of-concept to demonstrate the technique, with tip bias polarity, variable V_{sub} and tip-substrate separation distances considered. At the nanoscale, electrodeposited Au nanostructures and Au NPs on CF UMEs were used as the substrates. It has been shown that the structure of the nanomaterial (*e.g.*, the narrow gaps formed between Au NPs and the CF support) plays an important role in the distribution of ion fluxes around the reacting nanoentities, most noticeable at low overpotentials. This was explored with FEM simulations which supported the empirical results. Moreover, comparisons between the electrochemical activities of individual Au NPs was also possible and a few particles were seen to present higher activities, which is attributable to their intrinsic activity as it is known that this reaction is sensitive to the Au surface (crystallographic) orientation. This has demonstrated that SICM is thus a powerful tool for exploring such heterogeneities between nanoentities.

Finally, the fabrication and application of the double-channelled SICM-SECM nanoprobes has been demonstrated in Chapter 6. The SICM-SECM nanoprobe was fabricated with the aid of FIB milling to improve reproducibility and characterised by TEM, providing the inner and outer structural details of the probe. The SICM channel, in this work, has played two important roles, *i.e.*, maintaining a consistent probe-substrate distance and delivery of the molecule of interest (*i.e.*, $Ru(NH_3)_6^{3+}$) across an interface (*i.e.*, *Zea mays* root hair cells). The SECM channel electrochemically has detected $Ru(NH_3)_6^{3+}$ throughout the measurement and provides the uptake rate of $Ru(NH_3)_6^{3+}$ on *Zea mays* root hair cells. The SICM-SECM nanoprobe was utilised as a dynamic probe to simultaneously visualise the topography and spatially-resolve the uptake rate of $Ru(NH_3)_6^{3+}$ across the interface. The results highlight heterogeneities in uptake rate across a single root by monitoring responses on the SECM channel and quantitative analysis has been performed through FEM simulations based on the experimental setup, providing a powerful platform for mapping and quantifying the uptake rate of electroactive species across an interface. A significant feature of the scanning regime in this work is self-referencing of both the SICM and SECM response at each point in a map to overcome any drift in the response of the two channels. Demonstration of this SEPM regime opens up possibilities to study biological process (*e.g.*, the screening of drug molecules) as well as localised electrochemical activity on nanomaterials.

In summary, this thesis has shown that pipette based electrochemical measurements have significant potential to study dynamic (electrochemical) processes at the nanoscale interfaces. As WEIG has developed a versatile and advanced electrochemical operating system that has recently been available in public (www.warwick.ac.uk/electrochemistry/wec-spm), to which the author has contributed significantly, the presented methods can be further utilised and developed for a wide range of electrochemical studies at the nanoscale. Moreover, this can be integrated with spectroscopic techniques such as Raman or confocal microscopy, providing more detailed information on surface phenomena. It also needs to be noted that, especially for the SEPM techniques considered, in order to improve spatial resolution the development of more robust nanoprobe fabrication process with smaller dimensions (a few nanometers) is essential in future work, which will fulfil the demands of electrochemical activity probing at the nanoscale.